Ghent University
Faculty of Sciences
Department of Solid State Sciences
Krijgslaan 281/S1, 9000 Ghent, Belgium

Study of Chalcogenide Thin Films and Their Application as a Cation Supply Layer in Conductive Bridge Random Access Memory Devices

Wouter Devulder

Promotor: Prof. Dr. Christophe Detavernier

(Other) Members of the Jury:

Prof. Dr. Natalie Jachowicz (UGent, chair)
Dr. Ludovic Goux (imec)
Prof. Dr. Simone Raoux (Helmholtz Zentrum Berlin)
Prof. Dr. Philippe Smet (UGent)
Prof. Dr. ir. Henk Vrielinck (UGent)
Dr. ir. Dirk Wouters (RWTH Aachen University)

This research was supported by the
Agency for Innovation by Science and Technology (IWT)
through a doctoral fellowship.

Thesis submitted for the degree of
Doctor in Sciences: Physics
January 2016

Preface

In this PhD thesis, different chalcogenide materials are investigated for application as a cation supply layer in Conductive Bridge Random Access Memory (CBRAM), an emerging type of non-volatile memory. This thesis summarizes the results of the research started in September 2011 up to the end of 2015. The project was funded by a PhD scholarship from the *Agency for Innovation by Science and Technology (IWT)* and the experimental work was carried out at the Department of Solid State Sciences of Ghent University. The research was in collaboration with imec, which also provided substrates and more advanced characterization techniques that were not available in the laboratory in Ghent.

This thesis is article-based, and the presented results have been published in peer-reviewed journals. The different chapters summarize and compare the different materials that have been studied, while a detailed, more elaborated analysis can be found in the published manuscripts that are included at the end of each chapter. I hope that I managed to present the data in a comprehensive way, and that you will enjoy reading this thesis.

Wouter Devulder
Ghent, January 2016

Table of Contents

English Summary

Introduction and research questions

Nowadays, *flash* is a very popular type of non-volatile memory which can be found in USB sticks, SD-cards, solid state drives,... However, flash memory requires high programming voltages and is rather slow to program. This PhD project deals with materials research for a new type of non-volatile memory: *Conductive Bridge Random Access Memory (CBRAM)*. It is a *resistive* type of memory, where the memory states (i.e. binary 1 or 0) are conserved as different resistive states of the cell. Hence in the simplest case where a cell stores 1 bit, the cell can be cycled between a high (HRS) and low resistive state (LRS). A typical CBRAM cell consists of a cation supply layer (which typically contains copper or silver), a switching layer and a (relative) inert counter electrode. The cell can then be cycled between a high and low resistive state by growing or dissolving a conductive filament (i.e. a *conductive bridge*) through the insulating layer by applying a positive or negative bias respectively on the cation supply layer. This emerging type of memory combines good scaling potential with, in contrast to flash, low operating power and high programming speeds.

In this thesis work, chalcogenide materials (more specifically Cu and Ag containing tellurides) are investigated as cation supply layer in CBRAM. It has been shown that by using alloys, improved CBRAM functionality can be obtained. However, apart from the *functionality* of the material, also its *thermal stability* is of crucial importance, because it has to withstand processing temperatures up to typically $400°C$ during integration in a device. In this thesiswork, *in situ* X-ray diffraction is used to investigate the crystallinity, phase transformations and phase separation of the material under annealing. Also the influence of the composition is investigated, where combinatorial deposition and characterization techniques are used to allow for efficient materials screening. Next to the thermal stability of the materials, their functionality as a cation supply layer is investigated by implementing them in 580 µm diameter dot cells with a 3 nm Al_2O_3 layer as dedicated switching layer.

Binary tellurides

First copper- and silver-telluride were studied in chapter 4. An improved cycling behaviour for Cu_xTe_{1-x} in the range $0.5 < x < 0.7$ was reported in literature, and as an optimum composition, $x \sim 0.6$ was selected. The Pt/$Cu_{0.6}Te_{0.4}$/Al_2O_3/n^+

Si based cells show an improved reset compared to pure Cu as cation supply layer. This is attributed to the preferred formation of copper-telluride bonds, which is an additional driving force for the Cu from the filament to go back to the Cu-supply layer, and in this way enhances the reset. Note that Cu_2Te is also reported as a MIEC material (i.e. a *mixed ionic electronic conductor*), meaning that next to electronic conductivity, it also shows ionic conductivity (of copper ions in this case). This might improve the extraction of ions out of the switching layer, back into the supply layer and improve the reset.

The thermal stability of $Cu_{0.6}Te_{0.4}$ is rather limited. *In situ* XRD shows multiple phase transformations and phase separation. This is no surprise as multiple intermetallic Cu-Te compounds have been reported, and are present in that composition range. The major part of this thesis work hence deals with the optimization of the thermal stability of $Cu_{0.6}Te_{0.4}$, and is reported in chapter 5.

In chapter 4, Ag-Te was investigated as an alternative for Cu-Te. The binary Ag_xTe_{1-x} ($0 < x < 1$) system was deposited by means of a combinatorial sputter deposition technique. In this way, a 50 nm thin film is deposited on a 150 mm wafer, where the composition varies approximately in a linear way in one direction on the wafer. The thermal stability was investigated by means of *in situ* XRD. A single composition with the best materials properties, $Ag_{2-\delta}Te$, was selected for application as a cation supply layer in CBRAM. Its functionality was tested by implementing the material in Pt/$Ag_{2-\delta}Te$/Al_2O_3/n^+ Si dot cells. Functional CBRAM was demonstrated, and an improved reset over pure Ag was observed, like for $Cu_{0.6}Te_{0.4}$. However, higher programming currents were necessary compared to $Cu_{0.6}Te_{0.4}$ to obtain a stable filament. Hence the stability of the filament turns out to be lower than for Cu-Te based cells.

The most important conclusions of this chapter are:

- An improved reset behaviour, resulting in better cycling of the cells, is observed for memory cells with a Te-containing Cu or Ag cation supply layer compared to pure Cu or Ag.
- Higher programming currents are necessary for the $Ag_{2-\delta}Te$ based cells compared to $Cu_{0.6}Te_{0.4}$ to obtain a stable filament. For that reason, we further focussed on Cu-Te based supply layers in this thesis.
- The thermal stability of $Cu_{0.6}Te_{0.4}$ is rather limited and needs to be improved to be compatible with the temperatures that are applied during device processing ($\sim 400^\circ C$).

Ternary tellurides

The thermal stability of $Cu_{0.6}Te_{0.4}$ is improved by alloying the layer with other elements. Depending on the alloying element and the composition, intermetallic compounds may be formed. If the composition is different from the intermetallic compounds, and the material crystallizes at temperatures below $400^\circ C$, phase separation will occur, leading to an inhomogeneous supply layer. If this happens in a

device, this can result in variations of the device characteristics from device to device. This can be avoided in two ways: (i) the material should stay amorphous up to $400°C$, or (ii) a composition that crystallizes in 1 phase (that is, the composition of the intermetallic compound) should be used.

Alloying of $Cu_{0.6}Te_{0.4}$

In chapter 5, the influence of carbon, germanium and silicon as an alloying element in a $Cu_{0.6}Te_{0.4}$ layer has been investigated. Both the thermal stability and CBRAM functionality of the materials were investigated. These elements were selected because they have been reported to be effective in increasing the crystallization temperature (T_x) of phase change materials, and hence they might also increase T_x of $Cu_{0.6}Te_{0.4}$. The layers were 50 nm thin and deposited by co-sputtering from elemental sputter targets. First carbon was selected because it does not form carbides with Cu or Te, nor any ternary phase has been reported. Hence C would not make the phase sequence more complex by introducing additional phases. Carbon turns out to increase the crystallization temperature of the material. However, for concentrations up to 40 at%, T_x is lower than $400°C$, and phase separation occurs upon crystallization. If this happens in a device, this might lead to fluctuations from device to device due to inhomogeneities in the supply layer. Germanium as an alloying element also increased T_x, but the layer also crystallized below $400°C$. Silicon on the other hand is very efficient to increase T_x, and a $Cu_{0.6}Te_{0.4}$ layer with 20 at% Si avoids crystallization up to temperatures above $400°C$. Hence this material is compatible with typical process temperatures. The increased T_x is mainly ascribed to kinetic effects that avoid the reorganization of the atoms in a lattice. Formation of strong bonds between the alloying element and Cu and Te will also make the crystallization of Cu-Te phase more difficult because strong bonds need to be broken to allow reorganization in a lattice.

To summarize, although C does not form strong bonds with Cu or Te, T_x is increased significantly by the formation of strong C-C chains that hamper reorganization of the elements that is necessary for crystallization. Germanium forms bonds with Cu and Te and is a little more efficient in increasing T_x. The highest T_x is obtained for Si alloyed $Cu_{0.6}Te_{0.4}$ and can be related to the strong bonds that Si forms with Cu and Te, but also with other Si atoms. Hence strong Si chains can furthermore form an obstacle for crystallization.

Next to the thermal stability, the influence of the alloying elements on the CBRAM functionality was investigated. The different alloys showed good resistive switching behaviour when integrated in dot memory cells. The retention (i.e. how well a programmed memory state is maintained) of the different alloys was compared. While a degradation of the low resistive state (LRS) was observed for $Cu_{0.6}Te_{0.4}$, this was improved when the layer was alloyed with C, Ge and Si. The LRS degradation for $Cu_{0.6}Te_{0.4}$ can be explained by the influence of Te from the supply layer on the Cu-filament (i.e. the same mechanism that improves the reset). When the layer is alloyed with Ge and Si, these elements will also bind to Te and lower the influence of Te on the Cu from the filament, resulting in higher

LRS stability. The improved LRS stability for C can be understood because C is not miscible with Cu, and hence it results in a lower affinity of Cu towards the supply layer. For all the materials that were studied, some degradation of the high resistive state (HRS) was observed. This might be related to the low resistances that are reached in the initial cycles before programming to HRS. This can result in a large filament template path in the Al_2O_3 layer where filament reconstruction can take place. Also Cu that is left in the switching layer after reset can contribute to this filament reconstruction. The degradation of HRS was much more severe for the C-alloyed cells, which can be explained by the low affinity between C and Cu (and Te). As carbon does not form bonds with Cu, it will have a lower tendency to keep Cu in the supply layer, allowing more easy Cu diffusion in the switching layer.

The most important conclusions are:

- Carbon, germanium and silicon alloying of $Cu_{0.6}Te_{0.4}$ increases the crystallization temperature of the layer. Silicon is the most effective and addition of 20 at% increases T_x above $400°C$, making the material compatible with temperatures applied during device processing.

- The investigated alloys are functional as a cation supply layer in CBRAM cells, and they show an efficient reset like for $Cu_{0.6}Te_{0.4}$.

- Improved LRS stability was obtained for the C, Ge and Si alloyed cells compared to pure $Cu_{0.6}Te_{0.4}$.

- A fraction of the cells programmed in a HRS return to a LRS, and this is more severe for the C-containing cells.

Ternary compounds

If a ternary phase can be formed, like Cu_2GeTe_3 for the Cu-Te-Ge system, this composition can be used. Hence this phase will crystallize and a uniform composition of the supply layer is obtained.

In Chapter 5, this was done for Cu_2GeTe_3, which crystallizes at temperatures slightly above $200°C$, and has a melting temperature above $400°C$. Moreover, the material is functional as a cation supply layer for CBRAM, and shows good retention properties, making this material a promising candidate for integration in future memory devices.

In chapter 6, $CuInTe_2$ and $CuAlTe_2$ were investigated. These materials have a melting temperature far above $400°C$ and show some freedom in composition (a few atomic percent), which makes composition requirements less stringent for integration. The as-deposited layers are amorphous, but crystallize in the chalcopyrite structure upon annealing. The materials are demonstrated to be functional as cation supply layer, also showing an efficient reset. These materials are reported as MIEC, which can also contribute to the good reset behaviour.

The conclusions here are:

- Cu_2GeTe_3 combines good thermal stability with functional CBRAM characteristics that includes good retention behaviour, making this an attractive material for integration in a device.
- The ternary chalcogenides $CuInTe_2$ and $CuAlTe_2$ show good thermal stability and are functional as a cation supply layer.

Nederlandstalige Samenvatting –Summary in Dutch–

Inleiding en Onderzoeksvragen

Vandaag vormt *flash* het niet-vluchtige geheugen bij uitstek en men vindt het terug in USB geheugen sticks, SD-kaartjes, solid state drives,... Dit doctoraatsproject kadert in het onderzoek naar nieuwe types niet-vluchtig geheugen, meer bepaald naar *Conductive Bridge Random Access Memory (CBRAM)*. Men kan dit geheugentype klassificeren onder de *resistieve geheugens*, waar de geheugentoestand (binaire 0 of 1) wordt opgeslagen als een verschillende weerstandstoestand van de cel. In het eenvoudigste geval slaat een enkele cel 1 bit op en moet deze dus 2 mogelijke weerstandstoestanden kunnen aannemen (i.e. een hoog en laag resistieve toestand). Een typische CBRAM cel bestaat uit een kationenbronlaag (bevat koper of zilver), een schakellaag en een inerte tegenelektrode. De geheugencel wordt dan tussen een hoog en laag resistieve toestand geschakeld door een geleidend filament (Cu of Ag houdend, afhankelijk van de kationenbronlaag) te groeien of te verbreken in de schakellaag mits het aanleggen van een geschikte spanning op de elektrodes. Dit type geheugen heeft de eigenschap zeer goed schaalbaar te zijn en in tegenstelling tot flash bij veel lagere stromen en voltages te kunnen werken. Bovendien heeft dit type geheugen veel hogere schrijfsnelheden dan flash.

In dit thesiswerk is onderzoek verricht naar chalcogenide materialen (meer bepaald Te-houdende Cu en Ag legeringen) voor toepassing als kationenbronlaag in CBRAM. Uit onderzoek is gebleken dat koper of zilverhoudende legeringen als kationenbronlaag verbeterde CBRAM functionaliteit kunnen vertonen. Naast CBRAM *functionaliteit* is ook de *thermische stabiliteit* van deze materialen van cruciaal belang om integreerbaar te zijn in toekomstige geheugendevices. Het materiaal moet temperaturen tot $400°C$ kunnen weerstaan, zonder noemenswaardige degradatie te vertonen. In deze thesis wordt de thermische stabiliteit van verschillende chalcogenides onderzocht d.m.v. *in situ* X-stralen diffractie, die de detectie van kristallizatie, fasetransities en faseseparatie mogelijk maakt. De invloed van de compositie op de thermische stabiliteit wordt ook onderzocht, waarbij o.a. gebruik gemaakt wordt van combinatoriële depositie- en analysetechnieken zodoende een efficiënte materiaalscreening toe te laten. Naast de thermische stabiliteit worden de verschillende legeringen onderzocht op hun functionaliteit als kationenbronlaag in CBRAM door implementatie in 580 µm diameter dot geheugencellen, waarbij telkens een 3 nm Al_2O_3 laag als schakellaag fungeert.

Binaire tellurides

In hoofdstuk 4 werden eerst koper- en zilver-telluride onderzocht. Een beter schakelgedrag was reeds gerapporteerd in de literatuur voor Cu_xTe_{1-x}, waarbij $0.5 < x < 0.7$, en als optimale compositie werd $x \sim 0.6$ geselecteerd. De Pt/$Cu_{0.6}Te_{0.4}$/Al_2O_3/n^+ Si gebaseerde cellen vertonen een betere reset in vergelijking met puur Cu als kationenbronlaag. Dit wordt verklaard door het preferentieel vormen van Cu-Te verbindingen, waardoor Cu uit het filament een drijvende kracht ondervindt om terug te keren naar de telluur rijke bronlaag, wat de extractie van koper uit de schakellaag (en dus de reset) verbetert. Bovendien is Cu_2Te ook gerapporteerd als een MIEC materiaal (*Mixed Ionic Electronic Conductor*), wat betekent dat het materiaal naast elektronische ook ionaire geleidbaarheid (van Cu ionen) vertoont. Dit kan ook bijdragen tot een efficiëntere flux van ionen uit de schakellaag terug in de bronlaag, wat op zijn beurt de reset kan verbeteren.

De thermische stabiliteit van $Cu_{0.6}Te_{0.4}$ is eerder beperkt. *In situ* XRD toont verschillende fasetransformaties en faseseparatie aan, wat ook te verwachten is gezien de verschillende fases die gerapporteerd zijn in het fasediagram in dat compositiegebied. De optimalizatie van de thermische stabiliteit vormt dan ook het grootste onderdeel van dit thesiswerk en wordt behandeld in hoofdstuk 5.

Als alternatief voor Cu-Te werd in Hoofdstuk 4 Ag-Te onderzocht. Het binaire materiaalsysteem Ag_xTe_{1-x} ($0 < x < 1$) werd gedeponeerd d.m.v. een combinatoriële sputter depositietechniek. Hierbij werd in één depositierun een 50 nm laag van het binaire system gedoponeerd op een 150 mm wafer, waarbij de compositie bij benadering lineair varieert in één richting op de wafer. De thermische stabiliteit van de verschillende composities werd onderzocht d.m.v. *in situ* XRD. Hieruit werd een enkele compositie, $Ag_{2-\delta}Te$, geselecteerd die de beste thermische stabiliteit vertoonde. Het materiaal werd getest op zijn functionaliteit als kationenbronlaag in CBRAM en vergeleken met puur Ag door implementatie in Pt/$Ag_{2-\delta}Te$/Al_2O_3/n^+ Si dot cellen. Functioneel CBRAM werd aangetoond, en zoals voor $Cu_{0.6}Te_{0.4}$ konden de $Ag_{2-\delta}Te$ gebaseerde cellen efficiënter gereset worden. Ten opzichte van $Cu_{0.6}Te_{0.4}$ moesten wel hogere programmeerstromen gebruikt worden om een stabiel filament te vormen. De stabiliteit van het filament blijkt lager dan voor Cu-Te gebaseerd CBRAM.

De belangrijkste conclusies uit dit hoofdstuk zijn:

- Een beter schakelgedrag, meer bepaald een eficiëntere reset wordt waargenomen voor de Te-houdende Cu en Ag kationenbronlagen t.o.v. puur Cu of Ag.

- Een hogere programmeerstroom is nodig voor de $Ag_{2-\delta}Te$ gebaseerde cellen t.o.v. $Cu_{0.6}Te_{0.4}$ om een stabiel filament te bekomen. Daarom werd in deze thesis verder gewerkt met koper- i.p.v. zilver-tellurides.

- De thermische stabiliteit van $Cu_{0.6}Te_{0.4}$ is beperkt en moet verbeterd worden om compatibel te zijn met de temperaturen die bereikt worden bij device processing ($\sim 400°C$) .

Ternaire tellurides

De thermische stabiliteit van $Cu_{0.6}Te_{0.4}$ werd verbeterd door het legeren van $Cu_{0.6}Te_{0.4}$ met andere elementen. Afhankelijk van het legeringselement en de compositie van de legering, kunnen intermetallische fases gevormd worden. Als de compositie van de legering afwijkt van die fases zal faseseparatie optreden, wat tot een inhomogene kationenbronlaag leidt. Als dit in een device gebeurt kan dit resulteren in variaties in de schakelkarakteristieken van de cellen. Dit kan op twee manieren verholpen worden: (i) door een materiaal te nemen dat amorf blijft tot boven de $400°C$ of (ii) door een compositie te kiezen die in één fase kristallizeert (dus de compositie van die fase).

Legeren van $Cu_{0.6}Te_{0.4}$

In Hoofdstuk 5 werd de invloed van de legeringselementen koolstof, germanium en silicium op de thermische stabiliteit en de CBRAM functionaliteit onderzocht. Deze elementen werden gekozen omdat deze effectief blijken in het verhogen van de kristallizatietemperatuur (T_x) van "phase change" materialen. Lagen van 50 nm dik werden gedeponeerd d.m.v. co-sputteren van elementaire sputter targets. Koolstof werd eerst geselecteerd omdat het geen carbides vormt met Cu of Te, noch ternaire verbindingen, en op die manier de fasesequentie niet complexer zou maken. Koolstof blijkt inderdaad efficiënt te zijn om de kristallizatietemperatuur te verhogen, maar voor concentraties tot 40 at% C blijft T_x beneden de $400°C$, waarbij faseseparatie optreedt bij kristallizatie. Germanium verhoogt de kristallizatietemperatuur ook, maar ook hier kristallizeert het materiaal bij temperaturen beneden de $400°C$. Silicium daarentegen is wel zeer efficiënt om kristallizatie te voorkomen, en 20 at% Si verhindert kristallizatie tot temperaturen boven $400°C$. Dit materiaal is dus compatibel met de temperaturen die bereikt worden bij integratie van het materiaal in een device. Het uitstellen van de kristallizatie is voornamelijk toe te schrijven aan kinetische effecten die de reorganistatie van de atomen in rooster moeilijker maakt. De interactie van het legeringselement met Cu en Te (i.e. de bindingssterkte) zal de vorming van Cu-Te fases ook beïnvloeden aangezien bij kristallizatie deze bindingen verbroken moeten worden om reorganisatie in een rooster toe te laten.

Samenvattend kunnen we stellen dat ondanks dat koolstof geen sterke bindingen vormt met Cu en Te, T_x aanzienlijk verhoogd wordt door vorming van sterke C-C kettingen die een hindernis vormen voor kristallizatie van Cu-Te fases. Germanium vormt wel bindingen met Cu en Te, en is iets efficiënter in het verhogen van T_x. De hoge kristallizatie temperatuur voor Si gedopeerd $Cu_{0.6}Te_{0.4}$ is voornamelijk te wijten aan de sterkte bindingen van Si met Cu en Te, maar ook met andere Si atomen, zodat Si ketens een extra hindernis vormen voor kristallizatie.

Naast de thermische stabiliteit werd ook de invloed op de CBRAM functionaliteit onderzocht. De verschillende legeringen vertonen goed resistief schakelgedraag als ze geïmplementeerd worden in macroscopische cellen. De retentie (i.e. hoe goed een geprogrammeerde geheugentoestand behouden blijft) werd vergele-

ken voor de verschillende materialen. Terwijl voor $Cu_{0.6}Te_{0.4}$ een degradatie van de laag resistieve toestand (LRS) werd gemeten, verbeterde dit voor de materialen gelegeerd met C, Ge en Si. De lagere LRS stabiliteit voor $Cu_{0.6}Te_{0.4}$ kan begrepen worden door de invloed van Te in de bronlaag op het Cu-filament (zoals het ook de reset verbetert). Als de laag gelegeerd wordt met Ge of Si gaan deze elementen ook met Te binden, waardoor de invloed van Te op Cu verlaagd wordt, wat op zijn beurt de LRS stabiliteit verbetert. De verhoogde LRS stabiliteit in het geval van C kan begrepen worden door de lagere affiniteit van Cu naar de bronlaag doordat Cu niet mengbaar is met koolstof. Voor alle materialen werd wel een zekere degradatie van de hoog resistive toestand (HRS) naar LRS waargenomen. Dit kan te wijten zijn aan de lage weerstanden die bereikt worden in de initiële switches voordat de cel in HRS geprogrammeerd wordt. Dit kan een groot "template" pad in de Al_2O_3 laag veroorzaken waar Cu gemakkelijk in diffundeert en een filament gereconstrueerd wordt. Ook Cu dat bij de reset niet uit de schakellaag verwijderd was kan hiertoe bijdragen. De HRS degradatie was veel beduidender voor C-gedopeerd $Cu_{0.6}Te_{0.4}$, wat verklaard wordt door de lage affiniteit tussen C en Cu (en Te). Koolstof vormt geen bindingen met Cu, en gaat minder goed het Cu in de bronlaag houden, waardoor het veel makkelijker terug in de schakellaag een geleidende brug gaat vormen.

De belangrijkste conclusies zijn:

- Het legeren van $Cu_{0.6}Te_{0.4}$ met koolstof, germanium en silicium verhoogt de kristallizatietemperatuur. Si is hiervoor het meest effectief en stelt de kristallizatie uit tot temperaturen boven $400°C$, wat het materiaal compatibel maakt met typische proces temperaturen in geheugendevices.
- De onderzochte materialen zijn functioneel as kationenbronlaag in CBRAM, en vertonen nog steeds een efficiënte reset zoals voor $Cu_{0.6}Te_{0.4}$.
- Een verbeterde LRS stabiliteit werd bekomen voor de geheugencellen met C, Ge en Si legeringen t.o.v. $Cu_{0.6}Te_{0.4}$.
- Er is steeds een fractie van de HRS die naar een LRS terugkeren en dit is veel beduidender voor de C-houdende $Cu_{0.6}Te_{0.4}$-gebaseerde cellen.

Ternaire fases

Wanneer een ternaire fase gevormd kan worden, zoals Cu_2GeTe_3 in het Cu-Te-Ge systeem, kan deze compositie nagestreefd worden. Als het materiaal kristallizeert zal enkel deze fase gevormd worden, zodat een uniforme compositie behouden blijft.

Dit werd in Hoofdstuk 5 gedaan voor Cu_2GeTe_3, en deze fase kristallizeert net boven $200°C$, en smelt boven de $400°C$. Dit resulteert in een materiaal dat compatibel is met de proces temperaturen tijdens integratie. Het materiaal is functioneel als kationenbronlaag en vertoont een goede retentie van de geheugentoestanden.

In dit opzicht werden in Hoofdstuk 6 ook $CuInTe_2$ en $CuAlTe_2$ onderzocht. Deze materialen hebben een hoog smeltpunt (ruim boven de $400°C$) en bovendien

hebben ze een zekere vrijheid (enkele procenten) in compositie, wat integratie een stuk eenvoudiger maakt. De gedeponeerde lagen waren amorf maar kristallizeerden na anneal in één fase, de chalcopyrite kristalstructuur. Deze materialen vertoonden functioneel CBRAM gedrag, met een efficiënte reset. Bovendien zijn deze materialen ook gerapporteerd als MIEC materialen, wat ook kan bijdragen tot de goede reset.

De belangrijkste conclusies zijn:

- Cu_2GeTe_3 combineert goede thermische stabiliteit met functioneel CBRAM en goede retentie-eigenschappen, wat het een potentieel materiaal maakt voor integratie in een device.
- De ternaire chalcogenides $CuInTe_2$ en $CuAlTe_2$ vertonen goede thermische stabiliteit en zijn functioneel als kationenbronlaag.

List of Abbreviations

ALD	atomic layer deposition
BEOL	back end of line
CBRAM	conductive bridge random access memory
CF	conductive filament
CMOS	complementary metal-oxide-semiconductor
CV	cyclic voltammetry
ECM	electrochemical metallization bridge/cell
ERD	elastic recoil detection analysis
EDX	energy dispersive X-ray fluorescence spectroscopy
HRS	high resistive state
I_c	compliance current
IC	integrated circuit
ITRS	International Technology Roadmap for Semiconductors
LRS	low resistive state
MIEC	mixed ionic electronic conductor
MIM	metal-insulator-metal
MOSFET	metal-oxide-semiconductor field-effect transistor
NVSM	non-volatile semiconductor memory
PCM	phase change memory
PMC	programmable metallization cell
PVD	physical vapour deposition
RAM	random access memory
RBS	Rutherford backscattering spectroscopy
RRAM	resistive random access memory
SMU	source-measure unit, sourcemeter
T_g	glass transition temperature
T_x	crystallization temperature
XPS	X-ray photoelectron spectroscopy
XRD	X-ray diffraction
XRF	X-ray fluorescence spectroscopy
XRR	X-ray reflectivity

1 Introduction

1.1 Moore's law

The development of the transistor in 1947 by John Bardeen, Walter Brattain and William Shockley triggered a revolution in the field of electronics [1]. Nowadays, transistors are packed in integrated circuits (IC) allowing extreme high densities on a single chip. In 1965, Gordon E. Moore predicted that the number of transistors on an IC would increase exponentially over time. Since 1970, the number of components on a chip has doubled every two years, and this trend has become known as *Moore's law* [2]. Next to the transistor concept, also other components are of crucial importance for the development of the fast, powerful computers that we have today. One of them is *non-volatile semiconductor memory* (NVSM) which has a structure that is very comparable to a MOSFET (Metal-Oxide-Semiconductor Field-Effect Transistor), except that a *floating gate* is sandwiched between a tunnel oxide and a blocking oxide/gate stack. The floating gate is added to store electrical charge. The concept of a floating gate to obtain a non-volatile memory was proposed for the first time in 1967 by Kahng and Sze [3]. This concept is the backbone for FLASH memory technology that is widely used nowadays in USB memory sticks, solid state drives (SSD), smartphones, etc. The storage capacity of these devices increased tremendously the past decades due to cell size scaling and an increased density of states per memory cell (i.e. multilevel cells where a

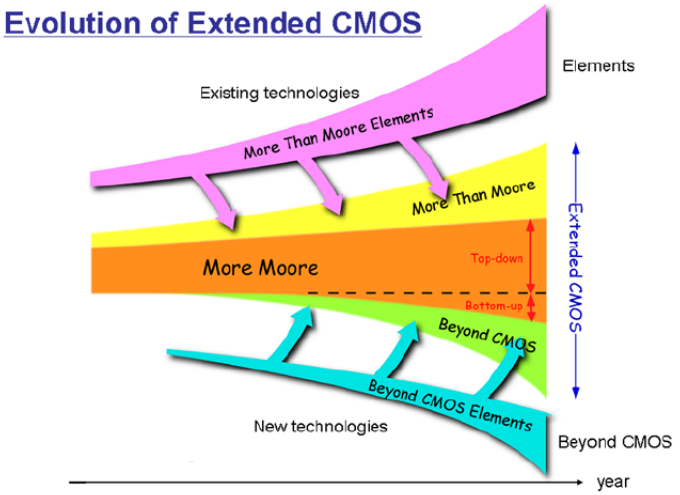

Figure 1.1. *The evolution to extended CMOS by combining continued scaling (More Moore) with new devices that allow scaling beyond CMOS (Beyond CMOS) and extension of the CMOS functionality by heterogeneous integration of new technologies (More than Moore). [6]*

single cell can store multiple bits). However, dimensional CMOS[1] scaling will eventually approach its fundamental limits. Scaling of Flash imposes additional challenges because of the difficulty in the tunnel oxide scaling, which cannot be too thin because it would induce leakage of charge from the floating gate, resulting in short retention times (i.e. less than the required ten years) [4]. Although the limited scaling of Flash has been announced already for a while, scaling to the 20 nm node has been realized [5].

To keep up with the scaling trend (or at least the decreasing cost per function trend) in the future, the International Technology Roadmap for Semiconductors (ITRS)[2] sees three main contributions which are schematically illustrated in Figure 1.1 [6]. First there will be a continued horizontal and vertical shrinking of the feature size of the devices to reduce the cost and to improve performance. This is referred to as *More Moore*. Secondly, new devices are investigated that may have much better scaling potential than traditional CMOS components[3], and these are

[1] CMOS stands for Complementary Metal-Oxide-Semiconductor and is a technology for constructing integrated circuits where both n-type and p-type MOSFETS are used in logic functions.

[2] The ITRS is sponsored by the leading chip manufacturing regions in the world: Europe, Japan, Korea, Taiwan and the United States. The Roadmap teams identify the technological challenges for the semiconductor industry and how these can be addressed in the future. With specifications for current and future technologies it provides research guidance in the field (`http://www.itrs.net/home.html`).

[3] These devices are mainly covered in the Emerging Research Device section in the ITRS [6].

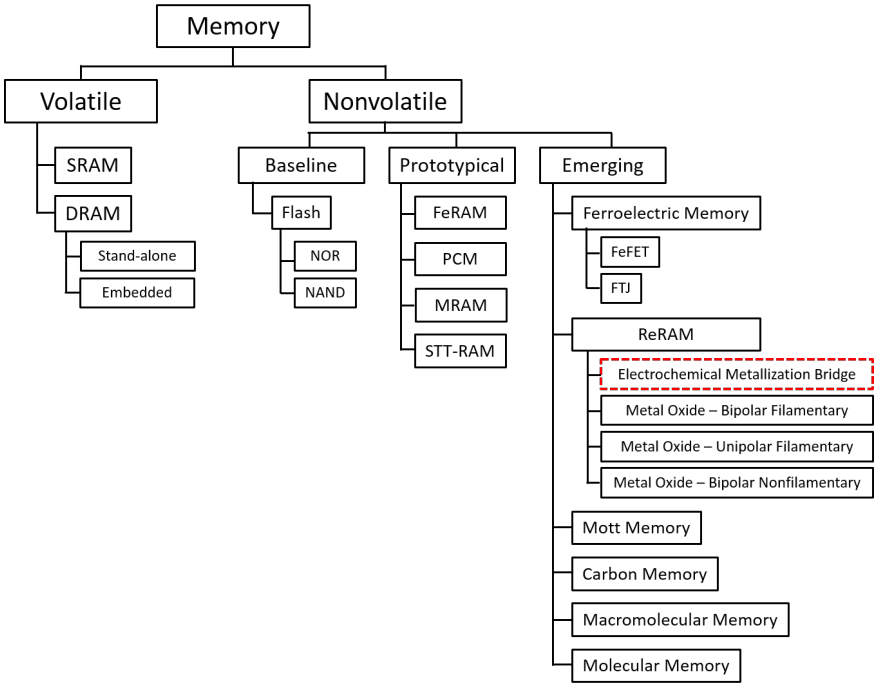

Figure 1.2. *The taxonomy of (emerging) memory devices (reproduced from [6]). The memory type that is studied in this work (electrochemical metallization brigde, better known as conductive bridge RAM) is highlighted.*

denoted by *Beyond CMOS*. As a third contribution, new technologies that do not necessarily scale according to Moore's law, but that add additional functionality to the device can be included. This includes Micro-Electro-Mechanical Systems (MEMS) like pressure sensors, accelerometers and lots of other intelligent components to interact with the outside world [7]. This is summarized under the term *More than Moore* [2, 8]. The combination and integration of the *Beyond CMOS* and *More than Moore* elements with further scaling (*More Moore*) will form the ultimate *Extended CMOS*.

1.2 Emerging memory technologies

New memory technologies that show better scaling properties and lower power consumption than current semiconductor memories are currently investigated. These devices can be categorized under the *beyond CMOS* elements in Figure 1.1. Figure 1.2 illustrates the taxonomy of the different memories according to the ITRS [6]. Although it is not the intention to discuss all the different technolo-

gies, Figure 1.2 gives a concise overview of the current memories, the prototypical and emerging technologies. First, memories are distinguished in their ability to retain data when they are powered off, as either *volatile* or *non-volatile*. Examples of volatile memory are DRAM and SRAM (Dynamic and Static Random Access Memory respectively). DRAM, the main RAM used in personal computers, makes use of a capacitor that is being charged or discharged (representing 1 or 0). It is *dynamic* in the sense that it needs to be periodically refreshed (i.e. the memory state has to be reprogrammed) because the capacitors will "slowly" discharge and lose the memory state. However, DRAM is very fast and allows high memory densities. SRAM is also volatile, but is *static* in the sense that it does not need to be periodically refreshed. It is faster than DRAM but has a lower density. It is typically used as CPU (Central Processing Unit) cache[4].

Among the non-volatile memories, we find Flash memory in general, which is a mature technology, and its two types NOR and NAND Flash. NAND Flash allows the highest densities and is used in storage applications as USB memory sticks and SSD's. The *prototypical devices* are at a point of maturity where they are commercially available, but generally only for very specific applications. The *emerging memories* are the least mature, but they show significant potential if various scientific and technological hurdles can be overcome. Among them we find the *Resistive Random Access Memories* (ReRAM or RRAM). Here, the memory states (i.e. logic 0 or 1) are kept as different resistive states of the memory cell. Typically these cells can be cycled between a high and low resistive state by applying the according voltage signals on the cells. The term *Random Access* means that all cells are equally accessible.

Among the resistive memories, we find the *Electrochemical Metallization Bridge*, also commonly referred to as *Conductive Bridge Random Access Memory* (CBRAM). Such memory cells have a simple Metal-Insulator-Metal structure and can be cycled between a high and low resistive state by the formation of a conductive filament through the insulating layer. In this thesis we will focus on materials for this type of RRAM. CBRAM is a promising non-volatile memory concept that allows fast and low power operation, and good scalability. As a comparison between the current memories and CBRAM, Figure 1.3 shows their programming time as a function of the write energy, with the size of the point being proportional to the write voltage. The figure[5] was made by means of numbers reported in the *Emergering Research Devices* section of ITRS 2013 edition [6]. For CBRAM, the demonstrated values are used, and even better values can be expected in the future. The plot illustrates how Flash memories are rather slow in programming and require high programming voltages (15-20 V for NAND Flash). CBRAM on

[4] CPU cache is a memory component that stores data so that it can be accessed very fast by the CPU for future use.

[5] See tables ERD 3 and ERD 4 [6]. For the emerging technologies, the best demonstrated values were used.

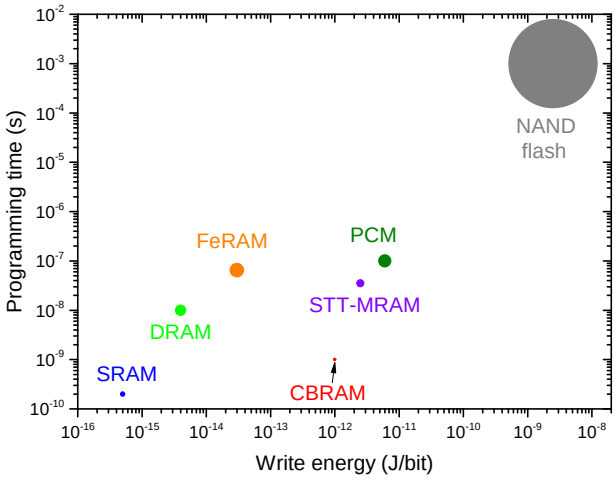

Figure 1.3. *Comparison between the current memories, some prototypical devices and CBRAM in terms of write energy (x-axis), programming speed (y-axis) and operating voltage (size of the symbol). Figure made from ITRS data [6] and the Flash energy consumption from Mohan et al. [9]*

the other hand has programming voltages as low as 0.6 V, and programming times that are in the range of nanoseconds. With this switching speed it is comparable to DRAM. If the endurance is high enough it can even replace DRAM. Replacing volatile memory with a non-volatile type would invoke a large reduction of power consumption because DRAM now continuously has to be refreshed (i.e. read and restore the data before it gets lost). The potential of CBRAM and the importance to further investigate this technology might already be clear from this short introduction. More information on CBRAM is given in Chapter 2.

1.3 Goal and outline of this thesis

CBRAM is a strong emerging memory candidate due to its high scalability ($\sim$10 nm), fast and low energy programming/read operations, and low voltage requirements. However, according to the ITRS, the main hurdles for CBRAM that need to be overcome are [6]:

- bit level variability
- random telegraph noise (RTN)
- reliability (endurance and retention)

- integration of new materials and issues with compatibility of thermal budgets and process tools.

In this thesis work, chalcogenide materials are investigated for application as a cation supply layer in CBRAM devices. From the above mentioned issue list, the *thermal stability* of the chalcogenide materials will be investigated and improved in order to be compatible with the thermal budget that is applied in device processing. To be compatible with temperatures reached during back end of line (BEOL) processes, the materials should be stable up to about $400°C$. Next to the thermal stability, the functionality of the materials as a cation supply layer in CBRAM is studied. The material is implemented in dot memory cells that can be tested on their cycling behaviour and retention of the memory states. Hence a second point of the issue list, the *reliability*, with a focus on the retention is dealt with, and the different materials are compared.

In Chapter 2 the operation principle of CBRAM is explained, and a short overview of the reported materials that are used in typical CBRAM stacks is given. A motivation for the materials that are used in this work is also provided. Chapter 3 gives an overview of the experimental techniques that were applied in order to deposit and characterize the different materials.

In chapters 4, 5 and 6, the results obtained in this thesis are presented. Every chapter gives an introduction and motivation of the work, and summarizes the main results in standardized plots to enable direct comparison between the different materials that have been investigated. Detailed discussions are provided in the published manuscripts at the end of each chapter. Chapter 4 discusses the binary Cu-Te and Ag-Te chalcogenides. In Chapter 5, the thermal stability of Cu-Te is improved by alloying with C, Ge and Si. Alternative ternary chalcogenides Cu(In,Al)Te_2, which were selected on their theoretical materials properties, are investigated and discussed in Chapter 6. Chapter 7 gives a conclusion and outlook for further work.

References

[1] Wikipedia The Free Encyclopedia, https://en.wikipedia.org/wiki/Transistor. *Transistor*.

[2] *"More-than-Moore" White Paper*. http://www.itrs.net/papers.html.

[3] Kahng, D. and Sze, S. *The Bell System Technical Journal* **46**, 1288–1295 (1967).

[4] Meena, J., Sze, S., Chand, U., and Tseng, T.-Y. *Nanoscale Res. Lett.* **9**(1), 526 (2014).

[5] Techinsights. *Technology Roadmap for NAND Flash Memory*.

[6] ITRS 2013 - The international Technology Roadmap for Semiconductors. *Emerging Research Devices*.

[7] ITRS 2013 - The international Technology Roadmap for Semiconductors. *Micro-Electro-Mechanical Systems (MEMS)*.

[8] Arden, W., Brillout, M., Cogez, P., Graef, M., Huizing, B., Mahnkopf, R., abd Jens-Uwe Pfeiffer, J. P., Rouzaud, A., Tartagni, M., Hoof, C. V., and Wagner, J. *Towards a "More-than-Moore" Roadmap*. CATRENE Scientific Committee, (2011).

[9] Mohan, V., Bunker, T., Grupp, L., Gurumurthi, S., Stan, M., and Swanson, S. *IEEE Transactions on Computer-Aided Design of Integrated Circuits and Systems* **32**(7), 1031–1044 (2013).

2

Conductive Bridge Random Access Memory

This chapter summarizes the operation and structure of a typical CBRAM cell. After a short introduction, the different processes that occur and contribute to resistive switching are briefly discussed in section 2.2. The materials that are typically used for the different layers in the memory stack are discussed in section 2.3 together with the materials that will be studied in this work.

2.1 Introduction

Conductive Bridge Random Access Memory (CBRAM) is a type of Resistive RAM (RRAM). In this type of memory devices, the logic states (0 and 1) are stored as a high (HRS) or low resistive state (LRS). Note that if more resistive states can be obtained, multiple bits can be stored in a single cell, which is known as *multilevel programming* and is also used in Flash technology to reach higher memory densities. Different types of RRAM are reported, but we can state in general that they have typically a Metal-Insulator-Metal (MIM) structure. The resistance of the cell can then be changed by growing or dissolving a conductive filament (CF) through the insulating layer. Depending on the materials that are used, the filament can be formed by Ag or Cu (that originates from a Cu or Ag containing electrode), or by oxygen vacancies. In the former, the LRS is formed due to a metallic filament, whereas for the latter the oxygen vacancies change the

valence state of the cation sublattice, resulting in a change in conductivity. The former is typically referred to as CBRAM[1] whereas the latter is typically referred to as Valence Change Memory (VCM). In this work we will further discuss and investigate the CBRAM concept. For more information on other types of RRAM, the reader is referred to literature [1–4].

2.2 Structure and operation of CBRAM

The MIM structure in a CBRAM cell typically consists of a Cu or Ag containing layer (the *electrochemically active electrode*), an insulating layer and an (relative) inert bottom electrode (Pt, Au, W, Ir,...). The reason why Cu or Ag are typically used as active electrode is because of their high ion mobility and ease of cation formation and their reduction [3]. Figure 2.1 shows a typical CBRAM stack and the resistive switching phenomenon when a triangular voltage sweep is applied, with Cu as example for the active electrode, and a switching layer with high ionic conductance[2]. The SET process where the cell is switched from a high to a low resistive state (positive voltage range in figure 2.1) occurs when a sufficient high positive voltage is applied on the Cu electrode. It contains the following steps:

- Anodic dissolution of Cu (Metal M) according to the reaction

$$\mathrm{M} \rightarrow \mathrm{M}^{z+} + ze^{-}. \tag{2.1}$$

  This is occurs in step (2) in Figure 2.1.

- Migration of the M^{z+} cations through the solid electrolyte towards the counter electrode under influence of the electric field. This occurs in steps (2) and (3) in Figure 2.1.

- Reduction and electrocrystallization of M on the surface of the (inert) counter electrode according to the cathodic deposition reaction

$$\mathrm{M}^{z+} + ze^{-} \rightarrow M. \tag{2.2}$$

  This occurs in step (3) in Figure 2.1.

In this way, a conductive Cu filament is formed. Upon *bridging* both electrodes, the cell resistance suddenly drops, and the current increases. Typically, the current is then limited (by a series transistor or resistor, or by the measurement device)

[1] In literature, other terms like Electrochemical Metallization bridge/cell (ECM) and Programmable Metalization Cell (PMC) are also used.

[2] The filament growth and shape generally depends on the nature of the switching layer, which is discussed more in detail in section 2.3.2.1.

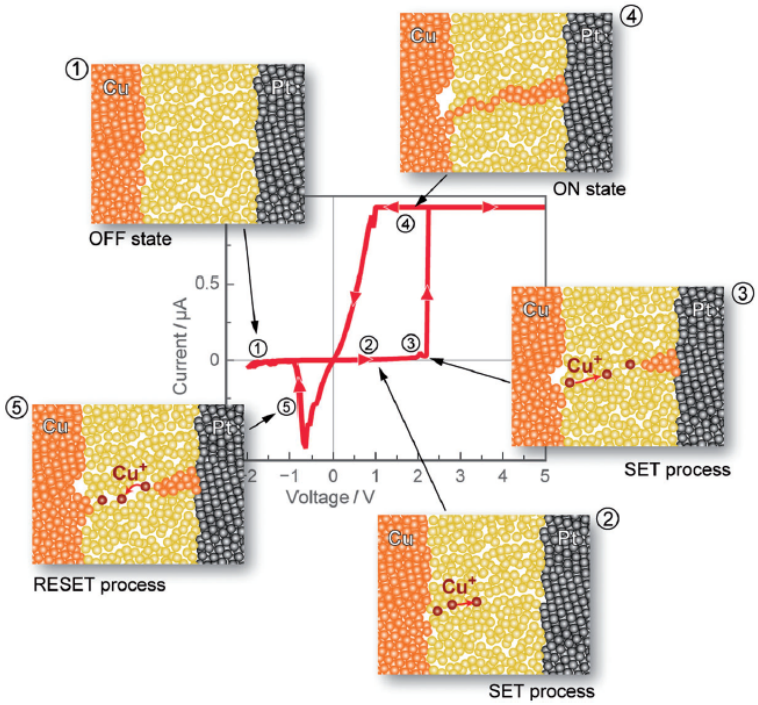

Figure 2.1. *Typical IV-curve of a Cu/solid electrolyte/bottom electrode CBRAM cell when a triangular voltage sweep is applied ($0\,V \rightarrow \pm\,3\,V \rightarrow 0\,V$ for set/reset), and the general accepted switching mechanism at every step in the switching cycle. (1) The cell is in a HRS. (2) By applying a positive bias on the Cu electrode, Cu is oxidized and Cu^{z+} cations move towards the counter electrode under influence of the electric field where (3) the cations reduce to form metallic copper. In this way a filament is grown that switches the cell to a LRS upon bridging both electrodes (4). (5) Applying a bias of opposite polarity causes oxidation of the filament (Cu^{z+} formation) and migration of the cations back to the Cu electrode, resulting in filament dissolution and switching the cell back to the HRS. [4]*

to the *compliance current (I_c)* to avoid overgrown filaments[3]. Consequently, in the erase operation by applying a sufficiently large negative voltage on the active electrode, the Cu is oxidized at the conductive filament side and the ions migrate back to the active electrode. When the bridge is broken, the cell switches back to the HRS (step 5 in Figure 2.1). This is the general accepted working hypotheses, however more physics than the simple concept above is involved, and research to

[3]It is generally demonstrated that the filament strength is related to the programming current (see section 2.2.4.2). If the current is not limited during set, the filament might become too strong which makes it impossible to reset the cell.

revealing the exact switching mechanism is still ongoing [5–8]. Note that the different material systems that are used can also invoke a slightly different switching mechanism, which is covered in section 2.3. However, they all rely on the formation and dissolution of a conductive filament through an insulating layer. In the following sections, we discuss the mechanisms governing CF formation more in detail.

2.2.1 Charge transfer: oxidation and reduction

Applying a positive bias on the active electrode causes Cu atoms to get ionized to Cu^{z+}, while the ions get reduced at the counter electrode. The current density i at the electrode/electrolyte interface at steady state conditions due to the anodic oxidation and cathodic reduction is given by the *Butler-Volmer* equation [1, 2, 9]:

$$i = i_0 \left[\exp\left(\frac{(1-\alpha) z_i e}{k_B T} \eta \right) - \exp\left(-\frac{\alpha z_i e}{k_B T} \eta \right) \right]. \tag{2.3}$$

In this equation, i_0 is the exchange current density, α the charge transfer coefficient and η the electrochemical overpotential. The overpotential η is the difference between the potential measured at equilibrium and the externally applied potential. Applying a voltage on the electrode changes the activation energy for a forward (oxidation) or backward (reduction) reaction, and is proportional to the applied voltage. This proportionality factor is the charge transfer coefficient α and the sum of the transfer coefficients for the anodic and cathodic reaction is one. The first term in equation 2.3 represents the anodic reaction, the second term the cathodic process. It is clear that for large η one of the terms can be neglected and an exponential relation applies. Figure 2.2 graphically illustrates the influence of an external applied potential on the energy diagram for the charge transfer reaction. By applying a positive bias ϕ on the active electrode, the Fermi level in the metal is shifted by the applied electrical potential and the barrier for electron transfer from the metal atom towards the metal electrode is reduced by $\alpha z e \phi$, making oxidation easier. The figure also includes the formation of a *space charge layer* that is formed at the electrode/electrolyte interface[4].

2.2.2 Ion migration and CF growth

After oxidation of the active species, the ions have to migrate towards the counter electrode where they are reduced. The migration can be described by the *Mott-Gurney* model for electric field driven, thermally activated ion hopping between

[4] A space charge layer can appear at the contact interface between the metal and the electrolyte. The potential is constant in the metal and then first drops linearly over a few Angstrom (at least one atomic radius) in the electrolyte and then more slowly towards the bulk value. The former is called the Helmholtz part and is denoted as the *Helmholtz double layer*. [2]

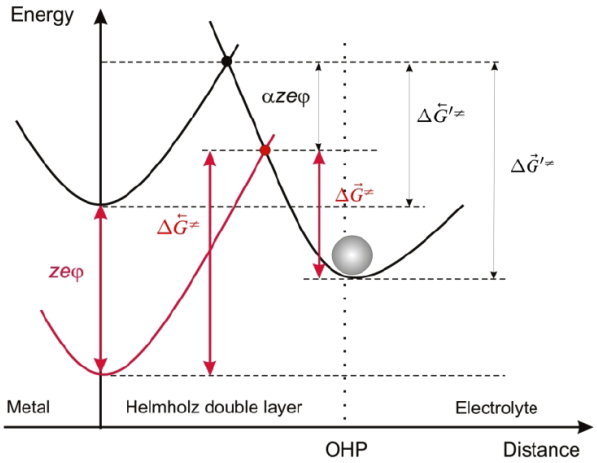

Figure 2.2. *Graphical representation of the potential energy diagram for the charge transfer reaction. The symbols $\Delta\vec{G}^{\neq}$, $\Delta\overleftarrow{G}^{\neq}$, $\Delta\vec{G}'^{\neq}$, $\Delta\overleftarrow{G}'^{\neq}$ represent the activation enthalphies for the forward (oxidation) and backward (reduction) reactions without and with applied potential ϕ respectively. In the figure a positive potential ϕ is applied, resulting in a lowering of the activation enthalphy $\vec{G}^{\neq}$ for oxidation by $\alpha ze\phi$. OHP stands for the outer Helmholtz plane. [2]*

adjacent sites. The ionic current density i is then described by [1, 9, 10]

$$i = 2zeca\nu \exp\left(-\frac{W_a^0}{k_BT}\right) \sinh\left(\frac{azeE}{2k_BT}\right), \tag{2.4}$$

with W_a^0 the energy barrier. The driving force for the ion migration is the electric field strength E, which is given by $E = \Delta\phi_{SE}/d$. Here $\Delta\phi_{SE}$ is the potential drop over the solid electrolyte and d the thickness of electrolyte layer. The concentration of the mobile cations is denoted by c, a is the jump distance of the ions and ν is a frequency factor. For high electric fields ($E \gg k_BT/aze$), this results in an exponential dependence of i on E:

$$i = zeca\nu \exp\left(-\frac{W_a^0}{k_BT}\right) \exp\left(\frac{azeE}{2k_BT}\right). \tag{2.5}$$

For low electric fields ($E \ll kT/aze$), equation 2.4 can be approximated by

$$i = \frac{(ze)^2cE}{k_BT}a^2\nu \exp\left(-\frac{W_a^0}{kT}\right) = \frac{(ze)^2cD\Delta\phi_{SE}}{k_BTd}, \tag{2.6}$$

which is the Nernst-Einstein relation giving the temperature dependence of the ionic conductivity. In this equation, $D = a^2\nu \exp(-W_a^0/k_BT)$ is the diffusion coefficient.

2.2.3 Nucleation of the metal phase

When the Cu^{z+} ions reach the bottom electrode, the charge transfer reaction for reduction takes place. However, formation of a metallic filament that grows on the counter electrode includes the nucleation and growth of a new phase (i.e. the Cu metallic phase). For large cathodic overpotentials, the critical nuclei usually consist only of a few atoms, and the atomistic theory for stationary nucleation predicts an exponential relation between the nucleation rate J and the overpotential η [1, 11, 12]:

$$J = K\left(Z_0, N_c\right) \exp\left(\frac{(N_c + \alpha) z e}{k_B T} \eta\right). \tag{2.7}$$

The pre-exponential factor $K(Z_0, N_c)$ depends on the number density of the nucleation sites Z_0 and on the number of atoms N_c constituting the critical nucleus.

2.2.4 Resistive switching of CBRAM cells

The discussed mechanism of resistive switching comprises the oxidation and reduction of the active species (described by equation 2.3) and the ion transfer through the electrolyte layer (equation 2.4). Usually, one of these steps will be the rate limiting step, determining the overall cell kinetics. Figure 2.3 shows the switching voltage as a function of the pulse width for $W\backslash Al_2O_3\backslash Ti\backslash CuTe$ CBRAM cells[5]. An exponential behaviour is observed, and can be fitted by Mott-hoping of Cu^+ species. The extracted hopping distance Δz is in agreement with the spacing between oxygen sites in ab initio generated amorphous Al_2O_3[13]. In the same graph it is observed that for long pulses, the switching is redox limited. For linearly varying voltage sweeps[6] with a sweep rate of $0.5\,V/s$ from 0 to 3 V and back, one can approximate this with a pulse[7] of $\sim$3 s. This is indeed in the DC regime in Figure 2.3, and on the border of the regime where Mott hoping is the rate limiting step. Hence in case of DC switching, both mechanisms may be important and determine the cell kinetics.

In the following subsections, we summarize some of the CBRAM properties that are relevant to this work, and show that simulations in literature (based on the basic mechanisms that were discussed in previous sections) reproduce this quite well [9, 10, 13].

2.2.4.1 Voltage-time dilemma

The *voltage-time dilemma* refers to the requirement for CBRAM to switch very fast (order of ns) and to have a long data retention time (i.e. under small volt-

[5] This example is given, because it is very similar to the used memory stack in this work.
[6] In this work, DC switching is used to characterize the cells, as discussed in section 3.5.2.
[7] This is done by taking $1/4$ of the period of the set sweep [14].

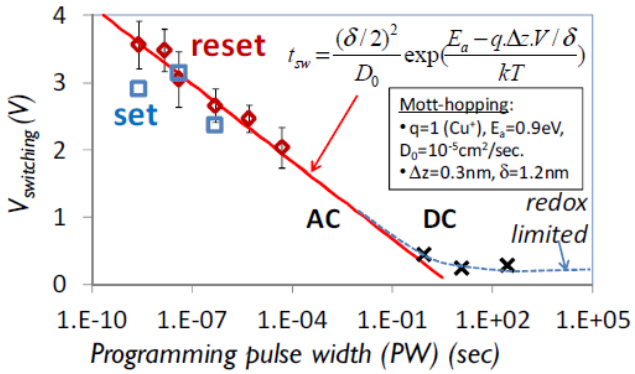

Figure 2.3. *Switching voltage as a function of the set or reset pulse width showing an exponential relation. The behavior can be modelled by Mott-hopping of Cu^+ species. ($W\backslash Al_2O_3\backslash Ti\backslash CuTe$ 1T1R CBRAM system) [13]*

ages and elevated temperatures it should keep its resistive state for years). This requires a strong non-linear field dependence in switching dynamics. This can be expected from the exponential dependence of the oxidation/reduction reaction (equation 2.3) and the hyperbolic sinusoidal dependence in the ion migration (equation 2.4). The exponential behaviour of the switching time on the applied voltage is also clear from Figure 2.3 for a $W\backslash Al_2O_3\backslash Ti\backslash CuTe$ CBRAM cell. Fast switching (i.e. short programming pulses) requires larger programming voltages, and the switching speed is limited by ion transport as modelled with Mott-hopping. For low switch voltages, the process is redox limited.

2.2.4.2 Influence of compliance current

It has been shown that by varying the compliance current, the resistance of the low resistive state can be adapted [9, 10, 15–17]. Higher compliance currents lead to lower LRS resistances or stronger filaments. This is expected to be the result of radial growth of the conductive filament (see also Figure 2.4), resulting in a thicker filament [9]. This sets the cell in a LRS state with lower resistance. A very nice paper was presented by Russo et al. [9], where the switching of a $Ag/GeS_2/W$ CBRAM cell was investigated and the results compared to simulations. The device was connected in series with a load resistor R_{load} to limit the current through the cell once it was set to a LRS. The cells were programmed using voltage pulses rather than linearly varying voltage sweeps. The voltage over the cell (V_C) as a function of time when a voltage pulse V_A is applied is given in Figure 2.4a, and the associated filament formation in Figure 2.4b. Figure 2.4a shows that when a pulse with amplitude V_A is applied during the time interval t_W, the cell switches to a low resistive state at t_1. It is also observed that after t_1, the voltage further

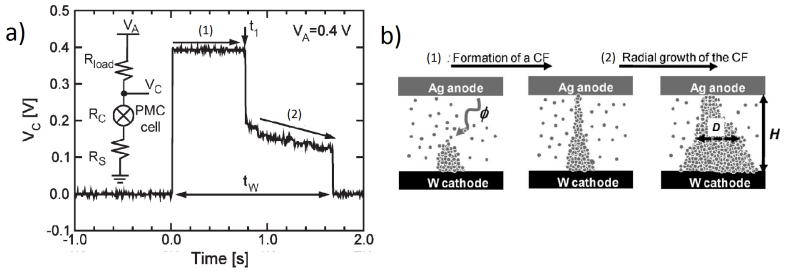

Figure 2.4. *(a) Cell voltage (V_c) as function of time when a voltage pulse V_A is applied over the memory device (Programmable Metallization Cell, PMC) and load resistance (R_{load}). A series resistance R_S was taken into account for resistances due to wiring. (b) Filament formation mechanism. [9]*

drops because the resistance of the filament further decreases. This suggests that the filament is becoming thicker (as illustrated in figure 2.4b). The associated cell resistance first decreases rapidly, but this slows down because of the decreasing voltage drop V_C over the cell due to the voltage divider $R_C/(R_{load} + R_C)$. This is also illustrated in Figure 2.5a. Indeed, the red dashed line represents the load line of R_{load}, and the black lines the IV characteristics for the memory cell in different resistive states. Initially, the cell is in a high resistive state, corresponding with the IV curve with the smallest slope (largest R_C). A large cell voltage V_C is present over the cell, which results in fast programming and in a sudden drop of R_C. The cell switches to a low resistive state, hence the slope of the IV curve increases, and we move to smaller voltages on the load line, and hence smaller voltages over the cell, which results in a slower decrease in R_C (i.e. step (2) in Figure 2.4a) due to radial filament growth. In the paper, it is shown that the radial filament growth follows a very similar growth mechanism as the initial CF formation (step (1) in Figure 2.4), and hence is also based on oxidation/reduction and ion migration [9]. The programming dynamics above show that the low resistive state can be modified by varying the pulse width (see Figure 2.5b) or the cell voltage V_C (see Figure 2.5c). Here V_C was changed by applying the same voltage pulse and by varying the load resistor[8]. Changing the pulse length with many orders of magnitude is less effective in varying the resistance (there is still a large spread), what is also to be expected due to the converging resistance towards lower values as function of time (see figure 2.4a). Changing the load resistor shows a better distinction between different low resistive states, which could be useful for multilevel

[8]This is the most convenient way for applications, where the resistor can then for example be replaced by a MOS transistor.

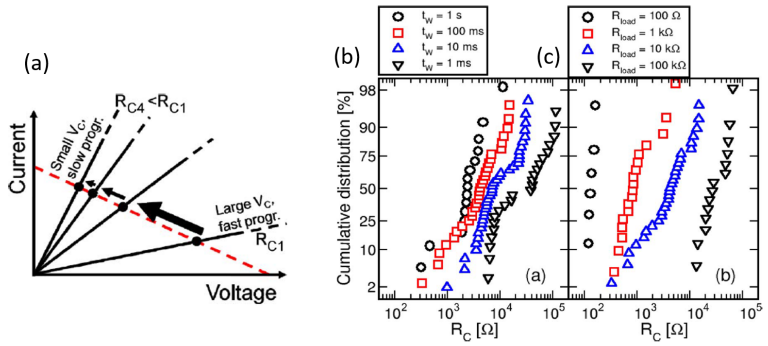

Figure 2.5. *(a) Graphical representation of the programming of a PMC cell that is in series with R_{load} (red dashed line). For large V_C, the cell switches fast. When the cell switches from HRS to a lower resistance, the potential V_C decreases because of the voltage divider $R_C/(R_{load} + R_C)$, hence it evolves towards a low V_C, where programming will be slow, explaining the saturating LRS resistance. (b) Cumulative distribution of the LRS resistance with varying pulse width or (c) with varying load resistor (the applied voltage puls is always V_A=1 V). [9]*

programming[9]. Lowering the load resistor increases the voltage over the cell (and will allow higher currents through the cell), which leads to fast programming and enhanced filament growth. Hence thick filaments are formed giving rise to the low resistance of the cell. This variation of V_C is also what is done by the measurement device in current compliance mode (what is used in this thesis work), where V_C is lowered when R_C decreases to maintain a constant current.

2.2.4.3 Influence of thermal effects

It should be noted that thermal effects will also have an influence on the filament growth dynamics, because the ion migration is next to field driven also thermally activated (see equation 2.4). Joule heating - i.e. heating due to power dissipation because of the current that flows through the filament - will enhance this process. In the work of Russo et al. [9] (and also in other simulation work [10, 18]), this is taken into account to improve the agreement between observed and calculated switching curves. Figure 2.6a shows the resistance of the cell by pulse programming as function of the pulse width with varying load resistor. Figure 2.6b shows the corresponding temperature in the filament [9]. Especially for the configuration

[9] A memory cell is called a multilevel cell if more than 1 bit can be stored. Hence if the cell can be programmed towards more than two resistive states, multilevel programming becomes possible. To store 2 bits, 4 resistive states are necessary. So a PMC cell with a HRS and 3 different LRS states as in Figure 2.5c can store 2 bits.

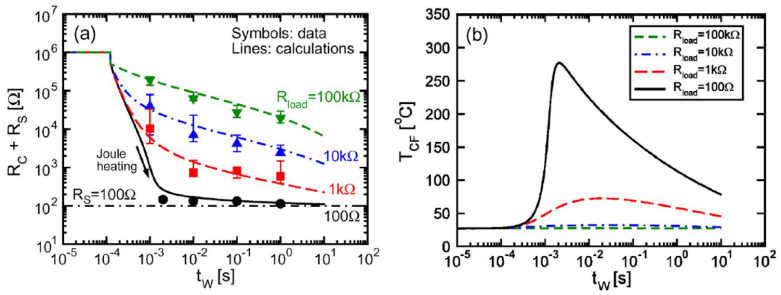

Figure 2.6. *(a) Resistance of the cell by pulse programming as function of the pulse width (t_W) with varying load resistor and (b) the calculated filament temperature. Note that especially for the low R_{load} a high current flows through the cell upon switching, and taking into account the Joule heating is necessary to correctly simulate the low ON resistance. [9]*

with a low load resistor (and high current flowing through the cell), the Joule heating plays an important role to correctly predict the LRS resistance. It can be seen that a remarkably faster transition to a lower resistance is obtained compared to higher load resistances. The Joule heating enhances the ion flow and reaction rates. Accordingly, Joule heating will play a similar role in the reset process [3, 10, 18].

2.2.5 Non-zero-crossing IV characteristics

In the discussions in previous sections, typical IV switching curves of a CBRAM cell (as in Figure 2.1) suppose a zero-crossing IV curve. This means that at zero voltage, no current flows through the cell. However, in recent publications [4, 19, 20], the influence of electrochemical reactions and a built-in voltage in the cell was reported, resulting in a non-zero-crossing IV curve. This is briefly discussed in this section, as it is inherent to the typical CBRAM structure, and hence contributes to the non-zero-crossing IV switching curves that are also observed in this thesis work.

Tappertzhofen et al. [19] used cyclic voltammetry (CV) to investigate the oxidation and reduction processes that occur in a Cu/SiO_2/Pt CBRAM cell. In this technique, a triangular positive and negative voltage sweep (0→ +V →0 and 0→ -V →0) is applied and the current is measured. When the positive sweep is applied on a CBRAM cell towards sufficiently high voltages, the cell switches to a low resistive state. Hence for CV measurements, the positive voltage sweep is limited to values *below* typical set voltages [4, 19]. An example of a CV measurement is given in Figure 2.7 for a Cu/SiO_2/Pt cell, where the potential is applied on the Cu electrode with respect to the Pt electrode. During the positive voltage sweep, and when a positive current is measured, oxidation of Cu at the Cu electrode occurs

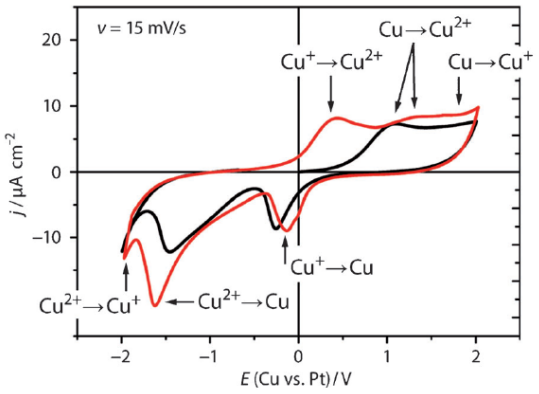

Figure 2.7. *Example of a cyclic voltammetry measurement on a Cu/SiO_2/Pt CBRAM cell with a sweep rate of 15 mV/s. Oxidation and reduction peaks are indicated. Note that the zero current crossing occurs at voltages different from zero after Cu has been oxidized and driven in the SiO_2 layer (i.e. after cycle 1, the black curve). The voltage is applied on the Cu electrode with respect to the Pt bottom electrode. [4]*

and the ions are injected into the SiO_2 layer under influence of the electric field. The different peaks can be associated to different oxidation reactions, as indicated in Figure 2.7. When the voltage in the positive sweep decreases again, the driving force for oxidation reduces and this is visible as a decrease in the measured current. At about 1 V the current becomes negative, which is related to the onset of reduction of Cu at the Pt electrode. So at the negative current side, reduction takes place, and the peaks in the CV curve at negative currents are associated with reduction reactions, as indicated in the figure. Note that at negative voltages on the Cu electrode, no reduction takes place anymore at the Pt electrode because of its positive sign, and reduction occurs at the Cu electrode. When the voltage returns towards zero, the current becomes zero around -1 V and becomes positive for negative voltages between -1 and 0 V. This means that at these low negative voltages, oxidation occurs. What is relevant to this thesis work is that these chemical reactions result in a non-zero crossing IV curve.

Valov et al. [20] reported the existence of a built-in voltage in CBRAM cells. This might have different contributions, but the most important will be the Nernst potential due to oxidation and reduction reactions at the active electrode/solid electrolyte and solid electrolyte/inert electrode respectively. This phenomenon is also known as the *nanobattery* effect [4, 20]. Hence this voltage also results in a non-zero crossing in the IV switching curves, as illustrated in Figure 2.8.

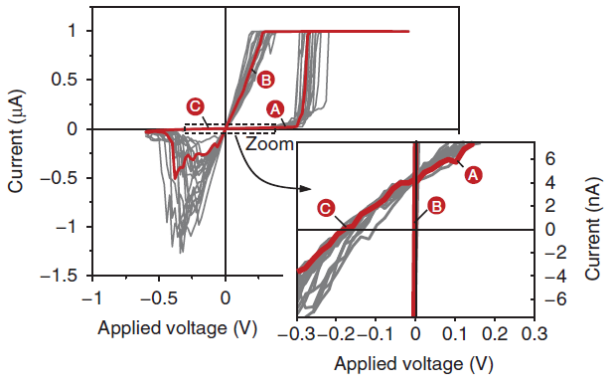

Figure 2.8. *IV switching curves of a Cu/SiO_2/Pt cell (electrode area $2 \times 10^{-4}\, cm^2$, sweep rate 400 mV/s), illustrating the zero-current crossing at a negative voltage of ∼-200 mV due to a built-in voltage. The built-in voltage thus has the same value but with opposite sign. [20]*

2.3 Materials for CBRAM

2.3.1 Literature

A typical CBRAM stack consists of a cation supply layer, an insulating layer and a (relative) inert counter electrode. Table 2.1 gives an example of different materials that have been used as cation supply layer, electrolyte layer and counter electrode. It is not the intention to give an exhaustive overview of all material systems that have been reported, and the reader is referred to recent review papers [2, 21, 22] for a complete overview. However, it is interesting to have a look at the combinations that have been made to understand where the materials that are studied in this work can be situated. Table 2.1 is divided into three groups. Memory cells in the first group consist of a Cu or Ag active electrode and a solid electrolyte, which is typically a chalcogenide showing high ionic conductivity, as switching layer. This was historically the first type of CBRAM stacks that have been reported [38]. In the second and third group, the ionic conducting layer is replaced by a binary metal oxide. Although these materials are rather poor ion conductors, switching through these layers can be very fast because they can be made very thin and with even modest voltages, high electric fields can be applied. Another advantage of these materials concerns their compatibility with current CMOS processes. However, this might have an implication on the switching dynamics, and will be discussed in section 2.3.2. The third group in table 2.1 has been separated from the others because instead of pure Cu or Ag as cation supply layers, *alloys* containing Ag or Cu have been used here. The main motivation to use alloys is to improve cycling performance [35–37]. In this thesis work, alloys are used as cation supply layer

Table 2.1. *Overview of different cation supply layers, electrolyte layers and counter electrodes that have been used in CBRAM.*

Cation supply layer	Electrolyte layer	Bottom elelectrode	Reference
Ag	Ge_xS_y	W	[9, 23, 24]
	Ge_xSe_y	W	[25]
		Pt	[26]
Cu	Ge_xS_y	W	[23]
Ag	Ge-Te	TiW	[27]
Cu	Ge-Te	TaN	[28]
Cu	Cu_2S	Pt	[29]
Cu	SiO_2	Pt, Au	[30]
		W	[31]
	Ta_2O_5	Pt	[32]
Ag	TiO_2	Pt	[33]
Cu-Te	GdO_x	W	[34]
	Al_2O_3	Si	[35]
Ag_2S, Ag_2Se	SiO_2, Al_2O_3, HfO_2, a-Si	Si	[36, 37]
Cu_2S, Cu_2Se	SiO_2, Al_2O_3, HfO_2, a-Si	Si	[36, 37]

in combination with Al_2O_3 as switching layer. Hence a CBRAM stack with a similar structure as the third group in table 2.1 is used. In section 2.3.2 we discuss the influence of using a binary oxide as switching layer instead of a (super) ionic conductor. In section 2.3.3 some background on alloys is given to motivate and explain their use in CBRAM.

2.3.2 Metal oxides as electrolyte

The switching mechanism discussed in section 2.2 (see Figure 2.1) includes the oxidation of species of the active electrode, and after transport through the electrolyte, the reduction of the ions at the counter electrode. However, the detailed switching mechanism depends on the materials that are used, especially on the switching layer. It has been shown that the shape and growth dynamics of the filament depend on the mobility of the cations in the switching layer [5, 6, 39]. The major difference is observed between the switching layers with low ionic conductivity (like metal oxides) and good ionic conductors (e.g. chalcogenides). This is discussed in section 2.3.2.1. The chalcogenide based switching layers typically contain already Cu or Ag species in the pristine state (e.g. Cu_2S, Ag-doped GeS_x),

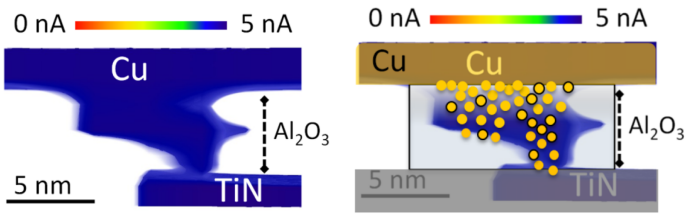

Figure 2.9. *3D reconstruction of the conductive filament in a Cu/Al_2O_3/TiN CBRAM cell by means of tomographic C-AFM. The filament shows a conical shape that is the widest at the active electrode. [6]*

whereas the metal oxides typically don't. For the latter, the influence of moisture on switching was reported, and this is briefly discussed in section 2.3.2.2.

2.3.2.1 Conductive filament shape

In section 2.2, conductive filament growth from the inert bottom electrode towards the cation supply layer was suggested (see Figure 2.1). This has been confirmed by TEM measurements for switching layers that show good ionic conductivity [40]. However, it was shown that for switching layers with low ionic conductivities (e.g. organic switching layer [5] or Al_2O_3 [6]) the filament growth is in the opposite direction, with a conical shape that is widest at the active electrode. This is illustrated in Figure 2.9 for a Cu/Al_2O_3/TiN CBRAM cell, by means of tomographic C-AFM [6, 7].

The dynamics of metallic inclusions in dielectrics has recently been investigated more in detail by Yang et al. [39], to account for the different filament morphologies that are observed. It was suggested that the metallic inclusions act as bipolar electrodes (BPEs), that have an effective anode ($\delta+$) and cathode ($\delta-$). This is illustrated in Figure 2.10c, where a metallic inclusion is localized between the anode (+) and cathode (-). Oxidation and reduction can then also occur at respectively the effective anode and cathode of the metallic inclusion. A qualitative model for the filament growth was then presented, depending on the oxidation and reduction rates $\Gamma^i_{red/ox}$of the metallic clusters i, and the ion mobility μ in the switching layer. Four different cases are illustrated in Figure 2.10. When the redox rates and the ionic mobility are high, the cations typically do not reduce in the switching layer but at the inert counter electrode, resulting in filament growth from the inert electrode towards the active electrode (Figure 2.10a). The high redox rates provide a large ion supply, leading to an invert cone-shaped filament. This is the filament growth mode that was shown in Figure 2.1, and that typically holds for ECM devices with a good ionic conductor as switching layer and a Cu or Ag cation supply layer (e.g. Cu doped GeTe [40]). On the other hand, when the

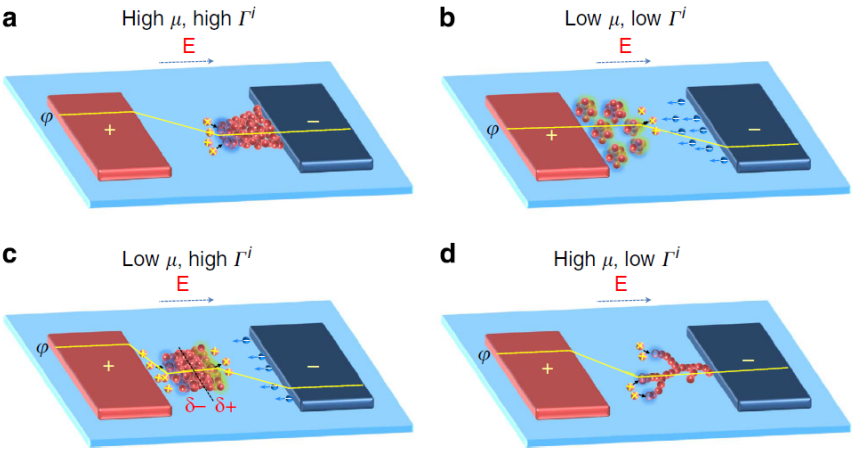

Figure 2.10. *Qualitative model of the filament growth dynamics depending on the redox rates Γ^i and ion mobility μ. (a) High μ and Γ^i resulting in filament growth from the inert toward the active electrode and an invert cone-shaped filament. (b) Low μ and Γ^i resulting in reduction in the dielectric and filament growth from the active toward the inert electrode by splitting and merging of nanoclusters and a forward cone shape. (c) Low μ but high Γ^i resulting in nucleation inside the dielectric and reconnection with the source. (d) High μ but low Γ^i leading to filament growth from the inert electrode in a branched way. [39]*

mobility and redox rates are low, the ions can pile up and nucleate in the switching layer (Figure 2.10b). Filament growth is then by cluster migration that consists of repeated splitting and merging of the clusters. This proceeds by oxidation of the metal from one cluster (that acts as a BPE) and reduction of the ions at another cluster. When the ion mobility is low and the redox rates are high (Figure 2.10c), nucleation can occur in the dielectric while the large amount of supplied ions get reduced at the cathodic side of the nuclei, which might lead to gap filling. This then acts as an extended active electrode and the process is repeated, leading to a net forward growth of the filament. Note that this mechanism was also already proposed by Gao et al. [5, 41] for a Cu active electrode on an organic polymer as switching layer. Finally, when the ion mobility is high but the redox rates low (Figure 2.10d), nucleation will occur at the counter electrode but the limited amount of ions will mainly get reduced at the edges of the filament with high field strength. The filament will hence have a branched structure towards the active electrode.

It can be concluded that the ion mobility determines the nucleation sites (at the inert electrode or in the dielectric) and the growth direction (from cathode to anode or vice versa), while the redox rates determine the ion supply and the filament geometry. This can explain the observation of the reverse growth mode

(active electrode towards inert electrode) and filament shape (conical shape that is widest at the active electrode) for Cu/Al_2O_3/TiN based CBRAM, as this CBRAM stack is similar to case (c) of Figure 2.10.

2.3.2.2 Influence of moisture

Different papers [3, 42, 43] report the influence of moisture (H_2O from ambient) on the switching behaviour of CBRAM cells with an oxide switching layer (i.e. a switching layer which does not initially contain Cu ions). The presence of H_2O is expected to play a role through formation of OH^- species at the counter electrode when an oxidation reaction occurs at the anode, and as such maintaining charge neutrality. For chalcogenide switching layers (e.g. demonstrated with Ag as active electrode and Ag_2Se as electrolyte [25]), usually ions are initially driven into the chalcogenide by photodiffusion. In this case, some Ag^+ will be present at the counter electrode and the reduction reaction (equation 2.2) can proceed [3]. However, when a metal oxide is used, initially (i.e. before forming[10]) no ions are in the switching layer. Hence a counter charge (electrons) is built up at the counter electrode, or another possibility is the reduction of *other* species that are available at the counter electrode. Moisture that comes from atmosphere or that is incorporated during fabrication[11] could supply hydrogen and oxygen containing species which could be reduced to form OH^- species. Figure 2.11 illustrates the switching principle in the case where ions are already present in switching layer before forming (a-c) and when no ions are present (d-f) and where moisture can play an important role in the counter electrode reaction.

Effect of moisture on chemical oxidation Tsuruoka et al. [42] reported the influence of moisture on the functionality of Cu/Ta_2O_5/Pt and Cu/SiO_2/Pt based CBRAM device. Forming in vacuum of the cells with an SiO_2 layer required very large voltages ($>$15 V) and the cells could not be reset after forming. Forming under ambient and subsequent cycling in vacuum on the other hand was possible. This suggests that chemical oxidation of Cu due to ambient H_2O enhances the formation of Cu^{z+} species, providing the cations for CF growth. Hence other reactions than the "anodization-like" reaction where Cu gets oxidized ($Cu \rightarrow Cu^{z+} + ze^-$) and is injected in the Al_2O_3 layer contribute to cation production. Note that other studies on Cu migration in dielectrics also mention the enhanced migration of Cu species when they are oxidized, for example by formation of CuO_x that acts as a cation source [4, 43–46]. Formation in vacuum of the Ta_2O_5 cells on the other hand was possible, but this was related to the presence of water in the Ta_2O_5 in

[10] The first cycle of a pristine cell where Cu or Ag ions are driven in the switching layer is called the *forming* cycle.

[11] For example when Al_2O_3 is deposited by an H_2O based atomic layer deposition technique, the presence of hydrogen and oxygen containing species in the alumina is not surprising.

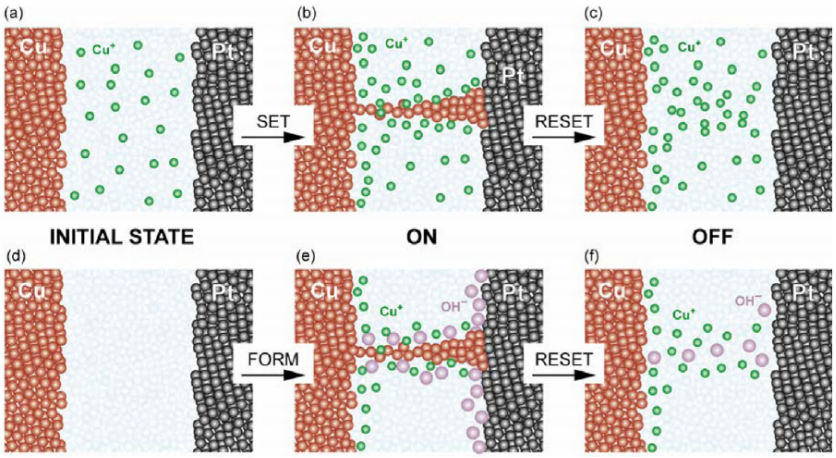

Figure 2.11. *Schematic of a set-reset operation and conductive filament formation in the case when initially Cu ions are present in the switching layer (a-c) or when there are no ions present in the switching layer (d-f). The former occurs when ions are already dissolved before forming (e.g. diffusion of Ag in $GeSe_x$ by photodiffusion [25]), or when the cell has been cycled before. [3]*

vacuum, whereas the water is much easier desorbed from silica. However, the dependence of the counter electrode reaction (i.e. formation of OH^- species) on the moisture was not clearly studied.

Effect of moisture on cathodic reduction Tappertzhofen et al. [43] investigated the influence of moisture on the counter electrode reaction. The ion concentration (this includes both Cu ions and other ions like OH^-) as a function of the partial H_2O pressure in $Cu/SiO_2/Pt$ cells was measured by means of cyclic voltammetry[12] (see Figure 2.12a). Higher ion concentrations were obtained for higher H_2O pressures because a higher counter electrode reaction rate (e.g. formation of OH^- species) induces higher Cu oxidation rate. This is illustrated in Figure 2.12b. This also shows that hydroxide ions are acting as counter charge rather than electrons (where the latter should not depend on humidity of the atmosphere). Note that the charge separation at the electrodes (i.e. Cu^{z+} at the Cu/SiO_2 interface and OH^- at the SiO_2/Pt interface) induces an electromotoric force (emf) in the cell, and hence a measurable cell voltage is present in the CBRAM device[13] (see also section 2.2.5). Depending on the ion concentration (which depends on the humidity in

[12]The ion concentration can be calculated from the integrated current measured in the CV measurements and the cell geometry. [43]

[13]The occurance of a cell voltage is not limited to CBRAM cells with metal oxides as switching layer, but will also occur in other CBRAM stacks. [20]

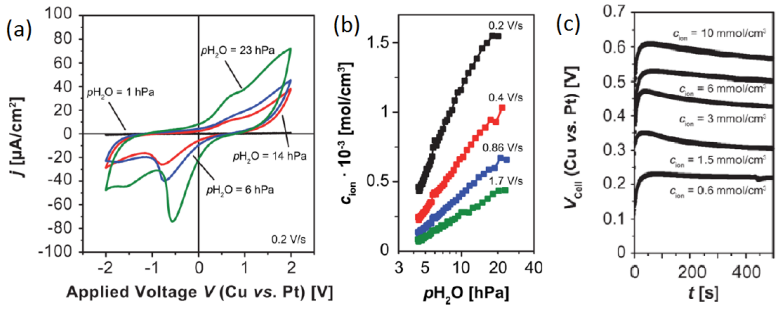

Figure 2.12. *(a) Cyclic voltammetry measurement of a Cu/SiO_2/Pt CBRAM cell at different H_2O partial pressures and with a constant sweep rate of 0.2 V/s. (b) Calculated ion concentration from the CV measurements as a function of the H_2O partial pressure for different voltage sweep rates. (c) Measured transient cell voltage as a function of the ion concentration for a constant H_2O pressure. Prior to the measurement, the number of ions was set by a single linear anodic oxidation sweep with different sweep rates. [43]*

the experiment and the CV sweep rate, as shown in Figure 2.12b), a different cell voltage was observed (see Figure 2.12c), which again emphasizes the importance of the counter electrode reaction and the role of species like OH^-.

To conclude this section, it has been shown that H_2O has an influence on the switching properties of CBRAM cells, because OH^- species can be formed. The Cu^{z+} ion concentration at the Cu/SiO_2 and OH^- concentration at the SiO_2/Pt interface will determine both half cell potentials and hence the built-in voltage in the cell (that was discussed in section 2.2.5, resulting in non-zero crossing IV curves).

2.3.3 Alloys as cation supply layer

Next to pure Cu or Ag, alloys containing these elements can be used as a cation supply layer (see Table 2.1). The influence of the alloys on the switching of CBRAM cells is not discussed in this section, but is explained in Chapter 4 for Cu-Te and Ag-Te. In this section, a brief overview of alloys and intermetallic phases is given. The alloy can be amorphous or crystalline, and a model for the calculation of the glass transition temperature is given in section 2.3.4.

2.3.3.1 Intermetallic compounds

Depending on the elements that are combined in an alloy, they can be mixable or not, and some elements might form intermetallic compounds. The thermodynamic

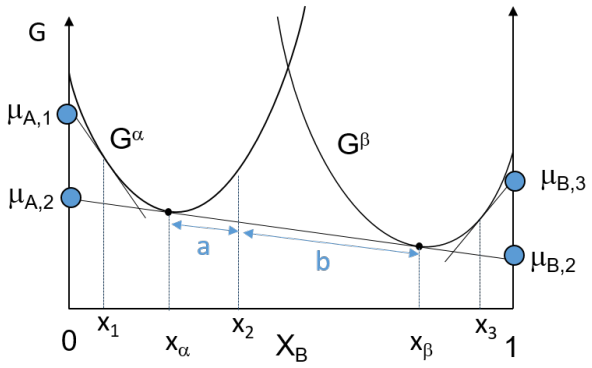

Figure 2.13. *Gibbs free energy as a function of the fraction of element B (x_B) in the mixture $A_{1-x_B}B_{x_B}$. The chemical potential of elements A (μ_A) and B (μ_B) in the mixture can be graphically represented by the intersection points of the tangent line of the Gibbs free energy curve with the respective y-axis. The binary system AB has two phases α and β. For compositions $x_B \leq x_\alpha$, only the α phase is present, for $x_B \geq x_\alpha$, only the β phase is present. For compositions in between, both phases coexist and species A and B have the same chemical potential in both phases.*

driving force for mixing or the formation of intermetallic phases is the lowering of the Gibbs free energy

$$\Delta_{mix}G_m = \Delta_{mix}H_m - T\Delta_{mix}S_m. \tag{2.8}$$

In this equation $\Delta_{mix}H_m$ is the enthalpy change and $\Delta_{mix}S_m$ the change in entropy. One can also associate a chemical potential μ to the species, and the transport of the species to mix or form intermetallic phases can be associated to a lowering of their chemical potential. This is also graphically illustrated in Figure 2.13 for a hypothetical binary system with 2 intermetallic phases α and β.

2.3.3.2 Crystalline versus amorphous alloys

Materials in the solid state can be *crystalline*, where the atoms or ions are periodically arranged in space in a lattice. This means a *long range order* of the elements. On the other hand, materials in the solid state that do not show this long range order are *amorphous*. However in these materials, *short range order* can occur. Typically, a material can end up in an amorphous state when it is cooled very quickly from the liquid state without crystallizing. Indeed, in a liquid there is no long-range order, and when it is quickly cooled down the atoms do not get the chance to reorganize into a more thermodynamically favourable crystal. This also means that the amorphous state is a metastable state, as is graphically illustrated in Figure 2.14. Note that amorphous materials can also be formed during

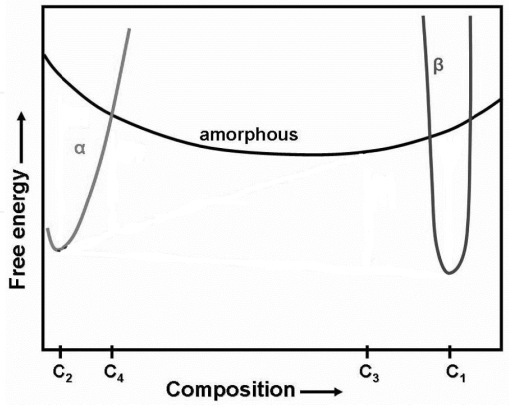

Figure 2.14. *Hypothetical diagram showing the free energy as a function of the composition of a binary material system. Two crystalline phases α and β exist, hence crystallization of the amorphous material in these structures would lower the energy of the system, illustrating the metastable nature of the amorphous state. (Adapted from [47])*

thin film deposition like magnetron sputtering. Indeed, in this technique, particles are ejected from a sputter target and condense on the substrate. In fact this is also a fast transition from a gaseous phase into a solid phase.

An amorphous material that shows a transition from a solid to a molten like, viscous material is called a *glass*[14]. The transition from the glass state to the viscous supercooled region occurs at the *glass transition temperature (T_g)*. The glass transition temperature is always lower than the melting temperature and the crystallization temperature of the amorphous material. Figure 2.15 shows a DSC measurement[15] of a $Ti_{50}(Cu_{0.45}Ni_{0.55})_{44-x}Al_xSi_4B_2$ alloy. The crystallization temperature T_x is observed as a minimum in the DSC curve. The glass transition temperature T_g is also indicated. It is indeed observed that crystallization occurs after the glass transition. The temperature range between T_g and T_x is called the *supercooled liquid region*.

Crystallization of an amorphous material requires first *nucleation* of the phase and then *growth* of the nuclei. A nucleation barrier has to be overcome for nucleation to become thermodynamically favourable. Growth of the nuclei then occurs

[14]Note that the terms amorphous and glass are sometimes intermixed. However, not all amorphous materials exhibit a glass transition temperature. Hence it is more appropriate to use the term glass only for those materials. In general in this work we will rather speak about amorphous materials as we do not experimentally measure glass transitions, but rather distinghuish between non-crystalline and crystalline. [48]

[15]DSC stands for Differential Scanning Calorimetry and is a technique where the absorbed heat flow to the sample is measured upon annealing of the sample. An exothermic (e.g. crystallization) or endotherm reaction is observed as a peak towards lower or higher values respectively in the DSC curve.

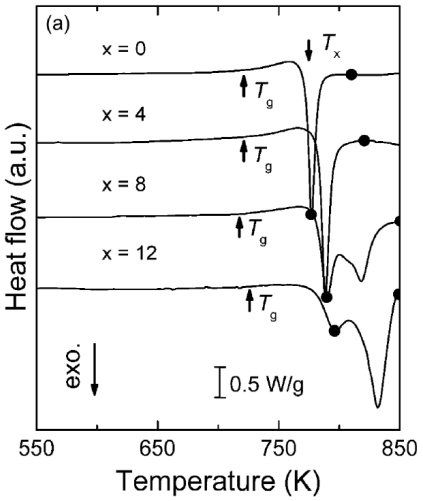

Figure 2.15. *DSC measurements of $Ti_{50}(Cu_{0.45}Ni_{0.55})_{44-x}Al_xSi_4B_2$ alloys ($x = 0, 4, 8, 12$). The crystallization temperature T_x and glass transition temperature T_g are indicated. [47]*

as diffusing species from the environment reach the nuclei and attach to it. Amorphous materials are often used in microelectronics, for example in Phase Change Materials (PCM) on rewritable compact disks (CD-RW), where crystallization and quenching in the amorphous state after melting of chalcogenide materials is controlled by laser irradiation. The amorphous and crystalline state have different reflectivity (and resistivity, which can be used in PCM based RRAM), which then represent the binary 0 and 1 states. It is clear that in these applications crystallization at too low temperatures is unwanted because crystallization might already be induced under long thermal stress and result in limited data retention. Hence controlling the stability of the amorphous state and the crystallization temperature has been the topic of various publications [49–52].

2.3.4 Lankhorst model for glass transition temperature

It is interesting to be able to calculate the crystallization temperature for a certain alloy. As the glass transition temperature (T_g) is a lower limit for the crystallization temperature (T_x), the calculation of the glass transition temperature would give already a lower limit for crystallization. This is discussed in this section and will be used in chapters 5 and 6.

It has been observed that the glass transition temperature increases with the coordination number of the atoms and an empirical relation was found [48, 53]. However, this relation does not distinguish between different atoms with the same

coordination number, where a different T_g can be observed. Indeed, it can be understood that the breaking of bonds for the atoms to reorganize in a crystalline structure is related to the number of bonds that are formed, but also to the strength of these bonds. Hence the stronger the bond, the more difficult this will be. Lankhorst [54] developed a model to calculate the glass transition temperature for predominantly covalent bonded materials which takes the number of bonds and their bond strength into account. This temperature hence is also a lower limit for the crystallization temperature. The model makes the following assumptions:

1. Each element in the covalent structure has a preferred coordination number m. For elements of group 14, 15 and 16 (the group of C, N and O respectively), m is 4, 3 and 2 respectively. These satisfy the '$8-N$' rule, where N is the number of s and p valence electrons. For elements from groups 11, 12 and 13 (the group of Cu, Zn and B respectively), this leads to coordination numbers larger than 4. Liu and Taylor [55] solved this problem by assuming that for these elements a formal charge transfer takes place from the chalcogenides or, when not available, from the group 15 elements towards these elements. In this way, also these elements have formally four valence electrons, and they obey the *generalized* "$8-n$" rule, with n the *formal* number of valence electrons. The average coordination number Z of the atoms in the glass is then obtained as

   $$Z = 8 - \langle n \rangle \,, \tag{2.9}$$

   where $\langle n \rangle$ is the average number of formal valence electrons. As the model is only applicable to covalent structures, $\langle n \rangle \geq 4$ because the mean coordination number cannot be larger than 4.

2. Heteronuclear bonds are preferred over homonuclear bonds.

3. Bonds are formed in the order of decreasing bond enthalpy (bond enthalpy is defined positive here and hence a larger value is equivalent to a stronger bond) until all formal valences are saturated and the total number of bonds equals $Z/2$.

4. Heteronuclear bond enthalpies can be derived from homonuclear bond enthalpies using Pauling's equation:

   $$H_{AB} = \frac{H_{AA} + H_{BB}}{2} + 96.14 * (S_A - S_B)^2. \tag{2.10}$$

   In this equation, H_{AA} and H_{BB} are the homonuclear and H_{AB} the heteronuclear bond enthalpies, and $S_{A,B}$ the electronegativity.

A list of homonuclear bond enthalpies can be found in the paper of Lankhorst [54], but a summary of the homonuclear and the calculated heteronuclear bond

Table 2.2. *Homonuclear (H_{AA}) and heteronuclear bond entalpy (H_{AB}), electronegativity (S) and the number of valence electrons (N_A) of C, Ge, Si, Te and Cu [54].*

Element	N_A	S_A	Bond	H_{AA} (kJ/mol)	H_{AB} (kJ/mol)
C	4	2.55	C-C	297	
Ge	4	2.01	Ge-Ge	186	
Si	4	1.9	Si-Si	225	
Te	6	2.1	Te-Te	197	
Cu	1	1.9	Cu-Cu	19/-67	
			Ge-Te		192.3
			Si-Te		214.85
			Cu-Si		122
			Cu-Ge		103.66
			Cu-Te		111.8

enthalpies that are relevant for this thesis work is given in table 2.2[16]. The glass transition temperature (in K) can then be calculated as

$$T_g(K) = 3.44H_a - 480, \tag{2.11}$$

where H_a is the total bonding enthalpy, which is given by

$$H_a = \sum n_{AB}H_{AB}. \tag{2.12}$$

In this equation, n_{AB} is the number of A-B bonds and H_a is simply a weighted sum of the different bond enthalpies. It also shows that the interaction (i.e. the bond strength) between the elements influences T_x. These relations are very interesting because these allow to calculate the glass transition temperature for a predominantly covalent bound alloy, and hence a lower limit for the crystallization temperature T_x. This model is used where possible in chapters 5 and 6 to get a lower limit for the expected T_x of the investigated alloys.

2.3.5 Materials studied in this work

In this work, CBRAM cells with a material stack similar to the third group in table 2.1 will be investigated, where Cu or Ag alloys are used as cation supply

[16]Note that H_{AA} for Cu is less accurately determined, and can be between 19 and -67 kJ/mol. In the calculations in this thesis, we use the highest value, in agreement with the calculations of Sutou et al. [56]. Hence we calculate the *upper limit* for T_g, and it should be taken into account that the value can be lower. Raoux et al. [50] for example used a value of -24 kJ/mol in their calculations.

layer and a binary metal oxide as switching layer. The focus in this thesis is to investigate the thermal stability of Cu and Ag tellurides and their functionality as cation supply layer in CBRAM cells. As switching layer, Al_2O_3 is used because of its high thermal stability (the as-deposited layer is amorphous and crystallizes at temperatures $\gg 400°C$), good functionality as electrolyte layer [35, 37], and compatibility with CMOS technology.

When studying different Cu or Ag alloys, the following properties are of importance and will be investigated:

- Thermal stability of the material: when an alloy is integrated in a CBRAM cell, this will typically occur in the back end of line, and hence it will also receive the thermal budget that is applied in BEOL. This means that the alloy should remain stable during this processing step, i.e. not phase separate or melt during anneals up to $400°C$.

- CBRAM functionality: the alloys should be functional as a cation supply layer, i.e. resistive switching should be observed when implemented in a CBRAM cell. A sufficient amount of cycles (i.e. *endurance*) should be possible. For integrated devices, to be competitive with Flash, 10^3-10^7 cycles (or more) should be reached [1]. For our macroscopic lab based cells that are not passivated and have more parasitic effects (see section 3.5.3), obtaining $\sim 10^2$ cycles is already promising.

- Retention properties: next to switching performance, *retention* of the memory cells (i.e. how well a programmed memory state is maintained) is studied. Data retention of $>$10 years at $85°C$ for storage class memory is required [1, 57]. Depending on the application, the retention requirements can vary.

The influence of alloy electrodes as cation supply layer on the resistive switching layer is explained in chapter 4, where the binary tellurides Cu-Te and Ag-Te are investigated. Then the thermal stability is improved by alloying, which is reported in chapter 5. In chapter 6, we investigate two other alloys, $CuInTe_2$ and $CuAlTe_2$ which have theoretically good material properties. Before presenting these results, the experimental techniques to investigate the materials properties and the memory characteristics are presented in the next chapter.

References

[1] R. Waser, R. Dittmann, G. Staikov, and K. Szot, *Adv. Mater.* **21**(25-26), 2632–2663 (2009).

[2] I. Valov, R. Waser, J. R. Jameson, and M. N. Kozicki, *Nanotechnology* **22**(25), 254003 (2011).

[3] I. Valov and M. N. Kozicki, *J. Phys. D: Appl. Phys.* **46**(7), 074005 (2013).

[4] I. Valov, *ChemElectroChem* **1**(1), 26–36 (2014).

[5] S. Gao, C. Song, C. Chen, F. Zeng, and F. Pan, *J. Phys. Chem. C* **116**(33), 17955–17959 (2012).

[6] U. Celano, L. Goux, A. Belmonte, A. Schulze, K. Opsomer, C. Detavernier, O. Richard, H. Bender, M. Jurczak, and W. Vandervorst, In *2013 IEEE Int. Electron Devices Meet. (IEDM)*, (2013).

[7] U. Celano, L. Goux, A. Belmonte, K. Opsomer, A. Franquet, A. Schulze, C. Detavernier, O. Richard, H. Bender, M. Jurczak, and W. Vandervorst, *Nano Letters* **14**(5), 2401–2406 (2014).

[8] W. A. Hubbard, A. Kerelsky, G. Jasmin, E. R. White, J. Lodico, M. Mecklenburg, and B. C. Regan, *Nano Letters* **15**(6), 3983–3987 (2015).

[9] U. Russo, D. Kamalanathan, D. Ielmini, A. Lacaita, and M. Kozicki, *IEEE Trans. Electron Devices* **56**(5), 1040–1047 (2009).

[10] S. Yu and H.-S. Wong, *IEEE Trans. Electron Devices* **58**(5), 1352–1360 (2011).

[11] E. Budevski, G. Staikov, and W. Lorentz, *Electrochemical Phase Formation and Growth*, Weinheim: VCH, (1996).

[12] G. Staikov, *Electrocrystallization in Nanotechnology*, Wiley-VCH, (2007).

[13] L. Goux, K. Sankaran, G. Kar, N. Jossart, K. Opsomer, R. Degraeve, G. Pourtois, G. M. Rignanese, C. Detavernier, S. Clima, Y. Y. Chen, A. Fantini, B. Govoreanu, D. Wouters, M. Jurczak, L. Altimime, and J. A. Kittl, *IEEE Symp. VLSI Technol.* , 69–70 (2012).

[14] C. Schindler, G. Staikov, and R. Waser, *Appl. Phys. Lett.* **94**(7), 072109 (2009).

[15] M. Kund, G. Beitel, C.-U. Pinnow, T. Rohr, J. Schumann, R. Symanczyk, K.-D. Ufert, and G. Muller, In *2005 IEEE International IEEE Int. Electron Devices Meet. (IEDM)*, 754–757, (2005).

[16] S. Rahaman and S. Maikap, In *2010 IEEE International Memory Workshop (IMW), 2010 IEEE International*, 1–4, (2010).

[17] A. Belmonte, W. Kim, B. T. Chan, N. Heylen, A. Fantini, M. Houssa, M. Jurczak, and L. Goux, *IEEE Trans. Electron Devices* **60**(11), 3690–3695 (2013).

[18] D. Ielmini, *IEEE Trans. Electron Devices* **58**(12), 4309–4317 (2011).

[19] S. Tappertzhofen, S. Menzel, I. Valov, and R. Waser, *Appl. Phys. Lett.* **99**(20),

203103 (2011).

[20] I. Valov, E. Linn, S. Tappertzhofen, S. Schmelzer, J. van den Hurk, F. Lentz, and R. Waser, *Nat. Commun.* **4**, 1771 (2013).

[21] F. Pan, S. Gao, C. Chen, C. Song, and F. Zeng, *Mater. Sci. Eng., R* **83**, 1 – 59 (2014).

[22] D. Jana, S. Roy, R. Panja, M. Dutta, S. Rahaman, R. Mahapatra, and S. Maikap, *Nanoscale Research Letters* **10**(1), 188 (2015).

[23] M. Kozicki, M. Balakrishnan, C. Gopalan, C. Ratnakumar, and M. Mitkova, In *Non-Volatile Memory Technology Symposium, 2005*, 7 pp.–89, (2005).

[24] D. Kamalanathan, U. Russo, D. Ielmini, and M. N. Kozicki, *IEEE Electron Device Lett.* **30**(5), 553–555 (2009).

[25] M. Kozicki, M. Park, and M. Mitkova, *IEEE Trans. Nanotechnol.* **4**(3), 331–338 (2005).

[26] C. Schindler, M. Meier, R. Waser, and M. Kozicki, In *Non-Volatile Memory Technology Symposium, 2007. NVMTS '07*, 82–85, (2007).

[27] C. J. Kim, S. G. Yoon, K. J. Choi, S. O. Ryu, S. M. Yoon, N. Y. Lee, and B. G. Yu, *Journal of Vacuum Science & Technology B* **24**(2), 721–724 (2006).

[28] S.-J. Choi, J.-H. Lee, H.-J. Bae, W.-Y. Yang, T.-W. Kim, and K.-H. Kim, *IEEE Electron Device Lett.* **30**(2), 120–122 (2009).

[29] S.-W. Kim and Y. Nishi, In *Non-Volatile Memory Technology Symposium, 2007. NVMTS '07*, 76–78, (2007).

[30] Y. Bernard, V. T. Renard, P. Gonon, and V. Jousseaume, *Microelectron. Eng.* **88**(5), 814–816 (2011).

[31] C. Schindler, S. Thermadam, R. Waser, and M. Kozicki, *IEEE Trans. Electron Devices* **54**(10), 2762–2768 (2007).

[32] T. Sakamoto, K. Lister, N. Banno, T. Hasegawa, K. Terabe, and M. Aono, *Appl. Phys. Lett.* **91**(9), 092110 (2007).

[33] K. Tsunoda, Y. Fukuzumi, J. R. Jameson, Z. Wang, P. B. Griffin, and Y. Nishi, *Appl. Phys. Lett.* **90**(11), 113501 (2007).

[34] K. Aratani, K. Ohba, T. Mizuguchi, S. Yasuda, T. Shiimoto, T. Tsushima, T. Sone, K. Endo, A. Kouchiyama, S. Sasaki, A. Maesaka, N. Yamada, and H. Narisawa, *Int. Electron Devices Meet.* , 783 –786 (2007).

[35] L. Goux, K. Opsomer, R. Degraeve, R. Muller, C. Detavernier, D. J. Wouters, M. Jurczak, L. Altimime, and J. A. Kittl, *Appl. Phys. Lett.* **99**(5), 053502 (2011).

[36] S. R. Hariharsudan, Master's thesis, Katholieke Universiteit Leuven, (2009).

[37] H. Radhakrishnan, In *15th IEEE Mediterranean Electrotechnical Conference*, 515–520, (2010).

[38] Y. Hirose and H. Hirose, *J. Appl. Phys.* **47**(6), 2767–2772 (1976).

[39] Y. Yang, P. Gao, L. Li, X. Pan, S. Tappertzhofen, S. Choi, R. Waser, I. Valov, and W. D. Lu, *Nat Commun* **5**, 4232 (2014).

[40] S.-J. Choi, G.-S. Park, K.-H. Kim, S. Cho, W.-Y. Yang, X.-S. Li, J.-H. Moon, K.-J. Lee, and K. Kim, *Adv. Mater.* **23**(29), 3272–3277 (2011).
[41] S. Gao, C. Song, C. Chen, F. Zeng, and F. Pan, *J. Phys. Chem. C* **117**(22), 11881–11882 (2013).
[42] T. Tsuruoka, K. Terabe, T. Hasegawa, I. Valov, R. Waser, and M. Aono, *Adv. Funct. Mater.* **22**(1), 70–77 (2012).
[43] S. Tappertzhofen, I. Valov, T. Tsuruoka, T. Hasegawa, R. Waser, and M. Aono, *ACS Nano* **7**(7), 6396–6402 (2013).
[44] B. G. Willis and D. V. Lang, *Thin Solid Films* **467**(1-2), 284 – 293 (2004).
[45] O. R. Rodriguez, W. Cho, R. Saxena, J. L. Plawsky, and W. N. Gill, *J. Appl. Phys.* **98**(2), 024108 (2005).
[46] L. P. Shepherd, A. Mathew, B. E. McCandless, and B. G. Willis, *J. Vac. Sci. Technol., B* **24**(3), 1297–1302 (2006).
[47] Y. Mastai, editor, *Advances in Crystallization Processes*, Intech, (2012).
[48] K. Tanaka and K. Shimakawa, *Amorphous Chalcogenide Semiconductors and Related Materials*, Springer, (2011).
[49] C.-M. Lee, Y.-I. Lin, and T.-S. Chin, *J. Mater. Res.* **19**, 2929–2937 (2004).
[50] S. Raoux, M. Salinga, J. L. Jordan-Sweet, and A. Kellock, *J. Appl. Phys.* **101**(4), 044909 (2007).
[51] S.-J. Park, I.-S. Kim, S.-K. Kim, S.-M. Yoon, B.-G. Yu, and S.-Y. Choi, *Semicond. Sci. Technol.* **23**(10), 105006 (2008).
[52] G. E. Ghezzi, J. Y. Raty, S. Maitrejean, A. Roule, E. Elkaim, and F. Hippert, *Appl. Phys. Lett.* **99**(15), 151906 (2011).
[53] K. Tanaka, *Solid State Commun.* **54**(10), 867 – 869 (1985).
[54] M. Lankhorst, *J. Non-Cryst. Solids* **297**(2-3), 210 – 219 (2002).
[55] J. Liu and P. Taylor, *Solid State Commun.* **70**(1), 81 – 85 (1989).
[56] Y. Sutou, T. Kamada, M. Sumiya, Y. Saito, and J. Koike, *Acta Mater.* **60**(3), 872 – 880 (2012).
[57] ITRS 2013 - The international Technology Roadmap for Semiconductors, *Emerging Research Devices*.

3 Experimental techniques

In this chapter, the techniques that were used to prepare and characterize the samples are discussed. First the methods to deposit the thin films are given. Then the techniques to determine the composition and the crystallinity are briefly discussed. A more in depth discussion is given on XPS and how information about the chemical state of the elements in the film can be extracted. In a final part, the preparation and characterization of the memory cells studied in this work is outlined. It is not the intention to give a detailed explanation of all techniques, but merely an overview of the different techniques and how and why they are used in this thesis work. For more information, the reader is referred to the cited references.

3.1 Preparation of chalcogenide thin films

3.1.1 Magnetron sputter deposition

The chalcogenide thin films are deposited by means of DC magnetron sputter deposition [1]. This is a physical vapour deposition (PVD) technique, where particles of a sputter target (i.e. the material that one wants to deposit on the sample) are ejected by bombardment of the target by Ar ions. The ejected particles then condense on the substrate where a layer is grown. A Balzers BAS 450 deposition tool is used, where a base pressure below 5×10^{-7} mbar is reached prior to deposition, and an Ar pressure of 5×10^{-3} mbar is used during sputtering. The power applied on the sputter target determines the sputter rate and hence the thickness of the deposited film for a certain sputter time. By adjusting the sputter power or sputter

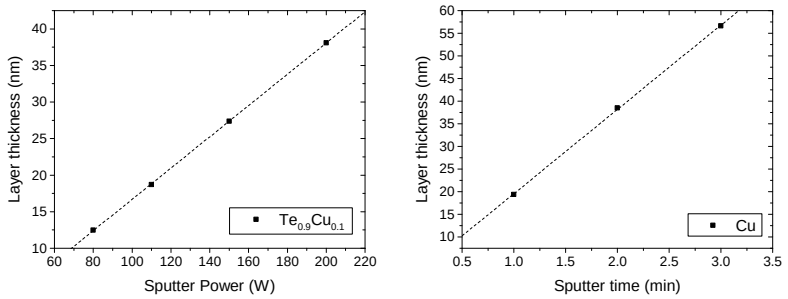

Figure 3.1. *(a) Thickness of a sputtered $Te_{0.9}Cu_{0.1}$ film as a function of the power applied on the sputter target for 2.5 min sputtering. (b) Thickness as a function of sputter time (and constant sputter power) for Cu.*

time, layers with different thickness can be deposited. Figure 3.1a illustrates the linear relation (at least in a limited power range) between the deposited film thickness and the sputter power of a $Te_{0.9}Cu_{0.1}$ sputter target. A linear relation between film thickness and sputter time can also be deduced (see Figure 3.1b for Cu). The Balzers deposition tool allows the mounting of 4 different sputter targets. The samples are mounted on a carousel and pass subsequently in front of each target. Depending on the number of sputter targets that are powered on, a single material or a mixed layer can be deposited. This allows the deposition of binary, ternary and quaternary alloys. The composition of the alloy is determined by the applied power on each sputter target. The total thickness of the alloy layer is adjusted by varying the sputter time.

In order to obtain a binary alloy A_xB_{100-x} with x at% A, the sputter power P_A and P_B for A and B respectively are determined by calculating an equivalent thickness of each element (d_A^P and d_B^P) that gives rise to the requested composition. The required sputter power is then calculated from the calibration curves that give the layer thickness of an element as a function of the sputter power (see Figure 3.1a). The ratio of the equivalent thicknesses d_B^P/d_A^P of the elements B and A is given by

$$d_B^P/d_A^P = \left(\frac{100}{x} - 1\right) \cdot \frac{M_B}{M_A} \cdot \frac{\rho_A}{\rho_B}. \tag{3.1}$$

In this equation, $M_{A,B}$ are the molar masses of the elements and $\rho_{A,B}$ the densities (in g/cm^3) of the sputtered films of pure A and B.

3.1.2 Combinatorial sputtering

In materials science, one is very often interested in the materials properties as a function of the composition. This can be studied by preparing different samples with varying composition. For a large number of compositions, this can be a time

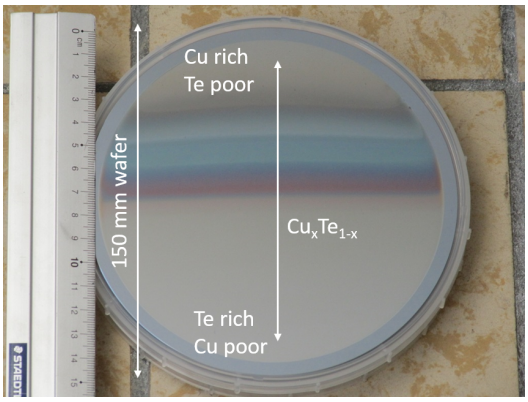

Figure 3.2. *Picture of a 150 mm Si wafer, where a ∼50 nm Cu_xTe_{1-x} layer ($0.2 < x < 0.8$) is deposited by means of combinatorial sputter deposition. The composition varies along the vertical direction on the wafer.*

consuming and expensive task. Discovery of new materials and the study of materials properties as a function of the composition is significantly speeded up by applying *combinatorial* techniques [2]. In essence, instead of the *serial* preparation and study of different samples, a library of materials is prepared at the same time and this library is then (automatically) analysed.

In this thesis, a combinatorial sputter technique was used for some materials (for Ag-Te and Cu-Te-C, see Papers I and III), to efficiently investigate the materials properties as a function of the composition. The approach to deposit these films is very similar to Dahn et al. [3–5], where shadow masks are placed in front of the sputter targets, which allows the modification of the particle flux and hence the deposited profile on the substrate. Figure 3.2 shows a picture of a 150 mm Si wafer, where a graded Cu_xTe_{1-x} layer ($0.2 < x < 0.8$) layer is deposited. This is done by placing specially designed shadow masks in front of the sputter targets of the Balzers BAS 450 deposition tool. This combinatorial wafer can then be analysed by characterization techniques in mapping mode, where the materials properties are probed as a function of the position on the wafer.

3.1.3 X-ray reflectivity

The thickness, roughness and density of the deposited layers is measured by means of X-ray reflectivity (XRR). The intensity of an X-ray beam that is specularly reflected from a sample is measured as a function of the incident angle (typically 0.6 to 6°). A typical XRR pattern is shown in Figure 3.3, and the most important features related to the physical properties of the film are indicated. For small angles, total external reflection occurs because the refractive index of solids is

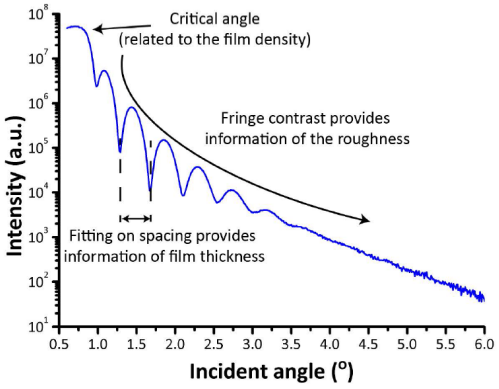

Figure 3.3. *XRR pattern and its interpretation of a 17.9 nm HfO_2 film on a 100 nm SiO_2 substrate. [6]*

smaller than 1 for X-rays. The angle where part of the X-rays start to penetrate in the film is called the *critical angle* and is related to the electron density of the film. For angles larger than the critical angle, the interference between X-rays that are reflected at the surface and at the film/substrate interface gives rise to the typical oscillating intensity pattern, where the period is determined by the thickness of the film. The intensity of the reflected beam at higher angles falls off rapidly, resulting in an overall decrease in intensity of the pattern, and this decrease can be related to the roughness of the film. Interface roughness results in subtle damping of the fringes [7].

3.2 Composition determination

As explained in the previous section, one can control the sputtering process to target a specific alloy composition. However, it is important to be able to verify and confirm the actual composition of the deposited alloys. The approach followed throughout this thesis work, is first the determination of the composition of a calibration sample by RBS (see section 3.2.1) that is able to determine the composition of this calibration sample with good accuracy. Then this sample is used to calibrate XRF and EDX (see section 3.2.2 and 3.2.3 respectively) that are routinely available in the lab in Ghent. These techniques can then routinely be used for composition determination of other samples (with the same constituents).

3.2.1 Rutherford backscattering spectroscopy

Rutherford backscattering spectroscopy (RBS) is a non-destructive technique that can determine the composition of an alloy as a function of the depth. The tech-

nique makes use of an incident beam of light ions (typically a He^+ beam is used) that is elastically scattered at the nuclei of the sample. The energy of the backscattered ions is measured and together with the known incident energy and scattering angle, the mass of the scattering centre can be extracted, allowing component identification. The technique also calculates the number of scattering centers per surface area, which allows very precise composition determination. This is what the technique is used for in this work.

Note that RBS is less sensitive for light elements like carbon, oxygen, nitrogen... To detect these elements, a variation on RBS exists where one detects the elastic recoiled atoms, i.e. particles of the sample that are ejected. This technique is known as Elastic Recoil Detection analysis (ERD), and this analysis was performed in this thesis for the carbon alloyed $Cu_{0.6}Te_{0.4}$. Usually an incident ion beam of heavier ions is used (in this case Cl^{4+}). Both RBS and ERD analysis are performed at imec to accurately determine the composition.

3.2.2 X-ray fluorescence spectroscopy

In X-ray fluorescence spectroscopy (XRF), an X-ray source is used as an excitation source, and the emitted characteristic X-rays are detected. If the photon energy of the source exceeds the binding energy of an inner shell electron, this electron can be ejected, leading to a vacancy in the respective shell (see Figure 3.4a). An electron from an outer shell can fill the hole and the difference in energy is then emitted as a photon (Figure 3.4), or an Auger electron is emitted. Because each atom has a unique set of energy levels, the emitted X-rays are characteristic for a certain element and the elements in the layer can be identified.

In this work, a Bruker Artax system equipped with a Mo excitation source and an XFlash 5010 silicon drift detector was used. The sample holder allows mounting of 300 mm wafers. In the framework of combinatorial materials research, XRF can then be performed as a function of the position on the wafer. Based on relative peak intensities in the XRF spectrum, the Artax software allows composition determination after calibration with a reference sample (here characterized by RBS).

Note that XRF has a lower sensitivity for light elements. This is due to the lower fluorescence yield (and larger probability for Auger electron emission for $Z<10$). The large difference in the incident photon energy and the binding energy of the inner shell electrons results also in a lower absorption probability of the incident photons. The XRF setup used in this work is in standard atmosphere, where ambient air also limits the detection of these low energetic characteristic lines [8]. Hence for light elements, another technique is used.

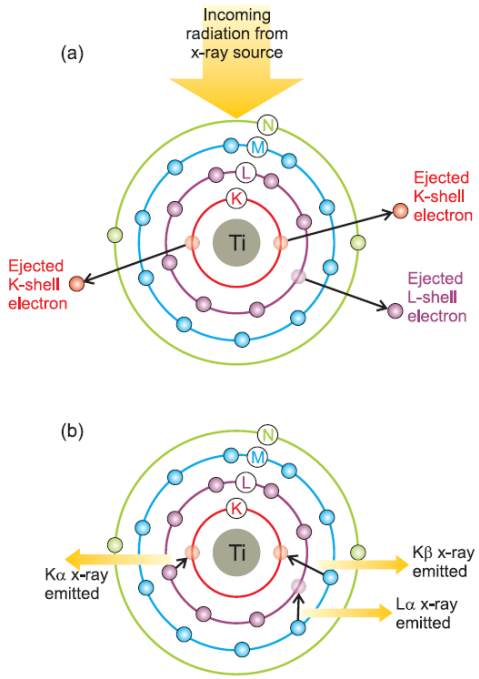

Figure 3.4. *Principle of X-ray Fluorescence Spectroscopy, showing the electronic transitions in a Ti atom that produce the characteristic fluorescent X-ray peaks. K- and L-characteristic lines in the XRF spectrum are produced when the inner vacancy that is created and filled is in the K or L shell respectively. Depending from which shell the outer electron comes to fill the vacancy, the K-or L-lines are labeled as α, β etc. [7]*

3.2.3 Energy-dispersive X-ray fluorescence spectroscopy

The principle of energy-dispersive X-ray fluorescence spectroscopy (EDX) is very similar to XRF, only the excitation source is different. In EDX, an electron beam (this can be the electron beam of a scanning electron microscope) is used as excitation source. In this work, a FEI Quanta 200F FEG scanning electron microscope (SEM), equipped with an Edax Genesis 4000 EDX detector was used. The same SEM is also used for SEM imaging in this work. The Edax software also allows calibration with a reference sample with known composition. Acquiring EDX spectra hence occurs in high vacuum, eliminating absorption of photons by ambient air. Moreover, the cross section for ionization by electron impact is larger compared to photons. Indeed, for electrons the cross section is inversely proportional to the square of the electron energy ($\sim E^{-2}$), whereas for photons it is $\sim E^{-7/2}$ [9]. Moreover, lowering the accelerating voltage of the electron gun

of the SEM increases the peak intensity of low energetic fluorescent lines. These factors make EDX more feasible for the detection of light elements.

3.3 Crystallinity

3.3.1 X-ray diffraction

The crystallinity of the films is investigated by means of X-ray diffraction (XRD). When a material is crystalline, an incident X-ray beam that is making an angle θ with the (hkl) lattice planes will get diffracted, where h,k and l are the *Miller indices*. The diffracted X-rays will interfere constructively according to Braggs law:

$$2d_{hkl} \sin\theta = n\lambda, \tag{3.2}$$

where d_{hkl} is the lattice spacing and n an integer number larger than 0, representing the order of the diffraction at the (hkl) planes. A diffraction peak will then be recorded at an angle 2θ with respect to the incident beam. This is measured in XRD and allows crystal structure determination. A Bruker D8 Discover, equipped with a Cu K_α X-ray source and a Vantec linear detector is used for this.

3.3.2 In-situ X-ray diffraction

The setup is equipped with an annealing chamber that can be evacuated to pressures below 5×10^{-2} mbar and filled with different atmospheres. Typically, He is used because it is inert and has a low scattering cross section for X-rays. The vacuum chamber has Kapton windows for transmission of the X-ray beam. The Vantec linear detector can record a spectrum in a 2θ-window of 20°. The sample is then annealed under constant He flow while an XRD spectrum is taken in a fixed 2θ-window. This allows monitoring of changes in crystallinity, phase transformations and melting as a function of temperature.

3.4 X-ray photoelectron spectroscopy

In this section, the working principle of X-ray photoelectron spectroscopy (XPS) is discussed. The technique can be used to determine the composition of the layer, but also for chemical state analysis. In this work, XPS is mainly used to get more information on the chemical state of the elements in the alloy. When a material is crystalline, one can determine the formal oxidation state based on the stoichiometry of the detected phase. However, when the material is amorphous, this is not possible and hence XPS can be used to determine whether for example Cu is in a metallic state or rather oxidized. After a short introduction on the principle of XPS, chemical state analysis is discussed more in detail in section 3.4.3.

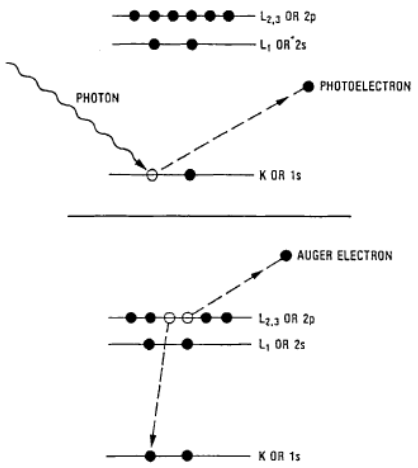

Figure 3.5. *Top: emission of a core hole photoelectron by irradiation of the sample with X-rays. Bottom: emission of an Auger electron after filling of the core hole that was created by photoelectron emission. [10]*

3.4.1 Principle and application

In this technique, the sample is illuminated with low energetic monochromatic X-rays, typically Mg K_α (1253.6 eV) or Al K_α (1486.6 eV) radiation. The photoelectric effect causes electrons to be emitted from the sample, of which the energy is then measured. The X-rays typically have a penetration depth of 1 to 10 µm, whereas the photoelectrons emitted from the sample come from the surface, because inelastic scattering causes energy loss limiting the depth from which photoelectrons can escape from the sample without losing energy. The electrons which leave the sample without inelastic scattering come from within the top tens of Angstroms [10]. This means that XPS is a surface sensitive technique. The process of photoelectron emission is sketched in Figure 3.5. The kinetic energy of the emitted photoelectron is measured and is given by

$$E_k = h\nu - E_b - \phi_{spec}, \tag{3.3}$$

where E_b is the binding energy of the photoelectron referred to the Fermi level, and ϕ_{spec} is the workfunction of the spectrometer. The energy reference is clarified in Figure 3.6. The spectrometer workfunction is a fixed value for the used setup and is transparent for the user. Figure 3.5 also shows the phenomenon of Auger electron emission, which occurs when the core hole is filled by an electron with higher energy. The energy that is released can then be used to emit another electron. It is clear that the kinetic energy of the photoelectron depends on the used photon energy, whereas the kinetic energy of an Auger electron does not (i.e.

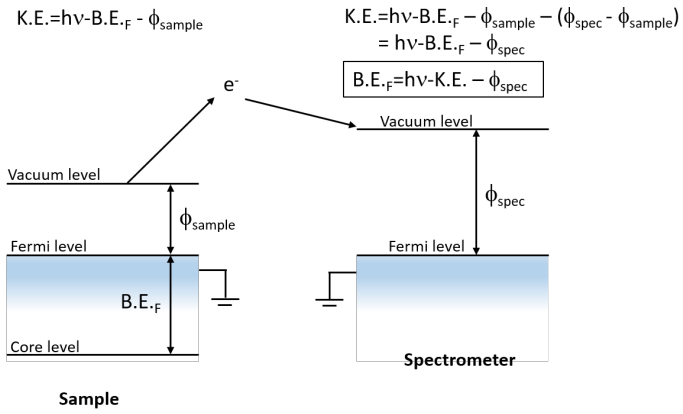

Figure 3.6. *Energy level diagram of the sample measured by XPS and the spectrometer used to measure the kinetic energy of the photoelectrons.*

it is fully determined by the involved electron transitions). In a typical XPS plot, the intensity is plotted as function of the binding energy, hence the position of the Auger lines on this scale will depend on the X-ray photon energy that is used.

With XPS, all elements except H and He can be detected and it has a detection limit of about 0.1 at%, while the lightest elements (Li, Be) have sensitivities closer to 1 at% [11]. The composition can be determined based on relative peak areas of the different elements in the sample. Based on the position op the photoelectron lines, useful information can be obtained about the chemical state of the elements. That explains why the technique is often denoted as *electron spectroscopy for chemical analysis (ESCA)*. This will be more elaborated in section 3.4.3.

3.4.2 XPS setup

The XPS measurements are performed on a Theta Probe system of Thermo Scientific[1]. The system has an Al X-ray source for excitation and a channel plate detector to detect the photoelectrons. A base pressure of $\sim 10^{-10}$ mbar is reached. An EX05 Ar ion gun allows sputtering of the surface, which enables depth profiling. In this work, usually a surface scan is taken, where the carbon signal of hydrocarbon at 284.6 eV serves as a binding energy reference [10]. Then a few sputter steps are performed to eliminate surface contamination (O and C) and to acquire spectra from the bulk of the sample.

[1] Only for CuTeC in Paper II, another XPS system was used, as described in the manuscript.

3.4.3 Chemical state analysis

An important application of XPS is the ability to gain information on the chemical state of a certain element in a compound (i.e. bond formation with other elements). Recall that the binding energy of the photoelectrons coming from a core level is measured. In a first approximation, the spectra can be interpreted based on simple electrostatic considerations. The core electrons are attracted to the nucleus, whereas the presence of the other electrons tend to screen the positive charge of the nucleus. When an element forms chemical bonds, a partial charge transfer can occur due to different electronegativities between the bonding partners, changing the attraction of the core electrons to the nucleus and hence the measured binding energy. When an element is partially oxidized (i.e. loses electrons), the screening of the nucleus due to the electron cloud is smaller, leading to a net larger attraction of the core electrons to the nucleus which results in a higher binding energy. On the other hand when the element is reduced (i.e. gains electrons), the binding energy will be lower due to a decrement of the electrostatic force between the core electrons and the nucleus. This is intuitive to understand and explains in many cases the observed peak shift very well [12]. However, one has to take into account that, when a core electron is emitted, the system will relax by screening the created core hole. Usually this relaxation will result in an increase of the kinetic energy of the photoelectron, and hence a decrease in the measured binding energy [13]. Hence a more careful analysis might be necessary, and one should at least be aware of this effect. This is relevant to this thesis work because this effect is quite pronounced for Cu, which is used in the cation supply layers under study. In the next section, the influence of this relaxation is further discussed, and how more information can be obtained by also measuring Auger electron lines[2]. The (modified) Auger parameter is introduced in section 3.4.3.2 and the Wagner plot (or chemical state plot) is discussed in section 3.4.3.3.

3.4.3.1 Initial and final state effects

When information is requested on the chemical state of an element, one is interested in the *initial state*, i.e. when no photoelectron is emitted yet. However, when probing the material by means of XPS, photoelectrons are emitted and the system ends up in the *final state* where the core hole that is created is screened by the electron orbitals. This screening or *relaxation* will affect the measured binding energy of the photoelectron. In what follows, we discuss the different contributions of the initial and final state effects on the measured binding energy more in detail.

[2]The discussion is mainly based on the review paper of Moretti [14]. We further refer to this paper for the detailed derivation of all relations and the used approximations.

Initial state effects Electrostatics learns that the larger the net positive charge, the more difficult it will be to remove a core electron from an atom. The potential energy of a core electron will have a contribution of the charge of the atom to which it belongs, but also of the other atoms in the compound. An expression for the atomic contribution can be derived by modeling the atoms as conductive spheres with an appropriate electronic charge. The contribution of the surrounding charged atoms on the other hand is related to the *Madelung potential*. The binding energy of a core electron C can then be written as [14]

$$E_b(C) = \text{constant} + kq + V_M. \tag{3.4}$$

In this equation, q is the valence charge in units of electron charge, k is in a first approximation equal to $14.4/R$ with R the radius of the sphere of the core level electron in units Å, and $V_M = 14.4\Sigma_j(q - q_0)_j/R_j$. The latter is the contribution of the net charges $(q - q_0)_j$ of all the other atoms, with R_j their distance to the core-ionized atom. The factor 14.4 is to get the binding energy in units eV. The constant term is related to the Hartree-Fock energy of the of the core electron C in the free atom. The quantity k can be seen as the change in the core potential when a valence electron is moved. From this equation, it is clear that the binding energy is linear in q (as in the simple interpretation in binding energy shifts) if V_M is constant or is also linear related to q. Moreover, *final state effects* and the associated relaxation are still not taken into account. These might lower the measured binding energy.

Final state effects When a photoelectron is emitted (see Figure 3.5), a core hole is created. The orbitals will respond to this by screening the hole, i.e. the system will *relax*. In the adiabatic approximation, the relaxation energy is entirely transferred to the outgoing photoelectron. The relaxation energy of core level C can be written as [14]

$$\begin{aligned} R(C) = R^a(\text{core electrons}) + R^a(\text{valence electrons}) \\ + R^{ea}(\text{extra-atomic contribution}). \end{aligned} \tag{3.5}$$

In this equation, R^a(core electrons) and R^a(valence electrons) are respectively contributions from the core and valence electrons of the core-ionized atom itself. The former does not depend of the chemical state in the initial and final state, whereas the latter does due to possible charge transfer from the neighbour ligands (i.e. the atoms that it binds to). The extra-atomic contribution contains the influences from all other atoms in the system. If we combine the contribution of the initial and final state effects to the measured binding energy of the photoelectron of core level C, we can write

$$\begin{aligned} E_b(C) = \text{constant'} + kq + V_M - R^a(\text{valence charge}) \\ - R^{ea}(\text{extra-atomic contribution}). \end{aligned} \tag{3.6}$$

In this equation, we included the relaxation term of the core electrons in the constant term, as it does not depend on the chemical state. Now that the influence of the final state effects are taken into account, it is clear that it is not always straightforward to relate the measured binding energies to a certain oxidation state.

Local and non-local screening The screening of the core hole mentioned before needs some further explanation. Two ways of screening can occur, *local* and *non-local* screening. For the former, an electron leaves the ligand to go in a localized atomic orbital of the core ionized atom. This occurs for example for Cu in a II+ oxidation state. Then the Cu has a (Ar)3d^9 electron configuration, and an electron from the ligand will fill the empty place in the d orbital, giving rise to a final state 3d10L (where L stands for electron transfer from the ligand to the core ionized atom). This type of screening is very efficient, and the relaxation energy is large. Moreover, the relaxation energy will only slightly be influenced by the type of the ligand (as the electron is fully transfered, whatever the ligand is). Note that screening in a metal is also very efficient because of effective screening by the electrons in the conduction band. Hence in case of *local* screening, the relaxation energy might approach that of a metal. In the case of *non-local* screening, the s and p valence orbitals of the ligand will induce the screening. The efficiency of the screening (and hence the relaxation energy) will depend on how easily these orbitals can be polarized.

3.4.3.2 Auger electrons and the Auger parameter

We mentioned before that next to photoelectrons, also Auger electrons are emitted. It was observed that also these lines show chemical shifts, which are sometimes even larger than for the photoelectron lines. Hence also these lines contain valuable information about the chemical state. Wagner defined the *Auger parameter* α as

$$\alpha = E_k(C'C''C''') - E_k(C), \tag{3.7}$$

where $E_k(C)$ is the kinetic energy of the photoelectron and $E_k(C'C''C'')$ is the kinetic energy of the Auger electron where the core levels C', C'' and C''' are involved. C does not need to be one of the levels involved in the Auger process, but usually it is. This parameter can have negative values, and hence it is more convenient to add the photon energy $h\nu$ to α, which defines the *modified Auger parameter* α' as

$$\alpha' = \alpha + h\nu = E_k(C'C''C''') + E_b(C). \tag{3.8}$$

Usually one uses the term Auger parameter also for the modified version. The advantage of α or α' is that the difference between two kinetic (or binding) energies is taken, making its value insensitive to any type of referencing of the energies

or static charging of the sample. Now one might wonder how information on the chemical state can be extracted from this parameter. It can be shown that the Auger parameter is equal to (apart from a constant) twice the relaxation energy [14]:

$$\alpha' = \text{constant} + 2R(C). \tag{3.9}$$

Hence a shift in the Auger parameter

$$\Delta\alpha' = 2\left[\Delta R^a(\text{valence charge}) + \Delta R^{ea}\right] \tag{3.10}$$

is related to a difference in relaxation energy [14]. Equation 3.10 shows that the Auger parameter is fully determined by the *final state effects*. When the valence charge does not change after the relaxation process (it could change if the relaxation includes charge transfer from the nearest neighbor ligands), then equation 3.10 reduces to

$$\Delta\alpha' = 2\Delta R^{ea}, \tag{3.11}$$

as was originally deduced by Wagner.

3.4.3.3 Wagner plot

In section 3.4.3.1 an expression was derived for the binding energy of the photoelectron coming from a core level C (equation 3.6), showing that it contains a relaxation energy. In section 3.4.3.2 the modified Auger parameter was defined as the sum of the binding energy of the photoelectron coming from core level C and the kinetic energy of an Auger electron involving core levels C', C'' and C''' (equation 3.8) and it was shown to be related to the relaxation energy of core level C (equation 3.9). Hence from equations 3.6, 3.8 and 3.9, the relation

$$E_k = [\text{const'} + 2\left(V_M + kq\right)] - 3E_b \tag{3.12}$$

can be deduced, giving the relation between the kinetic energy of the Auger electron and the binding energy of the photoelectron. If the kinetic energy of the Auger electron is plotted as function of the binding energy, one obtains a chemical state plot or *Wagner plot*, called after Charles D. Wagner who did a lot of pioneering work on this topic. An example of the Wagner plot for Cu of different Cu-compounds is shown in Figure 3.7. Recall that the Auger parameter is the sum of the Auger kinetic energy and the binding energy (equation 3.8), and hence lines of constant α' have a slope of -1 in the Wagner plot (note that the binding energy on the x-as decreases from left to right, and hence they appear to have a slope of +1). Lines with slope -3 are also indicated (again they appear to have a slope +3 due to the negative direction of the binding energy scale), and according to equation 3.12 the intercept with the y-axis gives information on the initial state effects. Hence from the position in the Wagner plot, information can be extracted on both

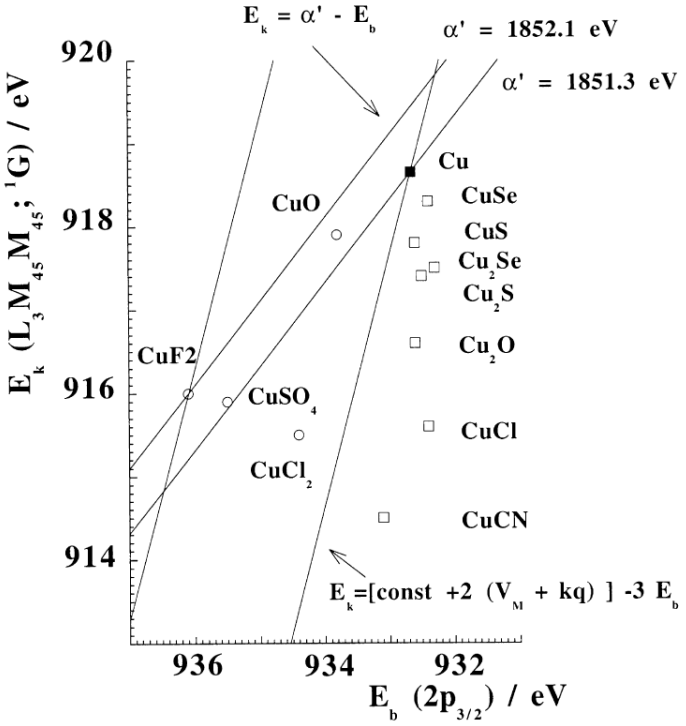

Figure 3.7. *Cu Wagner plot, showing the Cu $2p_{3/2}$ binding energy and the Cu $L_3M_{45}M_{45}$ Auger kinetic energy for different Cu compounds. [14]*

the initial and final state effects, both giving information on the chemical nature of the compound. This is further discussed in the next paragraphs for the Cu-Wagner plot.

Lines with slope -3 As was briefly mentioned before, the intercepts of these lines with the y-axis give information on the initial state, and the difference in intercept value for two states gives the chemical shift due to initial state effects. From equation 3.12 we find that the shift in intercepts $\Delta E_k^0(i-m)$ between an intermetallic compound and the metal is given by

$$\Delta E_k^0(i-m) = [E_k(i) + 3E_b(i)] - [E_k(m) + 3E_b(m)]\,. \tag{3.13}$$

In this equation, i and m stand for intermetallic and metallic respectively. This can also be written as

$$\Delta E_k^0(i-m)/2 = V_M(i) - V_M(m) + kq(i) - k_0 q_0(m). \tag{3.14}$$

Recall that the Madelung potential is the potential at the core ionized atom due to all the other atoms of the compound. For a cation, this is a negative quantity (the other atoms create a net negative charge), and for every chemical state $|V_M(i)| \gg |V_M(m)|$ due to the net larger charge. The valence charge q is also a negative quantity. If we now compare CuF_2 with Cu (see Figure 3.7, the lines with slope -3 are also drawn) it is clear that $\Delta E_k^0(CuF_2 - Cu) \gg 0$. Because $V_M(CuF_2) - V_M(Cu) \ll 0$, it is required that $kq(CuF_2) - k_0q_0(Cu) \gg 0$ and hence $|kq(CuF_2)| \ll |k_0q_0(Cu)|$. This means that compared to pure Cu, electrons and the associated charge are transferred *away* from the Cu atom towards the F in CuF_2. This is in agreement with the ionic character of CuF_2, where Cu is expected to have an oxidation state of +II. On the other hand, the shift in kinetic energy can also be negative as for CuCl. Note that $kq(CuCl) - k_0q_0(Cu)$ is positive because a charge transfer is expected from Cu to Cl due to the larger electronegativity of chloride. Hence the negative shift here must be caused by a very high negative value of the Madelung potential, pointing again to a more ionic character for CuCl compared to copper. From this it is clear that a shift in the kinetic energy can be linked to a higher ionic character of the bond. However note that a small error δ in peak positions (for example due to charging), results in a shift of the intercept value of 2δ. Hence for example for CuSe, Cu_2Se, CuS,... these shifts are very small and within the measurement uncertainty.

Lines with slope -1 and the Auger parameter From the definition of the modified Auger parameter (equation 3.8), it is clear that points that lie on lines with slope -1 have the same α'. Equation 3.11 showed that a shift in α' is related to the *final state*, i.e. the change in binding energy of a core electron due to relaxation (i.e. screening) effects. This suggest that no information can be extracted about the initial state. However, recall that screening can be local or non-local, as was discussed in section 3.4.3.1. In the case of copper, a different initial chemical state (i.e. I+ or II+) will result in a different screening mechanism. Local screening will occur in case of Cu(II+), which is very efficient and leads to large relaxation energies and hence a large α'. It might be close to α' of metallic Cu, which is also large due to efficient screening of the core hole by the electrons in the conduction band. Non-local screening on the other hand will occur for Cu(I+), which is less effective and results in smaller relaxation energies and hence in a smaller value for α'. This is confirmed for different Cu compounds in Figure 3.7. For example for Cu-Se compounds, it is observed that α'(CuSe) $>$ α'(Cu_2Se) and that α'(CuSe) is close to Cu. The same holds for Cu compounds with S and O. Considering the elements of the same group (e.g. O, S and Se) one observes for the copper compounds with non-local screening (Cu_2O, Cu_2S and Cu_2Se) an increase in Auger parameter with increasing polarizability of the ligand (the larger the atom, the more easily it is polarized), and hence α' is the smallest for Cu_2O and the largest for Cu_2Se.

Note that the binding energies of the Cu compounds with for example S or Se do not show a pronounced shift towards higher binding energies, which would be expected based on simple electrostatic considerations (as discussed in the beginning of section 3.4.3). If $\Delta E_b(i-m) \approx 0$, then $\Delta E_k^0(i-m) \approx E_k(i) - E_k(m)$ and with the definition of α' (equation 3.8)

$$\Delta E_k^0(i-m) = \alpha'(i) - \alpha'(m). \tag{3.15}$$

Together with equations 3.10 and 3.14 we find

$$V_M(i) + kq(i) - V_M(m) - k_0 q_0(m) \approx [R^{ea}(i) - R^{ea}(m)] + [R^a(i) - R^a(m)]\,. \tag{3.16}$$

Hence this happens when the initial and final state effects have the same size. So when the binding energy shift is negligible and the Auger parameter shift is negative compared to metallic Cu (as for the Cu compounds with S and Se), then

$$[V_M(i) - V_M(m)] - [k_0 q_0(m) - kq(i)] < 0. \tag{3.17}$$

As the second term is negative because of a smaller negative valence charge due to charge transfer, the Madelung potential in the intermetallic compound must be much more negative compared to pure Cu, which is in agreement with a higher ionicity of the bond. Hence the larger the Auger parameter shift in this case, the more ionic the bond. Indeed, looking to α' of the Cu compounds with similar binding energy show that size of the negative shift is in the order $|\Delta\alpha'(Cu_2Se)| < |\Delta\alpha'(Cu_2S)| < |\Delta\alpha'(Cu_2O)| < |\Delta\alpha'(CuCl)|$, in agreement with increasing ionicity (based on difference in electronegativity).

3.4.4 Summary

From the previous discussion, it is clear that XPS can be used for chemical state analysis. In a first approximation, when an element is oxidized, the core electrons will feel a larger attraction leading to a higher binding energy. However, peak positions measured by XPS depend on both initial and final state effects. The relaxation that occurs when the photoelectron is emitted typically leads to an increase in the kinetic energy of the photoelectron and hence a decrease in the measured binding energy. Hence the peak shift of the photoelectron line may become much smaller and not giving much information. This is the case for Cu, as could be observed in Figure 3.7. In this case it might be interesting to measure the kinetic energy of a specific Auger line, and plot this kinetic energy and the photoelectron binding energy in a Wagner plot. Depending on the position in the plot, information on the chemical state can be extracted:

- Metallic Cu should coincide with the reported value, and hence deviation from metallic Cu can be detected.

- Lines with slope -3 give information on the initial state effects. However, small errors in the shift in photoelectron lines cause a shift in the intercepts of these lines.
- Lines with slope -1 have a constant modified Auger parameter. This gives information on the final state effects. For Cu due to a significant difference in relaxation for a I+ or II+ oxidation state, the latter typically have a larger value for α'.
- In the same group (for example the chalcogenides), α' typically increases for larger atoms in case of non-local screening, because they can be polarized more easily leading to a larger relaxation energy. Hence α' increases from Cu_2O to Cu_2Se in Figure 3.7. Following this trend, α' of Cu_2Te is expected to be larger and closer to Cu.
- Depending on the measured Cu $2p_{3/2}$ and $L_3M_{45}M_{45}$ peaks, and hence the position in the Wagner plot of the Cu-Te compounds investigated in this work, it is possible to determine whether Cu is in a metallic state, or forming bonds with Te.

3.5 Memory cells

3.5.1 Device fabrication

Memory cells are prepared by magnetron sputter deposition of the Pt/Cu-alloy stack through a dot shadow mask that is clamped on the Al_2O_3/n^+ Si substrate. The Al_2O_3 is 3 nm thick and is deposited by a H_2O based atomic layer deposition (ALD) technique in the 300 mm fab at imec. The Cu alloy and Pt top electrode are 50 nm thick and the dots have a diameter of 580 µm. This is illustrated in Figure 3.8b.

3.5.2 Measuring DC switching characteristics

The dot cells are measured on a home built probe station, equipped with a Keithley 2601A Sourcemeter (SMU) to measure the current-voltage (IV) curves. The equivalent electrical scheme is represented in Figure 3.8a. The sourcemeter is used to apply a linear voltage sweep, and the current is measured. In this mode, it is possible to limit the current to a certain value (*current compliance, I_c*), which means that the device will adjust the voltage over the memory cell to lower voltages if the current would exceed I_c. The probe station has an automated mapping stage, which allows to automatically probe subsequent dots in the deposited array of cells. The control software for the measurements was programmed in a user-friendly LabView program.

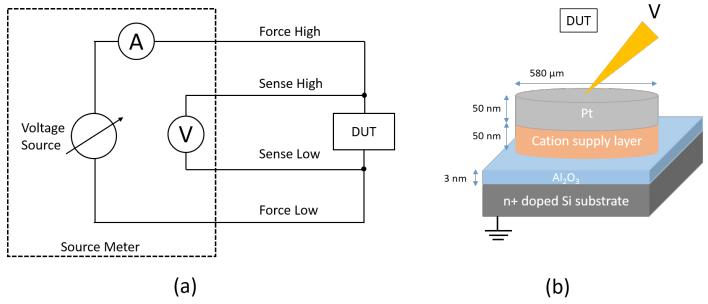

Figure 3.8. *(a) Schematic overview of the measurement setup. The device under test (DUT) is the memory cell and is schematically represented in figure (b). The memory cell is contacted at the Pt top electrode, and the potential is applied on the Pt contact with respect to the bottom electrode.*

Figure 3.9a shows a typical switching curve of a Pt/$Cu_{0.6}Te_{0.4}$/Al_2O_3/n^+ Si CBRAM cell when a voltage sweep from 0 V→+3 V→0 V is applied on the Pt top electrode with respect to the bottom electrode to set the cell. When applying the same sweep to -3 V, the cell is reset. A sweep rate of 0.5 V/s was applied. Usually, the absolute value of the current is plotted on a logarithmic scale, as is illustrated in Figure 3.9b. The inset in Figure 3.9a shows a detail of the negative voltage range around $0\,V$, showing that the current goes through zero at negative voltages. In Figure 3.9b this is visible as a minimum in the current. As discussed in previous chapter in section 2.2.5, this can be related to a built-in voltage (see Figure 2.8) or electrochemical processes (see Figure 2.7), but it can also be related to the capacitance of the cell (i.e. a capacitive current that contributes to the current). The influence of the capacitance on the switching of the memory cells is further discussed in the next section.

3.5.3 Parasitic effects

The millimetre-sized devices used in this work are easy to fabricate and allow a quick screening of the switching performance of cells with different cation supply layers. However, these memory devices are rather large, and have (when in HRS) the structure of a capacitor (metal/insulator/metal). Recall that the capacitance C is proportional to the area of the electrodes ($C = \epsilon A/d$, with A the area of the cell, ϵ the permittivity and d the thickness of the dielectric film), hence the larger the cells, the larger the capacitance. When the cell is in the high resistive state and a potential is applied, this capacitance will charge. However, when the cell switches to a low resistive state, this capacitance will discharge causing a high current through the cell. Figure 3.10 shows a simulation of current (Figure 3.10c)

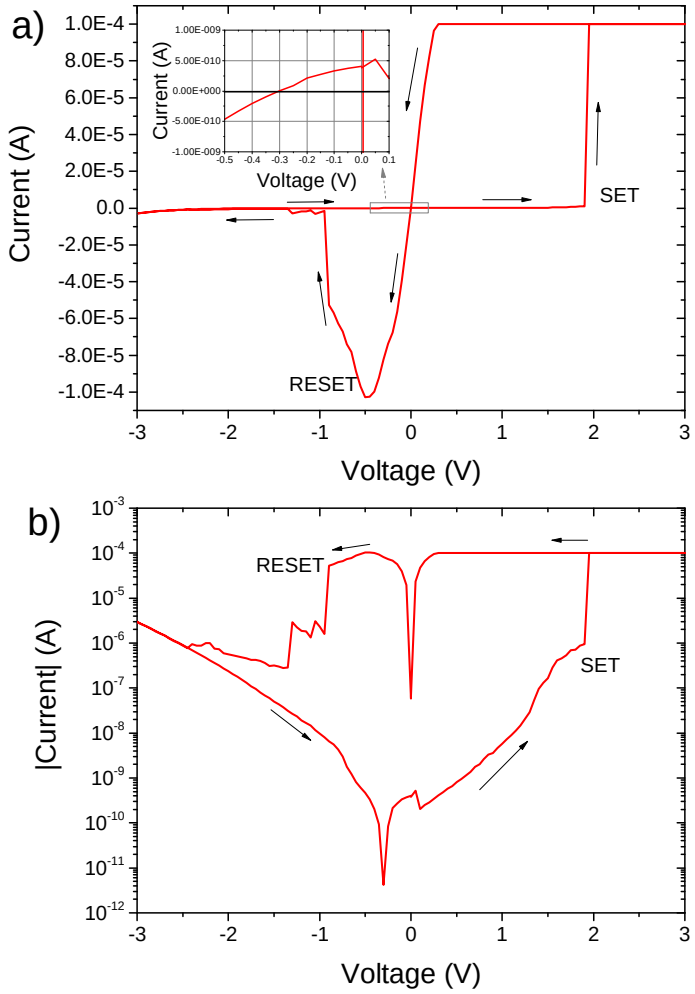

Figure 3.9. *(a) Switching curve of a Pt/$Cu_{0.6}Te_{0.4}$/Al_2O_3/n^+ Si CBRAM cell. The inset shows a detail of the current for low negative voltages, showing that the current becomes positive in the range ∼-0.3 to 0 V. (b) The same switching curve showing the absolute value of the current on a logarithmic scale. This is the usual way of plotting.*

and temperature (Figure 3.10d) when a memory cell switches from a high to low resistive state (see Figure 3.10b) for 3 different cell configurations. In scheme A and B, a load resistor and a transistor respectively are used as a current limiter. In scheme C, a resistor is also used as current limiter, but in this case a capacitance is put in parallel with the memory cell to simulate the capacitive behaviour. When the filament is formed, the discharge of this capacitor causes a large current flow

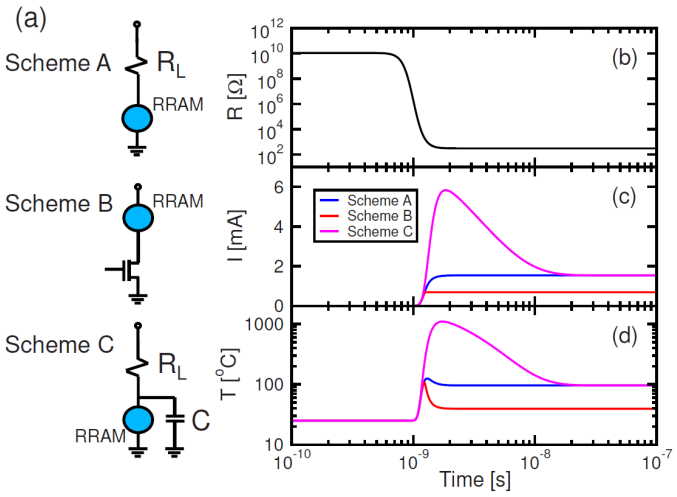

Figure 3.10. *(a) Three electrical schemes where a memory cell is put in series with a load resistor or transistor* without *parasitic capacitance (schemes A and B respectively) and when a parasitic capacitance is taken into account (scheme C). A HRS to LRS transition was simulated (b), and the corresponding current that flows through the cell (c) and temperature (d) in the cell was calculated. When a capacitor is taken into account, a current overshoot is present. [15]*

through the cell (often denoted as *parasistic current overshoot*), whereas this does not happen in absence of the capacitor.

Kinoshita et al. [16] compared different cell configurations (see Figure 3.11) and demonstrated that the parasitic current overshoot (and parasitic capacitance) also has a contribution from the measurement configuration. Using a conventional semiconductor parameter analyser (SPA) shows for all compliance currents below $\sim$1 mA the same reset currents (see Figure 3.11a). This might be related to the slow response of the SPA [17], because switching occurs very fast ($\sim$nanoseconds), whereas the SPA needs longer time before it can adjust the current to the required I_c. This also induces a current overshoot. However, in a configuration where the current is limited by a series resistor, the result is very similar to the first configuration (see Figure 3.11b), illustrating that the response of the SPA is not the cause. Using an integrated transistor in series with the memory cell (referred to as 1T1R configuration) on the other hand shows the expected correlation between compliance current during set (determined by the gate voltage of the transistor) and the reset current (see Figure 3.11c). As expected, a higher I_c leads to lower R_{on} and larger reset currents. Additional configurations were tested with an additional contact pad (which will also have a capacitance) between the memory cell

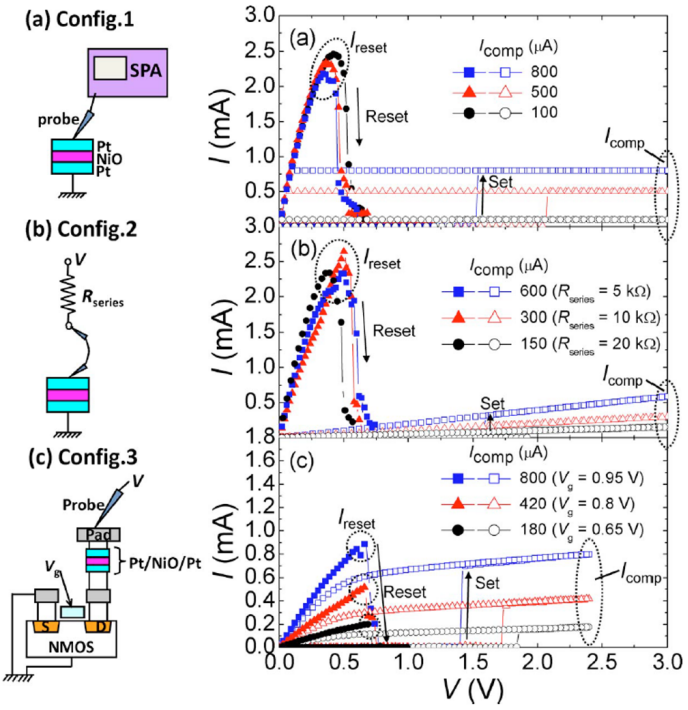

Figure 3.11. *DC switching curves of Pt/NiO/Pt based ReRAM cells for different cell configurations. (a) Single cell where the current is limited by the measurement device, (b) a series resistor is used to limit the current through the cell and (c) a closely packed 1T1R structure where the transistor limits the current, and additional capacitances apart from the internal cell capacitance are avoided. [16]*

and the transistor, and also when an external transistor was put in series with the memory cell. Both configurations lead to a behaviour similar to configurations a and b in Figure 3.11 and could be correlated to additional capacitances that were introduced in the cell configuration.

The conclusion is that for the dot cells in this work, where the current is limited by an external source meter, parasitic effects will be present by (i) the slow response of the measurement device to adjust the current compliance [17], (ii) the capacitance of the large cell and (iii) additional capacitances present in the cell configuration. These parasitics will lead to a lower control of LRS resistance.

References

[1] Brauer, G., Szyszka, B., Vergohl, M., and Bandorf, R. *Vacuum* **84**(12), 1354 – 1359 (2010). Selected Papers from the Proceedings of The Tenth International Symposium on Sputtering and Plasma Processes (ISSP 2009), 8th-10th July 2009, Kanazawa, Japan.

[2] Maier, W., Stowe, K., and Sieg, S. *Angewandte Chemie International Edition* **46**(32), 6016–6067 (2007).

[3] Dahn, J. R., Trussler, S., Hatchard, T. D., Bonakdarpour, A., Mueller-Neuhaus, J. R., Hewitt, K. C., , and Fleischauer, M. *Chem. Mater.* **14**(8), 3519–3523 (2002).

[4] Bonakdarpour, A., Hewitt, K., Hatchard, T., Fleischauer, M., and Dahn, J. *Thin Solid Films* **440**(1-2), 11 – 18 (2003).

[5] Barkhouse, D., Bonakdarpour, A., Fleischauer, M., Hatchard, T., and Dahn, J. *J. Magn. Magn. Mater.* **261**(3), 399 – 409 (2003).

[6] Deng, S. *Templated Synthesis of Porous Materials via Atomic Layer Deposition*. PhD thesis, Ghent University, (2015).

[7] Dendooven, J. *Modeling and In Situ Characterization of the Conformality of Atomic Layer Deposition in High Aspect Ratio Structures and Nanoporous Materials*. PhD thesis, Ghent University, (2012).

[8] Klockenkamper, R. *Total-Reflection X-Ray Fluorescence Analysis*. John Wiley & Sons, Inc., (1997).

[9] Feldman, L. C. and Mayer, J. W. *Fundamentals of surface and thin film analysis*. North-Holland, (1986).

[10] Wagner, C., Riggs, W., Davis, L., and Moulder, J. *Handbook of X-ray Photoelectron Spectroscopy*. Perkin-Elmer Corporation, Physical Electronics Division, (1979).

[11] Doering, R. and Nishi, Y., editors. *Handbook of Semiconductor Manufactering Technology, Second Edition*. CRC Press, (2007).

[12] Saito, Y., Sutou, Y., and Koike, J. *J. Phys. D: Appl. Phys.* **45**(40), 405302 (2012).

[13] Barr, T., Hoppe, E., Dugall, T., Shah, P., and Seal, S. *J. Electron Spectrosc. Relat. Phenom.* **9899**, 95 – 103 (1999).

[14] Moretti, G. *J. Electron Spectrosc. Relat. Phenom.* **95**(2-3), 95 – 144 (1998).

[15] Ielmini, D., Cagli, C., and Nardi, F. *Appl. Phys. Lett.* **94**(6), 063511 (2009).

[16] Kinoshita, K., Tsunoda, K., Sato, Y., Noshiro, H., Yagaki, S., Aoki, M., and Sugiyama, Y. *Appl. Phys. Lett.* **93**(3), 033506 (2008).

[17] Ielmini, D. *IEEE Trans. Electron Devices* **58**(12), 4309–4317 (2011).

4
Binary Tellurides

In this chapter, copper- and silver-telluride are investigated as cation supply layers in CBRAM. In the first part of this chapter, more information on chalcogenides in general is given, and their material properties that are relevant to this work are briefly discussed. Then binary Cu-Te is discussed. Starting from the results published in literature, a single composition is selected and further studied in this work. In a last part, Ag-Te is investigated and compared to Cu-Te. The main results of Ag-Te are presented in section 4.3, while a detailed discussion can be found in Paper I at the end of this chapter.

4.1 Chalcogenides

4.1.1 Chemical properties

Tellurium belongs to group 16 of the periodic system[1] (or to group VIa following the CAS[2] numbering). Other elements in that group are oxygen, sulphur, selenium (all above tellurium) and the radioactive polonium (below Te). The group is referred to as *chalcogenides*. When talking about chalcogenides, one usually refer to S, Se and Te, and alloys containing these elements, while O and its compounds are usually treated separately because of its deviating properties compared to the other chalcogens. Indeed, oxides have a rather large band-gap ($\sim$ 5 to 10 eV)

[1] This is in the modern group numbering convention recommended by IUPAC (International Union of Pure and Applied Chemistry).

[2] Chemical Abstract Service, this is part of the American Chemical Society.

whereas other chalcogenides are semiconductors with a band gap in the range of 1-3 eV [1]. Another variation is found in the bond type. In elemental solids like Si, Ge, Se, S, the bonds are purely covalent[3]. When heteropolar bonds are formed, the bonds get an ionic character. Assume a binary chalcogenide Ge-O(S,Se,Te), then the electronegativity difference between Ge and the chalcogen element decreases from O to Te. Hence the oxide has a higher degree of ionicity compared to the telluride[4].

4.1.2 Microstructure

In section 2.3.3.2 we briefly discussed the occurence of amorphous materials, i.e. materials where the atoms are not arranged in a crystal. The most famous amorphous material is *glass*, which is used to describe silica (SiO_2) based materials. Oxide glasses are known already for a long time and has a history of more than 5000 years. Apart from oxide glasses, chalcogenide glasses also exist, but they have only been studied from the 1950s. However, nowadays they play an important role in technological applications like phase change memories.

4.1.3 Ionic conductivity

Some chalcogenides have the property of being good ionic conductors (for example for Ag, Cu and Li ions). When the conductivity becomes larger than $1\,\mathrm{S/cm}$, and hence comparable to an ionic liquid, they are called *super-ionic* or *fast ionic conductors*. The ionic and electronic conductivities of a series of chalcogenides and halides[5] is presented in Figure 4.1. It is interesting to note that there are no binary ionic conducting glasses, the binary ionic conductors are crystalline. Note also that the amorphous structure of $AgAsS_2$ shows higher ionic conductivity than the crystalline form, which is most likely due to the less dense structure of the glass. In case of crystalline ionic conductors, the high ionic conduction is closely related to the structure of the lattice. Ag_2S (which has an ionic conductivity comparable to NaCl solution, see Figure 4.1), has a cubic structure similar to αAgI (which was the first super ionic conductor discovered [2]). Figure 4.2 shows the crystal structure, with the large spheres being the bcc anion (i.e. S^{2-}) sub-lattice. The squares indicate the octahedral 6b sites, the solid circles the tetrahedral 12d sites and the open circles the triangular 24h sites where the Ag^+ ion can reside. This large degeneracy leads to the liquid like diffusivity of Ag^+ ions. However, it

[3]Note that tellurium has a higher metallic character compared to the elements S and Se from the chalcogenide group.

[4]Sometimes tellurium has in some alloys rather a metallic character. In Ge-Sb-Te films for phase change materials it appeared to have a sixfold coordination instead of twofold that is expected in a covalent system. This can be regarded as a manifestation of metallic character where the six valence electrons are likely to mix up in energy. [1]

[5]With halides we mean materials containing an element from group 17.

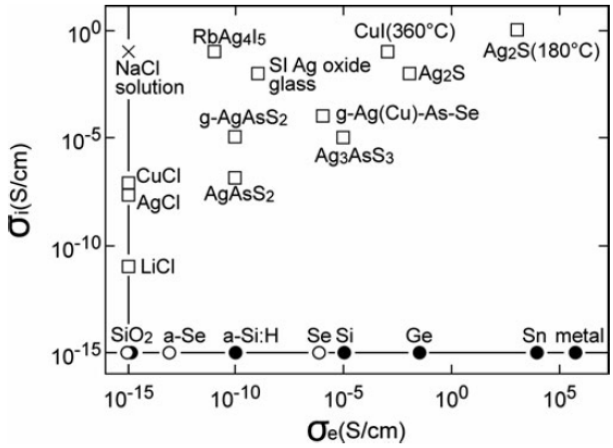

Figure 4.1. *Electronic (σ_e) and ionic (σ_i) conductivities of some halides and chalcogenides, and the reference for NaCl solution ($\times$). The solids without indication "g" or "a" are crystalline. The filled and open circles at ionic conductivities of $10^{-15}\,S/cm$ denote electron and hole mobilities respectively. Conductivities below $10^{-15}\,S/cm$ cannot be measured reliably and are also plotted at $10^{-15}\,S/cm$. [1]*

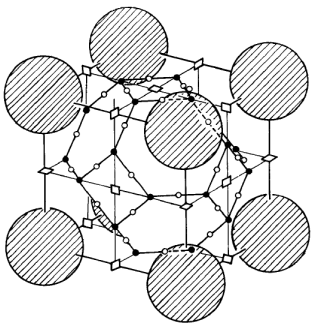

Figure 4.2. *Structure of $\alpha Ag_2(S,Se)$. The large hatched circles in a bcc structure (body centered anion not visible) are the chalcogenide anions. The squares are the octahedral 6b sites, the solid circles the tetrahedral 12d sites and the open circles the triangular 24h sites. [3]*

has been shown that the cations spend most of their time in the tetrahedral (12d) sites. The tetrahedrons formed by four S^{2-} ions surrounding an Ag^{+} ion in a 12d site are connected to each other, sharing each face through which the Ag ions can migrate between different 12d sites. Crystals that do not have this typical structure can still show a high ionic conductivity, which is also related to the polarizability

of the ions (i.e. how easily they are deformed). Ionic conduction generally occurs more easily in a crystal with a partially covalent nature composed of soft (i.e. polarizable) ions compared to a pure ionic crystal [2]. Generally, the polarizability increases with increasing atomic radius (the more extended the electron cloud, the easier it gets deformed). A softer anion sub-lattice deforms more easily, and stabilizes the transition state during cation migration. So generally, selenides will show higher ionic conductivities than sulphides or oxides [3]. Copper and silver are also special atoms in the sense that the Cu^+ and Ag^+ ions have a closed d-shell that is easily polarizable, explaining why so many electrolytes (also glasses) are good ionic conductors for Cu or Ag ions [4].

Finally it can be noted that the chalcogenides in Figure 4.1 also show some electronic conductivity (in contrast to the halides), which can be understood in view of their small band gap. Materials showing both ionic and electronic conductivities are also called *Mixed Ionic Electronic Conductors (MIEC)* [2, 5]. Typically, silver chalcogenides exist in a non-stoichiometric form with a slight excess of Ag (e.g. $Ag_{2+\delta}S$) whereas the copper chalcogenides are Cu deficient (e.g. $Cu_{2-\delta}S$). The former have an excess of electrons to compensate for the excess Ag^+ ions, resulting in a n-type semiconductor, whereas the latter are p-type semiconductors [3].

4.2 Copper-Tellurium

4.2.1 Phase diagram

The Cu_xTe_{1-x} system ($0 < x < 1$) has a complex phase diagram, as is illustrated in Figure 4.3. The solid solubility of Te and Cu is negligible, and intermetallic phases (e.g. CuTe, $Cu_{3-x}Te_2$ and $Cu_{2-x}Te$) are formed. Especially in the range 33-36 at% Te, a lot of intermetallic phases occur. The reader is referred to the review paper of Pashinkin and Fedorov [6] for an overview of the research that has been done on the Cu-Te system and the identification of the intermetallic phases. The formation of these intermetallic phases is energetically favourable because the Gibbs free energy upon mixing the elements and forming the intermetallic phases ΔG_f is negative. This can also be expressed as a lowering of the chemical potential of Cu in the copper telluride phase (μ'_{Cu}) compared to pure copper (μ_{Cu}). The same holds for the chemical potential of Te in the pure metal (μ_{Te}) or in the intermetallic Cu-Te phase (μ'_{Te}). The values of the standard Gibbs free energy change upon formation of the most important Cu_xTe_{1-x} phases are listed in table 4.1.

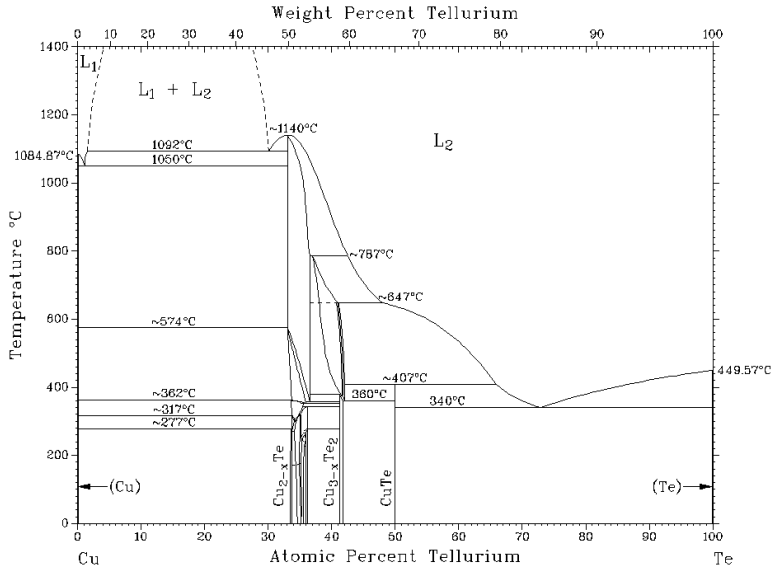

Figure 4.3. *Phase diagram of the binary Cu-Te system. [7]*

Table 4.1. *Standard enthalpies and Gibbs energies of formation for different copper tellurides (at 298 K) [8].*

Compound	-$\Delta_f G^0$ (kJ/mol)
CuTe	24.5 ± 0.8
Cu_3Te_2	73.1 ± 1.2
Cu_2Te	46.5 ± 0.84

4.2.2 Application in CBRAM

The application of Cu-Te in CBRAM was first introduced by Aratani et al. [9] in combination with a GdO_x layer as dedicated switching layer. A thorough study of the application of copper telluride as cation supply layer and the influence of the composition on the resistive switching behaviour has been presented by Goux et al. [10]. We briefly discuss the main results and theories of that paper here because Cu-Te based CBRAM is used as the starting material in this thesis work.

A graded Cu_xTe_{1-x} layer ($0.2 < x < 0.8$) was deposited by a combinatorial sputter technique, which makes the deposition of a layer with a varying composition over a 150 mm wafer possible. By depositing the layer through a dot shadow mask, separated dots with varying composition can be prepared. A dot shadow mask with 3 mm diameter was used to deposit a 50 nm thick Cu_xTe_{1-x}

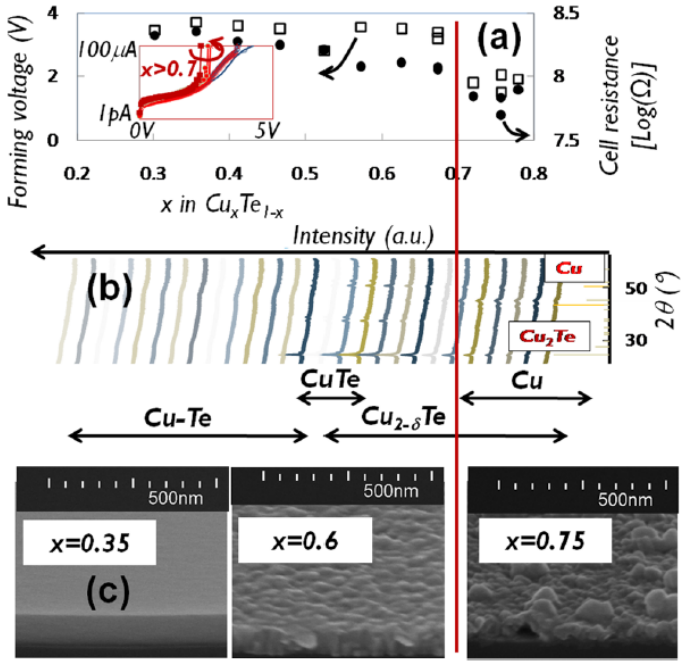

Figure 4.4. *(a) Influence of the composition on the forming voltage and the pristine cell resistance (measured at +0.2 V). (b) XRD patterns as a function of the composition. (c) SEM images showing the surface morphology for a copper poor ($x = 0.35$), Cu rich ($x = 0.75$) and an intermediate ($x = 0.6$) composition. [10]*

layer on a 3 nm thin Al_2O_3 switching layer. The alumina film is deposited by an H_2O based ALD technique on top of an n^+ doped Si substrate. A second shadow mask with 1 mm holes was used to deposit a 50 nm thick Pt top electrode. In this way, very easy to produce, macroscopic Pt/Cu_xTe_{1-x}/Al_2O_3/n^+ Si memory cells ($0.2 < x < 0.8$) were prepared of which the resistive switching characteristics were probed. Figure 4.4a shows the forming voltage and pristine resistance of the memory cells as a function of the compositions. Figure 4.4b gives the XRD patterns for the different compositions. For high Cu contents ($x > 0.7$), XRD peaks corresponding to pure Cu are observed, whereas for intermediate compositions copper telluride phases are present. For Te rich compositions, the as-deposited layer is amorphous. The surface morphology of the films (Figure 4.4c) also changes with composition, from a rough surface for the Cu rich compositions, to a very smooth film for the amorphous Te rich compositions. Figure 4.4a shows that for the Cu rich films a lower pristine resistance, and a lower forming voltage is measured. This is ascribed to a higher Cu in diffusion in the Al_2O_3 for the Cu

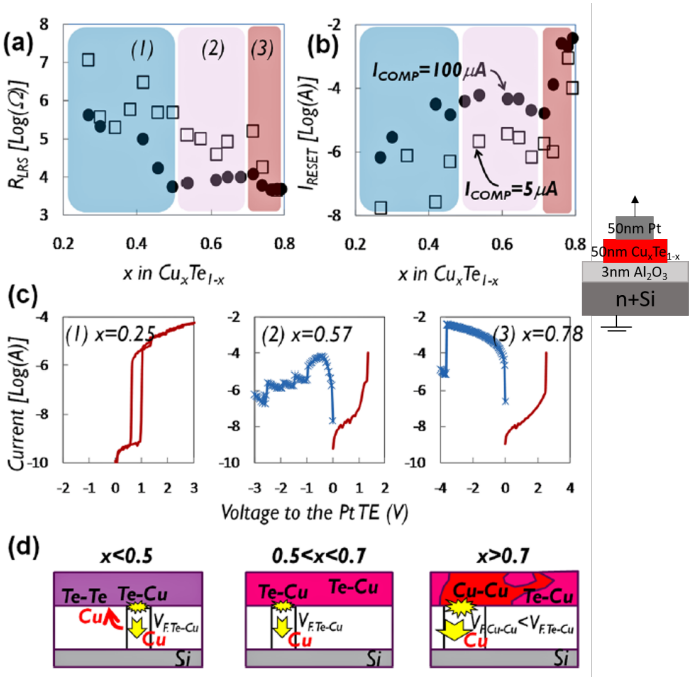

Figure 4.5. *(a) LRS resistance and (b) reset current as a function of the composition for two current compliances (5 and 100 μA). (c) Typical DC switching curves as a function of the composition and (c) a schematic of the influence of the composition of the copper supply layer on the switching behaviour. [10]*

rich films, lowering the initial on resistance and forming voltage. Hence adding Te has the effect of keeping the Cu in the supply layer, because it is energetically favourable to form tellurides (see also table 4.1).

The switching characteristics and an illustration of the influence of the Te on the filament formation/dissolution are shown in Figure 4.5. With increasing Cu content, the LRS resistances become lower for the same I_c (Figure 4.5a), pointing to a stronger, thicker filament. For Te rich cells, the LRS resistance is rather high, pointing to a failure of stable filament formation. The reset current scales accordingly, and increases with Cu content (Figure 4.5b). This is also visible in the switching curves in Figure 4.5c. The Cu poor cells show no stable filament[6], while the Cu rich layers show a strong filament with high reset currents. The latter also showed a higher failure rate. The composition with 57 at% Cu shows a

[6]See Figure 4.5c (1): a double voltage sweep in positive direction is applied. The current increases around 1 V, but when the applied voltage returns to 0 V, the current drops again to very low levels at voltages below 1 V.

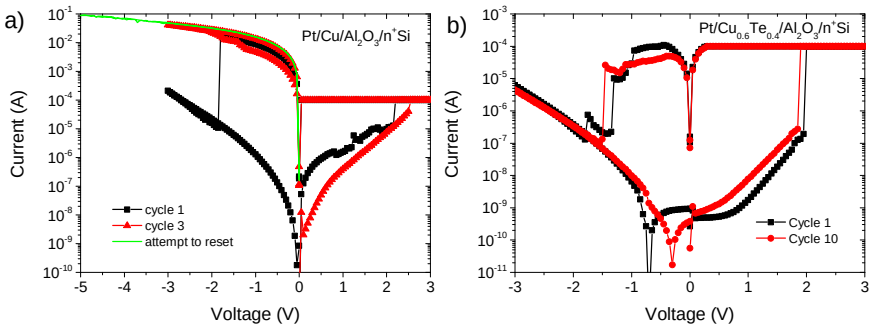

Figure 4.6. *(a) Switching curve of a Pt/Cu/Al_2O_3/n^+ Si cell. The cell gets stuck in a low resistive state after 3 cycles and cannot be reset anymore. (b) Resistive switching in a $Cu_{0.6}Te_{0.4}$ based memory cell. The cell can efficiently be reset and hence shows better cyclability.*

good trade off between the two extreme compositions. A stable filament is formed that can efficiently be reset. The improved reset when Te is added is explained by the affinity between Cu and Te to form tellurides. This acts as an additional driving force for the Cu to go back to the supply layer. When the layer contains too much Te, this does not allow the formation of a stable Cu filament and copper diffuses back to the supply layer after powering off. The conclusion from this paper is that a Cu_xTe_{1-x} based CBRAM stack with x in the range $0.5 < x < 0.7$ shows improved switching properties compared to a pure Cu electrode, and hence a $Cu_{0.6}Te_{0.4}$ composition is selected as optimum composition [10–12].

4.2.3 Resistive switching behavior of $Cu_{0.6}Te_{0.4}$ based CBRAM

In this work, a copper telluride supply layer with 60 at% Cu and 40 at% Te will be used, as suggested by Goux et al. [10]. As a reference, a pure Cu supply layer was also deposited. Figures 4.6a and 4.6b show the switching curves of a memory cell with pure Cu and $Cu_{0.6}Te_{0.4}$ as cation supply layer respectively. The cell with pure Cu shows high reset currents, and is difficult to reset. Most cells get stuck in the LRS after only a few cycles. The cell in Figure 4.6a fails to reset in the third cycle. Even higher reset voltages cannot reset the cell. Using $Cu_{0.6}Te_{0.4}$ improves the cycling behaviour, the cell can efficiently be reset. This results in good endurance properties, where more than 1000 DC cycles can be obtained [10].

It has been reported that both the electric field and thermal effects contribute to the reset [11, 13], because of the thermally and field driven ion migration (see the discussion in section 2.2.4.3). The improved reset for Cu-Te based CBRAM was ascribed to the tendency of Cu to form tellurides with the tellurium that is present in the supply layer. This is also graphically illustrated in Figure 4.7a,

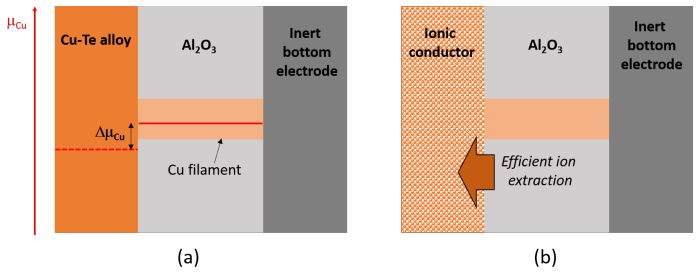

Figure 4.7. *(a) Graphical representation of a CBRAM stack with a Cu-Te alloy as cation supply layer and a Cu filament formed in the Al_2O_3 switching layer. The lower chemical potential of Cu in the Cu-Te alloy is an additional driving force for the Cu to go back to the supply layer. (b) Schematic representation of the Cu-Te alloy as an ionic conductor, which should be beneficial for the Cu ions to go back in the supply layer during reset.*

where the chemical potential of copper in the Cu filament and in the Cu-Te supply layer is schematically shown. The formation of Cu-Te phases can be presented as a lowering of the chemical potential of Cu (and Te). Hence next to the applied electrical field and thermal effects, the lower chemical potential for Cu when it forms a telluride contributes to the *drift* of the Cu from the filament/switching layer back to the supply layer, explaining the efficient reset.

Another property that might contribute to the efficient reset is the ionic conductivity of $Cu_{2-x}Te$, which is reported as a mixed ionic electronic conductor [14]. This was also already briefly mentioned in section 4.1.3 for other chalcogenides. This means that Cu ions can move in the $Cu_{2-x}Te$ lattice under influence of an applied potential. Using a material that shows ionic conductivity in contact with the Al_2O_3 layer instead of a pure metal can be expected to contribute to an efficient evacuation of the Al_2O_3 switching layer during reset. Indeed, instead of reduction of the Cu ions when they reach the supply layer, they can move to some extent in the supply layer, which should enhance Cu extraction from the switching layer [15]. This is also schematically shown in Figure 4.7b.

In section 2.3.2.2, the influence of moisture on the oxidation of Cu [16] and the influence of CuO_x that acts as a cation source [17] was briefly discussed. Note that in a Cu-Te electrode, the Cu is also in an oxidized state, by the presence of Te. This is also demonstrated by means of XPS, and is discussed in the next section. Hence this (partial) oxidized state of Cu can also contribute to the reliable, reproducible CBRAM operation.

4.2.4 XPS analysis of copper tellurides

The $Cu_{0.6}Te_{0.4}$ is investigated with XPS, and its position in the Wagner plot is determined. As discussed in section 3.4.3.3, chemical state analysis is possible based on the position of the compound in the Wagner plot. For the crystalline supply layers, one can deduce the formal oxidation state from the compounds that are detected by means of XRD. However, for an amorphous material this is not possible, and hence the XPS analysis performed on $Cu_{0.6}Te_{0.4}$ serves as a reference for the other alloys further investigated in this work.

Next to $Cu_{0.6}Te_{0.4}$, also $Cu_{2-x}Te$, $Cu_{1+x}Te$ and pure Cu were deposited. The $Cu_{2-x}Te$ sample contains 63.7 at% Cu, and diffraction peaks of the hexagonal $Cu_{2-x}Te$ phase [18] were present. Hence it is slightly Cu poor, but the XRD analysis learns that the main oxidation state of Cu should be (I+) as the oxidation state of Te is (II-). The $Cu_{1+x}Te$ sample has 50.5 at% Cu, and next to orthorhombic CuTe [19], diffraction peaks of $Cu_{3-x}Te_2$ [20] with some pure Te were present. Hence the XPS measurement should clearly have a signature of Cu(II+), however a contribution of a lower oxidation state might be present.

Figure 3.7a shows the position in the Cu Wagner plot of the different compositions, and Figure 3.7b the Te peaks. All the Te peaks are shifted towards lower binding energies, as Te is being reduced.

In the Cu Wagner plot, one observes that the Cu $2p_{3/2}$ peaks of the Cu-Te compounds are shifted towards higher binding energies compared to metallic Cu. This is explained by Cu being partially oxidized due to the formation of Cu-Te bonds. Indeed, the covalent bond is polarized because Te has the larger electronegativity (2.1) compared to Cu (1.9), which means that Te has a higher tendency to attract the electrons involved in the bonding, leaving the Cu in a partially oxidized state. The modified Auger parameter α' is the smallest when we have Cu(I+) (in case of $Cu_{2-x}Te$), whereas α' is the largest when we have Cu(II+) (in case of $Cu_{1+x}Te$). This is in agreement with the discussion in section 3.4.3.3, as the screening is much more efficient for Cu(II+), leading to higher relaxation energies and hence a larger α'. The value for pure Cu was also measured from a Cu sputtered film and indicated on the plot. The $Cu_{0.6}Te_{0.4}$ has α' in between the other Cu-Te compounds. Diffraction peaks of hexagonal $Cu_{2-x}Te$ phase [18] were observed, but because the compound is poor in Cu, also CuTe can be expected (note that orthorhombic CuTe [19] indeed crystallizes above $100°C$, as was observed from *in situ* XRD, see Figure 4.9 in the next section). The lines with slope -3 are also plotted through Cu and $Cu_{0.6}Te_{0.4}$, and it is clear that they are hardly shifted. Moreover, as pointed out before, a small error in reading the peak positions leads to a shift in the intercept, which might give a faulty conclusion about the initial state effects. Note that the values of α' are also larger compared to the corresponding sulphides and selenides, as was pointed out in the discussion in section 3.4.3.3.

It can be concluded that XPS is useful to investigate whether Cu is forming

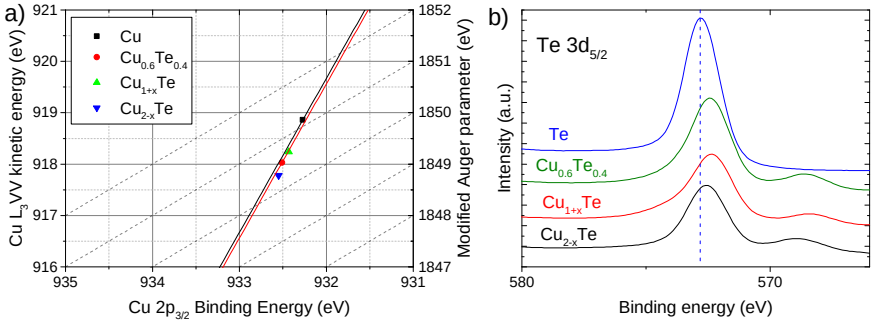

Figure 4.8. *Cu Wagner plot (a) and the Te $3d_{5/2}$ peaks (b) of different Cu-Te compounds, prepared by magnetron sputtering. As a reference, pure Cu and Te are also indicated.*

bonds with Te or if it is in a metallic state. The position in the Wagner plot allows for chemical state analysis. Hence for amorphous compounds, where no compound identification is possible from XRD, XPS can be used to get more insight in the oxidation state and the bonds that are formed. In Chapter 5, where $Cu_{0.6}Te_{0.4}$ is alloyed with other elements, XPS will also give information on the bonds of the alloying elements.

4.2.5 Thermal stability of $Cu_{0.6}Te_{0.4}$

To be useful for integration in memory devices, the material should be sufficiently stable, i.e. not transform or separate in multiple phases under the thermal budget applied during device processing. The phase diagram (see Figure 4.3) shows that for the selected composition, the $Cu_{3-x}Te_2$ phase appears and has a freedom in composition of 1.5 at%. Deviation from this composition will result in phase separation into $Cu_{3-x}Te_2$ and the neighbouring phases (CuTe for Te rich and $Cu_{2-x}Te$ for Te poor composition). Note that the phase in Figure 4.3 is drawn in the region 41-42 at% Te, while in the paper of Pashinkin and Fedorov [6] the phase is drawn from 40 to 41.5 at%. That paper also reports the transformation from an orthorhombic to tetragonal structure at $150°C$. At $\sim 360°C$ another transformation occurs[7]. The phase diagram shows also that the range 33-36 at% Te is a very complex region with multiple phases and hence is preferably avoided. It is also clear that more than 50 at% Te has to be avoided because of the presence of an eutectic point with a melting temperature as low as $340°C$ (and hence significantly below the required $400°C$ in BEOL).

Figure 4.9 shows the *in situ* XRD pattern of a 50 nm layer of $Cu_{0.6}Te_{0.4}$ showing phase separation, and multiple phase transformations upon annealing. The

[7] It has been reported to transform towards a cubic structure [6].

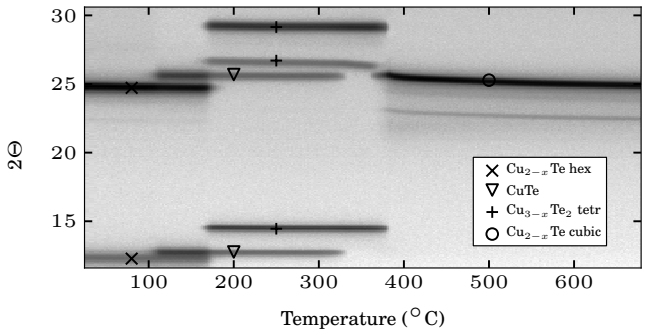

Figure 4.9. *In situ XRD plot of a 50 nm layer of $Cu_{0.6}Te_{0.4}$. The composition has slightly less Cu (58 at%).*

Table 4.2. *Standard Gibbs free energies of formation for different silver-tellurides.*

Compound	-$\Delta_f G^0$ (kJ/mol)
αAg_2Te	41.42 [26], 40.1 ± 0.3 [27]
αAg_5Te_3	102.24 ± 28 [28], 88.78 ± 3.40 [27]

pattern is discussed more in Papers II and III. In this thesis, alloying elements are added to avoid these transformations and to stabilize the copper supply layer. This is the topic of Chapter 5. In the next section, first Ag-Te is investigated in terms of material stability and CBRAM functionality.

4.3 Silver-Tellurium

4.3.1 Phase diagram

Next to copper, silver is often used as active electrode in CBRAM [21–25]. Hence it is interesting to investigate the binary Ag_xTe_{1-x} system ($0 < x < 1$), in analogy to copper-tellurium. The Ag-Te phase diagram is shown in Figure 4.10. The solid solubility of silver and tellurium is negligible, and intermetallic phases are formed. The phases that occur at room temperature are the low temperature αAg_2Te phase, which has a monoclinic structure and the low temperature αAg_5Te_3 phase with a hexagonal lattice. The Gibbs free energy of formation of the intermetallic phases at standard conditions[8] is given in table 4.2. Both phases transform at higher temperatures, which is also observed by *in situ* XRD and discussed in Paper I. The phase

[8]This is at a pressure of 1 atm and a temperature of 298.15 K (25°C).

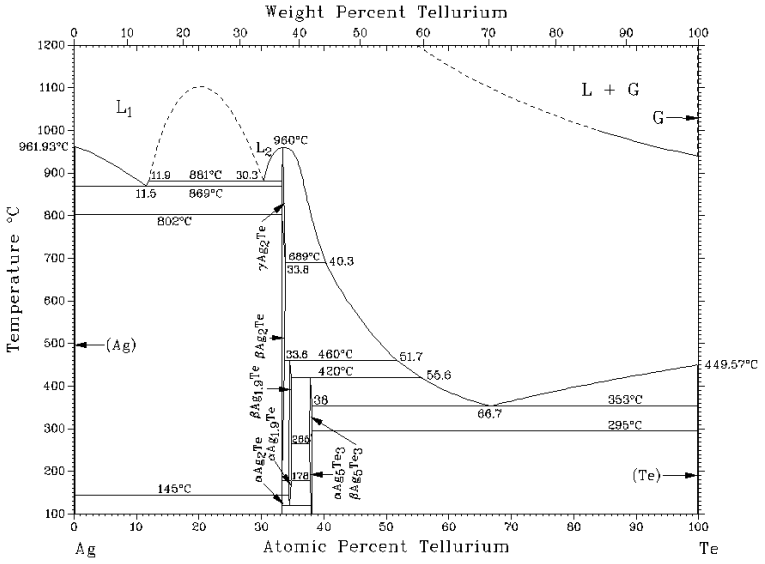

Figure 4.10. *Phase diagram of the binary Ag-Te system. [7]*

diagram also shows the existence of a high temperature $Ag_{1.9}Te$ phase in the 120-460°C temperature window, which exists in two polymorphs with a transformation temperature at 178°C [29]. A eutectic point at a composition of 66.7 at% Te has a melting temperature of only 353°C. Hence for alloys with more than 38 at% Te, a melting temperature below 400°C occurs, and hence they do not show the required thermal stability to sustain BEOL processing. Compared to the phase diagram of Cu-Te (Figure 4.3), the Ag-Te system is less complex, especially in the range of 33-38 at% Te, less phases are present. Note that also less Te (38 compared to 50 at% for Cu-Te) can be added because otherwise the alloy has a low melting temperature due to the eutectic point.

4.3.2 Application in CBRAM

A study of the use of Ag_xTe_{1-x} ($0 < x < 1$) as a cation supply layer is presented in Paper I at the end of this chapter. The material is evaluated on two aspects: (i) its thermal stability and (ii) its functionality as a cation (Ag^+) supply layer in Pt/Ag_xTe_{1-x}/Al_2O_3/n^+ Si CBRAM cells. The paper presents a combinatorial materials study where a graded Ag_xTe_{1-x} layer of 50 nm is deposited on a 150 mm wafer, delivering the whole binary material system in a single deposition run. Figure 4.11 shows a picture of a sample that was prepared in this way, with a gradient in the Te composition over the length of the substrate. At one end, the layer is Ag rich and Te poor, whereas at the other end the layer is Ag poor and Te rich.

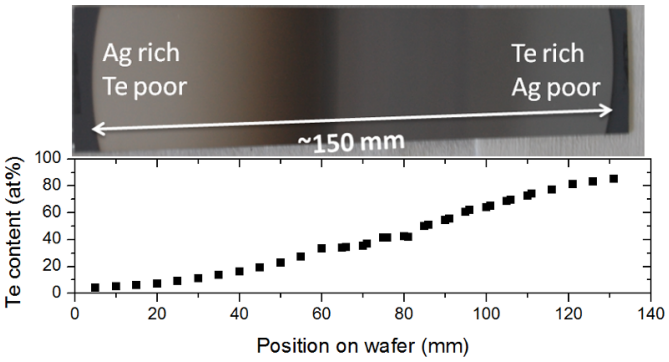

Figure 4.11. *Photograph of a graded Ag_xTe_{1-x} layer ($0 < x < 1$) over a length of 150 mm on an Al_2O_3/Si wafer (top) and the composition as a function of the position on the wafer, determined by RBS (bottom).*

This was verified by RBS and the composition as a function of the position on the substrate is shown on the graph in Figure 4.11. In the next subsections, we discuss the main observations and results. A thorough discussion is given in Paper I.

4.3.2.1 Thermal stability

From the phase diagram, one could exclude already the region with more than 38 at% Te, because of the low melting temperature as discussed above. One should also take into account that phase separation will occur if the alloy does not have the stoichiometry of the intermetallic phases. Both phenomena were clearly observed by (*in situ*) XRD of the graded layer, as discussed in Paper I. Surface morphology was inspected by SEM and showed smooth layers for pure Ag and compositions with 33 at% or more Te. However, at the Ag rich side of Ag_2Te, rough surface morphology with large protrusions appeared. EDX analysis showed the silver rich compositions of these grains, suggesting that the Ag that cannot be consumed in Ag_2Te segregates as large crystals. This is illustrated in Figure 4.12, where the *in situ* XRD patterns of a Ag rich ($\sim$ 70 at% Ag, Figure 4.12a) and Ag poor ($\sim$ 64.8 at% Ag, Figure 4.12b) layer are shown, together with a SEM image of the surface (Figures 4.12c and 4.12d). It is clear from the *in situ* XRD pattern that the Ag rich layer shows next to XRD peaks of Ag_2Te, also diffraction peaks of silver. The layer with a composition close to Ag_2Te at the Ag poor side (further denoted as $Ag_{2-\delta}Te$) shows a very smooth surface morphology and only diffraction peaks associated to Ag_2Te are measured. This composition is selected for further electrical characterization. Note that moving towards a composition of 38 at% Te results in more severe phase separation and is for that reason not selected.

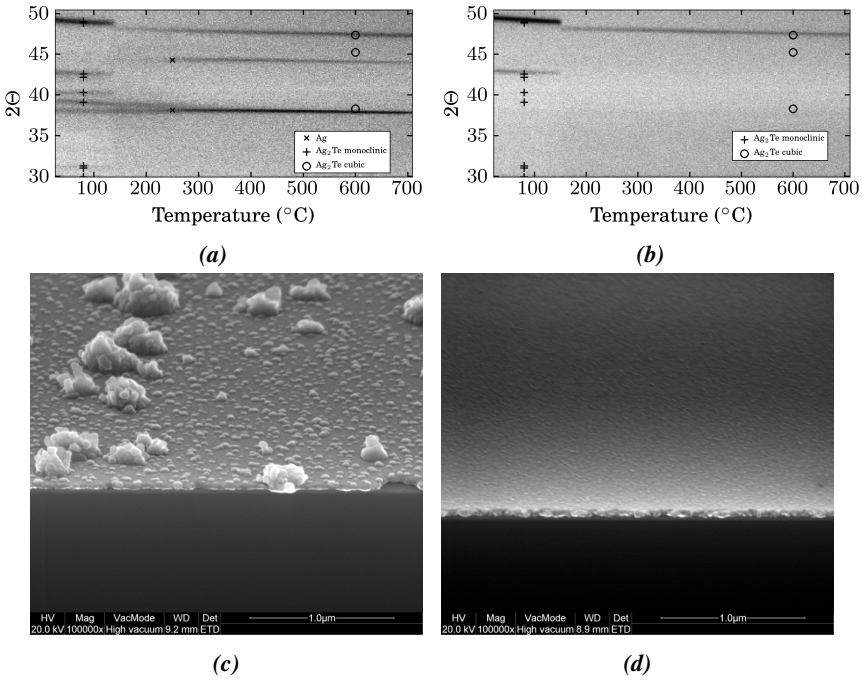

Figure 4.12. *In situ XRD patterns, measured at a heating rate of 0.5°C/s of a 50 nm layer $Ag_{70}Te_{30}$ (a) and $Ag_{64}Te_{36}$ (b). (c-d) The cross section SEM images under an angle of 20° of the as-deposited layers of (a) and (b), showing large Ag rich grains for the former, whereas a smooth surface is observed for the latter.*

4.3.2.2 Resistive switching behaviour

The switching behaviour of $Ag_{2-\delta}Te$ based CBRAM was investigated and compared to memory cells with pure Ag by implementing them in 580 µm diameter dot cells. Typical switching curves of pure Ag and $Ag_{2-\delta}Te$ are depicted in Figures 4.13a and 4.13b respectively. The most important observation is that a similar behaviour as with Cu and Cu-Te based CBRAM is observed. After only a few cycles, the silver based cells cannot be reset anymore. This was also reported in other work [15]. This illustrates again the role of tellurium to achieve an efficient reset. This might again be explained by the preferred telluride formation of Ag with Te, resulting in an additional driving force for the Ag from the filament to go back to the supply layer. Note that Ag_2Te is also reported to be a MIEC material, showing next to electronic also ionic conductivity (especially the cubic structure at higher temperatures) [30, 31]. This might contribute to an efficient flux from the silver ions from the switching layer back into the supply layer during reset.

It should be mentioned that a compliance current of 100 µA resulted in a cer-

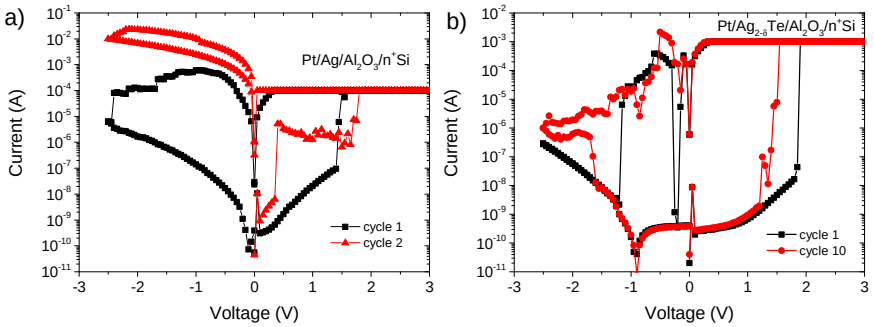

Figure 4.13. *(a) Switching curve of a Pt/Ag/Al_2O_3/n^+ Si cell. The cell gets stuck in the low resistive state in the second cycle. (b) Resistive switching of a $Ag_{2-\delta}Te$ based memory cell, showing good cycling and efficient reset.*

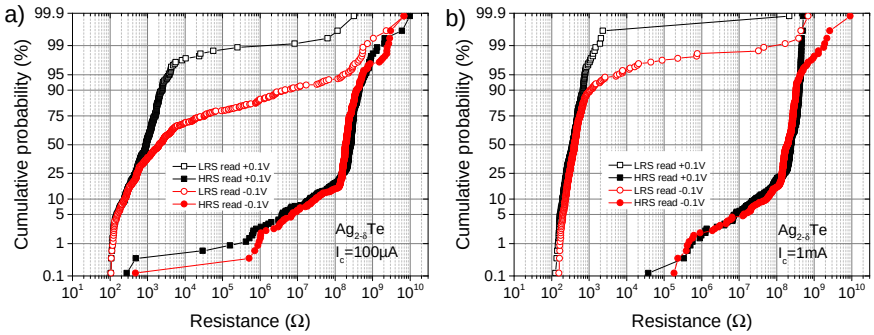

Figure 4.14. *Cumulative distributions of the LRS and HRS resistances extracted from the set-reset sweeps of 40 cells that were cycled 10 times each, when a current compliance of 100 μA (a) or 1 mA (b) was applied during the set sweep.*

tain amount of *volatile* switches, i.e. after setting the cell and when no voltage is applied anymore, the filament tends to dissolve and the cell returns to a high resistive state. This is illustrated in Figure 4.14a, which shows the LRS and HRS resistances extracted from the set and reset sweep at + and -0.1 V. For a stable filament, both values for LRS should coincide. However, about 50 % of the cells return to a higher resistance, and slightly more than 10 % even goes to a high resistive state (R>10^6 Ω). Using a higher compliance current during programming usually results in stronger, more stable filaments [32]. Indeed, Figure 4.14b shows the same plot for cells cycled with a I_c of 1 mA, where only about 1 % returns to a HRS.

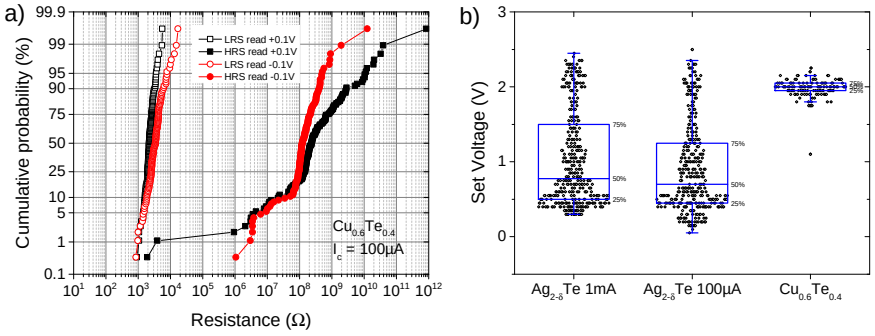

Figure 4.15. *(a) Cumulative distributions of the LRS and HRS resistances extracted from the set (at +0.1 V) and reset (at -0.1 V) sweeps of 14 $Cu_{0.6}Te_{0.4}$ based CBRAM cells that were cycled 10 times each, using a current compliance of 100 µA in the set sweep. (b) Boxplot of the set voltages of the Cu- and Ag-telluride based cells.*

4.3.2.3 Comparison Cu-Te versus Ag-Te

It is interesting to compare the resistive switching of silver- and copper-telluride based CBRAM. Figure 4.15a shows the LRS and HRS distribution extracted from the set and reset sweeps from $Cu_{0.6}Te_{0.4}$ based cells, using a current compliance of 100 µA during the set. It is clear that the LRS is much more stable, i.e. resistances extracted from set and reset sweep are similar, although the resistance extracted from the reset sweep is shifted towards slightly higher resistances, pointing to already a partial dissolution of the filament. However, no cells returned to HRS already. It can also be observed that the LRS resistance is higher compared to $Ag_{2-\delta}Te$ and the spread on LRS is much smaller (LRS spans only one order of magnitude, whereas for $Ag_{2-\delta}Te$ this is larger for both current compliances). Figure 4.15b shows the boxplot of the set voltage of $Ag_{2-\delta}Te$ cells for both current limits and of $Cu_{0.6}Te_{0.4}$ cells. This shows a larger scatter for the silver-telluride cells compared to copper-telluride. So to summarize, the $Ag_{2-\delta}Te$ cells show a LRS that is generally lower in resistance and more volatile compared to $Cu_{0.6}Te_{0.4}$.

To find the cause of this different behaviour for Cu- and Ag-Te based CBRAM, one should consider the main steps during CBRAM operation[9] to see which one can be different and hence cause the different cell behaviour. The formation enthalpy of Ag_2Te is very similar to the copper tellurides (see tables 4.2 and 4.1) and hence an electrode related effect is unlikely to explain the different filament stability. Reduction at the counter electrode will also not be rate limiting and cause

[9]This is (i) oxidation of the species, (ii) ion migration and (iii) reduction and nucleation of the metal phase (see sections 2.2.1, 2.2.2 and 2.2.3 respectively).

the lower filament stability as reduction of Ag^+ to Ag has a higher tendency to proceed compared to reduction of Cu^{2+} or Cu^+ to Cu (because of the higher redoxpotential of the Ag^+/Ag couple compared to Cu^{2+}/Cu or Cu^+/Cu [33, 34]). Hence this makes a difference in ion migration most likely the cause of the different behaviour. A higher mobility of the Ag ions in the switching layer may cause a lower filament stability. This could also explain the lower set voltages that are observed. As a suggestion for future work, this could be further investigated by comparing the diffusion of Ag and Cu in a Al_2O_3 layer. This could be done for example by annealing a Ag/Al_2O_3/Si stack (and the same with Cu) and comparing the Ag and Cu signal in the Al_2O_3 layer by ToF SIMS[10].

Although it is difficult to investigate, the difference in filament stability might also be related to a different filament morphology. The larger spread on LRS resistances suggests a worse control of the formed filament, for example of the filament thickness. However it can also be related to the formation of multiple filaments, and the variation on the number of filaments that are formed. The more volatile behaviour can be the result of thinner, easier to dissolve filaments. It was shown by TEM analysis that thin filaments are indeed unstable and tend to break up in spheres due to the Rayleigh instability [35]. If multiple filaments are formed, or can be formed, the set voltage might depend on which filament is formed, resulting in a larger fluctuation. However, to investigate the difference in filament morphology, microscopic techniques that can probe the filament (like TEM [36] or 3D C-AFM [37]) would be required, which is beyond the scope of this thesis.

4.4 Conclusion

In this chapter, the influence of alloying the Cu supply layer with tellurium on the resistive switching of Pt/Cu_xTe_{1-x}/Al_2O_3/n^+ Si was discussed. Improved cycling behaviour of memory cells with a $Cu_{0.6}Te_{0.4}$ layer compared to pure Cu was demonstrated. The cells show a more efficient reset, resulting in better cycling and endurance properties. The improved reset is explained by the preferred Cu-Te formation over pure Cu, acting as an additional driving force for the Cu from the filament to go back to the supply layer. Also the ionic conductivity of $Cu_{2-x}Te$ can contribute to the efficient reset by allowing an efficient flux of ions out of the switching layer back to the supply layer.

Next to Cu, Ag was used to provide the cations for CBRAM operation. The binary Ag_xTe_{1-x} system ($0 < x < 1$) was investigated in terms of materials stability and functionality as a cation supply layer. Based on materials properties, $Ag_{2-\delta}Te$ was selected and compared to pure Ag as cation source in CBRAM. A similar behaviour as for $Cu_{0.6}Te_{0.4}$ was observed. However, the filament turns out

[10]Time of flight secondary ion mass spectroscopy. This technique has also been used in Paper III.

to be more volatile compared to $Cu_{0.6}Te_{0.4}$. This could be related to a different mobility of the ions in the Al_2O_3 layer, but it could also be related to a different filament morphology. For example filament thickness and the number of filaments that are formed could influence this. Further research at the microscopic scale would be required to elucidate this.

In view of the inferior behaviour of the Ag-based devices, the rest of this thesis will focus on Cu-Te based CBRAM. However, it was shown that the binary Cu-Te system has a complex phase diagram in the composition range of interest. Hence in the next chapter, the thermal stability of $Cu_{0.6}Te_{0.4}$ is improved by alloying the material. Also the influence of the alloying elements on CBRAM functionality is investigated. In Chapter 6, alternative ternary alloys containing Cu and Te are investigated.

References

[1] K. Tanaka and K. Shimakawa, *Amorphous Chalcogenide Semiconductors and Related Materials*, Springer, (2011).

[2] T. Kudo and K. Fueki, *Solid state ionics*, Wiley-VCH, (1990).

[3] S. R. Hariharsudan, Master's thesis, Katholieke Universiteit Leuven, (2009).

[4] M. Aniya, *Solid State Ionics* **50**(1-2), 125 – 129 (1992).

[5] I. Riess, *Solid State Ionics* **157**(1-4), 1 – 17 (2003), Proceedings of the 6th International Symposium on Systems with Fast Ionic Transport (ISSFIT).

[6] A. Pashinkin and V. Fedorov, *Inorg. Mater.* **39**(6), 539–554 (2003).

[7] ASM International, The Materials Information Society, *Binary Alloy Phase Diagrams (Second Edition Plus Updates)*, (1990).

[8] A. Pashinkin and L. Pavlova, *Inorg. Mater.* **41**(10), 1050–1054 (2005).

[9] K. Aratani, K. Ohba, T. Mizuguchi, S. Yasuda, T. Shiimoto, T. Tsushima, T. Sone, K. Endo, A. Kouchiyama, S. Sasaki, A. Maesaka, N. Yamada, and H. Narisawa, *Int. Electron Devices Meet.* , 783 –786 (2007).

[10] L. Goux, K. Opsomer, R. Degraeve, R. Muller, C. Detavernier, D. J. Wouters, M. Jurczak, L. Altimime, and J. A. Kittl, *Appl. Phys. Lett.* **99**(5), 053502 (2011).

[11] L. Goux, K. Sankaran, G. Kar, N. Jossart, K. Opsomer, R. Degraeve, G. Pourtois, G. M. Rignanese, C. Detavernier, S. Clima, Y. Y. Chen, A. Fantini, B. Govoreanu, D. Wouters, M. Jurczak, L. Altimime, and J. A. Kittl, *IEEE Symp. VLSI Technol.* , 69–70 (2012).

[12] U. Celano, L. Goux, K. Opsomer, A. Belmonte, M. Iapichino, C. Detavernier, M. Jurczak, and W. Vandervorst, *Nanoscale* **5**, 11187–11192 (2013).

[13] D. Ielmini, *IEEE Trans. Electron Devices* **58**(12), 4309–4317 (2011).

[14] R. A. Yakshibaev, N. N. Mukhamadeeva, and R. F. Almukhametov, *Phys. Status Solidi A* **108**(1), 135–141 (1988).

[15] H. Radhakrishnan, In *15th IEEE Mediterranean Electrotechnical Conference*, 515–520, (2010).

[16] T. Tsuruoka, K. Terabe, T. Hasegawa, I. Valov, R. Waser, and M. Aono, *Adv. Funct. Mater.* **22**(1), 70–77 (2012).

[17] B. G. Willis and D. V. Lang, *Thin Solid Films* **467**(1-2), 284 – 293 (2004).

[18] International Centre for Diffraction Data, Newtown Square, PA, *JCPDS Data Card no. 00-049-1411*, (2004).

[19] International Centre for Diffraction Data, Newtown Square, PA, *JCPDS Data Card no. 01-089-4311*, (2004).

[20] International Centre for Diffraction Data, Newtown Square, PA, *JCPDS Data Card no. 01-085-0606*, (2004).

[21] I. Valov, R. Waser, J. R. Jameson, and M. N. Kozicki, *Nanotechnology* **22**(25), 254003 (2011).

[22] I. Valov and M. N. Kozicki, *J. Phys. D: Appl. Phys.* **46**(7), 074005 (2013).
[23] R. Waser, R. Dittmann, G. Staikov, and K. Szot, *Adv. Mater.* **21**(25-26), 2632–2663 (2009).
[24] S. Gao, C. Chen, Z. Zhai, H. Y. Liu, Y. S. Lin, S. Z. Li, S. H. Lu, G. Y. Wang, C. Song, F. Zeng, and F. Pan, *Appl. Phys. Lett.* **105**(6), 063504 (2014).
[25] H.-M. Seung, M.-J. Song, J.-G. Park, and K.-C. Kwon, *J. Korean Phys. Soc.* **64**(7), 949–953 (2014).
[26] T. Takahashi and O. Yamamoto, *J. Electrochem. Soc.* **117**(1), 1–4 (1970).
[27] F. Tesfaye, P. Taskinen, M. Aspiala, and D. Feng, *Intermetallics* **34**(0), 56 – 62 (2013).
[28] E. Echmaeva and E. Osadchii, *Geology of Ore Deposits* **51**(3), 247–258 (2009).
[29] I. Karakaya and W. Thompson, *J. Phase Equilib.* **12**(1), 56–63 (1991).
[30] I. Rom and W. Sitte, *Solid State Ionics* **70-71, Part 1**, 147 – 152 (1994).
[31] A. Bürgermeister and W. Sitte, *Solid State Ionics* **141-142**, 331 – 334 (2001).
[32] U. Russo, D. Kamalanathan, D. Ielmini, A. Lacaita, and M. Kozicki, *IEEE Trans. Electron Devices* **56**(5), 1040–1047 (2009).
[33] L. Goux and I. Valov, *Phys. Status Solidi A* **213**, 274–288 (2016).
[34] D. R. Lide, editor, *CRC Handbook of Chemistry and Physics 90th Edition*, CRC Press, (2009).
[35] C.-P. Hsiung, H.-W. Liao, J.-Y. Gan, T.-B. Wu, J.-C. Hwang, F. Chen, and M.-J. Tsai, *ACS Nano* **4**(9), 5414–5420 (2010).
[36] W. A. Hubbard, A. Kerelsky, G. Jasmin, E. R. White, J. Lodico, M. Mecklenburg, and B. C. Regan, *Nano Letters* **15**(6), 3983–3987 (2015).
[37] U. Celano, L. Goux, A. Belmonte, K. Opsomer, A. Franquet, A. Schulze, C. Detavernier, O. Richard, H. Bender, M. Jurczak, and W. Vandervorst, *Nano Letters* **14**(5), 2401–2406 (2014).

Paper I
Combinatorial Study of Ag-Te Thin Films and Their Application as Cation Supply Layer in CBRAM Cells*

Abstract

In this work, we investigate binary Ag-Te thin films and their functionality as a cation supply layer in conductive bridge random access memory devices. A combinatorial sputter deposition technique is used to deposit a graded Ag_xTe_{1-x} ($0 < x < 1$) layer with varying composition as a function of the position on the substrate. The crystallinity, surface morphology, and material stability under thermal treatment as a function of the composition of the material are investigated. From this screening, a narrow composition range between 33 and 38 at% Te is selected which shows a good morphology and a high melting temperature. Functionality of a single $Ag_{2-\delta}Te$ composition as cation supply layer in CBRAM with dedicated Al_2O_3 switching layer is then investigated by implementing it in 580 µm diameter dot Pt/$Ag_{2-\delta}Te$/Al_2O_3/Si cells. Switching properties are investigated and compared to cells with a pure Ag cation supply layer. An improved cycling behavior is observed when Te is added compared to pure Ag, which we relate to the ionic conducting properties of Ag_2Te and the preferred formation of Ag-Te phases.

*Published as: W. Devulder, K. Opsomer, J. Meersschaut, D. Deduytsche, M. Jurczak, L. Goux, C. Detavernier, *ACS Comb. Sci.*, 17, 334-340, 2015

A. Introduction

New memory concepts are currently investigated to replace the widely used Flash memory, which is expected to face its scaling limits in the future. Among the emerging technologies, resistive random access memory (RRAM) seems a viable candidate because it combines fast and low power operation with good scalability [1]. In RRAM, a memory element is switched between two resistive states, constituting the on and off or logic 1 and 0 states of the cell. Conductive Bridge Random Access Memory (CBRAM) is a kind of RRAM, and basically consists of an electrochemical active electrode containing Ag or Cu, an electrolyte layer and an inert counter electrode. When a positive bias is applied on the active electrode, cations drift through the electrolyte and are reduced at the counter electrode. A conductive filament of Cu or Ag is grown and when the filament connects both electrodes, the cell switches to a low resistive state (LRS). Applying a bias of opposite polarity dissolves the filament again and switches the cell back to the high resistive state (HRS). In this way reversible switching is possible [2]. Several materials for the electrolyte and active electrode are reported. Chalcogenide materials (Ag_2S [3], Cu_2S [4], GeSe [5], GeS [6]), organic materials [7,8] and binary metal oxides (HfO_2 [9], Ta_2O_5 [10], ZrO_2 [11], SiO_2 [12,13] and Al_2O_3 [14]) are reported as electrolyte. For the cation supply layer, besides of pure Cu or Ag, alloys containing these elements have been reported [15–17]. Devices using a chalcogenide material as cation supply layer like Cu_xTe_{1-x} [14] (x$\sim$ 0.6), Cu_2S or Cu_2Se [18](or with Ag instead of Cu) on top of an oxide as switching layer, showed an improved cycling behavior compared to a pure Cu or Ag supply layer. These chalcogenide materials are also reported as solid ionic conductors (SIC) [18,19]. From this point of view it is interesting to investigate the binary Ag-Te system, and compare the resistive switching behavior of Pt/Ag_xTe_{1-x}/Al_2O_3/Si CBRAM cells with cells where pure Ag is used. In this paper, we first investigate the material properties of Ag_xTe_{1-x} ($0 < x < 1$) as a function of the Te content. To allow for efficient material screening, a combinatorial deposition technique is used to create a thin Ag-Te film with a composition that varies as a function of the position on the wafer. Based on material properties, an optimum Ag-Te composition ($Ag_{2-\delta}Te$) is selected to implement in 580 µm diameter dot CBRAM cells and cycling is compared to cells with pure Ag.

B. Experimental Procedures

To investigate the material properties of Ag_xTe_{1-x} as a function of the composition ($0 < x < 1$), a 50 nm layer was deposited by magnetron sputtering, using a Balzers deposition tool. The elements are sputtered from two different sputter targets (a pure Ag and a pure Te target), and shadow masks in front of the sputter targets allow to modulate the particle flux and hence the deposition profile on

the substrate. A 150 mm diameter Si wafer passes subsequently in front of each sputter target and in this way a mixed Ag_xTe_{1-x} layer is deposited, with x varying approximately in a linear way from 1 to $\sim$ 0 in one direction over the 150 mm wafer. Material properties of the layer on different positions on the substrate can then be related to the composition. The thickness of the layer was kept constant to $\sim$ 50 nm. As substrate, Si(100) wafers covered with a 100 nm SiO_2 or 20 nm thin Al_2O_3 layer are used. The SiO_2 was thermally grown, whereas the Al_2O_3 was deposited by an H_2O-based atomic layer deposition (ALD) technique.

The composition was determined by Rutherford backscattering spectroscopy (RBS) on different points on the wafer. To this end, 10 nm layers were deposited instead of 50 nm to allow for better distinction between the Ag and Te signal. Composition could also be determined by X-ray fluorescence spectroscopy (XRF) after calibration of the system with a reference sample characterized by RBS. Crystallinity of the film is investigated by X-ray diffraction (XRD). A Bruker D8 Discover X-ray diffractometer, equipped with a 300 mm wafer mapping stage is used for XRD mapping, i.e. perform an XRD measurement every 3 mm on the wafer, to investigate the crystallinity as a function of the composition. The system also contains a Mo X-ray source and an XRF detector which is used for the XRF analysis in this work. The morphology of the graded layer is investigated by scanning electron microscopy (SEM), using a FEI Quanta 200F FEG SEM.

The stability of the different Ag-Te phases are investigated using *in situ* X-ray diffraction, as described in previous work[17,20]. Here, the XRD pattern in a fixed 2θ window of 20° is monitored while the sample is annealed at a heating rate of $0.5°C/\mathrm{s}$ in an inert He atmosphere. In this way, phase transformations as a function of temperature, or the occurrence of melting points are detected. A melting temperature (T_m) higher than $400°C$ is necessary to be compatible with back end of line temperatures in device processing.

On the basis of morphology results from SEM imaging and thermal stability observed by *in situ* XRD measurements, a narrow composition range between 33 and 38 at% Te is selected to implement as cation supply layer in CBRAM cells. We selected the composition with $\sim$64.8 at% Ag, further denoted as $Ag_{2-\delta}Te$. In analogy to previous work[14,17], cells with a dedicated switching layer of 3 nm Al_2O_3 are used. The alumina is deposited by an H_2O-based ALD process on highly n-doped Si. The CBRAM dot cells are then prepared by magnetron sputtering of a Pt/$Ag_{2-\delta}Te$ (50/50 nm) stack through a 580 µm diameter dot shadow mask on the Al_2O_3/Si substrates. Dots with pure Ag instead of $Ag_{2-\delta}Te$ are also prepared to investigate the influence of the tellurium.

Electrical characterization of the dot cells is carried out with a Keithley 2601A Sourcemeter. Linear current-voltage sweeps with a sweep rate of $0.5\,\mathrm{V/s}$ are applied on the Pt top electrode with respect to the Si bottom electrode. The current during the set operation is limited to avoid overgrown filaments. Typically a com-

pliance current (I_c) of 100 µA or 1 mA is used.

C. Results and Discussion

Combinatorial Study

The composition as a function of the position on the wafer was determined by RBS and the result is shown in Figure 1a. A graded layer with a linearly varying composition from $\sim$ 0 to $\sim$85 at% Te is obtained. The as-deposited layer is characterized by XRD in the $19-52^\circ$ 2θ window. The XRD intensities are plotted as a gray scale map as a function of the Te content (Figure 1b). According to the phase diagram[21], two low temperature intermetallic Ag-Te phases exist, which transform at higher temperatures. In this work, we will follow the notation of Karakaya and Thompson[21], and denote the low temperature phase with α and the high temperature phases with β, γ, and so on. At a composition of $\sim$33 at% Te, monoclinic Ag_2Te is formed (αAg_2Te), which transforms to a face-centered cubic (fcc) structure at $145^\circ C$ (βAg_2Te) and to a body-centered cubic (bcc) structure (γAg_2Te) at $689^\circ C$ in case of excess Te ($\sim$ $802^\circ C$ in case of excess Ag). At a composition of $\sim$37.5 at% Te, hexagonal Ag_5Te_3 exists ($\alpha Ag_{4.53}Te_3$), which transforms to a high temperature β phase at $\sim$ $295^\circ C$ in case of excess Te ($\sim$ $265^\circ C$ for excess Ag). Another phase, $Ag_{1.9}Te$, which exist in the temperature range 120-460$^\circ C$ has been reported, with a polymorphic transformation near $178^\circ C$. Unfortunately, to our knowledge, no crystallographic data has been reported on the $Ag_{1.9}Te$ and the high temperature Ag_5Te_3 phases. From the phase diagram[21], we expect for the as-deposited layer (when it is crystalline) three main regions:

1. 0 to 33.3 at% Te: two phase region with Ag and monoclinic Ag_2Te.
2. 33.3 to 37.5 at% Te: two phase region with monoclinic Ag_2Te and hexagonal Ag_5Te_3.
3. 37.5 at% Te to pure Te: two phase region with hexagonal Ag_5Te_3 and Te.

This is in agreement with the measured XRD map. Up to about 28 at% Te, the peak corresponding to the (111) direction of Ag[22] at 38.1° is observed. From 15 to 38 at% Te, also XRD peaks related to the monoclinic Ag_2Te phase[23] appear. In the range $\sim$ 35 to $\sim$49 at% Te, diffraction peaks of hexagonal $Ag_{4.53}Te_3$[24] are visible. It is apparent that for Te contents in the range of 29-38 at% Te mainly two peaks are very intense, corresponding to the {-121} planes of monoclinic Ag_2Te ((-121) and (-242) at respectively 23.9° and 48.8°). For Te contents higher than 65 at%, peaks related to tellurium[25] are present. The material in the composition region between 49 and 65 at% Te, where no diffraction peaks appear, is probably amorphous.

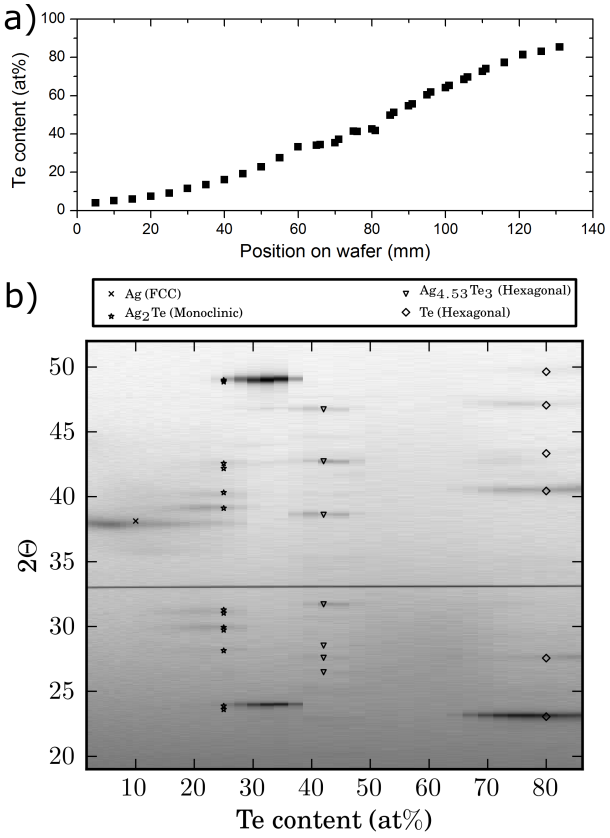

Figure 1. *(a) Te content of the Ag-Te layer as a function of the position on the substrate, determined by RBS. (b) XRD patterns as a function of the Te content of the as-deposited layer.*

Figure 2 shows the SEM images of the main composition regions. The surface morphology is strongly dependent on the Te content. For almost pure Ag, a smooth morphology is observed, whereas adding more Te creates a rough surface (e.g. for 16 at% Te in Figure 2). At the Ag rich side of Ag_2Te (<33 at% Te), large particles are observed which are related to the excess of Ag (see also Figure S2b in the Supporting Information), whereas at the Ag poor side (>33 at% Te) where only intermetallic Ag-Te phases or Te (>65 at% Te) occur, a smooth surface morphology is present. These results suggest that an excess of Ag that cannot be consumed in intermetallic phases results in a rough surface morphology and Ag particles. Only pure Ag or materials with more than 33 at% Te show good as-deposited surface morphologies.

The thermal stability of the Ag-Te layer as function of the Te content was fur-

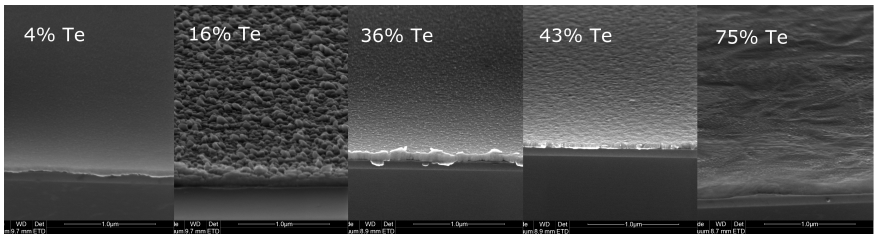

Figure 2. *Surface morphology of the $\sim$ 50 nm Ag-Te layer on 100 nm SiO_2 with 4, 16, 36, 43 and 75 at% Te. The images are taken under a tilted view of 20° and with a magnification of 100 k, the scale bar denotes 1 µm. A strong variation in surface roughness is observed.*

ther investigated using *in situ* XRD. The graded wafer was cleaved into pieces of about 7 mm and hence for 18 different compositions, a measurement is available. Figure 3 shows selected results for significantly different composition regions, as the regions in between show qualitatively similar patterns. The composition of every piece before and after the *in situ* XRD was measured by XRF to investigate whether the composition had changed during the anneal (for example by evaporation). Figure 4a shows a summary of the temperature windows where the different intermetallic phases appear as a function of the initial (i.e. before anneal) Te composition. The temperatures where these phases appear/disappear were extracted based on the appearance/disappearance of the corresponding diffraction peaks in the 30-50° 2θ window. The composition after the measurement is also indicated.

Figure 3a shows the result for a layer with almost pure Ag (only 4 at% Te). Indeed, only the (111) peak at 38.1° is visible as deposited, and the diffraction peak appearing from 200°C on at 44° corresponds to the (200) peak of Ag[22]. Adding more Te results in the formation of the monoclinic Ag_2Te phase[23], as is illustrated in Figure 3b for 28 at% Te. Near a temperature of 145°C, the peaks assigned to the monoclinic Ag_2Te phase disappear, which can be explained by the α- to βAg_2Te[26] phase transformation from a monoclinic to a fcc structure[21]. The sample with a composition around 37 at% (Figure 3c) is the most difficult to analyze. For temperatures below 145°C the (-242) peak of monoclinic Ag_2Te is visible. According to the phase diagram, one also expects hexagonal $Ag_{4.53}Te_3$[24], but no diffraction peaks of this phase are observed. The phase diagram also mentions a high temperature $Ag_{1.9}Te$ phase in the 120-460°C temperature window, which exists in two polymorphs with a transformation temperature of 178°C[21]. The *in situ* XRD measurement shows that at 145°C the monoclinic phase transforms, followed by an apparently second transformation around 265°C where the peaks at 32 and 41° disappear, and the peak at 42.7° becomes more intense. The diffraction peak at 42.7° becomes less intense only at 280°C. At 400°C, the peak at 42.7° disappears and diffraction peaks corresponding to fcc Ag_2Te appear[26].

To investigate this composition further and to identify the observed XRD peaks, a Ag-Te layer with 63.9 at% Ag was deposited. The *in situ* XRD measurement is very similar to the observed one of the gradient (Figure 3c) and is shown in Figure S1 in the Supporting Information. For this sample, also a second 2θ window was measured. The two 2θ windows in Figure S1 show that at $145°C$ two intense peaks at 23.3 and 47.7° appear, which can be related to the (111) and (222) planes of fcc Ag_2Te[27]. Additional measurements where the sample was annealed up to 220 and $390°C$ and cooled down to room temperature again were performed to investigate if the phases at that temperature are also stable at room temperature. Upon cooling, the present peaks shifted toward larger 2θ angles (which could be explained by thermal expansion) but also more diffraction peaks appeared which could be related to the monoclinic phase. These results suggest that the diffraction peaks formed above $145°C$ are merely high temperature phases that return to a low temperature phase at room temperature, and support the proposition that cubic Ag_2Te[26,27] appears from $145°C$ on. Other diffraction peaks appearing in the 145-400$°C$ temperature window are hard to identify, and might be related to other high temperature phases like $Ag_{1.9}Te$. Unfortunately no reference XRD data is available for the $Ag_{1.9}Te$ phase in the literature. Note that literature even reports the existence of a second medium temperature Ag_2Te phase[28] in the temperature range 146-260$°C$. In Figure 4, the occurrence of unidentified peaks are taken into account under the general notation of $Ag_{2-x}Te$. Also two notations (β and β') are used for the high temperature Ag_2Te phase, which only differ in the lattice constant.

When more than 38 at% Te is present, the material has a melting point around $350°C$, as can be seen in Figures 3d and e for respectively 65 and 81 at% Te. In case of 65 at% Te, the material is amorphous as deposited, and the hexagonal $Ag_{4.53}Te_3$ phase crystallizes at $75°C$. Around $295°C$, the diffraction peaks at 42.7 and 31.7°, corresponding to the (006) and (008) planes, shift toward 42° and 31°, respectively. Although no reference XRD data is available to verify, this temperature coincides with the reported α to β transition[21] of $Ag_{4.53}Te_3$. At $350°C$, the diffraction peaks disappear, corresponding to the melting temperature of the eutectic composition. At higher temperatures, diffraction peaks appear again, which can be explained by evaporation of Te. In this way, the material becomes Ag rich and solid phases (Ag_2Te) appear again. This is also in agreement with the measured composition after the *in situ* XRD measurement: for the samples where fcc Ag_2Te is formed, the composition is about 66 at% Ag (see Figure 4a). As we cannot exactly determine at which temperature no liquid is present anymore, we indicated on Figure 4a the whole temperature range above $350°C$ as a region where liquid can occur. For the sample with 81 at% Te, diffraction peaks associated with Te are clearly visible. On the basis of these results, the composition range with more than 38 at% Te is excluded for memory application because of the low T_m

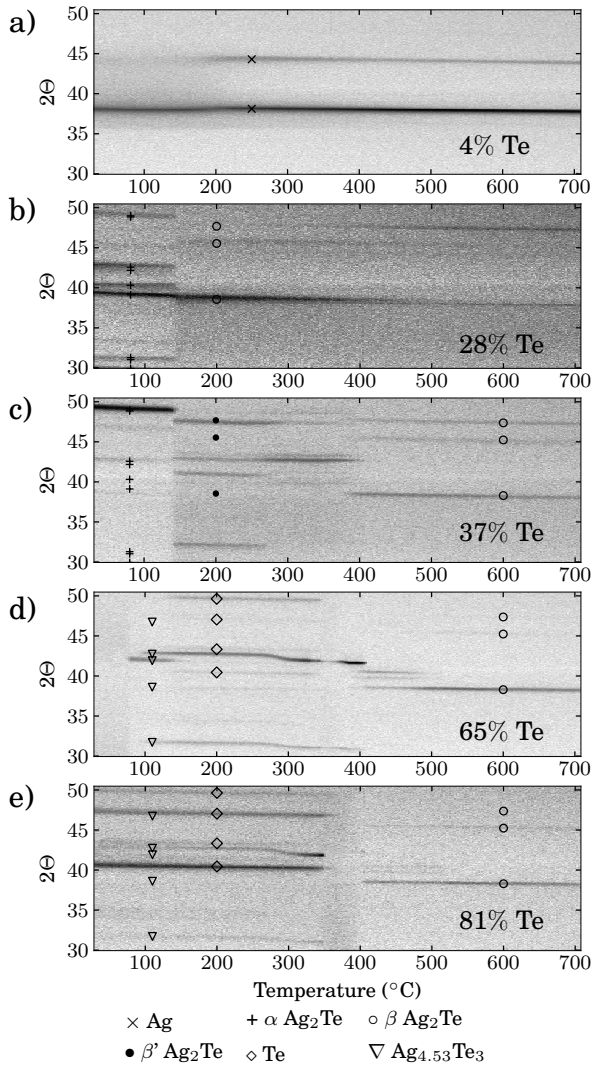

Figure 3. *In situ XRD patterns of the graded Ag-Te layer on 20 nm Al_2O_3 for the regions with (a) 4, (b) 28, (c) 37, (d) 65 and (e) 81 at% Te. The diffraction peaks are plotted as a gray scale map as a function of the temperature.*

of $350°C$. Figure 4b summarizes the composition regions selected by the combinatorial screening with good surface morphology (selected from SEM screening) and sufficiently high melting temperature (selected from *in situ* XRD).

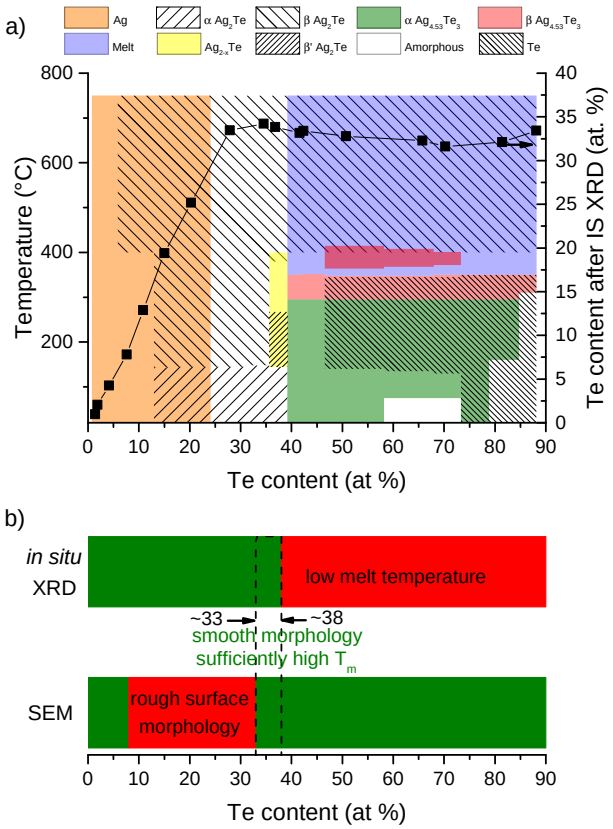

Figure 4. *(a) Summary of the observed phases in the 30-50° 2θ window. The temperature window where a certain phase appears as a function of the composition is hatched in the diagram. The composition after the* in situ *XRD measurement is also indicated. (b) Summary of the material properties investigated by* in situ *XRD and SEM.*

Optimum Composition: $Ag_{2-\delta}Te$

The combinatorial screening in the previous section allowed us to select a narrow composition range with acceptable material properties between 33 and 38 at% Te. For too low Te compositions, a rough surface morphology was observed whereas for too high Te contents, the material melts already at $350°C$. This is also illustrated in Figure 4b, where the regions with good surface morphology and sufficiently high melting temperature overlap. A composition close to Ag_2Te was selected, and at the Ag deficient side, to avoid the rough surface morphology. The composition was determined by XRF as 64.8 at% Ag and we will further refer to this composition as $Ag_{2-\delta}Te$. A slight excess of Ag results in large Ag grains on

the surface. This was confirmed by energy dispersive X-ray fluorescence spectroscopy (EDX) on a sample with 70 at% Ag. This is illustrated in Figure S2 in the Supporting Information, showing the SEM images of both compositions. The *in situ* XRD measurement of the $Ag_{2-\delta}Te$ (see Supporting Information Figure S3a) shows only the α to βAg_2Te transformation, whereas for the layer with 70 at% Ag (see Supporting Information Figure S3b), also diffraction peaks corresponding to Ag appear. For temperatures above $145°C$, βAg_2Te exists, but it is observed from *in situ* XRD that it transforms back to αAg_2Te upon cooling. The ionic conductivity is also higher for βAg_2Te[28] (the high temperature phase) compared to αAg_2Te[29].

Application in CBRAM

The DC cycling behavior of Pt/$Ag_{2-\delta}Te$/Al_2O_3/Si dot cells is compared to cells with pure Ag as a cation supply layer. The cells are cycled 10 times by applying a double linear voltage sweep from 0 to 3 V (and back) to set the cells to a LRS, and from 0 to -2.5 V (and back) to reset them into a HRS. Figure 5 shows typical switching curves for both supply layers. The cells with Ag (Figure 5a) show a forming, that is, Ag ions are driven into the Al_2O_3 switching layer to form a conductive filament and the cell is switched to a LRS during the first cycle, but it is difficult to reset the cells. Using $Ag_{2-\delta}Te$ on the other hand (Figure 5b) resulted in better cycling of the cells. In the case of Ag, the current was limited to 100 µA to avoid a too strong filament, as a higher compliance current generally leads to stronger filaments[5]. In case of $Ag_{2-\delta}Te$, the cells can even be reset when a I_c of 1 mA was used during set. This efficient reset for the Te alloyed supply layer was already reported for Cu-Te[14], but also for Cu or Ag based sulphides and selenides with a binary oxide as switching layer[18]. It is known that the copper[4,19] and silver[28,29] chalcogenides show ionic conductivity. It is very likely, as was proposed previously[18,30,31], that the good ionic conductivity of the supply layer allows for the efficient reset because of a more efficient flux of ions out of the switching layer back into the supply layer during reset. A better extraction of the Ag ions out of the switching layer is expected to contribute to the recovery of the high resistive state, and hence to an efficient reset. Another factor that might play a role is the thermodynamical driving force to form intermetallic Ag-Te phases. When a Ag filament is formed in the Al_2O_3 layer during the set operation, a Te rich region is left in the silver supply layer. However, as it is thermodynamically more favorable for Ag to form Ag-Te phases, the Ag atoms constituting the conductive filament will tend to go back to the Te rich region in the supply layer, which should contribute to filament dissolution and hence reset[14].

It is observed that for $Ag_{2-\delta}Te$ a compliance current of 1 mA is needed to obtain a stable filament that does not dissolve spontaneously or with very low reset

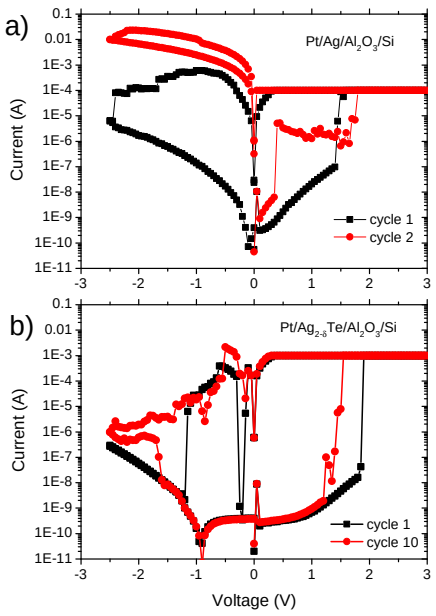

Figure 5. *DC sweeps of (a) Pt/Ag/Al_2O_3/Si and (b) Pt/$Ag_{2-\delta}$Te/Al_2O_3/Si CBRAM cells.*

voltages. This is illustrated in Figures 6a and b, where the cumulative distribution of the resistances of the $Ag_{2-\delta}Te$ cells are extracted from the set (read at +0.1 V) and reset (read at -0.1 V) cycles. In the ideal case, the curves at positive and negative read voltage should coincide. Using an operating current of 100 µA (Figure 6a) results in $\sim$ 50 % of the switches where the LRS returned already to a higher resistance at -0.1 V, and about 15 % returned to a HRS (i.e. $R > 10^6\,\Omega$). Using a compliance current of 1 mA (Figure 6b) results in much more successful cycles, that is, 90 % of the programmed LRS are still in the same state during reset at -0.1 V and only $\sim$ 1 % returned to a HRS again. As is generally observed in CBRAM, a higher compliance current generally leads to stronger and hence less volatile filaments. This agrees with the more stable LRS for the cells cycled with 1 mA, because of the thicker filaments that contain more silver atoms. Note that the influence of filament morphology on retention has been reported before [32], where better retention is reported for LRS states with lower resistance because of thicker filaments, which are less susceptible to filament dissolution. From the cumulative plots, it is also observed that a larger fraction of the LRS states has a lower LRS resistance for the cells cycled with 1 mA compared to the cells cycled with 100 µA, illustrating the more robust filament for the former. It is worth mentioning that the Joule heating because of the high current that flows through the filament might

induce the α to βAg_2Te phase transition in the Ag-Te layer close to the filament when temperatures above $145°C$ are reached. However, not much information on the phase transformation and existence of the high temperature phase on this local scale is known. Moreover, when no current flows through the cell and the material cools down, this phase is expected to transform back to the low temperature α phase. In case that βAg_2Te is formed, this might enhance the flux of Ag ions out of the silver supply layer when the cell has switched on during the set sweep, as a higher ionic conductivity is reported for the cubic high temperature phase[28,29]. This in turn can promote a more robust, thicker filament that contains more Ag atoms, which improves LRS stability. During reset, the higher ionic conductivity of the cubic phase might enhance the flux of Ag ions out of the Al_2O_3 back into the Ag-Te layer, and hence contribute to the efficient reset. Endurance of the 580 µm Ag-Te based dot cells was also tested by DC cycling of the cells with a I_c of 1 mA. Figure 6c shows the resistance of 500 consecutive set-reset cycles, extracted from a 100 mV read pulse after every set or reset operation.

D. Conclusions

We deposited a 50 nm thin film of Ag_xTe_{1-x} $(0 < x < 1)$ by a combinatorial deposition technique and investigated the material properties as a function of the composition. SEM measurements revealed a rough surface morphology when the Ag_2Te phase was formed with an excess of Ag, whereas a smooth morphology is observed when more Te is added and all Ag is consumed in intermetallic phases. X-ray diffraction mapping shows the formation of intermetallic Ag-Te phases, in agreement with the phase diagram. *In situ* XRD as a function of the Te composition allowed us to investigate the phase stability of the formed phases and showed the occurrence of a melting point at $350°C$ for more than 38 at% Te. The combined SEM and XRD data reveals only a narrow composition range between 33 and 38 at% Te, which shows suitable material properties for application as a cation supply layer in CBRAM. Resistive switching of Pt/$Ag_{2-\delta}Te$/Al_2O_3/Si CBRAM cells were investigated and compared to memory cells with pure Ag as a cation supply layer. A more efficient reset for the Te alloyed cells was observed, which might be explained by the ionic conductive properties of the cation supply layer, allowing an efficient extraction of the cations out of the switching layer back to the supply layer. This enhanced reset might also be related to preferred formation of Ag-Te phases in the supply layer by expense of the Ag atoms constituting the conductive filament.

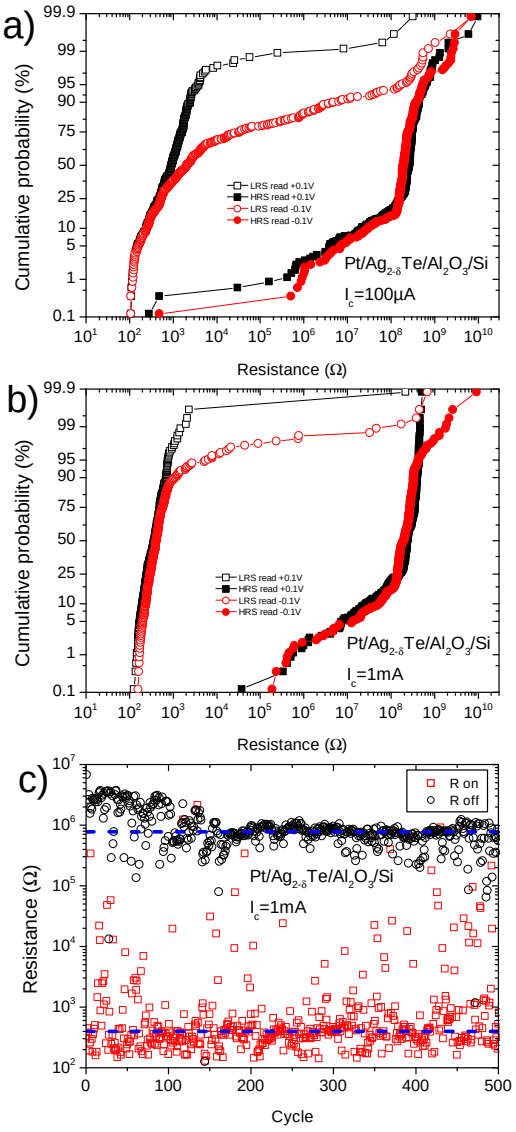

Figure 6. *Cumulative distribution of HRS and LRS extracted from the set sweep (R at +0.1 V) or reset sweep (R at -0.1 V) of Pt/$Ag_{2-\delta}$Te/Al_2O_3/Si CBRAM cells cycled with a I_c of (a) 100 µA and (b) 1 mA. (c) Endurance test of a Pt/$Ag_{2-\delta}$Te/Al_2O_3/Si cell, showing the resistance extracted from a 100 mV read pulse after every set (R_{on}) or reset (R_{off}) sweep. The median LRS and HRS are indicated by the dashed line.*

Acknowledgments

W.D. acknowledges the *Agency for Innovation by Science and Technology (IWT)* for a PhD scholarship.

References

[1] R. Waser, R. Dittmann, G. Staikov, and K. Szot, *Adv. Mater.* **21**(25-26), 2632–2663 (2009).

[2] I. Valov, R. Waser, J. R. Jameson, and M. N. Kozicki, *Nanotechnology* **22**(25), 254003 (2011).

[3] K. Terabe, T. Nakayama, T. Hasegawa, and M. Aono, *Appl. Phys. Lett.* **80**(21), 4009–4011 (2002).

[4] T. Sakamoto, H. Sunamura, H. Kawaura, T. Hasegawa, T. Nakayama, and M. Aono, *Appl. Phys. Lett.* **82**(18), 3032–3034 (2003).

[5] M. Kozicki, M. Park, and M. Mitkova, *IEEE Trans. Nanotechnol.* **4**(3), 331–338 (2005).

[6] M. Kund, G. Beitel, C.-U. Pinnow, T. Rohr, J. Schumann, R. Symanczyk, K.-D. Ufert, and G. Muller, *Tech. Dig. - Int. Electron Devices Meet.* , 754–757 (2005).

[7] S. Wu, T. Tsuruoka, K. Terabe, T. Hasegawa, J. P. Hill, K. Ariga, and M. Aono, *Adv. Funct. Mater.* **21**(1), 93–99 (2011).

[8] M. Tada, K. Okamoto, T. Sakamoto, M. Miyamura, N. Banno, and H. Hada, *IEEE Trans. Electron Devices* **58**(12), 4398–4406 (2011).

[9] Y. Wang, H. Lv, W. Wang, Q. Liu, S. Long, Q. Wang, Z. Huo, S. Zhang, Y. Li, Q. Zuo, W. Lian, J. Yang, and M. Liu, *IEEE Electron Device Lett.* **31**(12), 1470–1472 (2010).

[10] T. Tsuruoka, K. Terabe, T. Hasegawa, and M. Aono, *Nanotechnology* **21**(42), 425205 (2010).

[11] Q. Liu, S. Long, W. Wang, Q. Zuo, S. Zhang, J. Chen, and M. Liu, *IEEE Electron Device Lett.* **30**(12), 1335 –1337 (2009).

[12] C. Schindler, M. Weides, M. N. Kozicki, and R. Waser, *Appl. Phys. Lett.* **92**(12), 122910 (2008).

[13] Y. Bernard, V. T. Renard, P. Gonon, and V. Jousseaume, *Microelectron. Eng.* **88**(5), 814–816 (2011).

[14] L. Goux, K. Opsomer, R. Degraeve, R. Muller, C. Detavernier, D. J. Wouters, M. Jurczak, L. Altimime, and J. A. Kittl, *Appl. Phys. Lett.* **99**(5), 053502 (2011).

[15] K. Aratani, K. Ohba, T. Mizuguchi, S. Yasuda, T. Shiimoto, T. Tsushima, T. Sone, K. Endo, A. Kouchiyama, S. Sasaki, A. Maesaka, N. Yamada, and H. Narisawa, *Int. Electron Devices Meet.* , 783 –786 (2007).

[16] S. Kim, M. Jo, J. Park, J. Lee, W. Lee, and H. Hwang, *Electrochem. Solid-State Lett.* **14**(8), 322–325 (2011).

[17] W. Devulder, K. Opsomer, F. Seidel, A. Belmonte, R. Muller, B. De Schutter, H. Bender, W. Vandervorst, S. Van Elshocht, M. Jurczak, L. Goux, and C. Detavernier, *ACS Appl. Mater. Interfaces* **5**(15), 6984–6989 (2013).

[18] H. Radhakrishnan, In *15th IEEE Mediterranean Electrotechnical Conference*, 515–520, (2010).

[19] R. A. Yakshibaev, N. N. Mukhamadeeva, and R. F. Almukhametov, *Phys. Status Solidi A* **108**(1), 135–141 (1988).

[20] W. Devulder, K. Opsomer, A. Franquet, J. Meersschaut, A. Belmonte, R. Muller, B. De Schutter, S. Van Elshocht, M. Jurczak, L. Goux, and C. Detavernier, *J. Appl. Phys.* **115**(5), 054501 (2014).

[21] I. Karakaya and W. Thompson, *J. Phase Equilib.* **12**(1), 56–63 (1991).

[22] International Centre for Diffraction Data, Newtown Square, PA, *JCPDS Data Card no. 03-065-2871*, (2004).

[23] International Centre for Diffraction Data, Newtown Square, PA, *JCPDS Data Card no. 00-034-0142*, (2004).

[24] International Centre for Diffraction Data, Newtown Square, PA, *JCPDS Data Card no. 01-086-1953*, (2004).

[25] International Centre for Diffraction Data, Newtown Square, PA, *JCPDS Data Card no. 00-036-1452*, (2004).

[26] International Centre for Diffraction Data, Newtown Square, PA, *JCPDS Data Card no. 01-081-1822*, (2004).

[27] International Centre for Diffraction Data, Newtown Square, PA, *JCPDS Data Card no. 01-081-1821*, (2004).

[28] I. Rom and W. Sitte, *Solid State Ionics* **70-71, Part 1**, 147 – 152 (1994).

[29] A. Bürgermeister and W. Sitte, *Solid State Ionics* **141-142**, 331 – 334 (2001).

[30] J. Billen, S. Steudel, R. Mller, J. Genoe, and P. Heremans, *Appl. Phys. Lett.* **91**(26), 263507 (2007).

[31] R. Mueller, J. Genoe, and P. Heremans, *Appl. Phys. Lett.* **95**(13), 133509 (2009).

[32] J. Guy, G. Molas, E. Vianello, F. Longnos, S. Blanc, C. Carabasse, M. Bernard, J. Nodin, A. Toffoli, J. Cluzel, P. Blaise, P. Dorion, O. Cueto, H. Grampeix, E. Souchier, T. Cabout, P. Brianceau, V. Balan, A. Roule, S. Maitrejean, L. Perniola, and B. De Salvo, In *2013 IEEE Int. Electron Devices Meet. (IEDM)*, 30.2.1–30.2.4, (2013).

Supporting Information

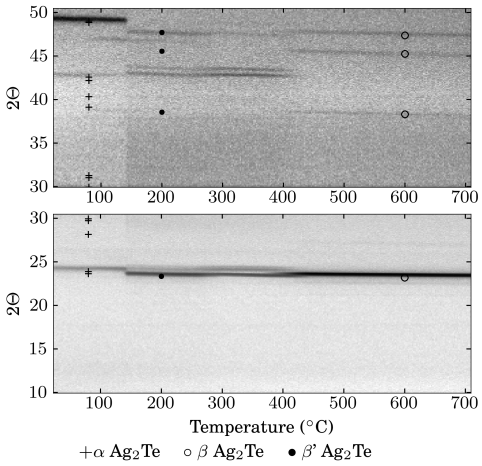

Figure S1. *In situ XRD patterns in the 10-30° and 30-50° 2θ window of a Ag-Te layer containing 63.9 at% Ag.*

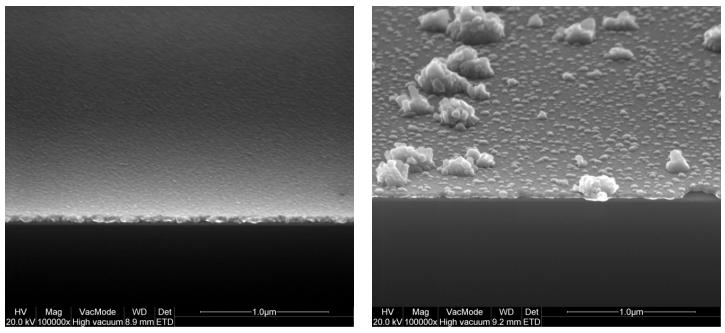

(a) ***(b)***

Figure S2. *SEM images of a 50 nm Ag-Te layer containing (a) 64.8 at% Ag and (b) 70 at% Ag on 20 nm Al_2O_3. In case of 70 at% Ag, there is an excess of Ag and next to Ag_2Te, pure Ag is also present and forms large protrusions on the surface, as was confirmed by EDX.*

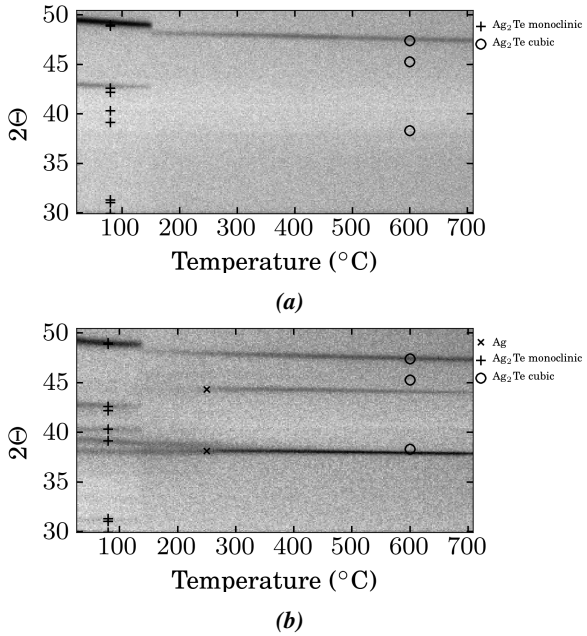

Figure S3. *In situ XRD patterns of a 50 nm Ag-Te layer on 20 nm Al_2O_3, containing (a) 64.8 at% Ag and (b) 70 at% Ag.*

5

Alloying of copper-tellurium

The copper-telluride system has a complex phase diagram, showing the existence of multiple intermetallic phases. Deviation from the stoichiometry of these phases will result in phase separation for a crystalline material. If this happens in memory devices, this might result in fluctuations in device characteristics from device to device. The different phases also have polymorphs, hence upon annealing (e.g. under thermal budget during device processing) the material transforms. The microstructure (amorphous or crystalline material) and phases that are formed can be altered by adding other elements, that is, by *alloying* the $Cu_{0.6}Te_{0.4}$ layer. First we give an overview of different areas in microelectronics where alloying has also been applied and how it improves the material properties. Similar mechanisms may apply to the materials investigated in this work. Next the results on carbon, germanium and silicon alloying of $Cu_{0.6}Te_{0.4}$ are presented. Both the thermal stability of the materials and the influence on resistive switching when they are implemented in CBRAM cells is investigated. The results for each material are presented in a similar way, allowing easy comparison. A more detailed discussion on each material can be found in the corresponding papers at the end of this chapter.

5.1 Alloying in microelectronics

5.1.1 Silicide contacts

Alloying of materials to improve their properties is commonly applied in microelectronics and in materials science in general. It has been successfully applied to improve the thermal stability of *silicides*, which are used for contacting the source and drain of transistors [1, 2]. A comprehensive discussion is given by Lavoie et al. [1], where the influence of alloying elements on the formation of the NiSi and $NiSi_2$ phase and the resistance against agglomeration of the thin films was studied. It was shown that depending on the solubility of the alloying elements in silicide phases, the nucleation temperature could be influenced. When the alloying element is soluble in the monosilicide (NiSi) and less soluble in the disilicide ($NiSi_2$) phase, the nucleation barrier of $NiSi_2$ is increased due to a decrease in the entropy term (see equation 2.8) because when the element is not miscible, the entropy is lower. Hence the Gibbs free energy change becomes also less negative, making the formation of the disilicide thermodynamically less favourable. The opposite occurs for elements that are soluble in the $NiSi_2$ and less soluble in the NiSi phase. Alloying elements that are not significantly soluble in either of the silicide phases will not influence nucleation temperature through mixing entropy effects. However, phase formation can still be influenced by *kinetic* effects, i.e. the elements need to reorganize for a phase transformation to occur. Elements that are not miscible typically will segregate to the grain boundaries and interfaces. Surfaces and grain boundaries are fast diffusion paths [3] that contribute to particle transport, which is necessary for phase transformations. Alloying elements that segregate here can block diffusing species, hence altering phase formation.

5.1.2 Copper interconnects

Alloying elements are also used in *interconnects*, i.e. the copper lines that connect the different components in IC's [4, 5]. One of the challenges in interconnects is to improve the resistance against electromigration, that is, the transport of Cu atoms due to the electrical current that flows through the Cu lines. A typical Cu interconnect line comprises a Ta/TaN liner, a Cu seed layer, an electroplated Cu line, and a capping layer. Especially the Cu/cap interface is a path for Cu migration. However, continuous scaling leads to smaller grains with more grain boundaries in the interconnect line. These grain boundaries are also fast diffusion paths and contribute to the electromigration problem. Figure 5.1 gives an overview of the different paths for copper diffusion. Selection of a good capping layer can enhance electromigration resistance at the Cu/cap interface significantly. Another route is the use of alloying elements in the Cu seed layer. A thorough review is given by Barmak et al. [4] on the selection of alloying elements in the seed layer.

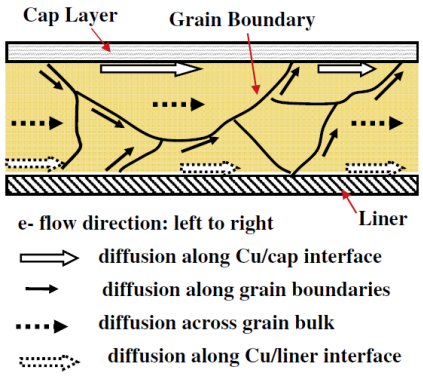

Figure 5.1. *Schematic of a Cu interconnect line and the different paths that contribute to Cu electromigration. [5]*

Upon annealing, the alloying elements mainly diffuse to the Cu/cap interface (if they have sufficiently low solubility in Cu), where they efficiently lower Cu electromigration. Good results were obtained with Mn as alloying element, where it was believed that part of the Mn also diffused to the Cu grain boundaries, limiting Cu diffusion along these paths as well [6].

5.1.3 Phase change memories

Alloying elements have also been used in materials for *phase change memories (PCM)* [7–13]. This type of memory cells[1] is switched between a high and low resistive state by transition between the amorphous and crystalline state of the material. By applying a voltage pulse, due to Joule heating, the amorphous material can crystallize and switches to a low resistive state. The cell can be reset to a high resistive state by applying a voltage pulse (and sufficiently high current) in order to melt the crystalline material. Fast cooling quenches the liquid-like disorder, resulting in an amorphous material and hence the cell returns to the high resistive state. It is clear that the melting temperature should not be too high, but also that the crystallization temperature should not be too low, in order to be sufficiently stable against crystallization (i.e. under long thermal stress, for example under operating temperatures of a memory device, it should not spontaneously crystallize). It has been reported that alloying of GeTe with carbon [12] or nitrogen [14], germanium alloying of $Sb_{3.6}Te$ [9] or Sb_2Te_3 [10], Si alloying of GeTe [15] and Cu doping of Sb_2Te [13], is effective in increasing crystallization temperature and hence thermal stability. This could be related to the increase in coordination number and the

[1] This type of device typically constists of the phase change material sandwiched between two electrodes.

formation of strong bonds, making reorganization of the species and hence crystallization more difficult to proceed. The influence of the bond strength on the glass transition temperature (which is an under limit for the crystallization temperature) was discussed already in section 2.3.4.

5.1.4 Alloys in CBRAM

As discussed in previous chapter, alloys are also used as cation supply layer in CBRAM [16–18] to improve resistive switching. It also has been used to improve the retention of the device (i.e. how well a programmed memory state is maintained) [19–21]. Guy et al. [21] reported improved LRS retention for a Ag/GeS_2/W based memory cell due to Sb doping (up to 20 at%) of the GeS_2 layer. The migration of Ag in the GeS_2 layer is mainly caused by the formation of Ag_2S complexes that migrate through the matrix. As S preferentially binds to Sb over Ag, the formation of Ag_2S is reduced and the migration lowered, resulting in a more stable Ag filament and hence stable LRS. Tada et al. [19] reported improved LRS stability in a Cu/TiAl/PSE[2]/Ru CBRAM structure. Their results indicate the incorporation of the alloying elements in the filament, showing a higher stability of the filament against rupture (much higher temperatures in the filament are necessary in order to dissolve the filament). Jameson et al. [20] reported a CBRAM cell with an amorphous semiconducting alloy[3] as cation supply layer and an oxide switching layer showing improved retention properties. They mainly explain this in the framework of the conductive filament as a quantum point contact. If the filament is a semiconductor, it will have a larger Fermi wavelength λ_F compared to a metallic filament. In case of a quantum point contact, the conductance is quantized and the first conductive channel becomes active when the dimension of the point contact becomes of the order of λ_F. Hence if the filament is a semiconductor, a thicker filament has to be formed to become conductive, and a thicker filament is inherently more stable [22], which explains the better LRS retention.

In this thesis, we start from the Cu-Te alloy with a composition of 60 at% Cu and 40 at% Te. Elements are added in order to influence/avoid the phase transformations (e.g. avoid subsequent transformations of the material), and in this way improve the thermal stability of the alloy. In analogy to the work on silicides and interconnects, alloying elements can influence nucleation through a change in the entropy term, or influence the phase transformations by changing the mobility of the elements (e.g. by lowering grain boundary diffusion). The alloying elements can also inhibit crystallization (as for phase change materials), resulting in an amorphous alloy where phase separation is expected to be less pronounced.

[2]Polymer Solid Electrolyte.

[3]They call it the *second generation* CBRAM cells, where the first generation is the metal/chalcogenide (e.g. Ag/GeS_2) based device.

The literature suggests also an influence of the alloying elements on the switching and retention properties, hence this is also investigated.

In the next section, we first give a more detailed analysis of the switching and retention of $Cu_{0.6}Te_{0.4}$ based CBRAM, that serves as a reference for other alloys as cation supply layer. Then we investigate the influence of alloying elements (carbon, germanium and silicon) on the phase formation and if the alloys are still functional as a cation supply layer for CBRAM applications. If still functional, the retention properties of the cells are studied and compared to pure $Cu_{0.6}Te_{0.4}$, because alloying elements were reported to influence the retention properties [19, 21].

5.2 Pure $Cu_{0.6}Te_{0.4}$-based CBRAM

The limited thermal stability of $Cu_{0.6}Te_{0.4}$ was already discussed in section 4.2.5 and the *in situ* XRD pattern was shown in Figure 4.9. Improved switching compared to pure Cu was discussed in section 4.2.3, and the comparison with $Ag_{2-\delta}Te$ was given in section 4.3.2.3. It was observed that the $Cu_{0.6}Te_{0.4}$ based CBRAM showed a more stable filament compared to $Ag_{2-\delta}Te$. This was extracted from the LRS resistance from the set sweep (at +0.1 V) and reset sweep (at -0.1 V). If the filament is sufficiently stable, both resistances should be the same. If the filament is already (partially) being reset, the resistance in the reset sweep will already be higher. Hence this plot gives a first indication of filament stability, and this will be further used for the other supply layers too. A typical switching curve of a Pt/$Cu_{0.6}Te_{0.4}$/Al_2O_3/n^+ Si cell is shown in Figure 5.2a, and the resistance extracted from the reset sweeps as a function of the resistance from the set sweeps is given in Figure 5.2b, together with the reset current as a function of the LRS resistance before reset. Note that the resistance extracted from the reset is already slightly higher than the value from the set sweep, pointing to a partial dissolution of the filament. The reset current[4] might give additional information on the reset mechanism and the filament strength. Indeed, the higher the reset current, the larger the current it can withstand and the more stable the filament will be against dissolution. Moreover, if higher currents are needed to reset the filament, it might point to a larger thermal contribution (i.e. due to Joule heating) to the reset compared to the drift contribution (i.e. due to chemical affinity between Cu from the filament and the elements in the supply layer). The cumulative distribution of the LRS resistances from set and reset sweep, together with the HRS resistance and pristine resistance (i.e. the cell resistance before cycling) are given in Figure 5.2c. The cumulative distribution of the reset currents is depicted in Figure 5.2d. These plots give valuable information on filament stability and can be used to evaluate the influence of the alloying elements on the switching behaviour.

[4]The reset current is defined here as the current where the maximum current drop occurs.

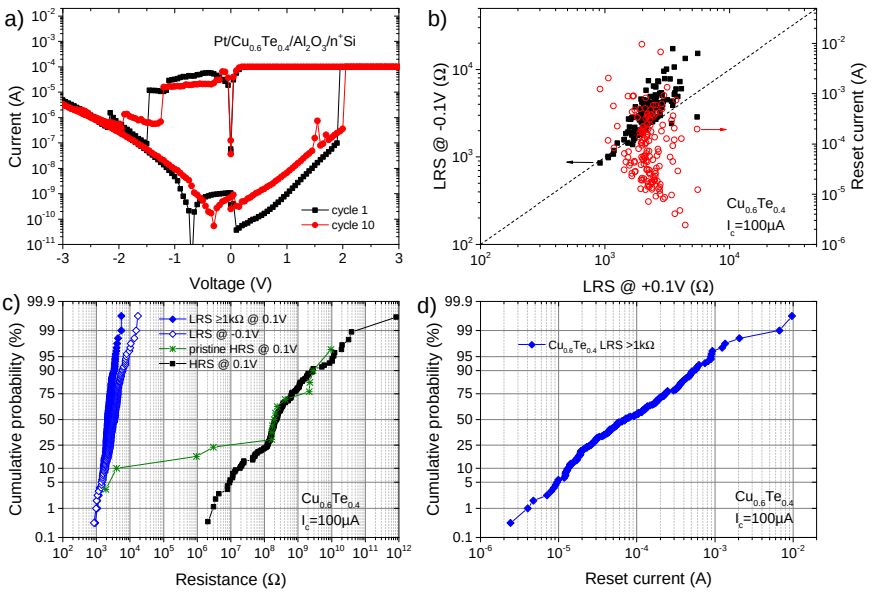

Figure 5.2. *(a) Typical IV-sweep of a Pt/$Cu_{0.6}Te_{0.4}$/Al_2O_3/n^+ Si cell (sweep rate 0.5 V/s). (b) Resistance extracted from the reset sweep (at -0.1 V) as a function of the resistance extracted from the set sweep (at +0.1 V) and the reset current as a function of the LRS resistance before the reset. (c) The corresponding cumulative probability of these resistances and of the HRS and pristine cell resistances. (d) Cumulative probability of the reset currents. (Data from 15 devices × 10 cycles)*

Retention is one of the properties in CBRAM that needs further optimization. For the different alloys that are further studied, the retention is investigated by programming the cells to a low or high resistive state after they have been cycled 2 times. Then the cells are baked at $85°C$ in inert He atmosphere and the cells are taken out of the annealing chamber after predefined time intervals to measure the resistance at a read voltage of +0.1 V. This was done for $Cu_{0.6}Te_{0.4}$ based cells for baking times up to 5 days. Figure 5.3a shows the resistance of every cell as a function of the baking time, together with the median value of LRS and HRS at every time step. A steady increase of LRS is observed, and finally after 121.6 h more than 50 % of the cells go to a high resistive state again. Note that this is in agreement with the easier reset of $Cu_{0.6}Te_{0.4}$ based CBRAM, and can be related to the tendency of Cu to go back to the cation supply layer. Note that typically a retention of more than 10 years at $85°C$ is requested, which is not achieved for these cells. From Figure 5.3b, it can also be observed that about 25 % of the cells in HRS degrade to a low resistive state. It is not straightforward to determine the cause of this HRS degradation. The fact that the cells return to a

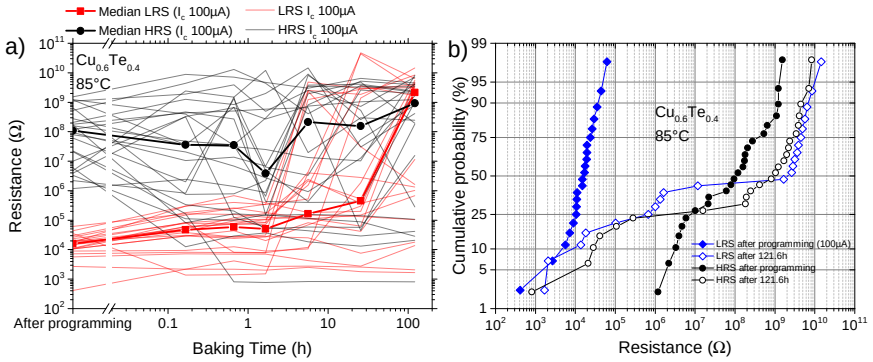

Figure 5.3. *(a) LRS (red) and HRS (black) resistance of* $Pt/Cu_{0.6}Te_{0.4}/Al_2O_3/n^+$ *Si cells. The resistance of every cell as a function of the baking time is shown, even as the median at every time step (thick line). (b) Cumulative probability of the LRS and HRS resistances after programming and after 121.6 h baking at* $85°C$.

lower resistance points to (partial) filament reconstruction. Assuming that Cu is the most mobile species, Cu species will reconstruct a conductive filament causing the resistance drop. Most likely this is through the template path that was formed during the initial sweeps. The Cu might come from the supply layer or from Cu species that are left in the switching layer. Note that the parasitic current overshoot during programming results in poor control of LRS resistance and that very thick filaments can be formed[5], which makes it more likely to have Cu species left in the supply layer that may contribute to filament reconstruction. Moreover, a thick filament might result in a large template path, which acts as a defect and a preferred location for filament reconstruction. A decrease of HRS retention was reported for cells that were cycled to low LRS state before reset to HRS [24].

5.3 Carbon alloying of $Cu_{0.6}Te_{0.4}$

The first alloying element that was investigated is carbon. The main motivation to use carbon is because it does not form any intermetallic phase with Cu or Te, nor a ternary phase. Figure 5.4 shows the phase diagram of the binary Cu-C system up to 0.6 at% carbon. No intermetallic compounds are formed, and the solubility of C in Cu is negligible, especially in the temperature window below $400°C$ that is of interest in this work. No phase diagrams for Te-C or Cu-Te-C, nor other materials data files of Cu- or Te-carbides were found in literature. This suggests that apart from Cu-Te phases, no other compounds should be formed, and hence carbon

[5] In the work of Celano et al. [23], the relation between LRS resistance and Cu filament volume was reported, showing a strong increase in filament volume with decreasing LRS resistance.

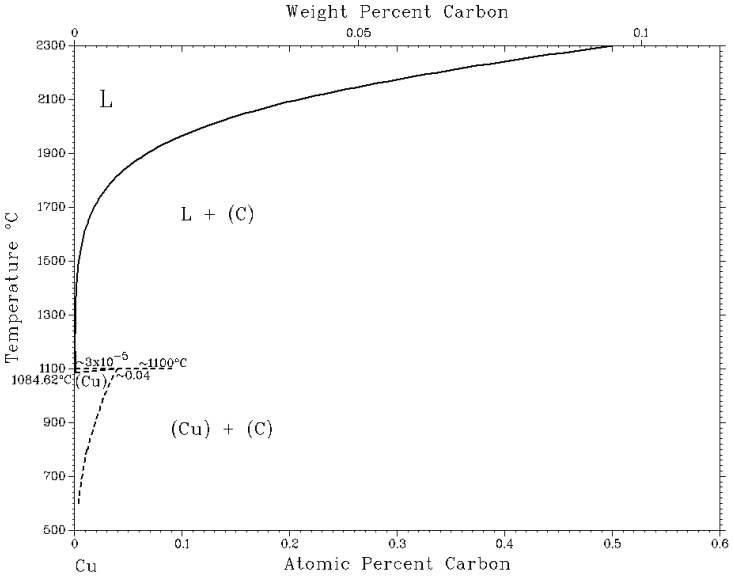

Figure 5.4. *Phase diagram of Cu-C up to 0.6 at% carbon, showing a maximum solid solubility of up to 0.04 at% carbon at temperatures slightly above 1000°C. [25]*

should not make the phase formation more complex with additional compounds. Carbon was also used as an alloying element in GeTe for phase change memories, where it was shown to improve the stability of the amorphous state [12, 26, 27].

The influence of carbon alloying is discussed in Paper II and Paper III. Paper II discusses the addition of ∼40 at% carbon on the Cu-Te phase formation and resistive switching behaviour, while Paper III discusses different carbon contents, first studied in a combinatorial way and also for discrete compositions. In the next subsections, we give a summary based on the results of these papers and we present a more thorough retention study.

5.3.1 Thermal Stability

Mixed Cu-Te-C layers with a constant layer thickness of 50 nm and with a Cu/Te ratio of 1.5 that contain $\sim$ 10, $\sim$ 20 and ∼40 at% carbon are deposited on 20 nm Al_2O_3 (further denoted as CuTeC10 up to CuTeC40). As a reference, a $Cu_{0.6}Te_{0.4}$ layer without carbon was also deposited. XRF measurements confirm for all samples a Cu/Te ratio close to 1.5. For the 20 and 40 at% carbon samples, the carbon content was verified by EDX (respectively 20.6 and 36.3 at% C and a Cu/Te ratio

of 1.52 and 1.6) after calibration of the system with RBS and ERD[6]. In the case of 10 at% carbon, the signal was too weak to determine the carbon content. The phase formation is investigated using *in situ* XRD. Figure 5.5 shows the *in situ* XRD measurements of the layers, taken at a fixed heating rate of $0.5°C/\text{s}$ in inert He atmosphere. For a detailed discussion, we refer to Paper III. The main observation is that the crystallization temperature increases with increasing carbon content. If no C is added, the hexagonal $Cu_{2-x}Te$ [28] phase is already formed during deposition. Addition of only $\sim$10 at% carbon inhibits crystallization[7] up to about $135°C$. This is evidenced by the absence of diffraction peaks[8]. Crystallization can be inhibited up to temperatures in between 300 and $400°C$ for the layer with 40 at% carbon.

The good ability of carbon to keep a material amorphous was also reported in literature. For bulk materials, it was reported that addition of small atoms could increase the supercooled liquid region by increasing the crystallization temperature while the glass transition temperature remained unaffected [29, 30]. This was ascribed to the increased packing density due to the small atoms, which makes rearrangement on a large scale more difficult and hence inhibits crystallization. It was also used in thin films ($\sim$100 nm) for phase change memories, where it proved to be efficient to increase the crystallization temperature of GeTe [12, 26]. One of the main reasons was the formation of strong C-C chains, which are difficult to break. This is also supported by the strong bond enthalpy extracted from table 2.2. These long chains are obstacles for the crystallization of the Cu-Te, leading to an increased T_x. Both effects might also explain the increased T_x for CuTeC. Another observation is that the observed diffraction peaks can all be related to Cu-Te compounds, which is in agreement with the proposition that carbon is not making strong bonds with Cu or Te (i.e. no carbides are formed), but most likely with other C atoms.

To conclude this section, the sample with 20 at% C looks interesting because upon crystallization, a large temperature window up to temperatures above $400°C$ without transformations is present. Addition of 40 at% C shows the largest amorphous window. However, crystallization occurs slightly below typical BEOL temperatures. Moreover, when it crystallizes, separation will occur in Cu-Te phases and carbon rich regions. Note that this also occurs for the sample with 20 at% carbon, however, the carbon content is much lower there and will be located at the

[6]The carbon content determined by EDX is expected to be within $\pm$2-3 at% accurate. Especially for compositions deviating strongly from the calibration sample, a measurement error of this order is expected. As a reference, if the composition is determined by EDX with the calibration based on a sample that contains 43.6 at% C, EDX measures 23.2 at% for a sample that contains 20.6 at% C.

[7]The crystallization temperature is defined here as the temperature where the maximum change in integrated intensity in the 23-30° 2θ range occurs. This temperature is indicated in Figure 5.5.

[8]Note that the absence of diffraction peaks can also related to a strongly textured layer. However, on an amorphous Al_2O_3 layer this is unlikely to occur. Furthermore, the amorphous nature was also verified by TEM measurements of a CuTeC40 layer, as reported in Paper II, Figure 1.

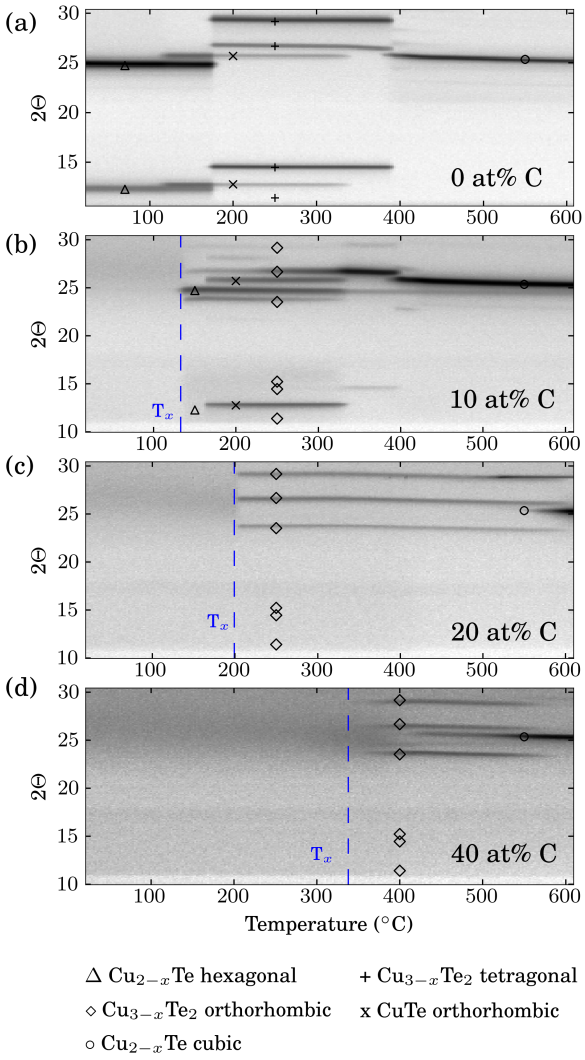

Figure 5.5. *In situ XRD pattern in the 10-30° window of a 50 nm $Cu_{0.6}Te_{0.4}$(-C) layer (a) without carbon, (b) with ∼10 at% C, (c) with ∼20 at% C and (d) with ∼40 at% C. The measurements are collected at a fixed heating rate of 0.5°C/s in He atmosphere.*

grain boundaries (where it blocks diffusing species and in this way inhibits further transformations). So in both cases, phase separation occurs, but it will be more pronounced for the highest C contents. The influence of such an inhomogeneous

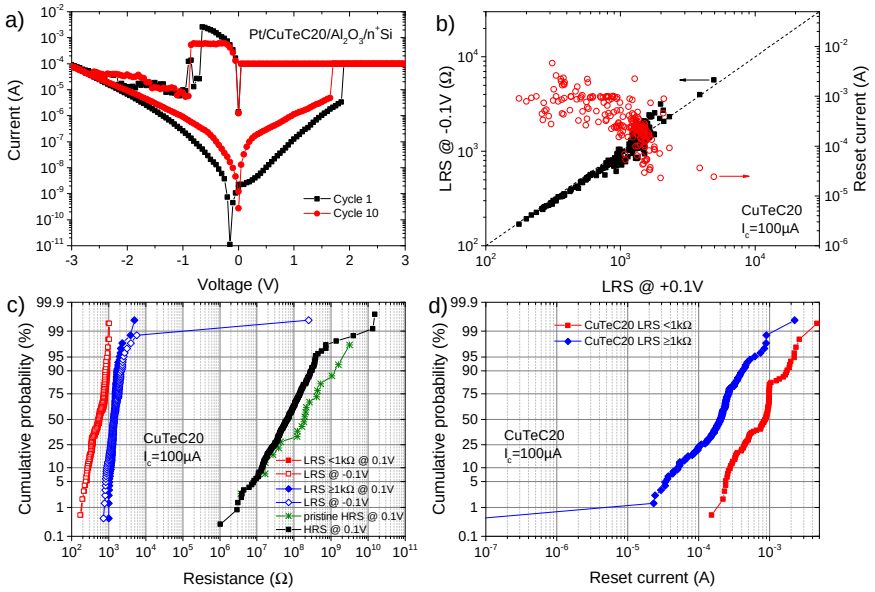

Figure 5.6. *(a) Typical IV-sweep of a Pt/CuTeC20/Al_2O_3/n^+ Si cell (sweep rate 0.5 V/s). (b) Resistance extracted from the reset sweep (at -0.1 V) as a function of the resistance extracted from the set sweep (at +0.1 V) and the reset current as a function of the LRS resistance before the reset. (c) The corresponding cumulative probability of these resistances and of the HRS and pristine cell resistances. (d) Cumulative probability of the reset currents. Note that a distinction was made in (c) and (d) between LRS larger and smaller than 1 kΩ. (Data from 20 devices × 10 cycles)*

supply layer on device variation should be tested on small devices. However, although the crystallization is slightly below $400°C$, it might be useful already in integration schemes where lower temperatures are used for passivation masks.

5.3.2 CBRAM functionality

A thorough study of the switching behaviour of CuTeC as a function of the carbon content is given in Paper III. In this section, we give a summary of the switching behaviour of the as-deposited cells with a CuTeC20 and CuTeC40 layer as a cation supply layer. Apart from the functionality of the cells, we investigate the filament stability and the retention behaviour, which can then be compared with $Cu_{0.6}Te_{0.4}$ and with other alloying elements further in this thesis. Figures 5.6 and 5.7 summarize the switching analysis for the CuTeC20 and CuTeC40 based CBRAM cells respectively. A typical switching curve is shown for each composition (see Figures 5.6a and 5.7a), suggesting good cycling behaviour with an efficient reset. This

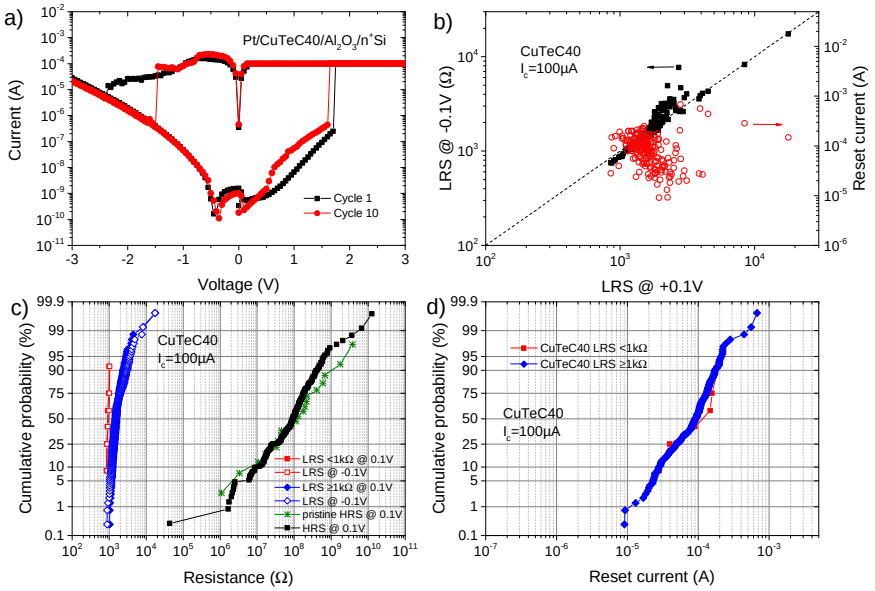

Figure 5.7. *(a) Typical IV-sweep of a Pt/CuTeC40/Al_2O_3/n^+ Si cell (sweep rate 0.5 V/s). (b) Resistance extracted from the reset sweep (at -0.1 V) as a function of the resistance extracted from the set sweep (at +0.1 V) and the reset current as a function of the LRS resistance before the reset. (c) The corresponding cumulative probability of these resistances and of the HRS and pristine cell resistances. (d) Cumulative probability of the reset currents. Note that a distinction was made in (c) and (d) between LRS larger and smaller than 1 kΩ. (Data from 20 devices × 10 cycles)*

is also evidenced by the HRS resistances that are very similar to the pristine resistances (see Figures 5.6c and 5.7c). This also results in promising endurance results, that is, the cells can be cycled up to 1000 times (see papers II and III). In analogy with pure $Cu_{0.6}Te_{0.4}$, the resistances were extracted from the set and reset sweeps, and the correlation plots are depicted in Figures 5.6b and 5.7b. The cumulative distributions are given in Figures 5.6c and 5.7c, where the cells with an LRS resistance smaller and larger than 1 kΩ are depicted separately. This is done because the filament stability is influenced by the LRS resistance [22], and hence to evaluate filament stability, cells with similar resistance should be compared. Accordingly, the reset currents (Figures 5.6d and 5.7d) are divided in two groups depending on the LRS resistance of the filament that is being reset.

It is observed already from the correlation plots that the filament tends to be more stable compared to pure $Cu_{0.6}Te_{0.4}$, because the resistances collected at + and -0.1 V coincide better (they follow the line $LRS_{+0.1V} = LRS_{-0.1V}$ much better). This is also visible in the cumulative distribution plots of LRS (Figures 5.6c

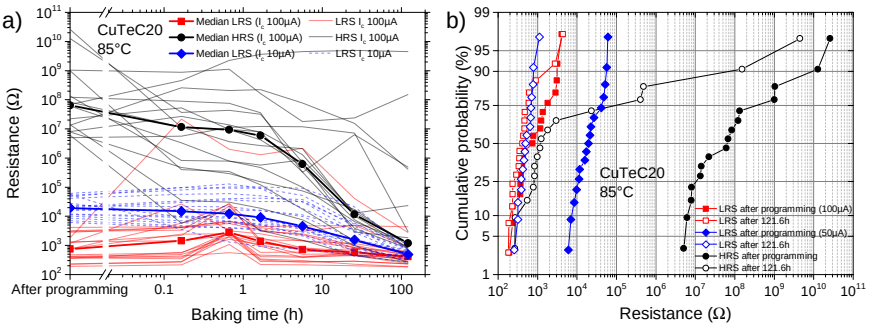

Figure 5.8. *(a) LRS (red and blue) and HRS (black) resistance of Pt/CuTeC20/Al_2O_3/n^+ Si cells. The resistance of every cell as a function of the baking time is shown, even as the median at every time step (thick line). (b) Cumulative probability of the LRS and HRS resistances after programming and after 121.6 h baking at 85°C.*

and 5.7c). The cells with LRS smaller than 1 kΩ do not occur for pure $Cu_{0.6}Te_{0.4}$, however they occur for the cells with 20 at% carbon (and a few for 40 at% carbon), and these are very stable (i.e. both values extracted from set and reset sweep coincide). Because of their very low resistance, these filaments are most likely thick filaments, which explains why they are less vulnerable for dissolution. Note that these also show a clearly higher reset current compared to the cells with LRS larger than 1 kΩ (Figure 5.6d). The LRS states with resistances larger than 1 kΩ, which also occur for pure $Cu_{0.6}Te_{0.4}$, coincide much better compared to $Cu_{0.6}Te_{0.4}$, suggesting a more stable LRS for the carbon alloyed cells. Note that their reset current (median value of 2×10^{-4} A for CuTeC20 and 1×10^{-4} A for CuTeC40) is slightly higher compared to $Cu_{0.6}Te_{0.4}$ (median value slightly lower than 1×10^{-4} A), which would suggest that the filaments can sustain higher currents before they get dissolved. However, the slightly higher reset current can also be related to the slightly lower median LRS resistance.

Retention was very briefly touched in Paper II (see Figure 7), where the resistance of a Pt/CuTeC40/Al_2O_3/n^+ Si cell was monitored at 85°C up to 2.7 h, which demonstrated the stability of the resistive states. However, a more thorough study including a statistical amount of cells and baking times for longer times are necessary to draw conclusions on the retention of the memory states. Hence a similar test as for $Cu_{0.6}Te_{0.4}$ was carried out for the CuTeC20 and CuTeC40 cells. Figures 5.8 and 5.9 show the retention results for CuTeC20 and CuTeC40 respectively. Figures 5.8a and 5.9a show the resistance of every cell as a function of the baking time, together with the median value, and Figures 5.8b and 5.9b show the corresponding cumulative distribution of the resistances after programming and after 5 days baking at 85°C. The median LRS resistances of the $Cu_{0.6}Te_{0.4}$ based

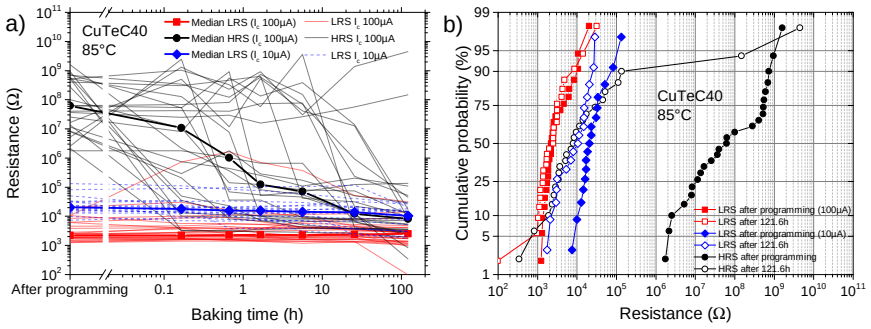

Figure 5.9. *(a) LRS (red and blue) and HRS (black) resistance of Pt/CuTeC40/Al_2O_3/n^+ Si cells. The resistance of every cell as a function of the baking time is shown, even as the median at every time step (thick line). (b) Cumulative probability of the LRS and HRS resistances after programming and after 121.6 h baking at 85°C.*

cells in the retention test was slightly higher than 10 kΩ by using a programming current of 100 µA, while lower resistances are obtained for both CuTeC20 and CuTeC40 (median LRS slightly below and above 1 kΩ respectively) with the same current compliance. That is why also lower programming currents (10 µA) are used to program the cells to LRS. Note that the cells suffer from parasitic current overshoots (see discussion in Chapter 3, section 3.5.3), which makes it difficult to tightly control the LRS resistance, and even though a lower I_c is used, there will always be a fraction of the cells that ends up in a LRS state with very low resistance. For CuTeC20 and CuTeC40, the cells programmed with 10 µA with LRS in the range 5 kΩ-100 kΩ and 10 kΩ-100 kΩ respectively were selected and their resistance was also monitored. These cells are plotted separately in Figures 5.8 and 5.9.

The results clearly show a decrease in HRS resistance for both CuTeC20 and CuTeC40. After 121.6 h, about 90 % of the HRS cells return to a low resistive state (i.e. R$<10^6$ Ω), while this is only about 25 % for $Cu_{0.6}Te_{0.4}$. This can be explained by the very low resistances that are reached during the initial cycles[9], which might have created a large template path in the Al_2O_3 switching layer. This acts as a defect where Cu from the supply layer, or some residual copper in the switching layer, can diffuse to restore the filament. As carbon does not mix or form strong bonds with Cu or Te, it will lower the affinity of Cu towards the supply layer. This might result in both a larger fraction of Cu species that is left in the switching layer after reset, and a lower tendency to keep the Cu in the supply layer. This will further enhance Cu diffusion in the template path and filament reconstruction

[9]Note that the LRS dependence on the retention of HRS has been reported by Xu et al. [24], where a lower HRS retention was measured for cells with low LRS resistances before programming to HRS.

that leads to the HRS degradation. Note that in Paper III (Figure 8) ToF SIMS of a CuTeC40 layer showed a much higher Cu, Te and C trace in the Al_2O_3 layer after anneal compared to CuTeC20 and $Cu_{0.6}Te_{0.4}$. This also suggests a lower tendency for the Cu to stay in the supply layer when much carbon is added.

The cells programmed to LRS do not return to a high resistive state, whereas about 50 % of the $Cu_{0.6}Te_{0.4}$ cells lose their LRS. The results suggest that carbon has the tendency to stabilize the low resistive state. This could also be observed already from the switching analysis[10]. Tada et al. [19] explained improved LRS stability by the incorporation of the alloying element in the filament, which lowers Cu mobility in the filament like in interconnects (see section 5.1.2). However this work also suggests that carbon alloying results in a lower affinity of Cu towards the supply layer, which results in a more stable LRS. Moreover, when considering the LRS behaviour of the CuTeC20 cells (Figure 5.8), even a decrease in LRS is observed. This is more pronounced than for CuTeC40 (Figure 5.9), but this might be related to the lower LRS resistances that are obtained for the CuTeC20 cells. Indeed, the cells were cycled twice before programming, and lower resistances than the final programmed LRS might be reached. So the cells in the range 10 to 100 kΩ might have reached a lower resistance in the initial cycles. This might have created a large template path in the Al_2O_3 switching layer. Cu from the supply layer, or some residual copper in the switching layer, might than restore the thicker filament and further lower the resistance. This is actually very similar to the observed HRS degradation.

5.3.3 XPS analysis

To get more information on the chemical state of the different elements in the CuTeC40 layer, XPS measurements were performed on both the CuTeC40 and a pure $Cu_{0.6}Te_{0.4}$ layer. The as-deposited $Cu_{0.6}Te_{0.4}$ layer is crystalline (showing diffraction peaks of the hexagonal $Cu_{2-x}Te$ phase [28]) and hence XRD reveals the formation of Cu-Te bonds. However, for CuTeC40, the as-deposited layer is amorphous and no information on the interaction between the constituting elements is known. The Cu 2p, Te 3d and C 1s photoelectron peaks were measured[11] and are depicted in Figures 5.10b, c and d respectively. From the discussion in section 3.4.3, we know that for chemical state analysis of Cu it is interesting to construct the Wagner plot, and this is given in Figure 5.10a. The position of CuTeC40 and $Cu_{0.6}Te_{0.4}$ is indicated together with a reference of a sputtered Cu film.

The Cu $2p_{3/2}$ peaks of both $Cu_{0.6}Te_{0.4}$ and CuTeC40 are shifted towards

[10] See also the discussion in Paper III for cells with 50 at% carbon, where a degradation of HRS is observed already during switching.

[11] These measurements were conducted using a S-Probe monochromatized XPS spectrometer of Surface Science Instruments (VG), as is presented in Paper II, whereas all other XPS measurement are conducted at the setup discussed in section 3.4.2.

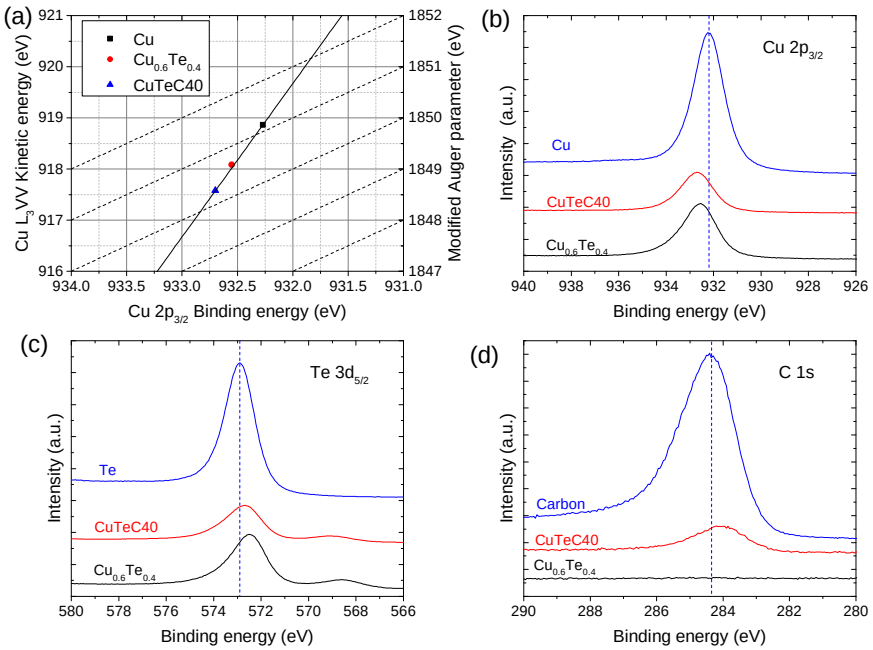

Figure 5.10. *XPS analysis of a CuTeC40 layer after sputtering away the surface contamination. (a) Copper Wagner plot, showing CuTeC40 together with $Cu_{0.6}Te_{0.4}$ and pure Cu as a reference. (b) Cu $2p_{3/2}$, (c) Te $3d_{5/2}$ and (d) C 1s peaks of CuTeC40 and $Cu_{0.6}Te_{0.4}$. As a reference, the corresponding peak of a sputterd pure Cu, Te and C film is also given.*

higher binding energies compared to metallic Cu. For $Cu_{0.6}Te_{0.4}$ this was to be expected because Cu was partially oxidized due to the formation of Cu-Te bonds (see section 4.2.4) The peak shift to higher binding energies is also observed for CuTeC40, suggesting that also here still Cu-Te bonds are present. Accordingly, the Te $3d_{5/2}$ peak is shifted towards lower binding energies, as it gets a partially negative charge and gets reduced in this way. The Modified Auger parameter α' was also calculated, as the Auger L_3VV line was also measured in the same window together with the Te 3d peaks. The main advantage of α' is its insensitivity to static charging, as a difference of binding energies of two peaks is taken. For metallic copper, a value for α' of 1851.1 eV was found, which is in good agreement with literature. A shift of α' to 1850.3 eV is observed for the CuTeC40 layer, which is equal to α' of Cu_2Te, and slightly lower than $Cu_{0.6}Te_{0.4}$ (1850.6 eV). Hence these results also suggest the presence of oxidized Cu. Note that the similarity of α' of CuTeC40 and Cu_2Te suggest similar final state effects for both materials, and a formal Cu(I+) state of Cu, since a Cu(II+) state would have more efficient screening and a value of α' closer to metallic Cu. Note that this is in agreement with

the shift of the Te3d$_{5/2}$ peak of CuTeC40 towards slightly larger binding energies compared to $Cu_{0.6}Te_{0.4}$, due to some pure Te that might be left. A line with slope -3 through metallic Cu was also drawn, because compounds with similar initial state effects would lay on this line. Note that all elements lay close to this line, and small shifts in binding energy due to charging effects may cause a shift in the position, that's why no further conclusions are drawn from this.

The carbon peak of the CuTeC40 sample is slightly shifted towards lower binding energies compared to the pure sputtered graphite film. This is still in the reported range for carbon bonds, and the difference is most likely related to the different chemical environment and coordination of carbon atoms in the sputtered graphite film and the CuTeC40 layer. Note that the absence of carbide phases was also reported in XPS analysis of mixed Cu-C films [31]. Moreover, the typical position of the C 1s peak for reported carbides is also much lower and in the range 280.5-283 eV [32].

To conclude this section, the XPS results of CuTeC40 suggest that Cu is still in an oxidized state by the presence of Te and hence that still Cu-Te bonds are formed. Carbon is most likely forming bonds to other carbon atoms, supporting the proposed mechanism of the formation of carbon chains that might hamper crystallization of Cu-Te phases. This also confirms the low miscibility of carbon with copper, tellurium and Cu-Te.

5.4 Germanium alloying of $Cu_{0.6}Te_{0.4}$

Promising results were obtained with carbon, i.e. the crystallization temperature could be significantly increased, and the phase formation could be influenced. However, the crystallization temperature was slightly below $400°C$, and phase separation occurs upon crystallization. Other elements of group 14 might be interesting to use as alloying elements. They are often used in phase change materials to increase the crystallization temperature because they generally increase the mean coordination number (like Ge in Sb_2Te_3 [10]). According to the model of Lankhorst (see section 2.3.4), the bond strength between the elements in the alloy also influences the crystallization temperature. In this section, we report the result of Ge as an alloying element. From table 2.2, it is clear that the bond enthalpy of Ge-Te is significantly higher (192.3 kJ/mol) while the Cu-Ge is slightly lower (103.66 kJ/mol) than Cu-Te (111.8 kJ/mol). Hence these strong bonds that are introduced might also increase T_x, because it is more difficult to break these bonds, which is necessary for the elements to reorganize into a lattice.

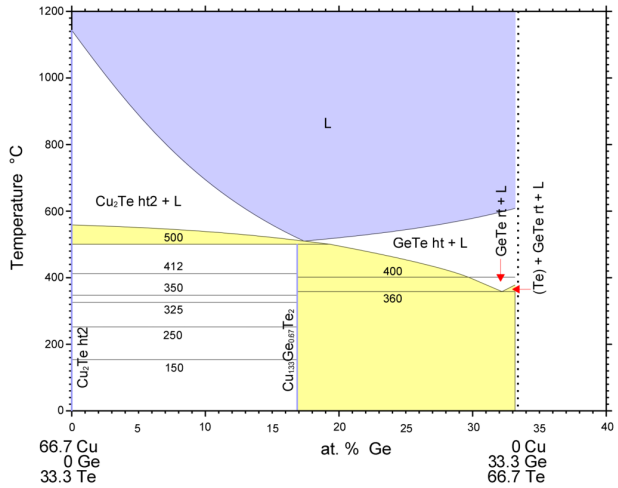

Figure 5.11. *Cross section of the Cu-Te-Ge phase diagram from 66.7 at% Cu and 33.3 at% Te to 66.7 at% Te and 33.3 at% Ge as a function of the Ge content. [37]*

5.4.1 Thermal Stability

Study of literature and phase diagrams learns that Ge forms compounds with Cu [33] and Te [34] (see Figures A.1 and A.2 respectively in Appendix A for the phase diagrams). Moreover, a ternary Cu-Te-Ge phase exists with the Cu_2GeTe_3 stoichiometry and a cubic crystal structure [35]. Note that the phase was also reported to be orthorhombic [36], however, it is not straightforward to discriminate the XRD patterns from the two structures. Figure 5.11 shows a cross section of the ternary Cu-Te-Ge phase diagram[12]. Additional cross sections are given in Appendix A. Figure 5.11 shows the presence of the Cu_2GeTe_3 phase. It shows that the Cu_2GeTe_3 is a line phase, i.e. it has a fixed composition and deviation from that composition will result in phase separation (the obtained phases at a certain temperature are those that are found by drawing a tie line). From the phase diagram it is also clear that for higher Ge contents (and more specifically for layers with more than 50 at% Te, see also diagrams A.6 and A.10), the melting temperature where part of the material is in the liquid phase occurs below $400°C$.

From the phase diagrams, we can conclude that, when the material is crystalline and has a composition different from Cu_2GeTe_3, it will phase separate, which will result in an inhomogeneous cation supply layer. This can result in vari-

[12] In these colored phase diagrams, purple colored regions are single phase regions, white regions contain two phases (i.e. the adjecent phases that are met when drawing a tie line at the temperature of interest) and the yellow regions contain 3 or more phases.

ation of the device characteristics when this happens in memory devices. Melting temperatures below 400°C occur for Te rich layers (more than 50 at% Te), which has of course to be avoided because melting and evaporation of the material is a serious degradation. This is also thoroughly discussed and illustrated in Paper IV. In the next subsections, we investigate the influence of Ge alloying of a $Cu_{0.6}Te_{0.4}$ layer on the Cu-Te crystallization and phase formation. The single phase composition Cu_2GeTe_3 is also studied. These results are also reported in Paper IV. Note that the phase diagrams that are cited in that paper can be found in Appendix A.

5.4.1.1 Alloying of $Cu_{0.6}Te_{0.4}$

The influence of Ge alloying was investigated by preparing different samples of $Cu_{0.6}Te_{0.4}$ with varying Ge contents. Samples with 5, 10, 20, 30, 40 and 50 at% Ge were prepared (further referred to as CuTeGe5 up to CuTeGe50), and the layer thickness was fixed to 50 nm. XRF could be used after calibrating the system with a reference sample quantified by means of RBS. Detailed compositions can be found in Paper IV and its Supporting Information. The *in situ* XRD patterns for compositions up to 30 at% Ge are shown in Figure 5.12, higher Ge contents did not significantly increase T_x. From the *in situ* XRD measurements, it is observed that addition of Ge is effective in increasing T_x, however, crystallization occurs at temperatures below 400°C, and phase separation occurs upon crystallization. Note that for some compositions, diffraction peaks corresponding to the ternary Cu_2GeTe_3 phase occur (e.g. for 10 at% Ge). Hence if crystallization below 400°C cannot be avoided, it might be interesting to investigate that composition. Note that the phase diagrams also shows no transformation of that material up to 500°C, where it melts and forms a liquid, Cu_2Te and GeTe.

The sample with 20 at% Ge shows a T_x slightly above 200°C, which is actually very comparable to the 20 at% carbon alloyed $Cu_{0.6}Te_{0.4}$ layer. The material with 30 at% Ge shows already a significantly increased T_x, and can be used in combination with low temperature passivation schemes.

5.4.1.2 Single phase composition

A layer with a composition of 32.7 at% Cu, 17 at% Ge and 50.3 at% Te was deposited to obtain the single Cu_2GeTe_3 phase upon crystallization. The *in situ* XRD measurement is shown in Figure 5.13a. The material crystallizes[13] at 203°C and the diffraction peaks corresponding to the Cu_2GeTe_3 phase exist up to about 470°C, where it transforms to the high temperature $Cu_{2-x}Te$ [38] phase. The abrupt disappearance of the Cu_2GeTe_3 phase is most likely due to melting of the

[13]The crystalliation temperature is defined here as the temperature where the maximum change in integrated intensity of the peak at 25.9° occurs.

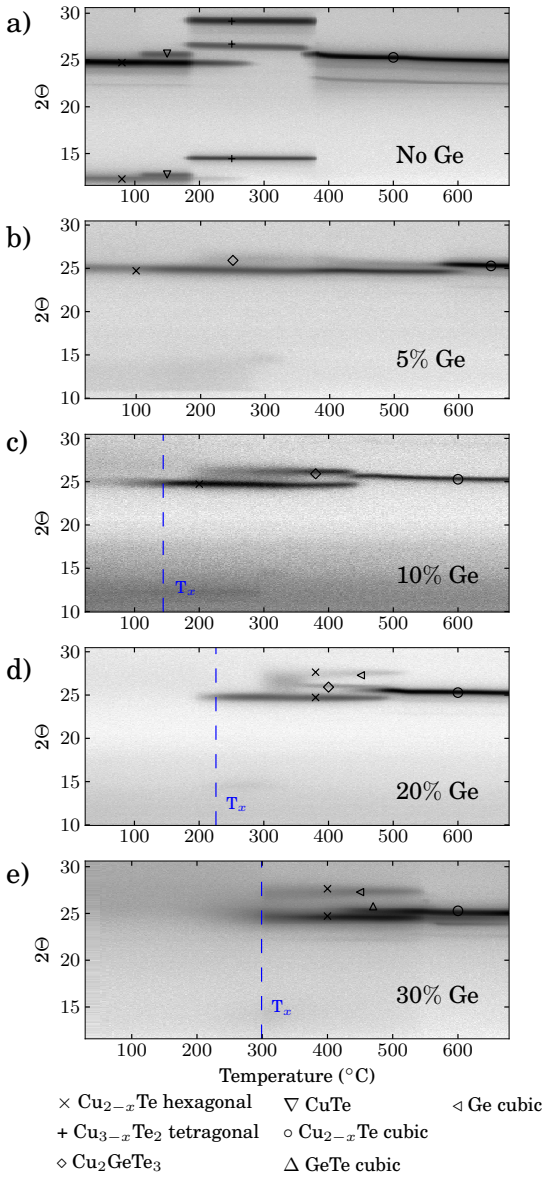

Figure 5.12. *In situ XRD patterns measured at a heating rate of $0.5°C/s$ in He atmospere of alloyed $Cu_{0.6}Te_{0.4}$ layers without Ge (a), with 10 at% Ge (b), 20 at% Ge (c) and 30 at% Ge (d).*

phase, although this temperature is slightly below the reported value for bulk material ($\sim 500°C$). This can occur in thin films, and especially when nano particles

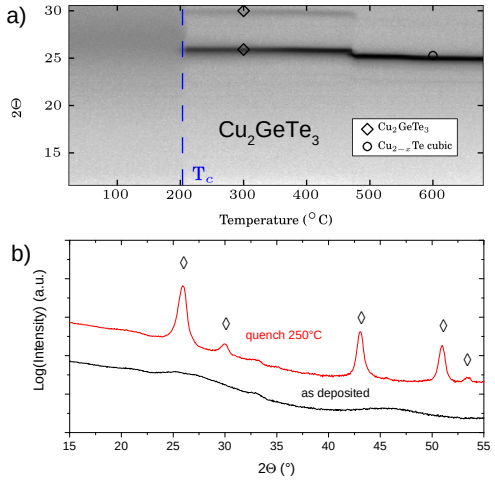

Figure 5.13. *(a) In situ XRD pattern of a 50 nm Cu_2GeTe_3 layer measured at a heating rate of $0.5^\circ C/s$ in He atmosphere. (b) XRD pattern of an as-deposited Cu_2GeTe_3 layer and after anneal to $250^\circ C$.*

are formed (for example if the layer starts to agglomerate), due to a change in surface-to-volume ratio, altering their thermodynamical properties. Apart from the crystallization, no transformations occur. The phase that is formed then is stable up to its melting point which is significantly higher than $400^\circ C$.

For this composition, it is also possible to calculate the glass transition temperature according to the model of Lankhorst (see section 2.3.4). The model assumes a dominantly covalent bond structure, and hence the mean coordination number cannot be higher than 4. The other composition where $Cu_{0.6}Te_{0.4}$ was alloyed with Ge have a mean coordination number that would be higher than 4 because there is not enough Te to create a formal valence of Cu up to 4. The model is interesting because we can theoretically compare the ability of elements to keep a supply layer amorphous in this way, and compare it with the crystallization observed from *in situ* XRD measurements. Note that we did not do this for Cu-Te-C because theoretically, no Cu-C or Te-C bonds are formed. The calculation is illustrated in table 5.1. The mean coordination number in the material is 4. Cu has a valence of only one, and hence 2 Te atoms give each 2 electrons to a Cu atom. Then each Cu atom still needs one electron, which is delivered by the third Te atom that is left. In this way, all Cu atoms have a formal valence of 4, as well as the Te atoms[14]. The Ge atoms had already 4 valence electrons. According to the model, heteronuclear bonds are preferred and formed in order of decreasing bond enthalpy. Hence Ge-Te bonds are formed first, and there is more Te than Ge, so all

[14]Note that the *formal* valence in table 5.1 is explicitly indicated with Roman numbers in superscript.

Table 5.1. *Calculation of the glass transition temperature of Cu_2GeTe_3. Z is the mean coordination number, H_{AB} the heteronuclear bond enthalpy, n_{AB} the number of A-B bonds, H_a the bond enthalpy of the alloy, T_g the glass transition temperature and T_x the measured crystallization temperature.*

Material	Z	A-B bond	H_{AB} (kJ/mol)	n_{AB}	H_a (kJ/mol)	T_g ($^\circ C$)	T_x ($^\circ C$)
Cu_2GeTe_3	4				277.3	200.68	203
		Ge-Te^{IV}	192.3	0.6668			
		Cu^{IV}-Te^{IV}	111.8	1.3332			

Ge is consumed in Ge-Te bonds. The number of Ge-Te bonds (n_{GeTe}) is equal to the fraction of Ge in the compound (0.1667) multiplied with the number of bonds that it forms (4). The Te that is left is then consumed in Cu-Te bonds. Note that the total number of bonds ($n_{GeTe} + n_{CuTe}$) is indeed equal to $Z/2$. The mean bond enthalpy of the Cu_2GeTe_3 compound is then calculated from equation 2.12 (which is simply the weighted sum of bond enthalpies), and the glass transition temperature T_g from equation 2.11. This temperature is useful, because this is an under limit for the crystallization temperature. In this way T_g was found to be $\sim 200^\circ C$, while the measured T_x is $203^\circ C$.

5.4.2 CBRAM functionality

The functionality of CuTeGe20, CuTeGe30 and Cu_2GeTe_3 as cation supply layer in CBRAM has been studied. In this section, we will not show the results of CuTeGe30, as they are similar to CuTeGe20. However, they are reported in Paper IV and can be found there. Similar to the switching analysis of $Cu_{0.6}Te_{0.4}$ and the carbon alloyed $Cu_{0.6}Te_{0.4}$, the CuTeGe20 and Cu_2GeTe_3 cells were cycled up to ten times. The resistance from the set and reset sweeps, as well as the reset current was extracted. The results are presented in Figures 5.14 and 5.15 for CuTeGe20 and Cu_2GeTe_3 respectively. From the switching curves (Figures 5.14a and 5.15a), it is clear that the cells show functional CBRAM behaviour. As with $Cu_{0.6}Te_{0.4}$ and carbon alloyed $Cu_{0.6}Te_{0.4}$, the cells can be efficiently reset. This is also visible in Figures 5.14c and 5.15c, showing HRS resistances that are very similar to the pristine cell resistance.

The correlation plots of the resistances extracted from set and reset sweep (Figures 5.14b and 5.15b) show that the resistances are following the trend line $LRS_{0.1V}$=$LRS_{-0.1V}$ much better compared to $Cu_{0.6}Te_{0.4}$ (Figure 5.2b). While the resistance during reset already slightly increased for $Cu_{0.6}Te_{0.4}$, this is less pronounced for the Ge containing cells, giving a first indication of a filament that is more stable against dissolution (see also Figure 6 in Paper IV). The reset cur-

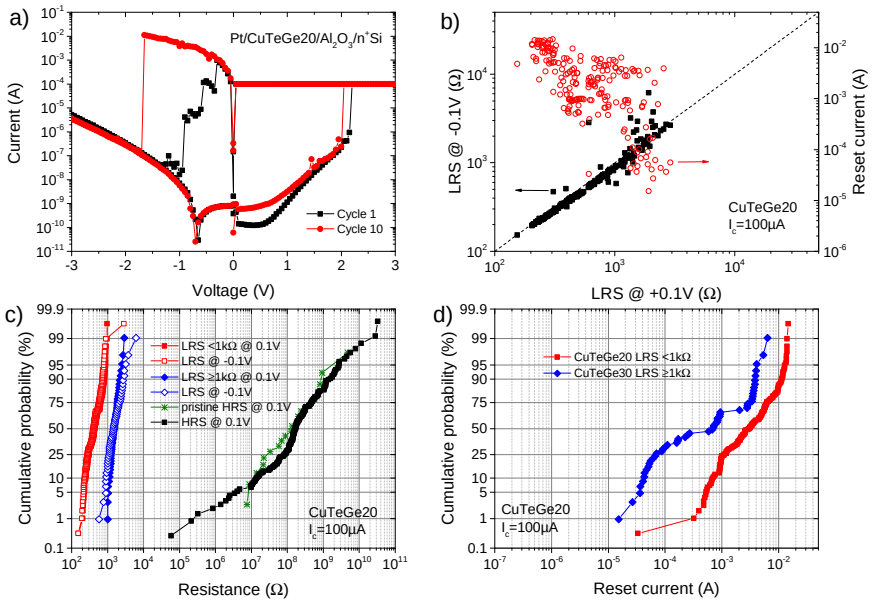

Figure 5.14. *(a) Typical IV-sweep of a Pt/CuTeGe20/Al_2O_3/n^+ Si cell (sweep rate 0.5 V/s). (b) Resistance extracted from the reset sweep (at -0.1 V) as a function of the resistance extracted from the set sweep (at +0.1 V) and the reset current as a function of the LRS resistance before the reset. (c) The corresponding cumulative probability of these resistances and of the HRS and pristine cell resistances. (d) Cumulative probability of the reset currents. Note that a distinction was made in (c) and (d) between LRS larger and smaller than 1 kΩ. (Data from 20 devices × 10 cycles)*

rent, defined as the current where the maximal current drop occurs, is depicted in Figures 5.14d and 5.15d. The reset currents of filaments that had an LRS resistance larger or smaller than 1 kΩ are depicted separately, because thicker filaments will be able to sustain larger currents. Recall that the median reset current for filaments with LRS larger than 1 kΩ for $Cu_{0.6}Te_{0.4}$ is slightly below $1 \times 10^{-4}\,A$, while for CuTeGe20 and Cu_2GeTe_3 this is slightly below or above $1 \times 10^{-3}\,A$ respectively. Note that this is even more pronounced for CuTeGe30 as shown in Paper IV. Again, this points to a more stable filament against dissolution, because higher currents are needed to break the filament. The fact that higher reset currents are necessary to break the filament also points to a larger thermal contribution to the reset (i.e. due to Joule heating), that might be necessary to erase the filament because of a lower drift contribution. Hence the switching analysis suggests a lower affinity of the Cu from the filament to the supply layer.

Retention was tested in the same way as before and also here, next to a programming current of 100 µA, a lower I_c was used to obtain more cells in a LRS

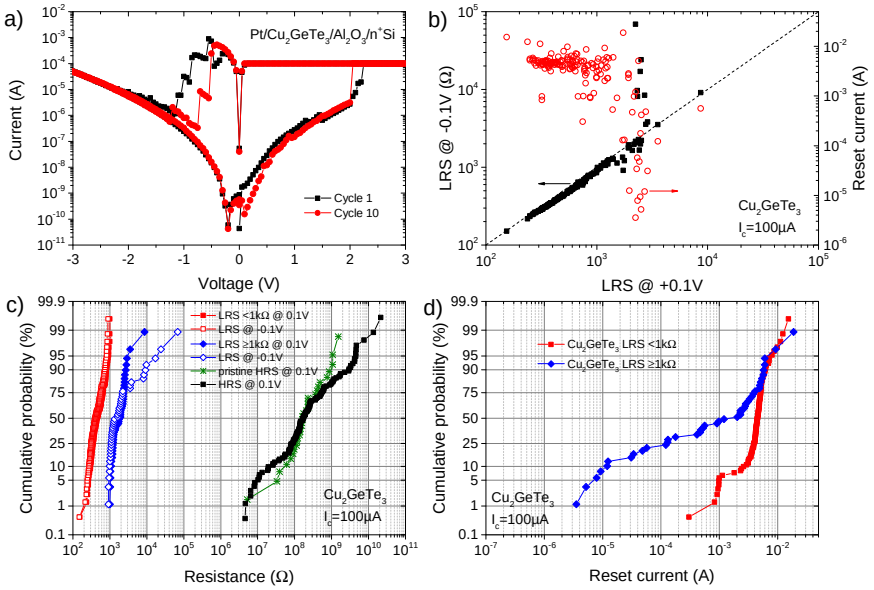

Figure 5.15. *(a) Typical IV-sweep of a Pt/Cu_2GeTe_3/Al_2O_3/n^+ Si cell (sweep rate 0.5 V/s). (b) Resistance extracted from the reset sweep (at -0.1 V) as a function of the resistance extracted from the set sweep (at +0.1 V) and the reset current as a function of the LRS resistance before the reset. (c) The corresponding cumulative probability of these resistances and of the HRS and pristine cell resistances. (d) Cumulative probability of the reset currents. Note that a distinction was made in (c) and (d) between LRS larger and smaller than 1 kΩ. (Data from 30 devices × 5 cycles)*

with higher resistance. The resistances for all cells, together with the median value are shown as a function of the baking time in Figures 5.16a and 5.17a for CuTeGe20 and Cu_2GeTe_3 based cells respectively. The cumulative distribution plots of the corresponding resistances are shown in Figures 5.16b and 5.17b. It is clear that the LRS for both materials is stable over more than 5 days baking at $85°C$, even for the cells with LRS resistance in the range 10-100 kΩ. Hence an improved LRS retention compared to $Cu_{0.6}Te_{0.4}$ is measured. Concerning the HRS, about 25 % of the cells (slightly less for Cu_2GeTe_3) relax to a low resistive state (R$<1 \times 10^6\,\Omega$). This is similar to $Cu_{0.6}Te_{0.4}$, and was ascribed to filament reconstruction. However, compared to CuTeC20 and CuTeC40, the HRS is conserved much better. This can be understood by the formation of bonds between Ge and Cu/Te, leading to a higher tendency to keep the Cu in the supply layer compared to carbon. This counteracts Cu diffusion and filament reconstruction, and hence is beneficial for HRS retention. We can conclude that Ge as an alloying element has the ability to improve the LRS retention compared to $Cu_{0.6}Te_{0.4}$, while conserving

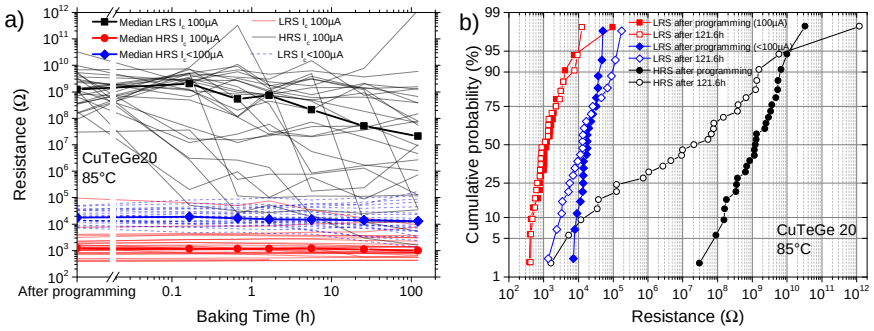

Figure 5.16. *(a) LRS (red and blue) and HRS (black) resistance of Pt/CuTeGe20/Al_2O_3/n^+ Si cells. The resistance of every cell as a function of the baking time is shown, even as the median at every time step (thick line). (b) Cumulative probability of the LRS and HRS resistances after programming and after 121.6 h baking at 85°C.*

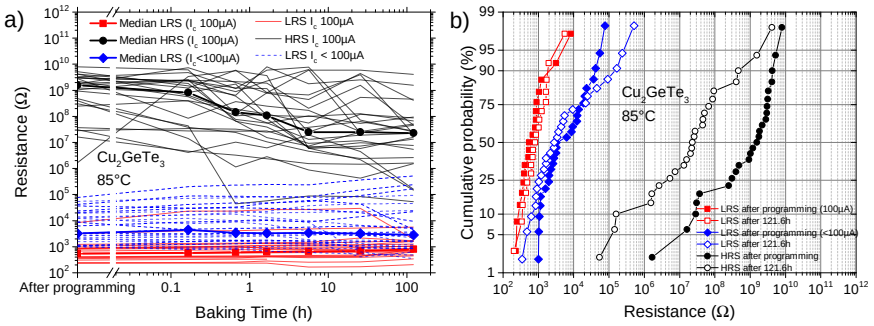

Figure 5.17. *(a) LRS (red and blue) and HRS (black) resistance of Pt/Cu_2GeTe_3/Al_2O_3/n^+ Si cells. The resistance of every cell as a function of the baking time is shown, even as the median at every time step (thick line). (b) Cumulative probability of the LRS and HRS resistances after programming and after 121.6 h baking at 85°C.*

the HRS retention characteristics.

5.4.3 XPS analysis

In order to get more insight in the chemical state of the different elements, XPS analysis was performed on a CuTeGe20 and Cu_2GeTe_3 sample. Figures 5.18a and 5.18b show the Cu-Wagner plot and the Cu $2p_{3/2}$ peaks respectively. In the Wagner plot, the positions of pure Cu and $Cu_{0.6}Te_{0.4}$ are also given as a reference. The Te $3d_{5/2}$ and Ge 3d peaks are given in Figures 5.18c and 5.18d respectively. For each photoelectron peak, a reference of the pure material is also shown. It is

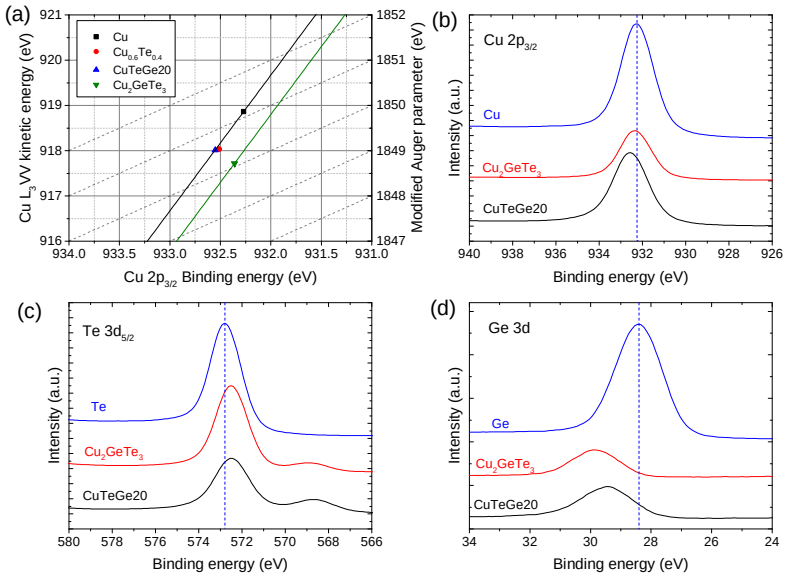

Figure 5.18. *XPS analysis of a CuTeGe20 and Cu_2GeTe_3 layer after sputtering away the surface contamination. (a) Copper Wagner plot, showing CuTeGe20 and Cu_2GeTe_3 toghether with $Cu_{0.6}Te_{0.4}$ and pure Cu as a reference. (b) Cu $2p_{3/2}$, (c) Te $3d_{5/2}$ and (d) Ge 3d peaks of CuTeGe20 and Cu_2GeTe_3 . As a reference, the corresponding peak of a sputterd pure Cu, Te and Ge film is also given.*

observed that the Cu peak of CuTeGe20 is shifted towards higher values, as was also observed for $Cu_{0.6}Te_{0.4}$ and CuTeC40. This can in a first approximation be explained by a partial charge transfer from Cu to the bonding partner, resulting in a net smaller screening of the nucleus and hence a larger bond energy of the core electrons. Hence it can be explained as an oxidation of the Cu. Accordingly, the Te peak is shifted towards lower binding energies. Note that the shift towards lower energies can also have a contribution due to oxidation of Ge [15]. The shift in Cu peak position is less pronounced for Cu_2GeTe_3 while the Wagner plot however shows a clear shift of the modified Auger parameter α' (1850.1 eV) compared to metallic Cu (1851.1 eV). This large shift of α' suggests a Cu(I+) state (because a Cu(II+) state typically has α' closer to metallic Cu). This is also what is expected if one takes the formal oxidation state of Ge (IV+) and Te (II-) into account. The measurement for Cu_2GeTe_3 was also performed after anneal to $300°C$ to crystallize the material (not shown), and gives similar results. Hence this suggests a similar chemical environment for the amorphous and crystalline Cu_2GeTe_3 supply layer. Another observation is that the line with slope -3 through Cu_2GeTe_3 is clearly shifted compared to metallic Cu, which points to a larger ionic degree of the

bonds where Cu is involved compared to pure Cu and the other Cu-Te compounds.

The Ge 3d peak of both alloys shows a clear shift towards higher binding energies compared to pure Ge, and is in the reported range for Ge-Te bonds [15, 39]. This shows that Ge is forming bonds with the Te, as was to be expected from the high bond enthalpy (see table 2.2 and the calculation of T_g in table 5.1).

These observations can give an explanation for the retention results reported in previous section. Addition of Ge to $Cu_{0.6}Te_{0.4}$ introduces Ge-Te bonds, hence there will be a lower tendency for Cu-Te formation, which will lower the driving force for Cu from the filament to go back to the supply layer. This is expected to have a stabilizing effect on the low resistive state. An important difference with the carbon is that Ge is also forming bonds to Cu and Te. This is expected to have a positive influence on HRS retention because it has the tendency to keep the Cu (and other elements) in the supply layer. The carbon on the other hand is not willing to form bonds with Cu or Te, and hence Cu species at the Al_2O_3/Cu-supply interface tend to go back in the conductive filament pathway, whereas Ge (that is forming bonds) will rather prevent this.

5.5 Silicon alloying of $Cu_{0.6}Te_{0.4}$

Next to carbon and germanium, silicon is used as an alloying element. Also here a ternary compound, Cu_2SiTe_3, is reported [40]. One of the reasons to use Si instead of Ge is because the melting temperature for bulk Cu_2SiTe_3 is higher (which is 578$^\circ C$ compared 500$^\circ C$ for bulk Cu_2GeTe_3). A cross section of the ternary Cu-Te-Si diagram is shown in Figure 5.19, illustrating the existence of the Cu_2SiTe_3 phase. Additional phase diagrams can be found in Appendix B. Also for this material system, melting temperatures below 400$^\circ C$ occur for Te rich compositions, which can be related to the occurrence of a eutectic point at 380$^\circ C$ (see Figure B.3 in Appendix B). A similar approach as for C and Ge was followed, and $Cu_{0.6}Te_{0.4}$ layers were alloyed with 5, 10 and 20 at% Si. The mixed Cu-Te-Si layers were 50 nm thin and deposited by magnetron sputtering. The compositions were verified by RBS, and also EDX could be used after calibration of the system. The exact compositions are tabulated in table 1 in Paper V. Note that for these compositions, the phase diagrams (see Appendix B) show melting temperatures exceeding 400$^\circ C$. Also here a layer with 33.3 at% Cu, 16.7 at% Si and 50 at% Te was deposited to obtain the single phase (Cu_2SiTe_3) material. The thermal stability of the alloys is investigated, and the most promising alloy is tested on its functionality as cation supply layer in CBRAM.

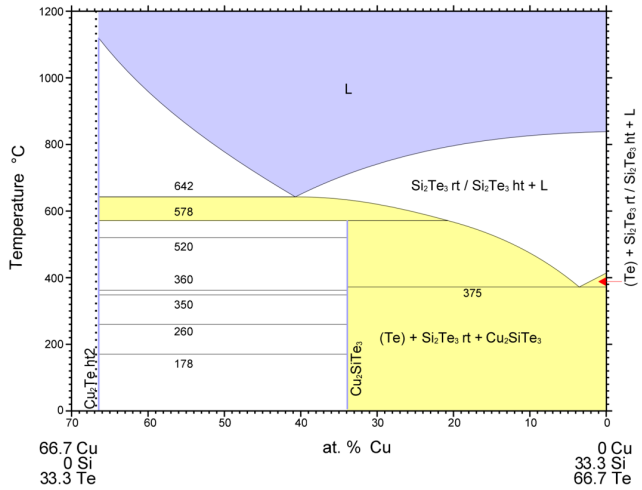

Figure 5.19. *Cross section of the Cu-Te-Si phase diagram from 66.7 at% Cu and 33.3 at% Te to 66.7 at% Te and 33.3 at% Si as a function of the Cu content. [41]*

5.5.1 Thermal Stability

The films are characterized by means of *in situ* XRD to study the cristallinity and to identify the different phases that occur. The measurements are shown in Figure 5.20, where also a $Cu_{0.6}Te_{0.4}$ layer is given as a reference. It is clear that addition of Si also inhibits crystallization. Indeed, the as-deposited layers are amorphous and crystallization occurs at 138 and 255°C for layers with 5 and 10 at% Si respectively (see Figures 5.20b and c). The layer with 20 at% Si (Figure 5.20d) shows no clear diffraction peaks up to temperatures exceeding 500°C. This is very promising, because the material does not show significant changes up to the temperatures that are applied during BEOL processing (typically around 400°C). The layer with the single phase composition (Figure 5.20e) shows upon crystallization at 292°C only diffraction peaks related to the Cu_2SiTe_3 phase [40]. Note that the diffraction peaks diminish and transform to cubic Cu_2Te [38] at temperatures above 500°C, which is higher than for Cu_2GeTe_3.

The strong tendency of Si to keep the material amorphous is remarkable. While crystallization is inhibited to temperatures around 200°C for $Cu_{0.6}Te_{0.4}$ layers with 20 at% C or Ge, T_x exceeds 500°C when 20 at% Si is added. This can be related to the strong interaction between Si and Cu and Te, as is clear from the strong heteronuclear bond enthalpies reported in table 2.2. This can also be illustrated by comparing the theoretical glass transition temperature (as calculated by the model

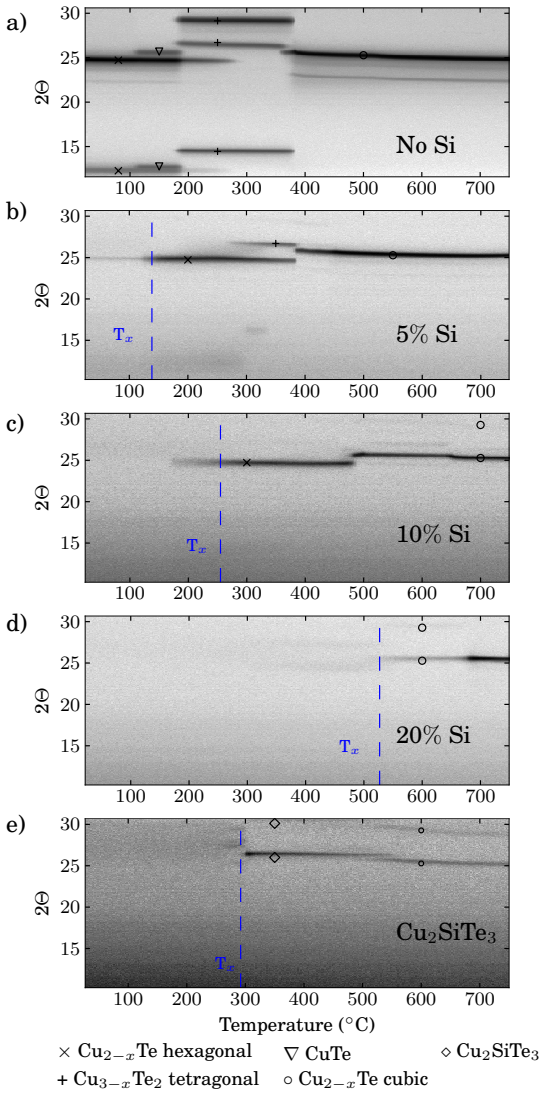

Figure 5.20. *In situ XRD patterns measured at a heating rate of 0.5°C/s in He atmospere of Si alloyed $Cu_{0.6}Te_{0.4}$ layers containing (a) no Si, (b) 5 at% Si (c) 10 at% Si and (d) 20 at% Si. (e) The single phase composition Cu_2SiTe_3.*

of Lankhorst [7]), and the measured crystallization temperature of Cu_2SiTe_3 and compare it with Cu_2GeTe_3. The calculation of T_g is given in table 5.2 and is similar to Cu_2GeTe_3, which was discussed in section 5.4.1.2. It is indeed clear that a

Table 5.2. *Calculation of the glass transition temperature of Cu_2SiTe_3.*

Material	Z	A-B bond	H_{AB} (kJ/mol)	n_{AB}	H_a (kJ/mol)	T_g ($^\circ C$)	T_x ($^\circ C$)
Cu_2SiTe_3	4				292.31	252.4	292
		Si-Te^{IV}	214.85	0.6668			
		Cu^{IV}-Te^{IV}	111.8	1.3332			

higher bond enthalpy H_a is found for Cu_2SiTe_3 compared to Cu_2GeTe_3, resulting in a higher glass transition temperature. T_g is calculated to be at $252^\circ C$, which is more than $50^\circ C$ higher than for the Ge compound. Accordingly, crystallization should not occur below this temperature. This is in agreement with the measured crystallization temperature of $292^\circ C$, which is about $90^\circ C$ higher compared to Cu_2GeTe_3. Hence this shows clearly the influence of the role of the alloying element and the bond strength with the other elements.

Apart from the strong bonds of Si with the other elements, Saito et al. [15] reported that also strong Si-Si bonds might be formed. According to the model of Lankhorst, heteronuclear bonds are formed first. However, the Si-Si bond (see table 2.2) is very strong and even stronger than the heteronuclear bonds, making the formation of Si-Si chains likely to occur. Saito et al. came to the conclusion that in Si alloyed GeTe for higher Si contents (>10 at% Si), both Si-Te and Si-Si bonds are formed. The formation of Si chains can lower the mobility of the species and inhibit crystallization. This can also occur in the Si alloyed $Cu_{0.6}Te_{0.4}$, and might further explain the high T_x. To get more insight in the role of Si and the bonds that it forms, XPS measurements were performed.

5.5.2 XPS analysis

XPS measurements were conducted on the CuTeSi20 and Cu_2SiTe_3 samples and the results are shown in Figure 5.21. Figures 5.21a and b give the Cu Wagner plot and the Cu $2p_{3/2}$ peaks respectively, while Figures 5.21c and d show respectively the Te $3d_{5/2}$ and Si 2p peaks. For each peak, a reference for the pure material, prepared by magnetron sputtering, is also shown. It is clear that the Si peak for both alloys is shifted towards higher binding energies compared to the pure Si film. This confirms the occurrence of Si-Te bonds. Because the Te is the most electronegative element in the alloy, Te will have the tendency to attract the electrons in the bond more compared to Si, resulting in a net positive charge on the Si atoms. This leaves the Si in a partially oxidized state, explaining the shift of the Si 2p binding energy towards higher values. The Si 2p peak of CuTeSi20 however shows a smaller shift compared to Cu_2SiTe_3. This suggest the occurrence of more Si-Si bonds in the

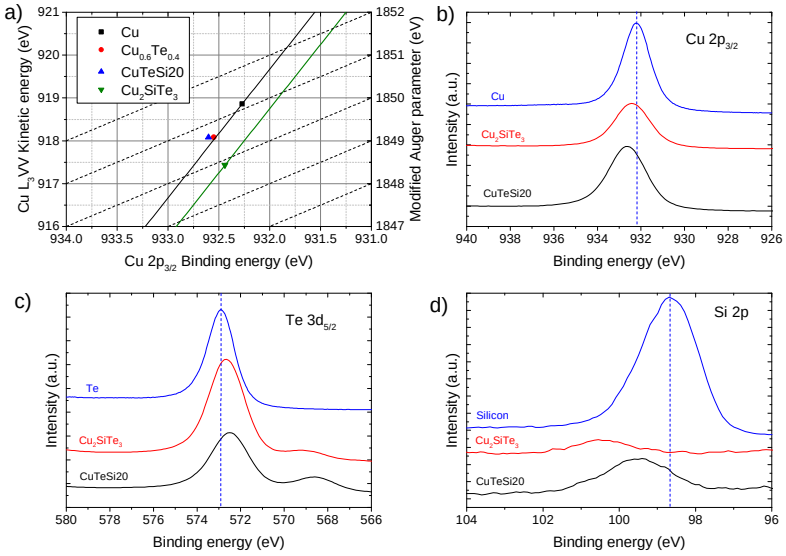

Figure 5.21. *XPS analysis of a CuTeSi20 and Cu_2SiTe_3 layer after sputtering away the surface contamination. (a) Copper Wagner plot, showing CuTeSi20 and Cu_2GeTe_3 toghether with $Cu_{0.6}Te_{0.4}$ and pure Cu as reference. (b) Cu $2p_{3/2}$, (c) Te $3d_{5/2}$ and (d) Si 2p peaks of CuTeSi20 and Cu_2SiTe_3. As a reference, the corresponding peak of a sputterd pure Cu, Te and Si film is also given.*

CuTeSi20 sample. This is reasonable because less Te is present here to form bonds with, and this also confirms the suggested formation of Si-Si bonds contributing to the high T_x.

The Cu and Te peaks show a shift towards respectively higher and lower binding energies, as was also observed for $Cu_{0.6}Te_{0.4}$ and when it was alloyed with C or Ge. As for Cu_2GeTe_3, the shift of the Cu peak for Cu_2SiTe_3 is less pronounced compared to CuTeSi20. Also for these alloys, the modified Auger parameter (α') was determined, and the Wagner plot is constructed (Figure 5.21a). Cu_2SiTe_3 has an α' of 1849.9 eV, which is similar to Cu_2GeTe_3. It is also more than 1 eV smaller than metallic Cu, suggesting a less metallic state, and the presence of oxidized Cu. This can also be deduced from the shift of the line with slope -3, which is clearly shifted compared to metallic Cu, as indicated in Figure 5.21a. CuTeSi20 has an α' of 1850.7 eV and is comparable to α' of $Cu_{0.6}Te_{0.4}$.

5.5.3 CBRAM functionality

The CuTeSi20 was selected among the other Si-containing alloys because of its high thermal stability. The material is integrated in Pt/CuTeSi20/Al_2O_3/n^+ Si dot

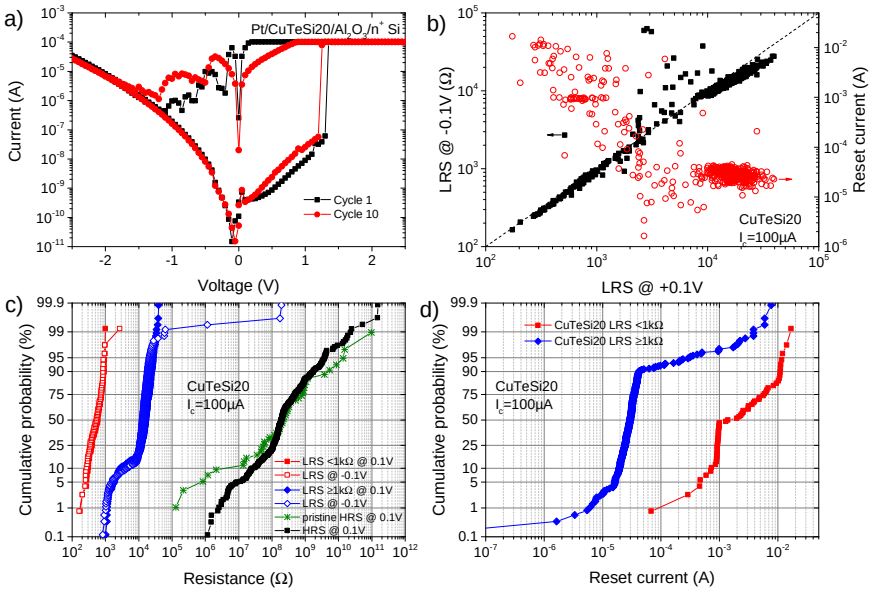

Figure 5.22. *(a) Typical IV-sweep of a Pt/CuTeSi20/Al_2O_3/n^+ Si cell (sweep rate 0.5 V/s). (b) Resistance extracted from the reset sweep (at -0.1 V) as a function of the resistance extracted from the set sweep (at +0.1 V) and the reset current as a function of the LRS resistance before the reset. (c) The corresponding cumulative probability of these resistances as well as the HRS and pristine cell resistances. (d) Cumulative probability of the reset currents. Note that a distinction was made in (c) and (d) between LRS larger and smaller than 1 kΩ. (Data from 45 cells × 10 cycles)*

cells and the same switching analysis was performed as for the other alloys in previous sections. The result is given in Figure 5.22. Functional CBRAM is observed, illustrated by the consistent DC switching curves in Figure 5.22a. The cells showed good endurance properties, allowing over 1000 DC cycles (see Figure 7c in Paper V). The ON and OFF resistances of the cells that are cycled with 100 µA, together with the pristine resistance is shown in Figure 5.22c. Again a HRS resistance similar to the pristine resistance is observed, illustrating the efficient reset. Figure 5.22b shows the LRS resistance extracted from the reset sweep as function of the value extracted from the set sweep. The resistances coincide very well, and even high LRS resistances (>10 kΩ) follow this trend. This points to a more stable filament for the Si alloyed cells compared to $Cu_{0.6}Te_{0.4}$. The reset currents (Figure 5.22d) for LRS resistances larger than 1 kΩ are slightly lower than for $Cu_{0.6}Te_{0.4}$, however, this is mainly related to the higher LRS resistances (>10 kΩ) compared to $Cu_{0.6}Te_{0.4}$ (which are in between 1 and 10 kΩ).

Retention of the memory cells was investigated by programming the cells to

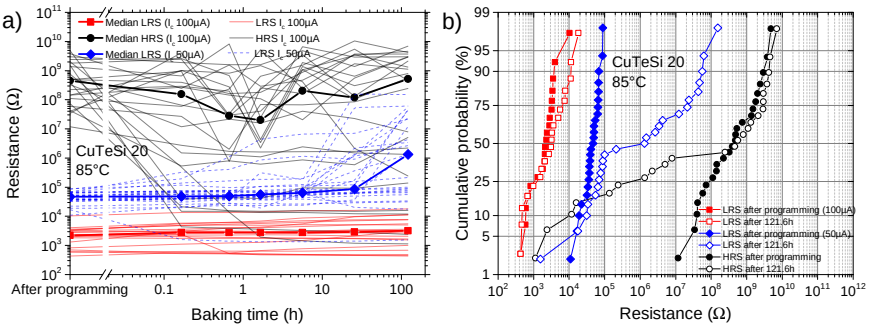

Figure 5.23. *(a) LRS (red and blue) and HRS (black) resistance of Pt/CuTeSi20/Al_2O_3/n^+ Si cells. The resistance of every cell as a function of the baking time is shown, even as the median at every time step (thick line). (b) Cumulative probability of the LRS and HRS resistances after programming and after 121.6 h baking at 85°C.*

a low or high resistive state, and measuring the resistance after predefined baking times at 85°C. Figure 5.23a shows the resistance of every cell as a function of the baking time, together with the median value at every time step. The cumulative distribution of the LRS and HRS states after programming and after more than 5 days baking is shown in Figure 5.23b. Also here, a lower compliance current was used to get more cells in the LRS with a resistance between 1 and 10 kΩ, and these cells are plotted separately. It is clear that low LRS resistances retain their state during the test, most likely because these are strong, big filaments that are more difficult to dissolve. The LRS states in the range 10 to 100 kΩ are less stable compared to the cells with Ge. After 5 days at 85°C, about 50 % of the cells return to a HRS (R>1 MΩ). However, the cells still show a better retention compared to $Cu_{0.6}Te_{0.4}$, because no continuous increasing trend is observed, and the 50 % of the cells that stay in the LRS do not show a large increase in resistance.

The slightly lower LRS retention compared to Ge is interpreted as follows. Similar to Ge, the Si might form bonds with Te, which in turn will lower the tendency for Cu-Te formation and hence a lower driving force for Cu to go back to the supply layer is expected. This in turn should improve filament stability. Based on the bond enthalpies (see table 2.2) and as was also observed from XPS, the Si-Si bond is strong, and might be preferred over Si-Te. This in turn can result in a higher tendency of the Te to bond with Cu, and in this way result in lower filament stability compared to the cells with Ge.

Finally, it can be noted again that a fraction of the cells in the HRS (about 25 %) return to a LRS. This was also discussed for Ge (see section 5.4.2), and mainly related to the limited control of filament formation in the cycles before programming to the HRS.

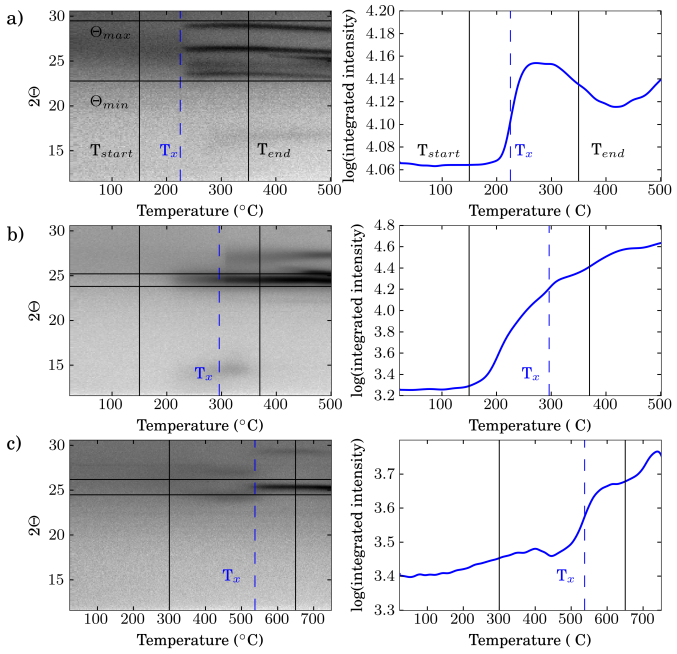

Figure 5.24. *In situ XRD patterns of a (a) CuTeC20, (b) CuTeGe20 and (c) CuTeSi20 layer, collected at a heating rate of 0.5°C/s in He. The graphs at the right show the integrated intensity in the [θ_{min},θ_{max}] region as a function of the temperature. The crystallization temperature T_x is determined as the temperature where the maximum increase in integrated intensity occurs in the temperature range [T_{start}, T_{end}].*

5.6 Kissinger analysis

The higher stability of the amorphous phase for Si-alloyed $Cu_{0.6}Te_{0.4}$ was quantified and compared to Ge and C as alloying elements by means of Kissinger analysis [42]. The crystallization of a phase involves nucleation and growth. Many models for extracting kinetic parameters of the crystallization process have been proposed, and the Kissinger method is one of them. The method requires the knowledge of the temperature at which an equivalent stage of reaction occurs for different heating rates. The method assumes a maximum reaction rate at the peak temperature T_p of crystallization. This also assumes the same degree of conversion at this stage. In this work, *in situ* XRD is used to determine the crystallization temperature T_x of the alloy. The crystallization of the material is defined here as the temperature with the maximum change in intensity of a diffraction peak that appears of the phase that crystallizes first. Hence T_x is used as T_p in the analysis. The activation

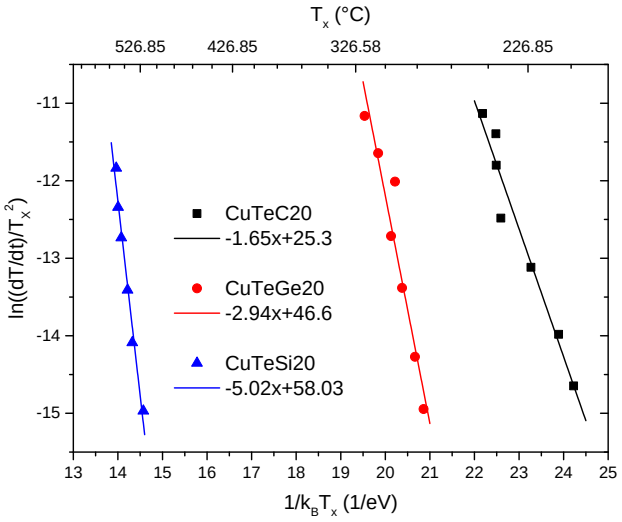

Figure 5.25. *Kissinger analysis of 50 nm thin CuTeC20, CuTeGe20 and CuTeSi20 layers. The samples are annealed at heating rates from 0.1 to 5°C/s under He atmosphere.*

energy E_A can then be found from the relation

$$\ln\left[\left(\frac{\mathrm{d}T}{\mathrm{d}t}\right)\frac{1}{T_x^2}\right] = -\frac{E_A}{k_B T_x} + C, \tag{5.1}$$

where $\mathrm{d}T/\mathrm{d}t$ is the heating rate, k_B the Boltzmann constant and C a constant. For the three alloying elements (C, Ge and Si), the $Cu_{0.6}Te_{0.4}$ layers with 20 at% of the alloying element are annealed at heating rates from 0.1 up to $5°C/s$ in He, and the crystallization is monitored by means of *in situ* XRD, from which T_x is determined. This is illustrated in Figure 5.24, for the three materials. Plotting $\ln((\mathrm{d}T/\mathrm{d}t)/T_x^2)$ as a function of $1/k_B T_x$ gives a straight line with slope E_A. This is shown in Figure 5.25, together with the extracted value for E_A.

A value for E_A of 1.65 eV for carbon and 2.94 eV for germanium is extracted, while the activation energy of CuTeSi20 is far higher and about 5 eV. Hence the Kissinger analysis is in agreement with the bond strength of the alloying element to the other elements. For carbon, which mainly binds to other carbon atoms and not to Cu or Te, the lowest E_A is found. Germanium, which also binds to Cu and forms strong bonds with Te, has a higher E_A. Silicon forms the strongest bonds to Cu , Te and also with other Si atoms, and has the highest E_A.

5.7 Conclusion

The influence of carbon, germanium and silicon as an alloying element in $Cu_{0.6}Te_{0.4}$ has been investigated. The crystallization behaviour of the films and the functionality of the alloys as a cation supply layer was presented. The alloying elements have the ability to create an amorphous as-deposited layer and to inhibit crystallization of Cu-Te phases. Upon crystallization however, phase separation occurs, which might lead to fluctuations in device parameters when this would happen in the cation supply layer of CBRAM cells. Addition of 20 at% Si keeps the material amorphous up to temperatures exceeding $500°C$, making it compatible with typical BEOL temperatures. For C and Ge, crystallization occurs below $400°C$. For Ge, the single phase composition Cu_2GeTe_3 is in that case the best material because upon crystallization, a single phase with homogeneous composition is formed, with a melting temperature above $400°C$.

The investigated supply layers show functional CBRAM, and the alloys show improved LRS retention compared to $Cu_{0.6}Te_{0.4}$. In case of carbon alloying, this is believed to be related to the low solubility of carbon in Cu, Te or Cu-Te, and the absence of bonds with Cu and Te. It hence has the lowest tendency to react with Cu and to get Cu from the filament back to the supply layer. The high resistive state showed even a degradation to low resistances, which can also be related to the low driving force to keep Cu in the cation supply layer. Si and Ge on the other hand do form bonds with Cu, resulting in a better HRS retention and a higher tendency to keep Cu in the supply layer. This results in an acceptable HRS retention, approaching that of $Cu_{0.6}Te_{0.4}$. The LRS retention is better compared to $Cu_{0.6}Te_{0.4}$, which we relate to the formation of Ge-Te or Si-Te bonds. This lowers the tendency of Te to form bonds with Cu, resulting in a lower driving force for the Cu to go back to the supply layer and improving filament stability.

The best results in terms of material stability, CBRAM functionality and retention of the memory states are obtained for Cu_2GeTe_3. It is a stable material up to temperatures above $400°C$, and the retention of the CBRAM cells show a median resistive window of more than 3 orders of magnitude after more than 5 days baking at $85°C$.

References

[1] C. Lavoie, C. Detavernier, C. C. Jr., F. dHeurle, A. Kellock, J. Jordan-Sweet, and J. Harper, *Microelectron. Eng.* **83**(11-12), 2042 – 2054 (2006), Materials for Advanced Metallization (MAM 2006).

[2] D. Deduytsche, C. Detavernier, R. L. Van Meirhaeghe, J. L. Jordan-Sweet, and C. Lavoie, *J. Appl. Phys.* **101**(4), 044508 (2007).

[3] H. Mehrer, *Diffusion in Solids*, Springer, (2007).

[4] K. Barmak, C. Cabral, K. P. Rodbell, and J. M. E. Harper, *J. Vac. Sci. Technol., B* **24**(6), 2485–2498 (2006).

[5] B. Li, C. Christiansen, D. Badami, and C.-C. Yang, *Microelectron. Reliab.* **54**(4), 712 – 724 (2014).

[6] M. Lin and A. Oates, *Device and Materials Reliability, IEEE Transactions on* **13**(1), 330–332 (2013).

[7] M. Lankhorst, *J. Non-Cryst. Solids* **297**(2-3), 210 – 219 (2002).

[8] C.-M. Lee, Y.-I. Lin, and T.-S. Chin, *J. Mater. Res.* **19**, 2929–2937 (2004).

[9] B. J. Kooi and J. T. M. De Hosson, *J. Appl. Phys.* **95**(9), 4714–4721 (2004).

[10] J. Yu, B. Liu, T. Zhang, Z. Song, S. Feng, and B. Chen, *Appl. Surf. Sci.* **253**(14), 6125 – 6129 (2007).

[11] S.-J. Park, I.-S. Kim, S.-K. Kim, S.-M. Yoon, B.-G. Yu, and S.-Y. Choi, *Semicond. Sci. Technol.* **23**(10), 105006 (2008).

[12] G. B. Beneventi, L. Perniola, V. Sousa, E. Gourvest, S. Maitrejean, J. Bastien, A. Bastard, B. Hyot, A. Fargeix, C. Jahan, J. Nodin, A. Persico, A. Fantini, D. Blachier, A. Toffoli, S. Loubriat, A. Roule, S. Lhostis, H. Feldis, G. Reimbold, T. Billon, B. D. Salvo, L. Larcher, P. Pavan, D. Bensahel, P. Mazoyer, R. Annunziata, P. Zuliani, and F. Boulanger, *Solid-State Electron.* **65-66**, 197 – 204 (2011), Selected Papers from the ESSDERC 2010 Conference.

[13] Y. Lu, S. Song, Z. Song, F. Rao, L. Wu, M. Zhu, B. Liu, and D. Yao, *Appl. Phys. Lett.* **100**(19), 193114 (2012).

[14] Y. Lai, B. Qiao, J. Feng, Y. Ling, L. Lai, Y. Lin, T. Tang, B. Cai, and B. Chen, *J. Electron. Mater.* **34**(2), 176–181 (2005).

[15] Y. Saito, Y. Sutou, and J. Koike, *J. Phys. D: Appl. Phys.* **45**(40), 405302 (2012).

[16] L. Goux, K. Opsomer, R. Degraeve, R. Muller, C. Detavernier, D. J. Wouters, M. Jurczak, L. Altimime, and J. A. Kittl, *Appl. Phys. Lett.* **99**(5), 053502 (2011).

[17] H. Radhakrishnan, In *15th IEEE Mediterranean Electrotechnical Conference*, 515–520, (2010).

[18] K. Aratani, K. Ohba, T. Mizuguchi, S. Yasuda, T. Shiimoto, T. Tsushima, T. Sone, K. Endo, A. Kouchiyama, S. Sasaki, A. Maesaka, N. Yamada, and H. Narisawa, *Int. Electron Devices Meet.* , 783 –786 (2007).

[19] M. Tada, T. Sakamoto, N. Banno, K. Okamoto, N. Iguchi, H. Hada, and M. Miyamura, *IEEE Trans. Electron Devices* **60**(10), 3534–3540 (2013).

[20] J. Jameson, P. Blanchard, C. Cheng, J. Dinh, A. Gallo, V. Gopalakrishnan, C. Gopalan, B. Guichet, S. Hsu, D. Kamalanathan, D. Kim, F. Koushan, M. Kwan, K. Law, D. Lewis, Y. Ma, V. McCaffrey, S. Park, S. Puthenthermadam, E. Runnion, J. Sanchez, J. Shields, K. Tsai, A. Tysdal, D. Wang, R. Williams, M. Kozicki, J. Wang, V. Gopinath, S. Hollmer, and M. Van Buskirk, In *2013 IEEE Int. Electron Devices Meet. (IEDM)*, 30.1.1–30.1.4, (2013).

[21] J. Guy, G. Molas, E. Vianello, C. Carabasse, P. Blaise, M. Bernard, E. Souchier, P. Francois, F. Aussenac, V. Delaye, F. Clermidy, and B. D. Salvo, *Thin Solid Films* **563**, 15 – 19 (2014), European Materials Research Society (E-MRS) Spring Meeting 2013 Symposium H: Multifunctional Binary and Complex Oxide Films and Nanostructures for Microelectronic Applications.

[22] J. Guy, G. Molas, E. Vianello, F. Longnos, S. Blanc, C. Carabasse, M. Bernard, J. Nodin, A. Toffoli, J. Cluzel, P. Blaise, P. Dorion, O. Cueto, H. Grampeix, E. Souchier, T. Cabout, P. Brianceau, V. Balan, A. Roule, S. Maitrejean, L. Perniola, and B. De Salvo, In *2013 IEEE Int. Electron Devices Meet. (IEDM)*, 30.2.1–30.2.4, (2013).

[23] U. Celano, L. Goux, A. Belmonte, K. Opsomer, A. Franquet, A. Schulze, C. Detavernier, O. Richard, H. Bender, M. Jurczak, and W. Vandervorst, *Nano Letters* **14**(5), 2401–2406 (2014).

[24] X. Xu, H. Lv, H. Liu, Q. Luo, T. Gong, M. Wang, G. Wang, M. Zhang, Y. Li, Q. Liu, S. Long, and M. Liu, *Nanoscale Res. Lett.* **10**(1), 61 (2015).

[25] ASM International, The Materials Information Society, *Binary Alloy Phase Diagrams (Second Edition Plus Updates)*, (1990).

[26] G. Beneventi, E. Gourvest, A. Fantini, L. Perniola, V. Sousa, S. Maitrejean, J. Bastien, A. Bastard, A. Fargeix, B. Hyot, C. Jahan, J. Nodin, A. Persico, D. Blachier, A. Toffoli, S. Loubriat, A. Roule, S. Lhostis, H. Feldis, G. Reimbold, T. Billon, B. De Salvo, L. Larcher, P. Pavan, D. Bensahel, P. Mazoyer, R. Annunziata, and F. Boulanger, In *2010 IEEE International Memory Workshop (IMW)*, 1–4, (2010).

[27] G. E. Ghezzi, J. Y. Raty, S. Maitrejean, A. Roule, E. Elkaim, and F. Hippert, *Appl. Phys. Lett.* **99**(15), 151906 (2011).

[28] International Centre for Diffraction Data, Newtown Square, PA, *JCPDS Data Card no. 00-049-1411*, (2004).

[29] W. Wang, Q. Wei, and H. Bai, *Appl. Phys. Lett.* **71**(1), 58–60 (1997).

[30] W. Wang and H. Bai, *J. Appl. Phys.* **84**(11), 5961–5968 (1998).

[31] M. Pyun, H. Choi, J.-B. Park, D. Lee, M. Hasan, R. Dong, S.-J. Jung, J. Lee, D.-j. Seong, J. Yoon, and H. Hwang, *Appl. Phys. Lett.* **93**(21), 212907 (2008).

[32] J. F. Moulder, W. F. Stickle, P. E. Sobol, and K. D. Bomben, *Handbook*

of X-ray Photoelectron Spectroscopy, Perkin-Elmer Corporation, Physical Electronics Division, (1992).

[33] J. Wang, S. Jin, C. Leinenbach, and A. Jacot, *J. Alloys Compd.* **504**(1), 159 – 165 (2010).

[34] A. Schlieper, Y. Feutelais, S. Fries, B. Legendre, and R. Blachnik, *Calphad* **23**(1), 1 – 18 (1999).

[35] International Centre for Diffraction Data, Newtown Square, PA, *JCPDS Data Card no. 01-089-2880*, (2004).

[36] G. E. Delgado, A. J. Mora, M. Pirela, A. Velasquez-Velasquez, M. Villarreal, and B. J. Fernandez, *Phys. Status Solidi A* **201**(13), 2900–2904 (2004).

[37] Springer & Material Phases Data System (MPDS), Switzerland & National Institute for Materials Science (NIMS), Japan, 2014, `http://materials.springer.com/isp/phase-diagram/docs/c_0926573`, *LINUS PAULING FILE Multinaires Edition - 2012 Dataset ID c_0926573*.

[38] International Centre for Diffraction Data, Newtown Square, PA, *JCPDS Data Card no. 00-045-1288*, (2004).

[39] C. Wagner, W. Riggs, L. Davis, and J. Moulder, *Handbook of X-ray Photoelectron Spectroscopy*, Perkin-Elmer Corporation, Physical Electronics Division, (1979).

[40] International Centre for Diffraction Data, Newtown Square, PA, *JCPDS Data Card no. 03-065-5591*, (2004).

[41] Springer & Material Phases Data System (MPDS), Switzerland & National Institute for Materials Science (NIMS), Japan, 2014, `http://materials.springer.com/isp/phase-diagram/docs/c_0927205`, *LINUS PAULING FILE Multinaires Edition - 2012 Dataset ID c_0927205*.

[42] Y. Mastai, editor, *Advances in Crystallization Processes*, Intech, (2012).

Paper II

Influence of carbon alloying on the thermal stability and resistive switching behavior of copper-telluride based CBRAM cells*

Abstract

We report the improved thermal stability of carbon alloyed $Cu_{0.6}Te_{0.4}$ for resistive memory applications. Copper-tellurium-based memory cells show enhanced switching behavior, but the complex sequence of phase transformations upon annealing is disadvantageous for integration in a device. We show that addition of about 40 at% carbon to the Cu-telluride layer results in an amorphous material up to 360°. This material was then integrated in a TiN/$Cu_{0.6}Te_{0.4}$-C/Al_2O_3/n^+ Si resistive memory cell, and compared to pure $Cu_{0.6}Te_{0.4}$. Very attractive endurance (up to 1×10^3 cycles) and retention properties (up to 1×10^4 s at $85°C$) are observed. The enhanced thermal stability and good switching behavior make this material a promising candidate for integration in memory devices.

*Published as: W. Devulder, K. Opsomer, F. Seidel, A. Belmonte, R. Muller, B. De Schutter, H. Bender, W. Vandervorst, S. Van Elshocht, M. Jurczak, L. Goux, C. Detavernier, *ACS Appl. Mater. Interfaces*, 5, 6984-6989, 2013

A. Introduction

The increasing demand for smaller, faster and less power consuming memories has driven research for new types of memories. Among the emerging technologies, resistive random access memory (RRAM) seems very promising, combining low power and fast operation with good scalability[1]. One type of RRAM is conductive bridge RAM (CBRAM). Such a memory cell consists of a Cu or Ag containing electrode which acts as a cation source, an insulating layer that serves as electrolyte for metal cation drift and an inert electrode. Applying a positive electrical potential on the active electrode induces cation drift through the insulating layer[1,2]. A conductive filament is grown and the cell switches to a low resistive state (LRS) when the filament bridges the two electrodes. By applying a negative potential, the cations drift back to the supply layer and the cell returns to a high resistive state (HRS). For the electrolyte layer, chalcogenide materials like Ag_2S[3], Cu_2S[4], GeSe[5], GeS[6] and organic materials[7] have been used. Recently, binary metal oxides like HfO_2[8], Ta_2O_5[2], ZrO_2[9], SiO_2[10,11] and Al_2O_3[12] were introduced and are very promising because of their high compatibility with the fabrication of complementary metal oxide semiconductor (CMOS) devices. Next to pure Cu or Ag as active electrode, alloys containing Cu have been reported[13,14]. Very good memory properties have been demonstrated for the Cu-Te alloy[14], moreover a strong influence of the Cu-Te composition on the switching properties of a Pt/Cu_xTe_{1-x}/Al_2O_3/Si memory cell was shown, with enhanced switching behavior in the range $0.5 < x < 0.7$[12] (henceforth referred to as $Cu_{0.6}Te_{0.4}$). However, the thermal stability of $Cu_{0.6}Te_{0.4}$ turns out to be limited, showing multiple phase transitions upon annealing[15]. For integration in a device, a material that is stable up to $400°C$ is necessary. In this work we use carbon as an alloying element to stabilize the $Cu_{0.6}Te_{0.4}$ source layer. Carbon is chosen because it does not form a carbide phase with Cu or Te, and hence will not introduce new phases next to the copper telluride phases. We show that the alloying element inhibits the phase formation up to $360°C$, creating a large thermal window where no transformation of the material occurs. The material is then used as a Cu-supply layer in a CBRAM cell, showing good switching behavior as deposited and after annealing for 5 min at $200°C$. The improved thermal stability and good switching behavior make this material a promising candidate for integration in memory devices.

B. Experimental Section

The mixed Cu-Te-C layer is deposited by DC-magnetron sputtering, using a commercial Balzers BAS 450 deposition tool. Materials properties were investigated on n-doped Si(100) substrates, covered with a 20 nm thin Al_2O_3 layer, deposited by an H_2O-based atomic layer deposition (ALD) technique. The substrates are

mounted on a rotating carousel in the deposition chamber with a base pressure of 5×10^{-7} mbar. The layer is then deposited by co-sputtering from three different sputter targets. The substrates on the rotating carousel pass subsequently in front of each sputter target, resulting in a closely intermixed Cu-Te-C layer. The composition of the layer was determined by energy-dispersive X-ray spectroscopy (EDX), using a FEI Quanta 200F FEG scanning electron microscope (SEM) equipped with an Edax Genesis 4000 EDX detector. Additionally, X-ray fluorescence spectroscopy (XRF) was used to verify the Cu and Te content (carbon cannot be detected with XRF). The composition could be determined after calibrating both systems using a reference sample that was characterized by Rutherford backscattering spectroscopy (RBS) and elastic recoil detection (ERD) for the Cu/Te and Cu/C ratio respectively. X-ray photoelectron spectroscopy (XPS) was used both for investigation of the chemical bonds between Cu, Te and C and for composition determination. These are carried out on a S-Probe monochromatized XPS spectrometer of Surface Science Instruments (VG), using monochromatic Al K_α radiation (1486.6 eV) under a base pressure of 1×10^{-9} mbar. The photoelectron emission direction and the plane of the sample is kept constant at 45°. Depth profiling and hence information about the bulk of the material was obtained by abrasion of the surface by Ar^+ sputtering. Charging of the sample was eliminated using an electron flood gun.

Table 1 summarizes the results of the composition determination using these techniques. A Cu/Te ratio of 1.5 was pursued, as this ratio showed enhanced switching behavior[12], whereas the carbon content was aimed to be about 40 at%. A nearly perfect 1.5 ratio of copper and tellurium is obtained, and the carbon content is close to 40 at%. Henceforth this composition will be referred to as $Cu_{0.6}Te_{0.4}$-C.

Table 1. *Composition of the 50 nm Cu-Te-C mixed layer determined by EDX, XPS and XRF.*

	C (at%)	Cu (at%)	Te (at%)
EDX	36.3	39.3	24.4
XPS	34.1	42.5	23.4
XRF	/	60.96	39.04

The stability of the material against phase transformations is investigated by means of *in situ* X-ray Diffraction (XRD). A material which is stable and does not transform under annealing is favourable to survive the thermal budget it receives in the process flow of device manufacturing. *In situ* XRD allows us to characterize the phase formation as function of temperature and hence gives us information about the thermal stability. A home-built setup consisting of a heating chamber

mounted in a Bruker D8 Discover XRD system is used. The samples are subjected to a constant heating rate of $0.5°C/s$ under an inert He atmosphere while a diffraction pattern was recorded every 4 s over a fixed 2θ window.

To study the microstructure of the material, the samples are investigated by high-resolution transmission electron microscopy (HR-TEM), using a FEI Technai F30 ST microscope. The TEM specimen were prepared with a FEI Dual Beam FIB/SEM STRATA 400, using the in-situ lift-out technique, and milled electron transparent with a 30 keV Ga^+ ion beam. A spin on carbon (SOC) and Pt layer were deposited prior to the lift-out, to protect the surface from Ga^+ beam damage.

Next to the material properties, the functionality of the stabilized $Cu_{0.6}Te_{0.4}$-C layer as a Cu-supply layer in CBRAM is investigated. The $Cu_{0.6}Te_{0.4}$-C is integrated in a 580 µm diameter CBRAM cell and the resistive switching behavior is compared to a memory cell with pure $Cu_{0.6}Te_{0.4}$. The cells are prepared by subsequently magnetron sputtering of 50 nm $Cu_{0.6}Te_{0.4}$(-C) and 50 nm TiN through a dot shadow mask on a Si substrate covered with 3 nm thin Al_2O_3. The memory cells are characterized using a Keithley 2601A sourcemeter, operating in linear voltage sweep mode, with a constant sweep rate of $0.33\,V/s$. The cells are switched to a LRS and HRS by applying a double linear voltage sweep from respectively 0 V to +3 V (and back) and 0 V to -3 V (and back). During the set operation, the current is limited to 100 µA (compliance current I_c) to protect the cell from breakdown.

C. Results and Discussion

Thermal stability

Figure 1a compares the XRD patterns of the pure and carbon alloyed as-deposited $Cu_{0.6}Te_{0.4}$(-C) layer. The (003) and (006) peaks of hexagonal $Cu_{2-x}Te$[16] at 12.28° and 24.72°, respectively, are clearly visible for pure $Cu_{0.6}Te_{0.4}$. In contrast, no diffraction peaks are observed for the $Cu_{0.6}Te_{0.4}$-C, suggesting it is in an amorphous state. The amorphous nature of the $Cu_{0.6}Te_{0.4}$-C is also confirmed by TEM. Figure 1b shows the HR-TEM images of both layers. Although for the pure $Cu_{0.6}Te_{0.4}$ the presence of Moiré fringes confirms the polycrystalline nature of the film, the C-alloyed layer instead evidently misses these Moiré fringes and therefore is amorphous or very small grained. HR-TEM reveals the presence of some small nanocrystals, which cannot be detected by XRD. From these results, it is clear that already during deposition the carbon atoms suppress the formation of a polycrystalline Cu-Te layer.

Figure 2 shows the XPS spectra of the C 1s, Cu $2p_{3/2}$ and Te $3d_{5/2}$ regions of both samples. The peaks for bulk C, Cu and Te, measured from a reference sample fabricated by magnetron sputtering of the pure elements on 100 nm SiO_2,

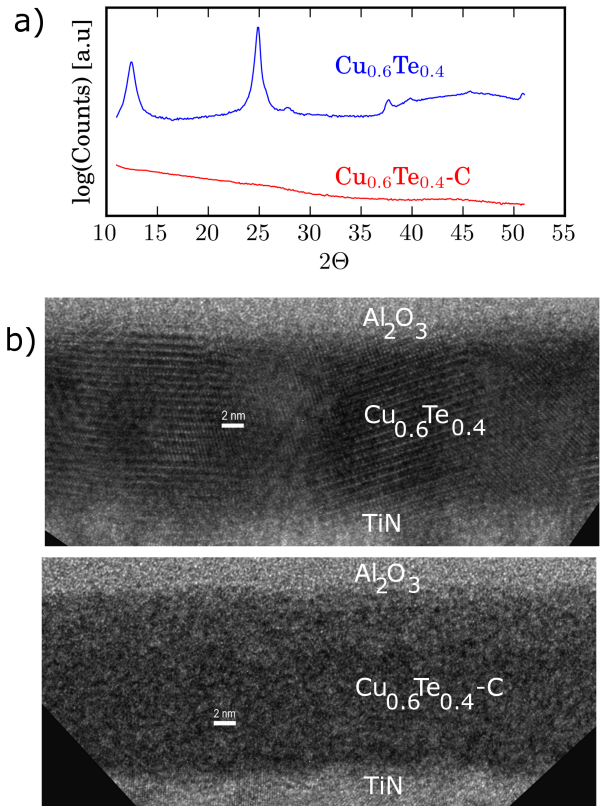

Figure 1. *(a) XRD pattern of a $Cu_{0.6}Te_{0.4}/Al_2O_3$ and $Cu_{0.6}Te_{0.4}$-C/Al_2O_3 (50 nm/20 nm) sample. (b) HR-TEM image of a pure and a carbon alloyed TiN/$Cu_{0.6}Te_{0.4}$(-C)/Al_2O_3 (40/15/4 nm) sample, showing the $Cu_{0.6}Te_{0.4}$(-C) layer.*

are also shown. All spectra are calibrated to the C 1s transition at 284.6 eV of the hydrocarbon from contamination on the sample surface. The maximum of the carbon 1s peak of bulk carbon is situated at 284.4 eV whereas the carbon peak for the $Cu_{0.6}Te_{0.4}$-C sample is slightly shifted over 0.25 eV toward lower energies. However, with a maximum at 284.15 eV, this is still in the reported range for C-C bonds[17–19]. This suggests that the carbon is mainly bonded with other carbon atoms. This was to be expected as no carbides are formed with Cu and Te. The pure Cu $2p_{3/2}$ and Te $3d_{5/2}$ peaks are located at respectively 932.25 eV and 572.9 eV. For pure $Cu_{0.6}Te_{0.4}$, hexagonal $Cu_{2-x}Te$ is observed by XRD (see Figure 1a) and reveals the presence of Cu-Te bonds. In the XPS spectra, this is visible as a shift of the Cu $2p_{3/2}$ peak toward higher energy (932.6 eV, Cu is oxidized) and

a shift of the Te $3d_{5/2}$ toward lower energy (572.5 eV, Te is reduced). The shifts are rather small, as reported in literature for tellurides[20–22]. For $Cu_{0.6}Te_{0.4}$-C, the peaks are also shifted with respect to the pure Cu and Te (932.7 eV for Cu $2p_{3/2}$ and 572.65 eV for Te $3d_{5/2}$), and small differences with $Cu_{0.6}Te_{0.4}$ are observed. It is very difficult to unambiguously analyse the difference between $Cu_{0.6}Te_{0.4}$-C and $Cu_{0.6}Te_{0.4}$, but the slightly shifted Cu peak might be related to a mix of Cu(I) and Cu(II) oxidation states in $Cu_{0.6}Te_{0.4}$-C, while merely Cu(I) is expected in $Cu_{0.6}Te_{0.4}$ due to the $Cu_{2-x}Te$ phase[20]. The small difference in binding energy for the Te peak might indicate the presence of more pure Te in $Cu_{0.6}Te_{0.4}$-C. However, the shifts indicate that also for $Cu_{0.6}Te_{0.4}$-C the copper is oxidized by the presence of Te, suggesting bonds between Cu and Te atoms.

Both samples are investigated with *in situ* XRD to study the phase stability upon annealing. Figure 3a shows the *in situ* XRD pattern of a $Cu_{0.6}Te_{0.4}/Al_2O_3$/Si stack, exhibiting multiple phase transitions. As deposited, hexagonal $Cu_{2-x}Te$[16] is present. At 120°C orthorhombic CuTe[23] is also formed. Both phases react and form tetragonal $Cu_{3-x}Te_2$[24] at 180°C, but some CuTe is still present up to 350°C. Finally, cubic $Cu_{2-x}Te$[25] is formed for $T > 400°C$. These subsequent transformations are in agreement with the phase diagram[26]. The *in situ* XRD plot of the $Cu_{0.6}Te_{0.4}$-C layer (Figure 3b) clearly shows the absence of any diffraction peaks up to 360°C, suggesting an amorphous layer up to this temperature, and hence a large temperature window where no transformation of the material occurs. The integrated XRD-intensity in the 11°-31° 2θ window (see Figure S1 in the Supporting Information) starts to increase from 270°C on, and reaches a local maximum at 360°C, where distinct diffraction peaks appear. We define this temperature as the crystallization temperature of the $Cu_{0.6}Te_{0.4}$-C layer. The diffraction peaks are identified as orthorhombic $Cu_{3-x}Te_2$[27] and CuTe[23], and cubic $Cu_{2-x}Te$[25]. The (111) and (010) peaks of graphite[28] coincide with the (052) and (154) peaks of $Cu_{3-x}Te_2$ at $\sim$ 26.6° and $\sim$43.5°, respectively. However, the disappearance of these peaks above 580°C together with the other peaks of $Cu_{3-x}Te_2$ suggest no contribution of graphite. After crystallization of the Cu-telluride phases, the carbon is most likely at the grain boundaries of the copper-tellurium crystals. We believe that the inhibited phase formation is mainly related to kinetic aspects and the microstructure of the material. The combination of rather large elements like Cu and Te with a small element like C increases the packing density in the amorphous solid, which makes interdiffusion difficult. This impedes the rearrangement in a crystalline structure and hence inhibits the crystallization[29]. The increased thermal stability of amorphous alloys due to addition of small atoms like Be and C has been reported before[30,31], showing an increased crystallization temperature after glass transition. Moreover, differential scanning calorimetry (DSC) of carbon doped $Zr_{41}Ti_{14}Cu_{12.5}Ni_9Be_{22.5}C_1$ showed a decrease in crystallization enthalpy, meaning that the formation of crystal phases becomes also thermodynamically less

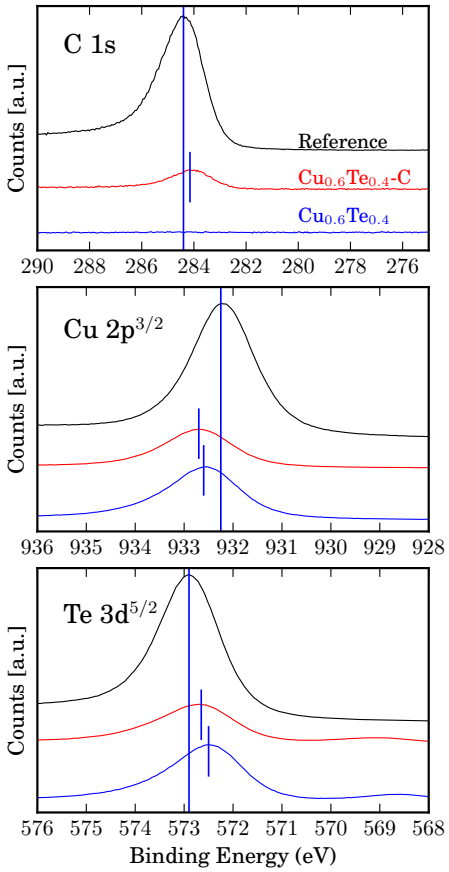

Figure 2. *XPS measurement showing the C 1s, Cu $2p_{3/2}$ and Te $3d_{5/2}$ peaks. In each graph, the reference peak of pure C, Cu or Te is given and the measured peak of both the $Cu_{0.6}Te_{0.4}$-C and $Cu_{0.6}Te_{0.4}$ sample.*

favorable compared to the undoped material.

Figure 4a shows the XRD pattern of both the pure and the C-alloyed $Cu_{0.6}Te_{0.4}$(-C)/Al_2O_3 stack after 5 min anneal at 300°C, confirming the results of the *in situ* XRD measurements. The increased integrated intensity above 270°C in the *in situ* XRD pattern and the somewhat broad maximum around 25° in Figure 4a suggest the presence of nanocrystals at higher temperatures. This is reasonable as with TEM nanocrystals could be observed even in the as-deposited layer. A 50 nm TiN capping layer is further added to preserve a good surface morphology, and at the same time can serve as top electrode in a memory device. SEM analysis (Fig-

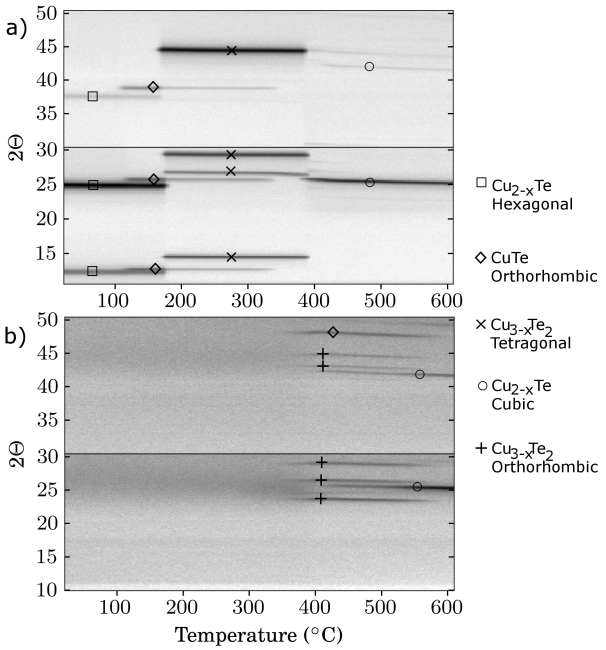

Figure 3. *In situ XRD pattern, measured at a constant heating rate of 0.5°C/s, of a $Cu_{0.6}Te_{0.4}$(-C)/Al_2O_3 (50 nm/20 nm) stack (a) without carbon and with (b) 40 at% carbon.*

ure 4b) shows a very smooth surface morphology up to 400°C. To conclude this section, the large temperature window without phase transformations combined with a good surface morphology up to 400°C show the improved thermal stability of the TiN capped $Cu_{0.6}Te_{0.4}$-C layer compared to pure $Cu_{0.6}Te_{0.4}$, rendering his material attractive for integration in memory devices.

Integration in a CBRAM Device

The functionality of the stabilized $Cu_{0.6}Te_{0.4}$-C as Cu-supply layer in a CBRAM cell is investigated and compared to CBRAM cells with pure $Cu_{0.6}Te_{0.4}$. The 580 µm diameter dot CBRAM cells are cycled 20 times, from which the set voltage and the resistance of the LRS and HRS state is determined. Figure 5 shows the first and 20th set-reset cycle for both the pure and the C-alloyed $Cu_{0.6}Te_{0.4}$(-C) sample. The first cycle is the forming step, where Cu is driven into the Al_2O_3 layer to form a conductive filament (this in contrast to most chalcogenide systems were Cu or Ag is already present in the resistive switching layer). However, the set voltage of the first cycle and the subsequent cycles are the same, showing no difference between the forming and the subsequent cycles. This indicates an ef-

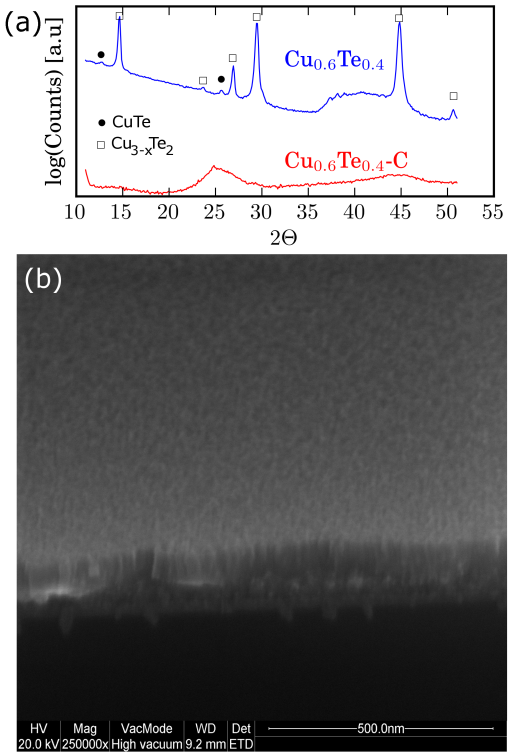

Figure 4. *(a) XRD pattern of a pure and a C-alloyed $Cu_{0.6}Te_{0.4}$(-C)/Al_2O_3/Si stack after a 5 min anneal at 300°C under He-atmosphere. (b) SEM image showing the surface morphology of the C-alloyed stack, capped with a 50 nm TiN layer after annealing for 5 min at 400°C.*

fective erasure of the entire filament after reset. This dependence of the set voltage on the partial or complete erasure of the filament has been pointed out before[32]. It is clear that the C-alloyed cell shows a good switching behavior and is very comparable to pure $Cu_{0.6}Te_{0.4}$. The reset current of both cells is comparable and lower than I_c, which leads to an efficient reset, as was already reported for pure $Cu_{0.6}Te_{0.4}$ [12]. The set voltage (Fig. 6a) of the C-alloyed cell is slightly lower than for pure $Cu_{0.6}Te_{0.4}$. Although the resistivity of the $Cu_{0.6}Te_{0.4}$-C is higher than $Cu_{0.6}Te_{0.4}$ ($9.54 \times 10^{-3}\,\Omega \cdot$cm and $2.99 \times 10^{-4}\,\Omega \cdot$cm respectively), this is still many orders of magnitude lower than Al_2O_3 [33]. As a result, the resistance of the layer will not affect the set voltage because the voltage will always drop over the Al_2O_3. The lower set voltage may be attributed to the amorphous nature of the $Cu_{0.6}Te_{0.4}$-C layer. The amorphous state is a metastable state, and the Cu has a lower binding energy than in a crystal structure. From this point of view a lower

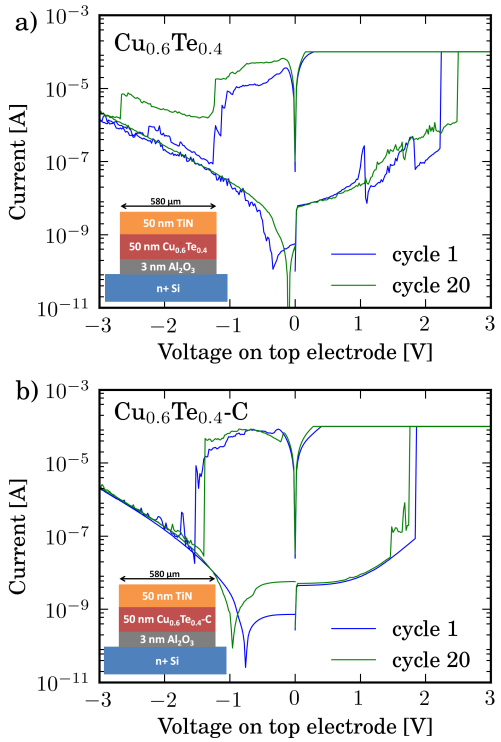

Figure 5. *First and 20th set-reset operation of (a) pure and (b) C-alloyed TiN/$Cu_{0.6}Te_{0.4}$(-C)/Al_2O_3/n^+ Si memory cells.*

potential may already result in the removal of Cu ions from the source layer compared to a crystalline material. However, we do not want to exclude the presence of pure Cu, which has a lower set voltage because of the lower bonding energy of Cu compared to Cu-Te [12]. The pure Cu can be present in nanocrystals which cannot be detected with XRD. Figure 6b shows a boxplot of the resistance of the LRS and HRS of both cells, which turn out to be very comparable.

To be a viable candidate as CBRAM source layer, good endurance and retention properties should be observed. The $Cu_{0.6}Te_{0.4}$-C memory cell was cycled up to 1000 times at room temperature, and after annealing for 5 min at 200°C in He atmosphere (both with $I_c = 100\,\mu A$). Figure 7a shows the cumulative distribution of the HRS and LRS for both the as deposited and annealed device (see Figure S2 in the Supporting Information for the detailed endurance results). Even after annealing, the difference between the LRS and HRS is more than 2 orders of magnitude, although a small shift of the HRS toward lower resistances is observed.

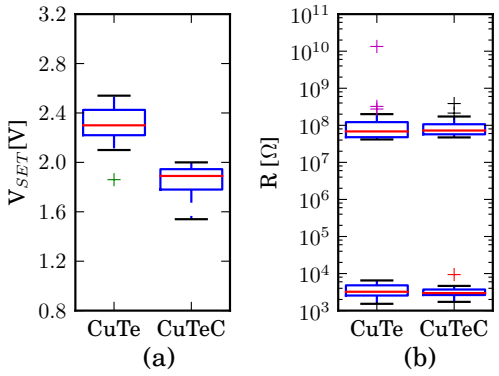

Figure 6. *(a) Set voltage and (b) the resistance of the LRS and HRS of a pure and a C-alloyed TiN/$Cu_{0.6}Te_{0.4}$(-C)/Al_2O_3/n^+ Si memory cell. The data are presented in a boxplot, indicating the first, second (median) and third quartile. The whiskers extend form the box and are maximum 1.5 times the inner quartile length (if any data reaches this value). The crosses are flyer points, falling out of this region.*

This could be related to Cu diffusion into the Al_2O_3 layer. As a suggestion for future work, this might be further improved by adding a titanium diffusion barrier in between the $Cu_{0.6}Te_{0.4}$-C layer and the aluminum oxide[15]. The retention was tested by applying a constant read voltage of 20 mV at an elevated temperature of $85°C$. The LRS and HRS did not change for up to 1×10^4 s (Figure 7b), proving the stability of the states.

D. Conclusions

We showed the ability of carbon to influence the crystallization and stability of copper tellurium. Adding about 40 at% C to a Cu_xTe_{1-x} ($x \sim 0.6$) layer results in an amorphous material up to $360°C$. We attribute this inhibited phase formation to an increased packing density in the amorphous solid, making the rearrangement in a crystalline structure much more difficult. A TiN capping layer on top ensures a good surface morphology up to $400°C$ and serves as a top electrode. A functional memory cell was demonstrated, showing controlled switching and good reliability characteristics.

Acknowledgments

W.D. acknowledges the *Institute for the Promotion of Innovation through Science and Technology in Flanders (IWT-Vlaanderen)* for funding. Nico De Roo and

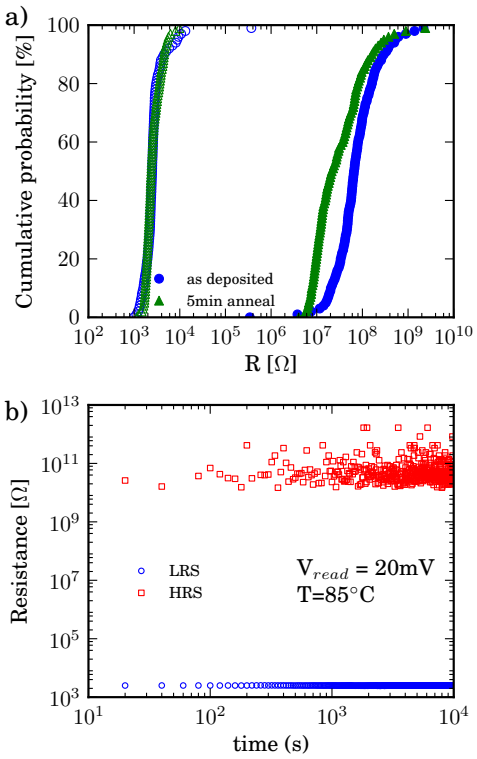

Figure 7. *(a) Cumulative probability of the LRS (open markers) and HRS (filled markers) of the memory cell as deposited and after anneal ($5\,min$ at $200°C$). (b) Retention test at $85°C$ and using a constant read bias of $20\,mV$. The LRS and HRS are not altered for up to 10^4 s.*

Johan Meersschaut are acknowledged for physical characterization support (XPS and RBS/ERD).

References

[1] R. Waser, R. Dittmann, G. Staikov, and K. Szot, *Adv. Mater.* **21**(25-26), 2632–2663 (2009).

[2] T. Tsuruoka, K. Terabe, T. Hasegawa, and M. Aono, *Nanotechnology* **21**(42), 425205 (2010).

[3] K. Terabe, T. Nakayama, T. Hasegawa, and M. Aono, *Appl. Phys. Lett.* **80**(21), 4009–4011 (2002).

[4] T. Sakamoto, H. Sunamura, H. Kawaura, T. Hasegawa, T. Nakayama, and M. Aono, *Appl. Phys. Lett.* **82**(18), 3032–3034 (2003).

[5] M. Kozicki, M. Park, and M. Mitkova, *IEEE Trans. Nanotechnol.* **4**(3), 331–338 (2005).

[6] M. Kund, G. Beitel, C.-U. Pinnow, T. Rohr, J. Schumann, R. Symanczyk, K.-D. Ufert, and G. Muller, *Tech. Dig. - Int. Electron Devices Meet.* , 754–757 (2005).

[7] S. Wu, T. Tsuruoka, K. Terabe, T. Hasegawa, J. P. Hill, K. Ariga, and M. Aono, *Adv. Funct. Mater.* **21**(1), 93–99 (2011).

[8] Y. Wang, H. Lv, W. Wang, Q. Liu, S. Long, Q. Wang, Z. Huo, S. Zhang, Y. Li, Q. Zuo, W. Lian, J. Yang, and M. Liu, *IEEE Electron Device Lett.* **31**(12), 1470–1472 (2010).

[9] Q. Liu, S. Long, W. Wang, Q. Zuo, S. Zhang, J. Chen, and M. Liu, *IEEE Electron Device Lett.* **30**(12), 1335 –1337 (2009).

[10] C. Schindler, M. Weides, M. N. Kozicki, and R. Waser, *Appl. Phys. Lett.* **92**(12), 122910 (2008).

[11] Y. Bernard, V. T. Renard, P. Gonon, and V. Jousseaume, *Microelectron. Eng.* **88**(5), 814–816 (2011).

[12] L. Goux, K. Opsomer, R. Degraeve, R. Muller, C. Detavernier, D. J. Wouters, M. Jurczak, L. Altimime, and J. A. Kittl, *Appl. Phys. Lett.* **99**(5), 053502 (2011).

[13] S. Kim, M. Jo, J. Park, J. Lee, W. Lee, and H. Hwang, *Electrochem. Solid-State Lett.* **14**(8), 322–325 (2011).

[14] K. Aratani, K. Ohba, T. Mizuguchi, S. Yasuda, T. Shiimoto, T. Tsushima, T. Sone, K. Endo, A. Kouchiyama, S. Sasaki, A. Maesaka, N. Yamada, and H. Narisawa, *Int. Electron Devices Meet.* , 783 –786 (2007).

[15] L. Goux, K. Opsomer, A. Franquet, G. Kar, N. Jossart, O. Richard, D. Wouters, R. Muller, C. Detavernier, M. Jurczak, and J. Kittl, *Thin Solid Films* **533**, 29–33 (2013).

[16] International Centre for Diffraction Data, Newtown Square, PA, *JCPDS Data Card no. 00-049-1411*, (2004).

[17] B. P. Swain, *Surf. Coat. Technol.* **201**(3-4), 1589–1593 (2006).

[18] F. Arezzo, N. Zacchetti, and W. Zhu, *J. Appl. Phys.* **75**(10), 5375–5381

(1994).
[19] W.-Y. Lee, *J. Appl. Phys.* **51**(6), 3365–3372 (1980).
[20] M. O. King, I. M. McLeod, D. Hesp, V. R. Dhanak, M. Kadodwala, and D. A. MacLaren, *Surf. Sci.* **606**(17-18), 1353–1359 (2012).
[21] E. Domashevskaya, V. Gorbachev, V. Terekhov, V. Kashkarov, E. Panfilova, and A. Shchukarev, *J. Electron Spectrosc. Relat. Phenom.* **114**, 901–908 (2001).
[22] H. Neumann, M. Mast, J. Enderlein, R. Tomlinson, and M. Yakushev, *Cryst. Res. Technol.* **31**(1), 75–85 (1996).
[23] International Centre for Diffraction Data, Newtown Square, PA, *JCPDS Data Card no. 01-089-4311*, (2004).
[24] International Centre for Diffraction Data, Newtown Square, PA, *JCPDS Data Card no. 01-085-0606*, (2004).
[25] International Centre for Diffraction Data, Newtown Square, PA, *JCPDS Data Card no. 00-045-1286*, (2004).
[26] A. Pashinkin and V. Fedorov, *Inorg. Mater.* **39**(6), 539–554 (2003).
[27] International Centre for Diffraction Data, Newtown Square, PA, *JCPDS Data Card no. 00-026-1117*, (2004).
[28] International Centre for Diffraction Data, Newtown Square, PA, *JCPDS Data Card no. 01-075-2078*, (2004).
[29] T. Zhang, A. Inoue, and T. Masumoto, *Mater. Trans., JIM* **32**(11), 1005–1010 (1991).
[30] W. Wang, Q. Wei, and H. Bai, *Appl. Phys. Lett.* **71**(1), 58–60 (1997).
[31] W. Wang and H. Bai, *J. Appl. Phys.* **84**(11), 5961–5968 (1998).
[32] L. Goux, K. Sankaran, G. Kar, N. Jossart, K. Opsomer, R. Degraeve, G. Pourtois, G. M. Rignanese, C. Detavernier, S. Clima, Y. Y. Chen, A. Fantini, B. Govoreanu, D. Wouters, M. Jurczak, L. Altimime, and J. A. Kittl, *IEEE Symp. VLSI Technol.* , 69–70 (2012).
[33] Y. Yamano, T. Komiyama, M. Takahashi, S. Kobayashi, K. Nitta, and Y. Saito, *Int. Symp. Discharges Electr. Insul. Vac., 23th* , 35–38 (2008).

Supporting Information

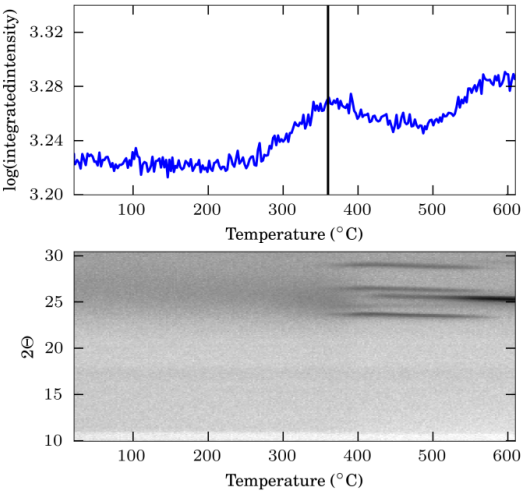

Figure S1. *In situ XRD pattern of the $Cu_{0.6}Te_{0.4}$-C layer in the 11-31° 2θ window (bottom) and the logarithm of the integrated intensity in this window for each temperature (top). From 270°C to 360°C, an increase is observed, reaching a maximum at 360°C where distinct diffraction peaks appear. We define this temperature as the crystallization temperature of the material.*

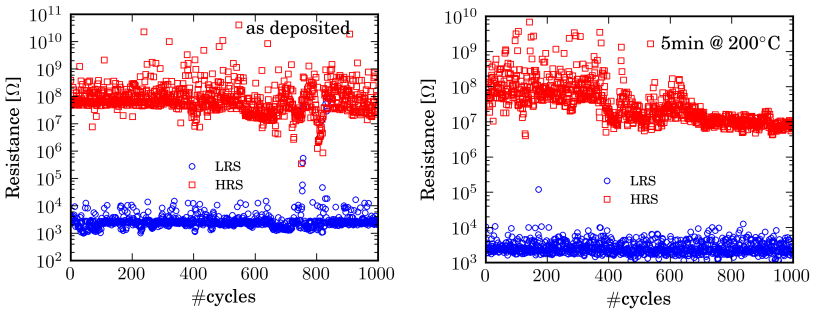

Figure S2. *Endurance results of the as-deposited $Cu_{0.6}Te_{0.4}$-C cells (left) and after 5 min anneal at 200°C (right). The resistance of the LRS and HRS state is plotted as function of the cycle number.*

Paper III

Influence of carbon content on the copper-telluride phase formation and on the resistive switching behavior of carbon alloyed Cu-Te conductive bridge random access memory cells*

Abstract

In this paper we investigate the influence of the carbon content on the Cu-Te phase formation and on the resistive switching behaviour in carbon alloyed $Cu_{0.6}Te_{0.4}$ based CBRAM cells. Carbon alloying of copper-tellurium inhibits the crystallization, while attractive switching behaviour is preserved when using the material as Cu-supply layer in CBRAM cells. The phase formation is first investigated in a combinatorial way. With increasing carbon content, an enlargement of the temperature window in which the material stays amorphous was observed. Moreover, if crystalline phases are formed, subsequent phase transformations are inhibited. The electrical switching behavior of memory cells with different carbon contents is then investigated by implementing them in 580 µm diameter dot TiN/$Cu_{0.6}Te_{0.4}$-C/Al_2O_3/Si memory cells. Reliable switching behaviour is observed for carbon contents up to 40 at%, with a resistive window of more than 2 orders of magnitude whereas for 50 at% carbon, a higher current in the off state and only a small resistive window are present after repeated cycling. This degradation can be ascribed to the higher thermal and lower drift contribution to the reset operation due to a lower Cu affinity towards the supply layer, leading cycle-after-cycle to an increasing amount of Cu in the switching layer, which contributes to the current. The thermal diffusion of Cu into Al_2O_3 under annealing also gives an indication of the Cu affinity of the source layer. Time of flight secondary ion mass spectroscopy

*Published as: W. Devulder, K. Opsomer, A. Franquet, J. Meersschaut, A. Belmonte, R. Muller, B. De Schutter S. Van Elshocht, M. Jurczak, L. Goux, C. Detavernier, *J. Appl. Phys.*, 115, 054501, 2014

was used to investigate this migration depth in Al_2O_3 before and after annealing, showing a higher Cu, Te and C migration for high carbon contents.

A. Introduction

Due to the continuous scaling down of memory devices, new memory concepts are investigated. Conductive bridge random acces memory (CBRAM) seems a promising candidate, combining low power and fast operation with good scalability[1]. A typical CBRAM device consists of a Cu or Ag containing layer (cation supply layer), an insulating electrolyte layer and an inert electrode. The cell can be switched to a low (LRS) or high resistive state (HRS) by respectively growing and dissolving a conductive filament in the electrolyte layer. Applying a positive potential on the cation supply layer induces filament growth through the insulating layer, switching the cell to a LRS when the filament bridges both electrodes, whereas a negative potential dissolves the filament again, switching the cell back to the HRS. For the insulating layer, chalcogenide materials[2–6] or binary metal oxides like HfO_2[7], Ta_2O_5[8], ZrO_2[9], SiO_2[10,11] and Al_2O_3[12] can be used. The latter being very promising due to high compatibility with the fabrication of complementary metal oxide semiconductor (CMOS) devices. Next to pure Cu or Ag as active electrode, alloys containing Cu have been reported[13,14]. Attractive memory properties have been demonstrated for the Cu-Te alloy[14], and a strong influence of the Cu-Te composition on the switching properties of a Pt/Cu_xTe_{1-x}/Al_2O_3/Si memory cell was shown, with enhanced switching behavior in the range $0.5 < x < 0.7$[12] (henceforth referred to as $Cu_{0.6}Te_{0.4}$). However, the thermal stability of $Cu_{0.6}Te_{0.4}$ turns out to be limited, showing multiple phase transitions upon annealing[15]. For integration in a device, a material which is stable up to $400°C$ is necessary.

In previous work[16] we showed that addition of ∼40 at% carbon to a Cu_xTe_{1-x} (x∼0.6) layer inhibited the crystallization of Cu-Te phases up to $360°C$. Carbon was chosen because it does not form a carbide phase with Cu or Te, and will not introduce new phases next to the copper telluride phases. Integrating this material in 580 µm diameter TiN/$Cu_{0.6}Te_{0.4}$-C/Al_2O_3/n^+ Si memory cells, showed attractive CBRAM functionality. This demonstrated the ability of carbon alloying to avoid the restructuring of the source layer. In this paper we investigate the influence of the carbon content on the Cu-Te phase formation in the range of ∼0-45 at% carbon. First a combinatorial study is performed where the influence of the carbon content on the phase formation is investigated. Afterwards, the thermal stability and functionality as CBRAM source layer of a selection of carbon contents in the $Cu_{0.6}Te_{0.4}$ layer (hence referred to as $Cu_{0.6}Te_{0.4}$-C) is further studied.

B. Experimental

A combinatorial screening method was used to investigate the influence of the carbon content on the Cu-Te phase formation. A set of 150 mm Si wafers, covered by 100 nm thermal grown SiO_2 are mounted in a commercial physical vapor de-

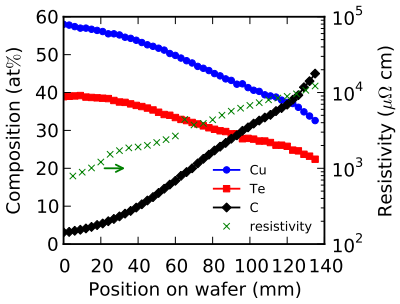

Figure 1. *Composition of the mixed Cu-Te-C layer as a function of the position on the wafer. The Cu/Te ratio is fixed to 1.5 and the carbon content increases from ∼3 to ∼45 at%.*

position tool with a base pressure of 5×10^{-7} mbar. The mixed Cu-Te-C layer is deposited by magnetron co-sputtering of Cu, Te and C from three different sputter targets. Shadow masks in front of the sputter targets allow for a spatial control of the material flux on the substrate, which gives the possibility to deposit a composition gradient along one direction on the wafer. This results in a deposited layer with a constant Cu/Te ratio and a gradient in the carbon content. There is an overall thickness gradient from $\sim$ 66 (carbon poor) to ∼36 nm (carbon rich), in agreement with the calculated thickness based on the deposition flux of each element through its shadow mask. The graded wafers are subjected to X-ray fluorescence spectroscopy (XRF) mapping, i.e. an XRF measurement is taken every 3 mm on the wafer in the composition gradient direction, to verify the Cu/Te ratio. This ratio was kept constant to 1.5, as this ratio showed enhanced switching behavior[12]. The gradient in carbon content on the other hand is calculated based on the deposited thickness of the Cu, Te and C layers, using the elemental densities. The composition of the maximum carbon content was confirmed by Energy dispersive X-ray fluorescence spectroscopy (EDX)[16]. This composition gradient was also confirmed by Rutherford backscattering spectroscopy (RBS) and elastic recoil detection (ERD) to determine the Cu/Te and Cu/C ratio respectively. Figure 1 shows the composition and the resistivity of the mixed Cu-Te-C layer: the Cu/Te ratio is constant and equal to 1.5 and the carbon content increases from $\sim$ 3 to ∼45 at%. The resistivity of the layer increases with increasing carbon content. To investigate the influence of the carbon content on the Cu-Te phase formation, the graded wafers are annealed in a He atmosphere using a ramp anneal ($5°C/$s) towards different temperatures and holding that temperature for 1 minute. The crystallinity of the layer is investigated by X-ray diffraction (XRD). XRD-mapping (i.e. an XRD measurement is taken every 3 mm on the wafer, and hence at different carbon contents) of the wafers after annealing at different temperatures gives an overview of the Cu-Te phases formed as a function of the carbon content and temperature.

A selection of compositions are investigated more in detail by means of *in situ* XRD. Here the samples are heated in an inert He atmosphere at a constant heating rate of $0.5°C/\mathrm{s}$ and an XRD pattern in a fixed 2θ window is taken every 4 s. *In situ* XRD monitors the phase transformations that occur and hence gives information about the thermal stability.

The functionality of the $Cu_{0.6}Te_{0.4}$-C as CBRAM source layer for different carbon contents is investigated by integrating the material in 580 µm diameter TiN/$Cu_{0.6}Te_{0.4}$-C/Al_2O_3/n^+ Si memory cells. These are created by subsequent magnetron sputtering of 50 nm $Cu_{0.6}Te_{0.4}$-C and 50 nm TiN through a dot shadow mask on a n^+ Si substrate that is covered with a 3 nm Al_2O_3 layer. The Al_2O_3 is deposited by a H_2O based atomic layer deposition (ALD) process. The switching behaviour is evaluated using a Keithley 2601A sourcemeter by applying a double linear voltage sweep from 0 to +3 V (and back) and from 0 to -3 V (and back) respectively to set and reset the cells. The cycle speed was kept constant at $0.33\,\mathrm{V/s}$ and the current in the set operation was limited to 100 µA to protect the cell from breakdown.

The thermal diffusion and migration depth of Cu, Te and C from the source layer into the Al_2O_3 under annealing conditions is also investigated and correlated to the electrical data. For this purpose, 10 nm $Cu_{0.6}Te_{0.4}$(-C) was deposited on a 20 nm Al_2O_3/Si substrate and annealed for 30 min at $200°C$ in He atmosphere. Depth profiles of Cu, Te and C in the Al_2O_3 layer were measured with Time of Flight Secondary Ion Mass Spectrometry (ToF-SIMS) using a TOFSIMS IV instrument from ION-TOF GmbH. Both positive and negative ion profiles were measured in a dual beam configuration using a Bi_3^+ (25 keV) gun for analysis and a Xe^+ (500 eV) gun for sputtering.

C. Results and discussion

Combinatorial study

An XRD map is made for the as-deposited wafer and after a one minute anneal at 100, 200, 300 and $350°C$. An XRD θ-2θ measurement was taken every 3 mm along the gradient direction, and hence the XRD patterns could be correlated to the carbon content (see Figure 1). Figure 2 shows the XRD intensities plotted as a gray-scale color map as function of the carbon content for the as-deposited wafer and after annealing at 200 and $350°C$. These maps are constructed for all annealing temperatures and allows us to identify most phases formed at discrete temperatures in the carbon range $\sim$ 3 to $\sim$45 at%. A summary of the identified phases is depicted in Figure 3. Figure 2a shows for carbon contents lower than $\sim$8 at% the presence of the (003) and (006) peaks of hexagonal $Cu_{2-x}Te$[17] at respectively 12.3 and 24.7°. The absence of these peaks for higher C contents il-

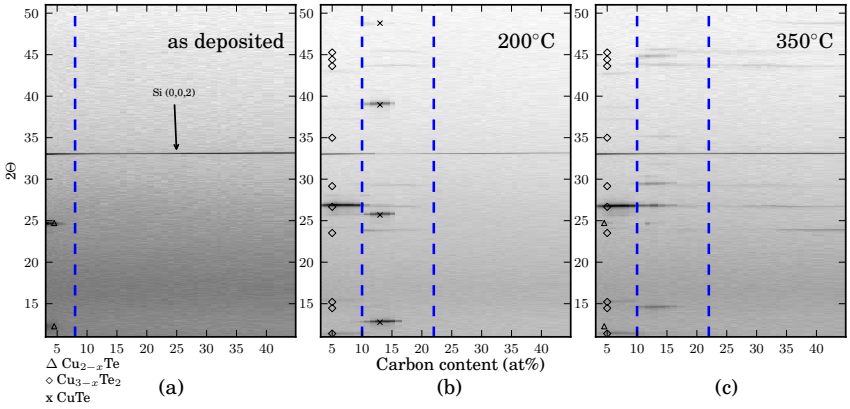

Figure 2. *XRD patterns of the graded $Cu_{0.6}Te_{0.4}$-C layer as a function of the carbon content for (a) the as-deposited wafer and after 1 min anneal at (b) 200 and (c) 300°C. The XRD intensities are plotted as a gray scale. The most prominent peaks of hexagonal $Cu_{2-x}Te$, orthorhombic $Cu_{3-x}Te_2$ and orthorhombic CuTe are indicated.*

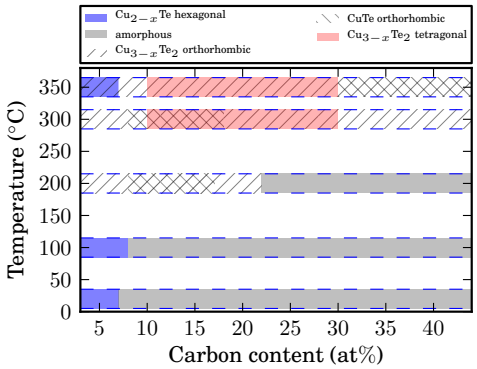

Figure 3. *The observed Cu-Te phases are shown for each annealing temperature as a function of the carbon content. These are determined from the observed XRD peaks in the XRD maps of the graded wafers.*

lustrate how addition of ∼8 at% carbon prevents the formation of polycrystalline Cu-Te phases already during deposition. The stoichiometry of the crystalline phase (2:1) is different from the 3:2 Cu:Te ratio, revealing also (non crystalline) Te rich regions in the as-deposited layer. After annealing at 100°C, no significant difference with the as-deposited sample is observed. At 200°C, compositions with more than ∼20 at% C are still amorphous. In the 0-10 at% C range, orthorhombic $Cu_{3-x}Te_2$ [18] is observed: typical are the (021), (031) and (051) peaks at respectively 11.4, 15.2 and 23.5° (they do not exist for the higher temperature tetragonal

$Cu_{3-x}Te_2$ [19] phase which forms at $\sim$ 172°C [20]). In the 10-20 at% C range, the (021) and (031) peaks are absent, but the (051) peak is detected, suggesting the orthorhombic phase. The (001), (002), (003) and (103) peaks of orthorhombic CuTe [21] are also clearly visible at respectively 12.8, 25.7, 38.9 and 48.8° for 10-17 at% carbon. After annealing at 300°C, no major differences are observed in the range 0-20 at% C, only the (002), (004) and (006) peaks at respectively 14.5, 29.2 and 44.4° of orthorhombic $Cu_{3-x}Te_2$ are more apparent (and also at 350°C in Figure 2c), whereas the (051) peak is fainter. The change in peak intensities suggests some preferred orientation, but can also be related to the tetragonal component of $Cu_{3-x}Te_2$, especially when the peaks that are typical for the orthorhombic phase can hardly be detected. For higher carbon contents, faint diffraction peaks of orthorhombic and/or tetragonal $Cu_{3-x}Te_2$ are now also observed. At 350°C finally, $Cu_{2-x}Te$ is detected again in the range <8 at%. In the 10-17 at% C range, the CuTe signal is no more detectable, and only orthorhombic and/or tetragonal $Cu_{3-x}Te_2$ are observed.

To summarize this section, we obtained a crystalline as-deposited $Cu_{0.6}Te_{0.4}$-C layer for carbon contents <8 at%. In the range ∼8-17 at%, the layer is amorphous as deposited, but subsequent transformations occur under annealing. For higher C contents (>17 at%), diffraction peaks of orthorhombic/tetragonal $Cu_{3-x}Te_2$ and orthorhombic CuTe (>30 at%) are visible, and next to the amorphous-crystalline transition, no apparent transformations are observed. An increase in crystallization temperature is observed with increasing carbon content. In the next section, the phase formation of $Cu_{0.6}Te_{0.4}$-C layers with a carbon content corresponding to each composition range is studied as a function of temperature using *in situ* XRD. This will give a clear view of the crystallization and subsequent phase transformation for each composition range.

Discrete compositions

Discrete samples with a constant layer thickness of 50 nm and with a Cu/Te ratio of 1.5 that contain $\sim$ 10, $\sim$ 20 and ∼40 at% carbon are deposited on 20 nm Al_2O_3. As a reference, a $Cu_{0.6}Te_{0.4}$ layer without carbon was also deposited. XRF measurements confirm for all samples a Cu/Te ratio close to 1.5. For the 20 and 40 at% carbon samples, the carbon content was verified by EDX (respectively 20.6 and 36.3 at% C and a Cu/Te ratio of 1.52 and 1.6). In the case of 10 at% carbon, the signal was too weak to determine the carbon content. The phase formation is investigated using *in situ* XRD. Figure 4 shows the result for the different compositions, confirming the general behavior that was observed in the combinatorial study. In the case of pure $Cu_{0.6}Te_{0.4}$ (see Figure 4a), hexagonal $Cu_{2-x}Te$ [17] is already formed during deposition. The 2:1 stoichiometry of the hexagonal phase is different from the 3:2 ratio that is expected from the composition, and hence more

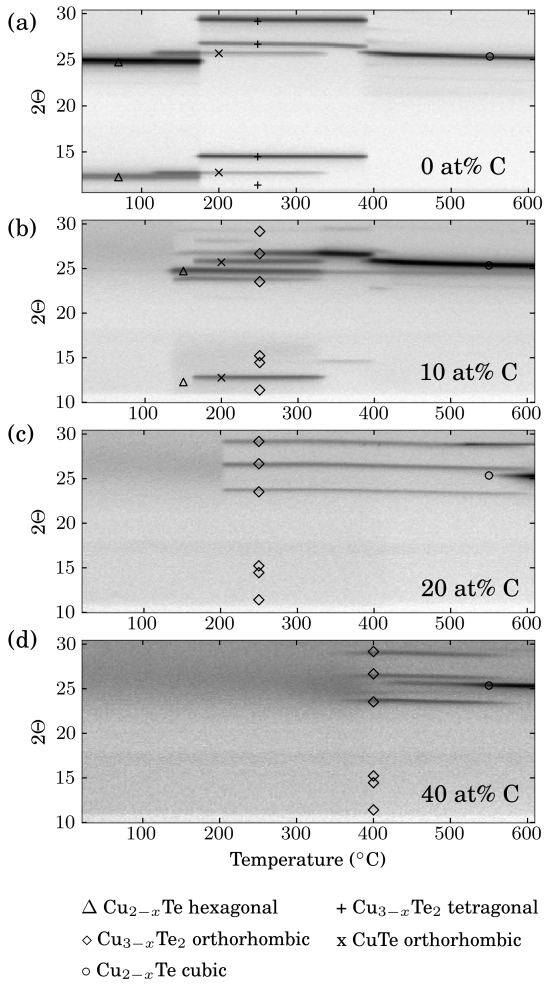

Figure 4. *In situ XRD pattern in the 10-30° window of a 50 nm $Cu_{0.6}Te_{0.4}$(-C) layer (a) without carbon, (b) with ∼10 at% C, (c) with ∼20 at% C and (d) with ∼40 at% C.*

Te rich regions are also expected in the layer. These Te rich regions crystallize as orthorhombic CuTe[21] at $120°C$. Both phases react to tetragonal $Cu_{3-x}Te_2$ [19] at $180°C$, but some CuTe is still present up to $350°C$. Finally, cubic $Cu_{2-x}Te$ [22] is formed for $T > 400°C$. For very low carbon contents in the combinatorial study, the (006) diffraction peak of $Cu_{2-x}Te$ at 24.7° was visible again after anneal at $350°C$, which is rather unexpected as for pure $Cu_{0.6}Te_{0.4}$, this phase does not appear in the *in situ* XRD pattern anymore after reaction with orthorhombic CuTe.

The most plausible explanation is some left over that did not fully transform during the anneal of the combinatorial sample at 350°C. Another observation was that cubic $Cu_{2-x}Te$ which is formed for $T > 400°C$ could not be quenched in and returns to the hexagonal form. This could also explain the occurence of the hexagonal phase in the combinatorial study, although the cubic phase is not expected to be formed below 400°C.

The combinatorial results demonstrated that a small amount of carbon could prevent the formation of any polycrystalline Cu-Te phase during deposition. Figure 4b illustrates this for a layer which contains ∼10 at% carbon. Starting from an amorphous as deposited layer, hexagonal $Cu_{2-x}Te$ and orthorhombic $Cu_{3-x}Te_2$ [18] are formed at 135°C (in contrast to tetragonal $Cu_{3-x}Te_2$ as for pure $Cu_{0.6}Te_{0.4}$). Diffraction peaks of orthorhombic CuTe appear at 165°C. These phases co-exist up to 330°C, and then react to the high temperature tetragonal $Cu_{3-x}Te_2$ [19] phase (i.e. the (051) peak of the orthorhombic lattice at 23.52° disappears whereas the (001) and (101) peaks of the tetragonal lattice at 14.5 and 26.7° become more apparent). As was already deduced from the combinatorial approach, still some transformations occur for this composition. However it illustrates the role of the carbon: the crystallization and further transformations are inhibited.

Figure 4c shows the *in situ* measurement for a 20 at% carbon alloyed $Cu_{0.6}Te_{0.4}$-C layer. The layer is amorphous up to 200°C, and then orthorhombic $Cu_{3-x}Te_2$ and CuTe are formed (the (103) peak of CuTe at 48.8° is visible in the 30-50° 2θ window, but not shown here). Both phases co-exist and do not transform up to 560°C. At higher temperatures, cubic $Cu_{2-x}Te$ is formed. In this way a large temperature window where the material does not transform is created. This stabilizing effect can be explained by the fact that after crystallization of the Cu-Te phases, the carbon is most likely located at the grain boundaries of the Cu-Te crystals, making diffusion along the grain boundaries more difficult and hence impeding further transformations. This is further supported by the fact that no clear shift of the Cu-Te diffraction peaks are observed, indicating that the carbon atoms are not incorporated in the lattice, and hence are located outside the grains. This is also in agreement with the fact that no Cu and Te carbides are formed, as was verified by XPS [16]. In previous work [16], we reported already that addition of ∼40 at% carbon results in a material which is amorphous up to 360°C. For completeness, this is also shown in Figure 4d.

The results of the combinatorial study and the discrete samples invigorate our assumption that the inhibited crystallization is mainly related to kinetic aspects and the microstructure of the material. The combination of rather large elements like Cu and Te with a small element like C increases the packing density in the amorphous solid. This makes interdiffusion difficult, impeding the rearrangement in a crystalline structure and hence inhibiting the crystallization [23]. When more carbon is added, and hence with increased packing density, we observed an increase

in the crystallization temperature. An increased thermal stability of amorphous alloys because of the addition of small atoms like Be and C has been reported before[24,25]. The samples with $\sim$ 20 and $\sim$40 at% carbon show attractive phase stability because of the large thermal window where no transformations occur.

Electrical characterization

The influence of the carbon content on the switching behavior of TiN/$Cu_{0.6}Te_{0.4}$-C/Al_2O_3/n^+ Si CBRAM is investigated. Memory cells with 0, 20, 40 and 50 at% carbon are prepared and the cells are cycled 20 times from which the set voltages are extracted. The resistance of the LRS and HRS state was measured by applying a read voltage of 20 mV after switching the cell on or off. Especially the 20 and 40 at% carbon samples are of interest, as these compositions have an improved thermal stability. Figure 5 shows the first and 20th cycle of a typical memory cell for every carbon content. The switching characteristics are very similar in the 0-40 at% range (Figure 5a-c). In the first cycle, Cu is driven into the Al_2O_3 layer to form a conductive filament (e.g. the *forming* step). The subsequent IV traces and switching voltages are comparable to the first cycle, implying a complete filament erasure[26] and hence every cycle can be considered as a *forming* cycle. In the case of 50 at% carbon (Figure 5d), a clear difference is observed between the first cycle and further switches. Whereas a deep reset could easily be achieved for lower carbon contents, for 50 at% the cell does not return to the pristine HRS after a few cycles. This behavior could be described as switching were forming is observed (i.e. Cu is driven into the Al_2O_3 layer to form the filament and not all Cu is extracted again after reset).

A higher reset current is observed for the carbon alloyed memory cells, especially in the case of 50 at% C. Both thermal effects and drift generally contribute to the reset operation[26,27]. The higher reset currents for the carbon alloyed cells suggest a more robust filament as higher currents are sustained. This will induce more Joule heating and hence the thermal component will have a larger contribution in the reset operation for carbon alloyed cells compared to pure $Cu_{0.6}Te_{0.4}$. The drift contribution on the other hand will be more important for the latter, evidenced by the low-current reset at already low voltages. This can be understood by a higher driving force for the Cu ions to go back to the supply layer due to the Cu-Te affinity, as pointed out before[12]. Consequently, the dominant thermal reset for the carbon alloyed cells might also suggest a lower Cu affinity towards the supply layer when more carbon is introduced, reducing the drift contribution. Furthermore, a different filament geometry (e.g. less conical for the carbon alloyed cells) can be present, inducing a more uniform field for the carbon alloyed cells during reset, which in turn leads to reduced drift and hence a thermal dominated reset.

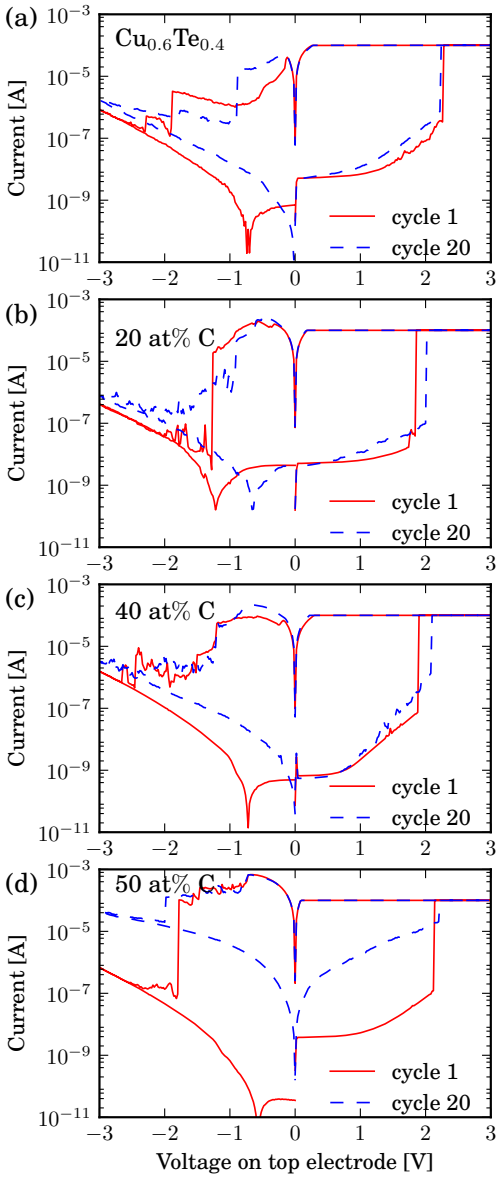

Figure 5. *Typical switching characteristics of a TiN/$Cu_{0.6}Te_{0.4}$(-C)/Al_2O_3/n^+ Si (50/50/3 nm) memory cell (a) without carbon, with (b) ∼20 at% C, (c) ∼40 at% C and (d) ∼50 at% C.*

Figure 6a compares the set voltage of the memory cells for different carbon contents, revealing a slightly lower set voltage for the carbon alloyed memory

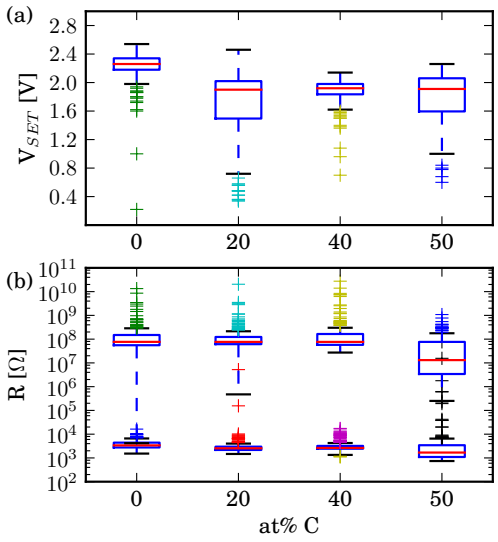

Figure 6. *(a) Set voltage and (b) resistance of the LRS and HRS of a TiN/$Cu_{0.6}Te_{0.4}$(-C)/Al_2O_3/n^+ Si (50/50/3 nm) memory cell for different carbon contents in the $Cu_{0.6}Te_{0.4}$(-C) layer. (Data from 10 devices × 20 cycles)*

cells. This suggests an easier extraction of Cu from the carbon alloyed $Cu_{0.6}Te_{0.4}$ layers. We ascribe this to the amorphous nature of the Cu-supply layer, as the binding energy in an amorphous matrix is lower than in a lattice structure. Moreover, the dependence of switching parameters on binding energy of Cu in a fcc crystal and Cu-Te compounds has been pointed out before [12,28] and hence it is also reasonable to explain the observed difference between amorphous and crystalline source layers in this way. Remark that this is in agreement with the proposed lower Cu affinity towards a carbon alloyed $Cu_{0.6}Te_{0.4}$ layer. Additionally, a more robust filament can be expected when the Cu ions are easier extracted from the supply layer, which is in agreement with the observed higher reset current. However, the lower set voltage may also be due to the presence of pure Cu. Small grains could be observed in HR TEM of a 40 at% $Cu_{0.6}Te_{0.4}$-C layer [16], and hence some pure fcc copper can be present here, without being detectable by XRD. The occurence of pure Cu could also not be excluded from XPS measurements [16]. It is worth mentioning that with increasing carbon content, the resistivity of the $Cu_{0.6}Te_{0.4}$-C layer increases (see Figure 1), however no clear influence of the resistivity on the switching voltage is observed. This is to be expected as the resistivity of Al_2O_3 is orders of magnitude higher than $Cu_{0.6}Te_{0.4}$-C and hence the voltage will always drop over the Al_2O_3 layer.

The endurance was investigated by cycling the memory cells a 1000 times us-

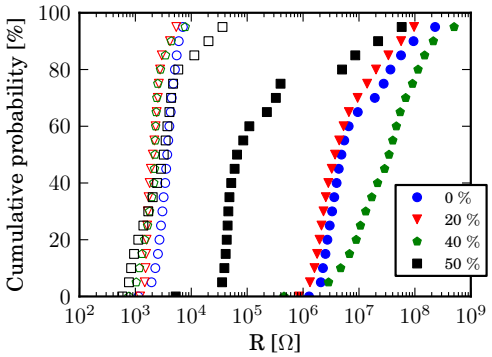

Figure 7. *Cumulative distribution of LRS (open markers) and HRS (filled markers) for 1000 cycles of a TiN/$Cu_{0.6}Te_{0.4}$-C/Al_2O_3/n^+ Si (50/50/3 nm) memory cell for different carbon contents.*

ing the before mentioned programming sequence. Figure 7 shows the cumulative distribution of the LRS and HRS for memory cells with carbon contents from 0 to 50 at%. It is clear that up to 40 at% carbon, good endurance is observed with a resistive window of more than 2 orders of magnitude. For the cell with 50 at% carbon, a similar resistive window is present in the first cycles, but after a few cycles the HRS decreases and finally a small switch between LRS and HRS around a central value of $10^4\,\Omega$ is observed, resulting in a very small resistive window. Although the presented switching curves for a memory cell with 50 at% carbon (Figure 5d) remind of a forming behavior, the endurance tests reveal that the HRS further decreases and hence it should be considered as a degradation of the memory cell. The decrease of the resistance of the HRS is also already visible in Figure 6b, showing the resistances of the HRS and LRS for all carbon contents. Whereas the LRS and HRS in the 0-40 at% carbon range are very similar, for 50 at% a larger spread in the HRS is already observed. This behavior can be understood as a result of the lower Cu affinity towards the supply layer. The enhanced thermal and lower drift contribution might result in a significant lateral diffusion of Cu ions from the filament during reset (instead of going back to the source layer), which leads cycle-after-cycle to an increasing amount of Cu in the switching layer and contributes to the current in the HRS.

ToF SIMS study

Next to a strong influence of carbon alloying on the Cu-Te phase formation, an influence on the switching behaviour is observed. To investigate the extraction and diffusion of Cu more in detail, the diffusion of Cu into the aluminum oxide due to thermal activation is investigated. A 10 nm $Cu_{0.6}Te_{0.4}$(-C) layer with 0, 20

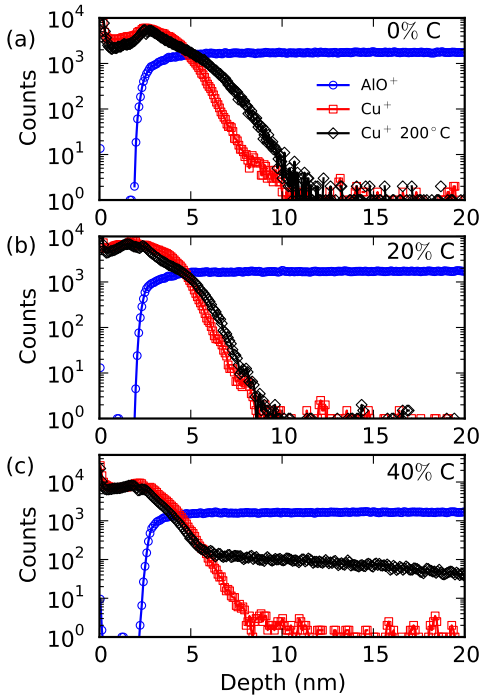

Figure 8. *Depth profile of Cu in the Al_2O_3 layer before and after anneal at 200°C for (a) pure $Cu_{0.6}Te_{0.4}$ and with addition of (b) 20 at% and (c) 40 at% carbon.*

and 40 at% carbon was deposited on a 20 nm Al_2O_3 layer and annealed for 30 min at 200°C. A depth profile of the elements was performed with ToF SIMS for both the as deposited and annealed samples. Figure 8 shows the depth profile of the recorded Cu^+ and AlO^+ ions. The x-axis (sputter time) of each profile has been calibrated in depth (nm), setting the top of the Si signal at 30 nm. This assumes an identical sputter rate of both $Cu_{0.6}Te_{0.4}$(-C) and Al_2O_3 layers which is most likely not the case. With this calibration, the $Cu_{0.6}Te_{0.4}$(-C) layer is seen much thinner than expected. For pure $Cu_{0.6}Te_{0.4}$ (Figure 8a) and with 20 at% (Figure 8b), a slight diffusion of Cu and Te (Te profile shown in Figure S1) into the Al_2O_3 after annealing is observed, which is evidenced by the slope of the Cu^+ profile, and is in agreement with previous observations [15]. The profiles suggest a slightly larger diffusion depth in the case of pure $Cu_{0.6}Te_{0.4}$. Figure 8c depicts the profile for the sample with 40 at% carbon and shows a much higher signal of Cu, Te and C (Te and C shown in Figure S1) in the Al_2O_3 layer after annealing compared to the sample without and with 20 at% C. This illustrates, next to the electrical data, an easier extraction by thermal activation from the source layer and hence a

lower Cu affinity for higher carbon contents. The ToF SIMS results suggest that with higher carbon contents the elements are less tightly bound and - at least at the Al_2O_3 interface - can more easily be extracted from the supply layer. Although a clear signal is observed in the aluminum oxide, the actual amount of Cu is limited, as CBRAM functionality after this thermal treatment was still observed.

D. Conclusions

In this paper we investigated the influence of the carbon content in a Cu_xTe_{1-x} layer (x$\sim$0.6) on the Cu-Te phase formation and on the switching behaviour when integrating them as Cu-supply layer in 580 µm diameter dot CBRAM cells. Addition of $\sim$8 at% carbon prevents already during deposition the formation of polycrystalline Cu-Te phases. Increasing the carbon content creates a larger temperature window where the material stays amorphous. Addition of 20 or 40 at% carbon to the $Cu_{0.6}Te_{0.4}$ layer results in a material with a large temperature window where no phase transformations occur or with a large amorphous region respectively. Both compositions show a good electrical switching behaviour. A higher reset current is observed for the carbon alloyed memory cells compared to pure $Cu_{0.6}Te_{0.4}$. This suggests a larger contribution of thermal effects during reset operation, while a reduced drift contribution might point to a lower Cu affinity from the filament towards the supply layer. Addition of carbon also leads to a slightly lower set voltage, which we mainly attribute to the amorphous nature of the Cu-Te layer, where the Cu has a lower binding energy compared to a crystalline material. Increasing the carbon content to 50 at% led to a degradation of the HRS after repeated cycling i.e. a resistive window of only one order of magnitude is present. This degradation can be ascribed to the enhanced thermal and lower drift contribution to the reset operation, resulting in a significant lateral diffusion of Cu ions from the filament instead of going back to the source layer, which leads cycle-after-cycle to an increasing amount of Cu in the switching layer. The easier extraction and looser bounding structure of the elements with increasing carbon content was also confirmed by ToF SIMS depth profiling of Cu, Te and C into Al_2O_3 after annealing a $Cu_{0.6}Te_{0.4}$-C/Al_2O_3/Si stack with different carbon contents. Higher diffusion of the elements into the oxide layer was observed when 40 at% carbon was added compared to a 20 at% carbon alloyed or a pure $Cu_{0.6}Te_{0.4}$ layer.

Acknowledgments

This research was funded by a Ph.D. grant of the Agency for Innovation by Science and Technology (IWT) and by the UGent-BOF GOA 01G01513.

References

[1] R. Waser, R. Dittmann, G. Staikov, and K. Szot, *Adv. Mater.* **21**(25-26), 2632–2663 (2009).

[2] K. Terabe, T. Nakayama, T. Hasegawa, and M. Aono, *Appl. Phys. Lett.* **80**(21), 4009–4011 (2002).

[3] T. Sakamoto, H. Sunamura, H. Kawaura, T. Hasegawa, T. Nakayama, and M. Aono, *Appl. Phys. Lett.* **82**(18), 3032–3034 (2003).

[4] M. Kozicki, M. Park, and M. Mitkova, *IEEE Trans. Nanotechnol.* **4**(3), 331–338 (2005).

[5] M. Kund, G. Beitel, C.-U. Pinnow, T. Rohr, J. Schumann, R. Symanczyk, K.-D. Ufert, and G. Muller, *Tech. Dig. - Int. Electron Devices Meet.* , 754–757 (2005).

[6] J. S. Kwak, E. J. Chi, J. D. Choi, S. W. Park, H. K. Baik, M. G. So, and S. M. Lee, *J. Appl. Phys.* **78**(2), 983–987 (1995).

[7] Y. Wang, H. Lv, W. Wang, Q. Liu, S. Long, Q. Wang, Z. Huo, S. Zhang, Y. Li, Q. Zuo, W. Lian, J. Yang, and M. Liu, *IEEE Electron Device Lett.* **31**(12), 1470–1472 (2010).

[8] T. Tsuruoka, K. Terabe, T. Hasegawa, and M. Aono, *Nanotechnology* **21**(42), 425205 (2010).

[9] Q. Liu, S. Long, W. Wang, Q. Zuo, S. Zhang, J. Chen, and M. Liu, *IEEE Electron Device Lett.* **30**(12), 1335 –1337 (2009).

[10] C. Schindler, M. Weides, M. N. Kozicki, and R. Waser, *Appl. Phys. Lett.* **92**(12), 122910 (2008).

[11] Y. Bernard, V. T. Renard, P. Gonon, and V. Jousseaume, *Microelectron. Eng.* **88**(5), 814–816 (2011).

[12] L. Goux, K. Opsomer, R. Degraeve, R. Muller, C. Detavernier, D. J. Wouters, M. Jurczak, L. Altimime, and J. A. Kittl, *Appl. Phys. Lett.* **99**(5), 053502 (2011).

[13] S. Kim, M. Jo, J. Park, J. Lee, W. Lee, and H. Hwang, *Electrochem. Solid-State Lett.* **14**(8), 322–325 (2011).

[14] K. Aratani, K. Ohba, T. Mizuguchi, S. Yasuda, T. Shiimoto, T. Tsushima, T. Sone, K. Endo, A. Kouchiyama, S. Sasaki, A. Maesaka, N. Yamada, and H. Narisawa, *Int. Electron Devices Meet.* , 783 –786 (2007).

[15] L. Goux, K. Opsomer, A. Franquet, G. Kar, N. Jossart, O. Richard, D. Wouters, R. Muller, C. Detavernier, M. Jurczak, and J. Kittl, *Thin Solid Films* **533**, 29–33 (2013).

[16] W. Devulder, K. Opsomer, F. Seidel, A. Belmonte, R. Muller, B. De Schutter, H. Bender, W. Vandervorst, S. Van Elshocht, M. Jurczak, L. Goux, and C. Detavernier, *ACS Appl. Mater. Interfaces* **5**(15), 6984–6989 (2013).

[17] International Centre for Diffraction Data, Newtown Square, PA, *JCPDS Data*

Card no. 00-049-1411, (2004).
[18] International Centre for Diffraction Data, Newtown Square, PA, *JCPDS Data Card no. 00-026-1117*, (2004).
[19] International Centre for Diffraction Data, Newtown Square, PA, *JCPDS Data Card no. 01-085-0606*, (2004).
[20] A. Pashinkin and V. Fedorov, *Inorg. Mater.* **39**(6), 539–554 (2003).
[21] International Centre for Diffraction Data, Newtown Square, PA, *JCPDS Data Card no. 01-089-4311*, (2004).
[22] International Centre for Diffraction Data, Newtown Square, PA, *JCPDS Data Card no. 00-045-1286*, (2004).
[23] T. Zhang, A. Inoue, and T. Masumoto, *Mater. Trans., JIM* **32**(11), 1005–1010 (1991).
[24] W. Wang, Q. Wei, and H. Bai, *Appl. Phys. Lett.* **71**(1), 58–60 (1997).
[25] W. Wang and H. Bai, *J. Appl. Phys.* **84**(11), 5961–5968 (1998).
[26] L. Goux, K. Sankaran, G. Kar, N. Jossart, K. Opsomer, R. Degraeve, G. Pourtois, G. M. Rignanese, C. Detavernier, S. Clima, Y. Y. Chen, A. Fantini, B. Govoreanu, D. Wouters, M. Jurczak, L. Altimime, and J. A. Kittl, *IEEE Symp. VLSI Technol.* , 69–70 (2012).
[27] D. Ielmini, *IEEE Trans. Electron Devices* **58**(12), 4309–4317 (2011).
[28] V. Afanas'ev, F. D. Stefano, M. Houssa, A. Stesmans, L. Goux, K. Opsomer, C. Detavernier, J. Kittl, and M. Jurczak, *Thin Solid Films* **533**(0), 34 – 37 (2013).

Supporting Information

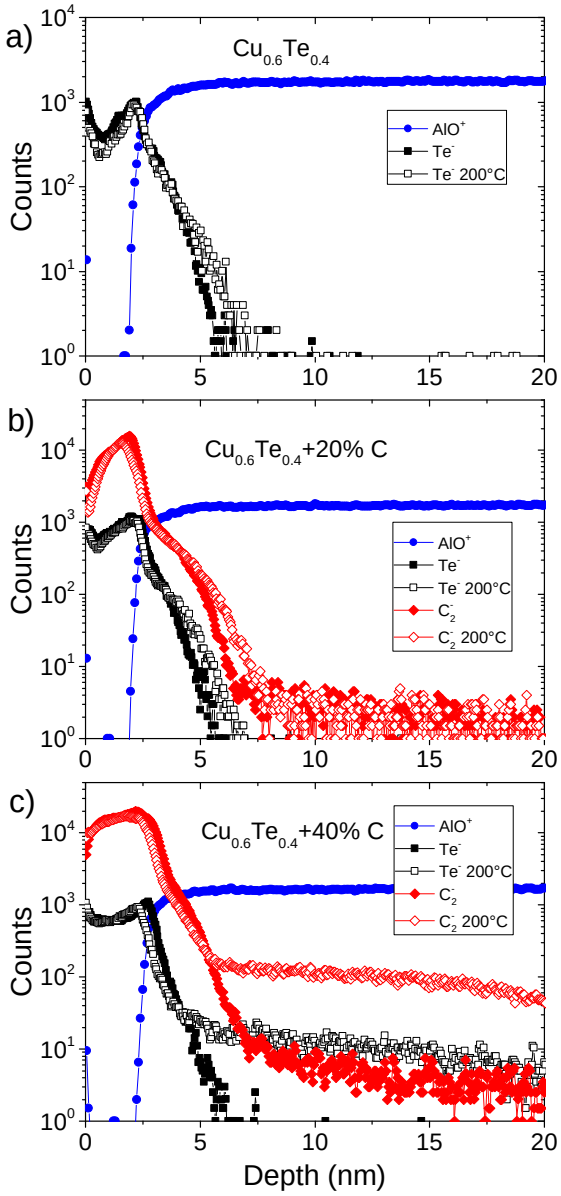

Figure S1. *Depth profile of Te in the Al_2O_3 layer before and after anneal at 200°C for (a) $Cu_{0.6}Te_{0.4}$ and with addition of (b) 20 at% and (c) 40 at% carbon. For the layers alloyed with carbon, the C profile is also shown.*

Paper IV
Improved thermal stability and retention properties of Cu-Te based CBRAM by Ge alloying*

Abstract

In this work we investigate the influence of Ge as an alloying element in Cu-Te based thin films for application as a cation supply layer in Conductive Bridge Random Access Memory (CBRAM). The thermal stability of the alloys and their functionality as copper supply layer in CBRAM are investigated. The thermal stability is studied by means of *in situ* X-ray diffraction, which reveals information on phase separation, phase transformations and melting of the material. We demonstrate that addition of Ge to $Cu_{0.6}Te_{0.4}$ inhibits crystallization up to $300°C$. However, phase separation occurs upon crystallization, which might result in device to device variability when this occurs in memory devices. This is solved by using Cu_2GeTe_3 that forms a single phase upon crystallization. The most promising alloys are implemented in 580 µm diameter dot Pt/$Cu_xTe_yGe_{1-x-y}$/Al_2O_3/n^+ Si CBRAM cells. Their functionality is verified by DC cycling and the influence of Ge is studied by comparing the switching to binary $Cu_{0.6}Te_{0.4}$ based memory cells. The retention of the programmed memory states is measured at $85°C$. Functional CBRAM is demonstrated, and improved filament stability and retention properties are observed for the Ge containing cells compared to $Cu_{0.6}Te_{0.4}$. We mainly attribute this to the Ge-Te bonds that are formed in the supply layer. This lowers the tendency for Cu-Te formation which results in a lower driving force for the Cu to go back to the supply layer, and hence contributing to a more stable filament. The formation of Ge-Te bonds was confirmed by XPS measurements.

*Published as: W. Devulder, K. Opsomer, G. Rampelberg, B. De Schutter, K. Devloo-Casier, M. Jurczak, L. Goux, C. Detavernier, *J. Mat. Chem. C*, 3, 12469-12476, 2015

A. Introduction

Non volatile memory nowadays is dominated by the Si based FLASH technology. However new memories are currently explored which show more promising results in terms of programming speed, power consumption and scaling. Resistive memory is one of them, and in these devices bits are stored as different resistive states of the memory cells. Different types of resistive random access memory (RRAM) are reported[1,2], and one of them is conductive bridge RAM (CBRAM). A typical CBRAM stack consists of a Cu or Ag containing layer, an insulating layer and an inert bottom electrode. By applying a positive bias on the Cu containing active electrode, Cu is oxidized and migrates through the insulating layer, where a conductive filament is grown. Upon bridging the two electrodes by the filament, the cell switches to the low resistive state (LRS). Applying a negative bias on the active electrode dissolves the filament again, switching the cell back to the high resistive state (HRS). Different material systems have been demonstrated to show CBRAM functionality. For the cation supply layer, pure Cu[3,4] or Ag[5] can be used, but also alloys containing these elements like Cu_2S or Cu_2Se[6], Cu-Te[7,8] and Ag-Te[9]. As the switching layer, chalcogenide glasses like GeSe[5,10] and GeS_2[11], organic polymers[12–15] and binary metal oxides like SiO_2[3,16] or Al_2O_3[4,8] can be used. The latter are of special interest as they are compatible with current CMOS processes. Improved cycling of Pt/Cu_xTe_{1-x}/Al_2O_3/n^+ Si CBRAM cells has been reported for the Cu_xTe_{1-x} alloy ($0.5 < x < 0.7$) compared to pure Cu[8]. However a drawback of the Cu-Te alloy is the existence of a multitude of intermetallic phases, resulting in phase separation in case of deviation from the stoichiometry of these compositions. Moreover polymorphs exist and hence phase transformations between different crystal structures can occur. Good thermal stability of the materials is required to be compatible with the temperatures that are reached during device processing. In this work we alloy a $Cu_{0.6}Te_{0.4}$ thin film with Ge to influence the Cu-Te phase formation. Germanium was used because it has been reported to be effective in increasing the crystallization temperature in phase change materials[17–19]. This is explained by the large coordination number of Ge and the relatively strong bonds they form, both contributing to the stability of the amorphous phase. Germanium can form bonds with Cu and Te (i.e. binary intermetallic phases exist) and literature reports the existence of a single ternary Cu_2GeTe_3 phase[20,21]. The available phase diagrams[22–27] show that phase separation is expected for a crystalline Cu-Te-Ge layer if the composition is different from Cu_2GeTe_3. This has to be avoided because it might lead to variation in device parameters. As a consequence, an amorphous material up to $400°C$ (i.e. typical back end of line (BEOL) temperatures) or a single crystalline phase is preferred. From that point of view, Ge is an interesting material because it has the tendency to increase crystallization temperature of the Cu-Te-Ge alloy, and if the crystal-

lization temperature is below 400°C, the single phase composition can be used. Hence the crystallinity and crystallization behavior of the Ge alloyed $Cu_{0.6}Te_{0.4}$ and Cu_2GeTe_3 films are studied. The most promising alloys are then implemented in 580 µm diameter dot Pt/$Cu_xTe_yGe_{1-x-y}$/Al_2O_3/n^+ Si CBRAM cells. The resistive switching behavior is investigated and the influence of Ge is evaluated by comparing with pure $Cu_{0.6}Te_{0.4}$. Next to switching performance, retention of the memory states (i.e. how well a programmed resistive state is maintained at elevated temperatures) is a key parameter for future memory devices. The retention at 85°C is investigated for the selected compositions and compared to $Cu_{0.6}Te_{0.4}$.

B. Experimental procedures

Materials characterization

Mixed Cu-Te-Ge layers were deposited by magnetron sputtering using a Balzers deposition tool. A base pressure of 5×10^{-7} mbar is reached and the Ar pressure during sputtering was 5×10^{-3} mbar. The Cu, Te and Ge were co-sputtered from 3 different elemental sputter targets. To study the material properties of the alloys, ∼50 nm thick films with different compositions were deposited on Si wafers that were covered by 100 nm thermally grown SiO_2 or 20 nm Al_2O_3. The latter is deposited by a H_2O based atomic layer deposition (ALD) process. By adjusting the sputter power of the Cu, Te and Ge sputter targets, the composition of the Cu-Te-Ge alloys could easily be varied. First the Cu/Te ratio was kept constant to 1.5, as good switching characteristics are obtained with this composition[8], and Ge contents ranging from 5 up to 50 at% were added. Finally also a sample with the correct composition to obtain Cu_2GeTe_3 was deposited. Compositions were verified by Rutherford backscattering spectroscopy (RBS) and also by X-ray fluorescence spectroscopy (XRF) after calibration of the system. X-ray reflectivity measurements (XRR) were performed to measure the thickness of the deposited films.

In situ X-ray diffraction (XRD) was used to study the crystallinity of the films and for determination of the different crystallographic phases and transformations that occur under annealing. A Bruker D8 Discover XRD, equipped with a home built annealing chamber, is used to anneal the sample at a constant heating rate of 0.5°C/s in He atmosphere. Meanwhile the XRD pattern in a fixed 2θ window of 20° is measured. In this way, subsequent transformations of the material as function of temperature and the occurrence of different phases can accurately be determined. It is clear that this gives important information about the stability of the material under thermal budget.

X-ray photoelectron spectroscopy (XPS) was performed to investigate the Ge bonding in the different alloys. Measurements were conducted on a Theta Probe

system of Thermo Scientific, operating at a base pressure of $\sim 10^{-10}$ mbar. The system has an Al X-ray excitation source and a channel plate detector. Next to a surface scan, from which the surface carbon peak at 284.6 eV was used as a binding energy reference, at least one sputter step was performed using an EX05 Ar ion gun in order to remove the surface contamination.

Memory characterization

The alloys which show good thermal stability are tested on their functionality as a cation supply layer in CBRAM. Memory cells were prepared by subsequently depositing a 50 nm thick layer of the Cu-Te-Ge alloy and a Pt top electrode through a 580 µm dot shadow mask on a 3 nm Al_2O_3/n^+ Si substrate. The Al_2O_3 layer was deposited by a H_2O based ALD process and serves as dedicated switching layer. The memory cells are then cycled between a high and low resistive state using a Keithley 2601A Sourcemeter. Linear voltage sweeps with a sweep rate of $0.5\,\mathrm{V/s}$ are applied on the Pt top electrode with respect to the bottom electrode. The current is limited in the set sweep by the sourcemeter to avoid overgrown filaments. For functional cells, the retention of the programmed memory states is investigated. After cycling the cells two times, the cells are programmed to a high or low resistive state. The cells are then baked at $85°C$ in an inert He atmosphere and after predefined time intervals, the cells are taken out of the oven and their resistance is measured using a read voltage of 100 mV. In this way the resistance is monitored for baking times up to 121.6 h. The results are compared with those of memory cells containing pure $Cu_{0.6}Te_{0.4}$ to see the influence of the Ge.

C. Results and discussion

Thermal stability

$Cu_{0.6}Te_{0.4}$ layers were alloyed with 5, 10, 20, 30, 40 and 50 at% Ge. We will further refer to them as CuTeGe5 up to CuTeGe50. The compositions are determined by RBS and XRF and they are depicted in Figure 1a, together with the compositions of the other layers that are studied further in this work. The compositions are also given in table S1 in the Supporting Information. The *in situ* XRD patterns of the $Cu_{0.6}Te_{0.4}$ alloyed layers with Ge contents up to 30 at% Ge are shown in Figure 2. Higher Ge contents exhibit a very similar crystallization behaviour as the sample with 30 at% Ge and are not shown. The crystallization temperatures of the different compositions, defined as the maximum change in the Cu_2Te peak intensity at 24.7°, are extracted from the *in situ* XRD patterns and summarized in Figure 1b. The resistivity of the as-deposited layers is indicated as well, showing an increase with Ge content. Figure 2a gives the result of a pure $Cu_{0.6}Te_{0.4}$ layer and was already discussed in previous work[28,29]. However, it

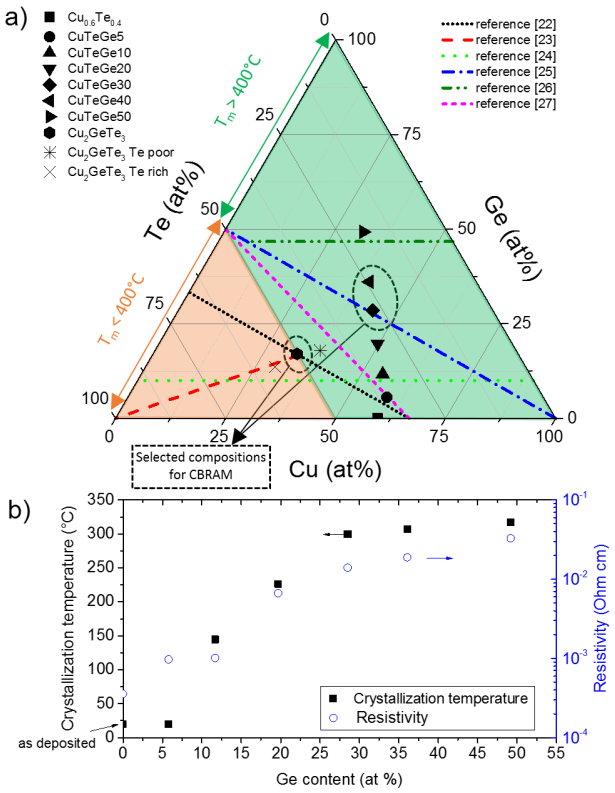

Figure 1. *(a) Compositions of the investigated thin films in this work. The graph also indicates cross sections that are reported in literature, from which it is observed that melting points below 400°C occur for compositions with more than 50 at% Te. (b) Crystallization temperature and resistivity of the 50 nm $Cu_{0.6}T_{0.4}$ alloyed layers as function of the Ge content.*

illustrates once again that multiple intermetallic phases[30] exist and that transformations occur upon annealing. Addition of only 5 at% Ge (Figure 2b) drastically changes the phase sequence. As deposited, the hexagonal $Cu_{2-x}Te$[31] phase is formed, but the transformation to a cubic structure occurs at an apparent higher temperature compared to $Cu_{0.6}Te_{0.4}$. Germanium is most likely segregating towards the $Cu_{2-x}Te$ grain boundaries, because Ge is not soluble in Cu_2Te, as can be seen in the reported phase diagrams[22,27]. This limits Cu diffusion along the grain boundaries (which are fast diffusion paths), lowering the Cu mobility and making phase transformations more difficult to proceed. Note that in interconnects, alloying elements are also used to lower Cu migration along grain boundaries and in this way improve electromigration resistance[32,33]. Note that from about 200°C

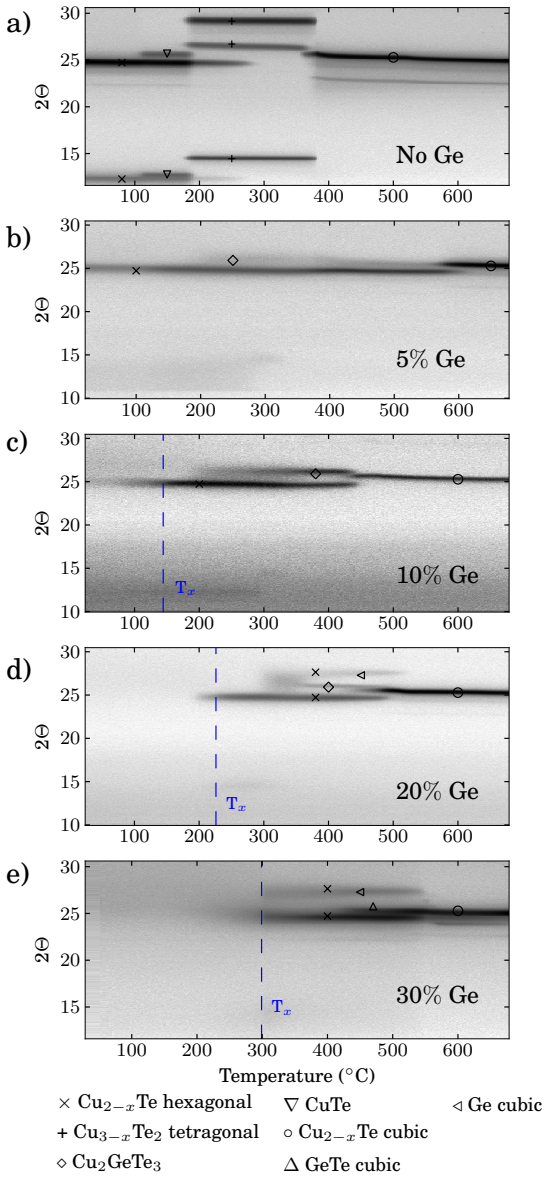

Figure 2. *In situ XRD patterns during annealing at 0.5°C/s of (a) a 50 nm $Cu_{0.6}Te_{0.4}$ layer and when (b) 5, (c) 10, (d) 20 and (e) 30 at% Ge is added. The crystallization temperature is also indicated.*

on, also a faint peak appears around 26°, which might be ascribed to Cu_2GeTe_3. Indeed, this is more clear in the spectrum of the sample with 10 at% Ge (Figure

2c). At 190°C, Cu_2GeTe_3 crystallizes and coexists with $Cu_{2-x}Te$[31], lasting up to about 430°C, where again high temperature $Cu_{2-x}Te$[34] is formed. Addition of 20 and 30 at% Ge on the other hand (Figures 2d and e) creates a material which is amorphous up to respectively 226 and 300°C. The increasing crystallization temperature with higher Ge contents can be explained by the addition of an element with high coordination number that will form bonds with the other elements. Diffusion of the elements (which requires breaking of the bonds) that is required for reorganization into a lattice becomes more difficult and hence a higher crystallization temperature can be expected[17,19,35,36]. However, also for these compositions, phase separation occurs upon crystallization. This was also expected from the reported phase diagrams in literature[22,24–27]. For CuTeGe30, it is not straightforward to unambiguously assign the diffraction peaks to a certain phase, as some peaks from different phases are close to each other. The diffraction peak around 27° can be linked to $Cu_{2-x}Te$[31], but also to the (111) peak of Ge[37]. The peak around 25.5° might have a contribution of GeTe[38–40] and cubic $Cu_{2-x}Te$[34], as is indicated in the plot.

From the *in situ* XRD measurements, it is clear that phase separation occurs upon crystallization. If we take into account that during BEOL processing temperatures up to 400°C are reached, the material should not show phase separation up to this temperature, because an inhomogeneous Cu supply layer might finally lead to unwanted fluctuations in device characteristics. From this point of view it might be interesting to investigate the Cu_2GeTe_3 composition which forms a single phase upon crystallization. This material was deposited and the composition was determined by XRF as 32.7 at% Cu, 50.3 at% Te and 17 at% Ge. Figure 3a shows the *in situ* XRD measurement of this material. The as-deposited layer is amorphous and crystallizes at 203°C. The crystallization causes a drop in the resistivity from 122 m$\Omega \cdot$ cm (as-deposited) to 0.35 m$\Omega \cdot$ cm (quenched at 300°C). Note that this material has also been reported as a candidate for phase change memory by switching it between the crystalline and amorphous state[41–43]. The observed XRD peaks can be associated to a cubic[21] or orthorhombic structure[20], but it is very difficult to discern the diffraction patterns of the two closely related structures. At 468°C, the peaks disappear and the cubic $Cu_{2-x}Te$[34] phase is formed. The disappearance of the peaks are associated with the melting of the Cu_2GeTe_3 phase. Indeed, inspection of the cross section of the phase diagram[22,41] shows that $Cu_{2-x}Te$ and a liquid is formed upon melting. A full XRD scan was also taken of the as-deposited layer and after annealing at 250°C (see Figure 3b), showing only diffraction peaks of Cu_2GeTe_3 after crystallization. The fact that no phase separation occurs and that the melting temperature exceeds 400°C makes it a viable candidate for integration in memory devices. However, an important remark has to be made here. Careful inspection of the phase diagrams in literature[22–27,41] shows the occurrence of an eutectic point and melting temperatures below 400°C for compositions with

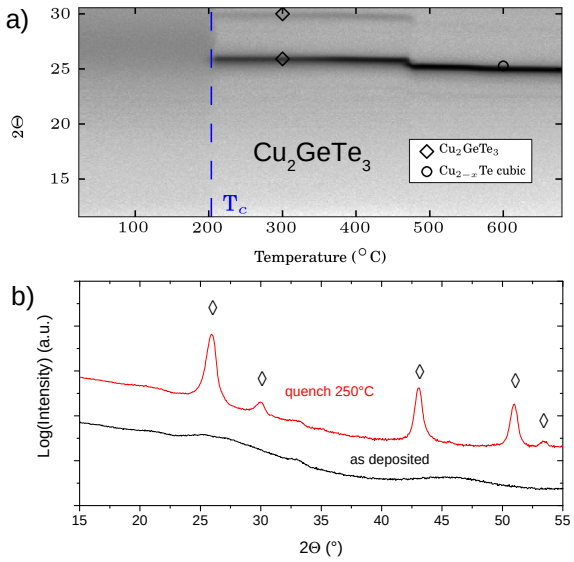

Figure 3. *(a) In situ XRD pattern during annealing at $0.5°C/s$ of a $50\,nm$ Cu_2GeTe_3 layer. (b) XRD measurement in the 15 to 55° 2θ window of the as-deposited layer and after annealing to $250°C$.*

more than 50 at% Te. This is also indicated in Figure 1. Hence these compositions need to be avoided to eliminate melting of the material below typical BEOL temperatures. The Cu_2GeTe_3 compound is on the border of the good composition region. To investigate the influence of a composition deviation of the Cu_2GeTe_3 compound, two layers with on the one hand an excess of Te ($\sim$ 57 at%) and on the other hand a lack of Te ($\sim$ 44.5 at%) are investigated. These points are also plotted in the ternary composition diagram in Figure 1. *In situ* XRD measurements are performed to detect any phase separation, and XRF spectra were acquired to investigate the composition. The measurements are shown in Figures 4 a and b for the Te rich and Te poor layers respectively. For the Te rich layer, next to the Cu_2GeTe_3 peak, also the (101) peak of Te[44] at 27.5° appears, as could be expected from the phase diagram[41]. However, the Te peak disappears at $342°C$ and is related to the melting of the eutectic composition. The composition of the films before and after an anneal towards $400°C$ could be extracted by means of XRF. The XRF spectra show a decrease in the Te intensity for the Te rich film after anneal, going from about 57 to 51 at%, hence the composition changes to Cu_2GeTe_3 (see also table S2 in the Supporting Information for the exact compositions). This is the result of Te evaporation, which occurs more easily when a liquid is formed. The Te poor composition on the other hand shows only the Cu_2GeTe_3 peak and a faint trace of hexagonal $Cu_{2-x}Te$ upon crystallization, but does not show a change in compo-

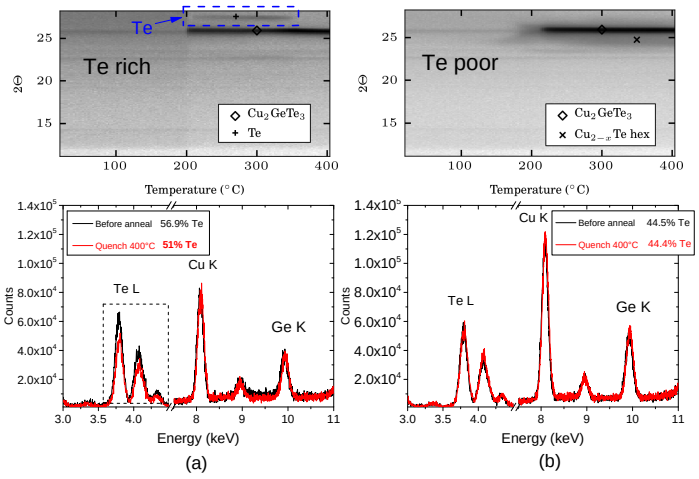

Figure 4. *In situ XRD pattern of the Te rich (a) and Te poor (b) layers up to 400°C and the recorded XRF spectra before and after anneal. A decrease in Te peak intensity is observed for the Te rich layer after anneal, which agrees with a decrease from about 57 to 51 at% Te.*

sition after anneal to 400°C. This illustrates that for optimal thermal stability, an excess of Te should be avoided.

In summary, the *in situ* XRD measurements show that for low Ge contents (e.g. 5 at% Ge) the as-deposited layer is crystalline and that phase separation occurs. When more Ge is added, the as-deposited layer is amorphous and the crystallization temperature increases with Ge content. For films with 20 and 30 at% Ge, crystallization is inhibited up to respectively 200 and 300°C. Higher Ge contents only marginally affect the crystallization temperature. If temperatures up to 400°C are reached during processing, Cu_2GeTe_3 is more interesting because only one phase is present upon crystallization.

CBRAM functionality and retention properties

As discussed in previous section, $Cu_{0.6}Te_{0.4}$ layers with 20 and 30 at% Ge show a temperature stable material up to respectively 200 and 300°C. Functionality and retention of these compositions is studied (and they are further referred to as CuTeGe20 and CuTeGe30 respectively) to investigate the influence of Ge. Higher Ge contents are not further investigated as they did not significantly increase the crystallization temperature. The memory properties of Cu_2GeTe_3, which does not show phase separation upon crystallization and hence has a promising thermal stability, is also investigated. The different Cu-supply layers are implemented in 580 µm diameter dot Pt/$Cu_xTe_yGe_{1-x-y}$/Al_2O_3/n^+ Si cells and the as deposited

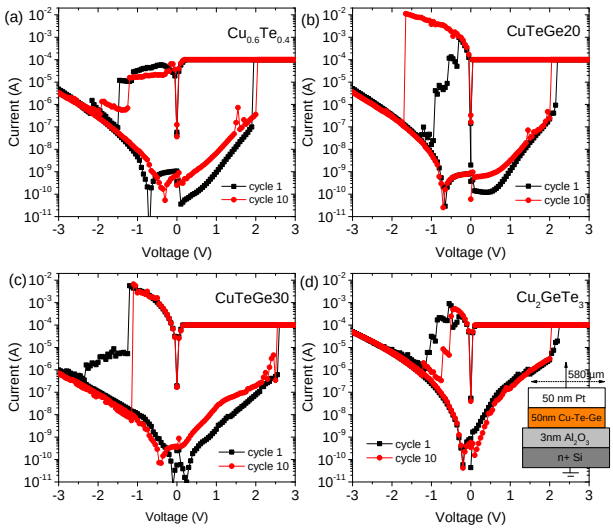

Figure 5. *DC cycling of Pt/$Cu_xTe_yGe_{1-x-y}$/Al_2O_3/n^+ Si cells with a (a) $Cu_{0.6}Te_{0.4}$, (b) CuTeGe20, (c) CuTeGe30 and (d) Cu_2GeTe_3 copper supply layer.*

cells are tested. Figure 5 shows the first and tenth cycle of a typical cell for a $Cu_{0.6}Te_{0.4}$ supply layer (Figure 5a), when 20 or 30 at% Ge is added (Figures 5b and c), and in case of a Cu_2GeTe_3 supply layer (Figure 5d). It is clear that for all materials, good switching characteristics are present. This was also verified by cycling the cells over 100 times. It is also observed that the Ge alloyed cells could efficiently be reset, as with $Cu_{0.6}Te_{0.4}$. This was pointed out before and related to the affinity of Cu and Te to form Cu-Te bonds. This acts as a driving force for the Cu from the conductive filament to go back to the supply layer that contains Te[8], and hence contribute to filament erasure and hence also to the reset. We will further refer to this contribution to the reset as the *drift contribution*. Note that a similar behavior was observed for Ag-Te[9].

Figures 6a-d show the LRS and HRS distribution of the investigated compositions by cycling the cells 5 to 10 times with a current compliance of 100 µA in the set sweep. The HRS values were collected from the IV sweeps at a voltage of +0.1 V. Also the pristine resistance (i.e. the resistance before forming) is shown. It is observed that for all compositions the HRS is very comparable to the pristine resistance, again pointing to an efficient reset. The LRS values are extracted from the IV sweeps at both positive and negative read voltages (+ and -0.1 V), and hence from the set and reset sweep respectively. If the filament is sufficiently stable, both values should coincide. For $Cu_{0.6}Te_{0.4}$, a drift towards slightly higher values is observed for negative read voltages. This indicates that at very low reset

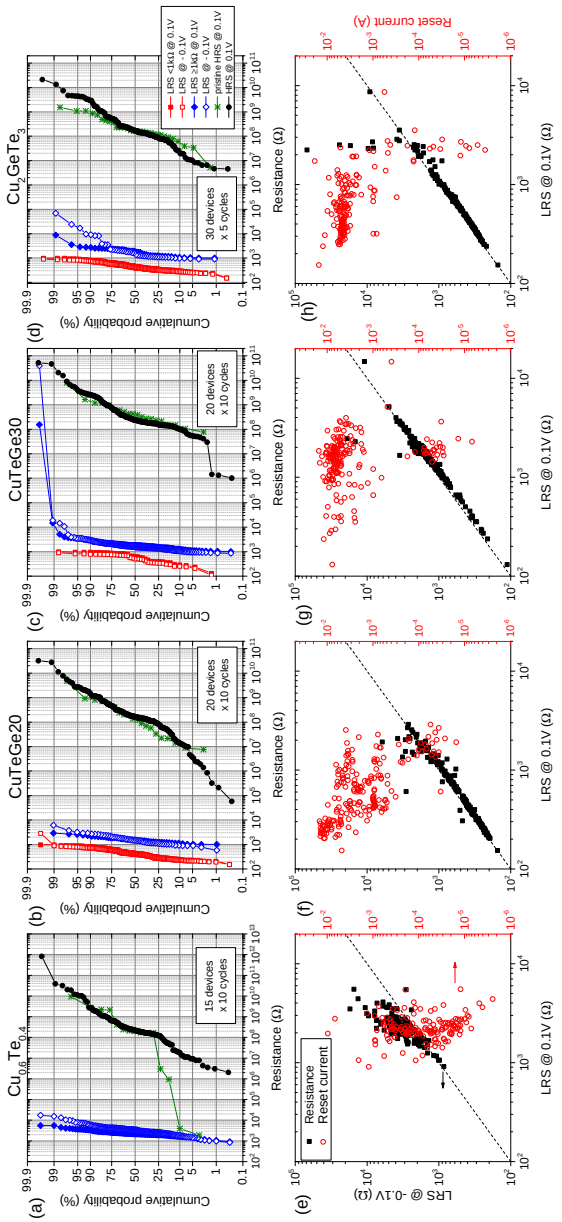

Figure 6. *Cumulative probability of the pristine resistance and HRS extracted at 0.1 V and LRS extracted at both + and -0.1 V from the cells with (a) $Cu_{0.6}Te_{0.4}$, (b) CuTeGe20, (c) CuTeGe30 and (d) Cu_2GeTe_3 as cation supply layer. Figures (e)-(h) show LRS at -0.1 V as a function of LRS at +0.1 V of respectively figures (a)-(d). The reset current is also depicted as function of the LRS resistance extracted from the set sweep before the reset.*

voltages, the filament tends to dissolve already, resulting in an increased resistance. The LRS of $Cu_{0.6}Te_{0.4}$ is always higher than 1 kΩ, whereas for the Ge containing cells also lower resistances are obtained. That is why for the latter the distribution of LRS was divided in two groups with LRS smaller or larger than 1 kΩ. For both CuTeGe20 and CuTeGe30, the distributions with positive and negative read voltages coincide much better, pointing to a more stable filament. This behavior is even better observed in Figures 6e-h, showing the resistance extracted from the reset sweep as function of the value from the set sweep. For $Cu_{0.6}Te_{0.4}$, the points deviate clearly from the $LRS_{0.1V}$=$LRS_{-0.1V}$ line, whereas for the Ge alloyed cells, the points clearly follow this line. The plot also shows the reset current, defined as the current where the maximum current drop occurs, as function of the LRS resistance. From this plot it is clear that higher reset currents are reached (and hence can be sustained) for the cells with Ge. This is very pronounced for the cells with 30 at% Ge. The cumulative probability of these reset currents are shown in Figure S1 in the Supporting Information. For the cells with Ge, cells with a LRS resistance smaller and larger than 1 kΩ are plotted separately (for $Cu_{0.6}Te_{0.4}$ all LRS values are larger than 1 kΩ). Low LRS resistances can be associated to thick, strong filaments and hence they are expected to sustain large currents, which is also observed in Figures 6e-h and Figure S1. The Ge alloyed supply layers show also for LRS resistances exceeding 1 kΩ a larger fraction of resets with a higher reset current compared to $Cu_{0.6}Te_{0.4}$. As a consequence of this higher reset current, the thermal contribution (i.e. due to Joule heating) to the reset operation of the Ge alloyed cells will be more important compared to the drift contribution (i.e. the tendency for the Cu ions to go back to the supply layer due to the chemical affinity, as was pointed out before).

The switching curves suggest a more stable filament for the Ge containing Cu supply layers. This in turn should result in better retention behaviour of the LRS. The retention was investigated for the three Ge containing alloys and compared to $Cu_{0.6}Te_{0.4}$. For every composition, a group of cells was first cycled two times and then programmed to a low or high resistive state. Usually a compliance current (I_c) of 100 µA was used in the set sweep, but also a lower I_c was used for the cells with Ge to obtain more cells with a higher LRS resistance. The cells are then baked at $85°C$ and the resistance is measured at subsequent time intervals. Figure 7 shows the result for the different compositions. The plots at the left side of Figure 7 show the resistance of every memory cell as function of the baking time, as well as the median value at every time step. The plots at the right show the associated cumulative probability of the resistances after programming and after 121.6 h baking at $85°C$. The cells programmed to LRS that end up in higher resistance by using lower compliance currents are plotted separately. It is clear that for $Cu_{0.6}Te_{0.4}$ more than 50 % of the cells in LRS return to a high resistive state (R>10^6 Ω). The cells with Ge on the other hand show a very stable LRS, also for those with a LRS

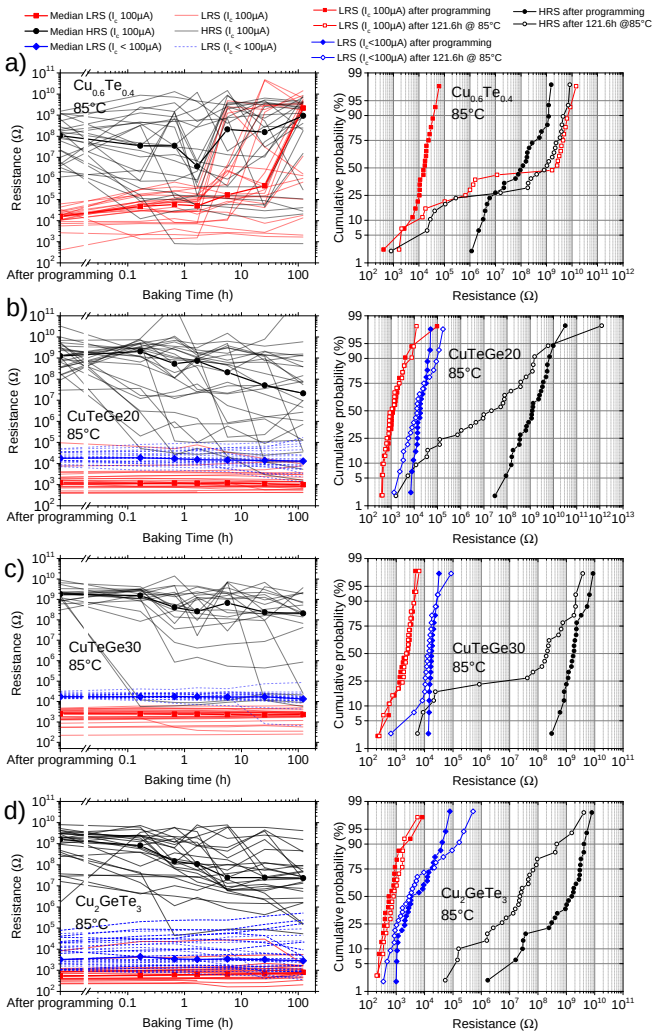

Figure 7. *Retention test at 85°C of memory cells with (a) $Cu_{0.6}Te_{0.4}$, (b) CuTeGe20, (c) CuTeGe30 and (d) Cu_2GeTe_3 as Cu supply layer. The plots at the left show the resistance of every memory cell programmed in LRS (red and blue) or HRS (black) as a function of the baking time. The median values at every time step are also plotted (thick line). The plots at the right show the corresponding cumulative probability of the resistances after programming and after 121.6 h baking at 85°C.*

resistance in between 10 and 100 kΩ. This is also illustrated in Figure S2 in the Supporting Information, by plotting the resistance after 121.6 h as a function of the programmed resistance. It should be mentioned however that there is always a

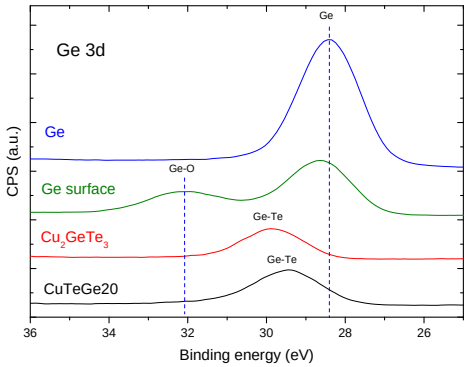

Figure 8. *XPS spectra of the Ge 3d peak of CuTeGe20, Cu_2GeTe_3, and a pure Ge thin film. The surface spectrum of the pure Ge film is also shown as a reference for the peak related to Ge-O bonds.*

tail in the distribution for the cells programmed in HRS towards lower resistance. This can be caused by the very low resistances that are reached during cycling before programming to HRS. This is expected to induce a large template path in the Al_2O_3 switching layer, which acts as a defect that can enhance Cu diffusion and causes filament reconstruction. Moreover, due to these low LRS resistances, some Cu can be left in the switching layer that can contribute to filament reconstruction. Note that this LRS dependence of HRS retention has been pointed out before in literature[45,46].

From the retention tests it can be concluded that a more stable LRS is obtained for the Ge alloyed cells compared to $Cu_{0.6}Te_{0.4}$. This confirms the results of the switching analysis (see Figure 6). A more stable filament can be due to a stronger, more robust and hence difficult to dissolve filament. This was reported before[47], and related to Ge incorporation in the filament. On the other hand, the improved filament stability can also be a result of a lower affinity of the copper towards the supply layer. Indeed, higher reset currents were observed for the Ge alloyed cells pointing to a larger thermal contribution to the reset. This will be necessary to reset the cells when there is a lower drift contribution to the reset. This will occur when there is a lower tendency of the Cu to go back to the supply layer to form copper tellurides. To investigate the chemical state of Ge and how it can lower the drift contribution and influence the observed retention behavior, XPS measurements were performed on a CuTeGe20 and a Cu_2GeTe_3 film. A reference spectrum of a pure Ge sputtered film was also measured to compare peak positions. Figure 8 shows the Ge 3d peaks of the layers after sputtering away the surface contamination. The surface spectrum of the Ge sample is also shown as a reference for the peak related to Ge-O bonds, which is shifted towards higher

binding energies[48]. It is clear that for CuTeGe20 and Cu_2GeTe_3 the Ge peak is shifted towards values in between metallic Ge and Ge-O, which are typical for Ge-Te bonds[49,50]. Hence the XPS results show that Ge is forming bonds with Te. This will lower the tendency for Te to bind to the Cu, which in turn lowers the tendency for the Cu in the filament to go back to the supply layer. This could explain the lower drift contribution to the reset which results in an improved filament stability.

D. Conclusions

We investigated the influence of Ge alloying a $Cu_{0.6}Te_{0.4}$ layer on its thermal stability and its functionality as cation supply layer in CBRAM. *In situ* XRD measurements show an amorphous as-deposited layer when more than 10 at% Ge is added. The crystallization temperature can significantly be increased up to $300°C$ by adding 30 at% Ge. Upon crystallization however, phase separation occurs which might lead to fluctuations in device parameters when implemented in CBRAM cells. To sustain typical BEOL temperatures up to $400°C$, the Cu_2GeTe_3 composition might be more interesting because upon crystallization, only one phase is formed. This was demonstrated by means of *in situ* XRD, showing only diffraction peaks of crystalline Cu_2GeTe_3. CBRAM functionality was investigated for pure $Cu_{0.6}Te_{0.4}$ and when the layer is alloyed with 20 and 30 at% Ge, as well as the Cu_2GeTe_3 composition. To this end, the alloys are implemented in 580 µm diameter dot Pt/$Cu_xTe_yGe_{1-x-y}$/Al_2O_3/n^+ Si memory cells. Functional CBRAM is demonstrated, with increased filament stability for the Ge alloyed cells. Improved retention properties compared to $Cu_{0.6}Te_{0.4}$ based cells are demonstrated. We attribute this to the formation of Ge-Te bonds in the copper supply layer, which is confirmed by XPS measurements. In this way, there is a lower tendency for Te to form copper-tellurides, lowering the driving force for Cu to go back to the supply layer and hence increasing LRS stability.

Acknowledgments

W. Devulder acknowledges the *Agency for Innovation by Science and Technology (IWT)* for a PhD scholarship. Johan Meersschaut is acknowledged for RBS measurements.

References

[1] R. Waser, R. Dittmann, G. Staikov, and K. Szot, *Adv. Mater.* **21**(25-26), 2632–2663 (2009).

[2] F. Pan, S. Gao, C. Chen, C. Song, and F. Zeng, *Mater. Sci. Eng., R* **83**, 1 – 59 (2014).

[3] Y. Bernard, V. T. Renard, P. Gonon, and V. Jousseaume, *Microelectron. Eng.* **88**(5), 814–816 (2011).

[4] A. Belmonte, W. Kim, B. T. Chan, N. Heylen, A. Fantini, M. Houssa, M. Jurczak, and L. Goux, *IEEE Trans. Electron Devices* **60**(11), 3690–3695 (2013).

[5] M. Kozicki, M. Park, and M. Mitkova, *IEEE Trans. Nanotechnol.* **4**(3), 331–338 (2005).

[6] H. Radhakrishnan, In *15th IEEE Mediterranean Electrotechnical Conference*, 515–520, (2010).

[7] K. Aratani, K. Ohba, T. Mizuguchi, S. Yasuda, T. Shiimoto, T. Tsushima, T. Sone, K. Endo, A. Kouchiyama, S. Sasaki, A. Maesaka, N. Yamada, and H. Narisawa, *Int. Electron Devices Meet.* , 783 –786 (2007).

[8] L. Goux, K. Opsomer, R. Degraeve, R. Muller, C. Detavernier, D. J. Wouters, M. Jurczak, L. Altimime, and J. A. Kittl, *Appl. Phys. Lett.* **99**(5), 053502 (2011).

[9] W. Devulder, K. Opsomer, J. Meersschaut, D. Deduytsche, M. Jurczak, L. Goux, and C. Detavernier, *ACS Comb. Sci.* **17**(5), 334–340 (2015).

[10] K.-H. Nam, J.-H. Kim, W.-J. Cho, and H.-B. Chung, *Appl. Phys. Lett.* **102**(19), 192106 (2013).

[11] E. Vianello, G. Molas, F. Longnos, P. Blaise, E. Souchier, C. Cagli, G. Palma, J. Guy, M. Bernard, M. Reyboz, G. Rodriguez, A. Roule, C. Carabasse, V. Delaye, V. Jousseaume, S. Maitrejean, G. Reimbold, B. De Salvo, F. Dahmani, P. Verrier, D. Bretegnier, and J. Liebault, In *2012 IEEE Int. Electron Devices Meet. (IEDM)*, 31.5.1–31.5.4. IEEE, IEEE, (2012).

[12] S. Wu, T. Tsuruoka, K. Terabe, T. Hasegawa, J. P. Hill, K. Ariga, and M. Aono, *Adv. Funct. Mater.* **21**(1), 93–99 (2011).

[13] M. Tada, K. Okamoto, T. Sakamoto, M. Miyamura, N. Banno, and H. Hada, *IEEE Trans. Electron Devices* **58**(12), 4398–4406 (2011).

[14] S. Gao, C. Song, C. Chen, F. Zeng, and F. Pan, *J. Phys. Chem. C* **116**(33), 17955–17959 (2012).

[15] S. Gao, C. Song, C. Chen, F. Zeng, and F. Pan, *Appl. Phys. Lett.* **102**(14), 141606 (2013).

[16] S. Gao, C. Chen, Z. Zhai, H. Y. Liu, Y. S. Lin, S. Z. Li, S. H. Lu, G. Y. Wang, C. Song, F. Zeng, and F. Pan, *Appl. Phys. Lett.* **105**(6), 063504 (2014).

[17] J. Yu, B. Liu, T. Zhang, Z. Song, S. Feng, and B. Chen, *Appl. Surf. Sci.*

253(14), 6125 – 6129 (2007).

[18] B. J. Kooi and J. T. M. De Hosson, *J. Appl. Phys.* **95**(9), 4714–4721 (2004).

[19] M. Lankhorst, *J. Non-Cryst. Solids* **297**(2-3), 210 – 219 (2002).

[20] G. E. Delgado, A. J. Mora, M. Pirela, A. Velasquez-Velasquez, M. Villarreal, and B. J. Fernandez, *Phys. Status Solidi A* **201**(13), 2900–2904 (2004).

[21] International Centre for Diffraction Data, Newtown Square, PA, *JCPDS Data Card no. 01-089-2880*, (2004).

[22] Springer & Material Phases Data System (MPDS), Switzerland & National Institute for Materials Science (NIMS), Japan, 2014, `http://materials.springer.com/isp/phase-diagram/docs/c_0926573`, *LINUS PAULING FILE Multinaires Edition - 2012 Dataset ID c_0926573*.

[23] Springer & Material Phases Data System (MPDS), Switzerland & National Institute for Materials Science (NIMS), Japan, 2014, `http://materials.springer.com/isp/phase-diagram/docs/c_0926569`, *LINUS PAULING FILE Multinaires Edition - 2012 Dataset ID c_0926569*.

[24] Springer & Material Phases Data System (MPDS), Switzerland & National Institute for Materials Science (NIMS), Japan, 2014, `http://materials.springer.com/isp/phase-diagram/docs/c_0926574`, *LINUS PAULING FILE Multinaires Edition - 2012 Dataset ID c_0926574*.

[25] Springer & Material Phases Data System (MPDS), Switzerland & National Institute for Materials Science (NIMS), Japan, 2014, `http://materials.springer.com/isp/phase-diagram/docs/c_0926568`, *LINUS PAULING FILE Multinaires Edition - 2012 Dataset ID c_0926568*.

[26] Springer & Material Phases Data System (MPDS), Switzerland & National Institute for Materials Science (NIMS), Japan, 2014, `http://materials.springer.com/isp/phase-diagram/docs/c_0926575`, *LINUS PAULING FILE Multinaires Edition - 2012 Dataset ID c_0926575*.

[27] Springer & Material Phases Data System (MPDS), Switzerland & National Institute for Materials Science (NIMS), Japan, 2014, `http://materials.springer.com/isp/phase-diagram/docs/c_0926570`, *LINUS PAULING FILE Multinaires Edition - 2012 Dataset ID c_0926570*.

[28] W. Devulder, K. Opsomer, F. Seidel, A. Belmonte, R. Muller, B. De Schutter, H. Bender, W. Vandervorst, S. Van Elshocht, M. Jurczak, L. Goux, and C. Detavernier, *ACS Appl. Mater. Interfaces* **5**(15), 6984–6989 (2013).

[29] W. Devulder, K. Opsomer, A. Franquet, J. Meersschaut, A. Belmonte, R.

Muller, B. De Schutter, S. Van Elshocht, M. Jurczak, L. Goux, and C. Detavernier, *J. Appl. Phys.* **115**(5), 054501 (2014).

[30] A. Pashinkin and V. Fedorov, *Inorg. Mater.* **39**(6), 539–554 (2003).

[31] International Centre for Diffraction Data, Newtown Square, PA, *JCPDS Data Card no. 00-049-1411*, (2004).

[32] K. Barmak, C. Cabral, K. P. Rodbell, and J. M. E. Harper, *J. Vac. Sci. Technol., B* **24**(6), 2485–2498 (2006).

[33] B. Li, C. Christiansen, D. Badami, and C.-C. Yang, *Microelectron. Reliab.* **54**(4), 712 – 724 (2014).

[34] International Centre for Diffraction Data, Newtown Square, PA, *JCPDS Data Card no. 00-045-1288*, (2004).

[35] C.-M. Lee, Y.-I. Lin, and T.-S. Chin, *J. Mater. Res.* **19**, 2929–2937 (2004).

[36] Y. Lu, S. Song, Z. Song, F. Rao, L. Wu, M. Zhu, B. Liu, and D. Yao, *Appl. Phys. Lett.* **100**(19), 193114 (2012).

[37] International Centre for Diffraction Data, Newtown Square, PA, *JCPDS Data Card no. 00-004-0545*, (2004).

[38] International Centre for Diffraction Data, Newtown Square, PA, *JCPDS Data Card no. 00-052-0849*, (2004).

[39] International Centre for Diffraction Data, Newtown Square, PA, *JCPDS Data Card no. 00-022-0312*, (2004).

[40] International Centre for Diffraction Data, Newtown Square, PA, *JCPDS Data Card no. 00-047-1079*, (2004).

[41] Y. Sutou, T. Kamada, M. Sumiya, Y. Saito, and J. Koike, *Acta Mater.* **60**(3), 872 – 880 (2012).

[42] T. Kamada, Y. Sutou, M. Sumiya, Y. Saito, and J. Koike, *Thin Solid Films* **520**(13), 4389 – 4393 (2012).

[43] Y. Saito, Y. Sutou, and J. Koike, *Appl. Phys. Lett.* **102**(5), 051910 (2013).

[44] International Centre for Diffraction Data, Newtown Square, PA, *JCPDS Data Card no. 00-036-1452*, (2004).

[45] J. Guy, G. Molas, E. Vianello, F. Longnos, S. Blanc, C. Carabasse, M. Bernard, J. Nodin, A. Toffoli, J. Cluzel, P. Blaise, P. Dorion, O. Cueto, H. Grampeix, E. Souchier, T. Cabout, P. Brianceau, V. Balan, A. Roule, S. Maitrejean, L. Perniola, and B. De Salvo, In *2013 IEEE Int. Electron Devices Meet. (IEDM)*, 30.2.1–30.2.4, (2013).

[46] X. Xu, H. Lv, H. Liu, Q. Luo, T. Gong, M. Wang, G. Wang, M. Zhang, Y. Li, Q. Liu, S. Long, and M. Liu, *Nanoscale Res. Lett.* **10**(1), 61 (2015).

[47] J. Jameson, P. Blanchard, C. Cheng, J. Dinh, A. Gallo, V. Gopalakrishnan, C. Gopalan, B. Guichet, S. Hsu, D. Kamalanathan, D. Kim, F. Koushan, M. Kwan, K. Law, D. Lewis, Y. Ma, V. McCaffrey, S. Park, S. Puthenthermadam, E. Runnion, J. Sanchez, J. Shields, K. Tsai, A. Tysdal, D. Wang, R. Williams, M. Kozicki, J. Wang, V. Gopinath, S. Hollmer, and M. Van Buskirk, In *2013*

IEEE Int. Electron Devices Meet. (IEDM), 30.1.1–30.1.4, (2013).

[48] Q. Xie, S. Deng, M. Schaekers, D. Lin, M. Caymax, A. Delabie, X.-P. Qu, Y.-L. Jiang, D. Deduytsche, and C. Detavernier, *Semicond. Sci. Technol.* **27**(7), 074012 (2012).

[49] C. Wagner, W. Riggs, L. Davis, and J. Moulder, *Handbook of X-ray Photoelectron Spectroscopy*, Perkin-Elmer Corporation, Physical Electronics Division, (1979).

[50] Y. Saito, Y. Sutou, and J. Koike, *J. Phys. D: Appl. Phys.* **45**(40), 405302 (2012).

Supporting Information

Table S1. *Composition of the prepared samples determined by RBS or XRF.*

Sample	Technique	Cu (at%)	Te (at%)	Ge (at%)
$Cu_{0.6}Te_{0.4}$	XRF	59.6	40.4	/
CuTeGe5	XRF	58.9	35.6	5.5
CuTeGe10	RBS	54.9	33.4	11.7
CuTeGe20	RBS	49.7	30.6	19.7
CuTeGe30	XRF	44.2	27.3	28.5
CuTeGe40	XRF	39.6	24.3	36.1
CuTeGe50	XRF	31.7	19.1	49.2
Cu_2GeTe_3	XRF	32.7	50.3	17
Cu_2GeTe_3 Te rich	XRF	29.5	56.9	13.6
Cu_2GeTe_3 Te poor	XRF	37.5	44.5	18

Table S2. *Composition of the Te rich and Te poor Cu_2GeTe_3 layers before and after anneal at 400°C, determined by XRF.*

Sample	Cu (at%)	Ge (at%)	Te (at%)
Cu_2GeTe_3 Te rich as-deposited	29.5	13.6	56.9
Cu_2GeTe_3 Te rich anneal 400°C	33.6	15.4	51
Cu_2GeTe_3 Te poor as-deposited	37.5	18	44.5
Cu_2GeTe_3 Te poor anneal 400°C	37.3	18.3	44.4

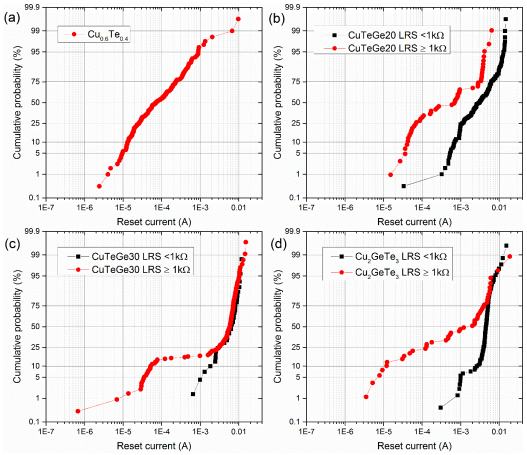

Figure S1. *Cumulative probability of the reset currents for (a) $Cu_{0.6}Te_{0.4}$, (b) CuTeGe20, (c) CuTeGe30 and (d) Cu_2GeTe_3 based CBRAM cells. All LRS resistances are larger than 1 kΩ in (a). For (b)-(d) the reset currents of filaments with LRS resistances smaller than or larger than 1 kΩ are represented separately. A larger fraction of the reset operations show higher reset currents for the Ge containing supply layers.*

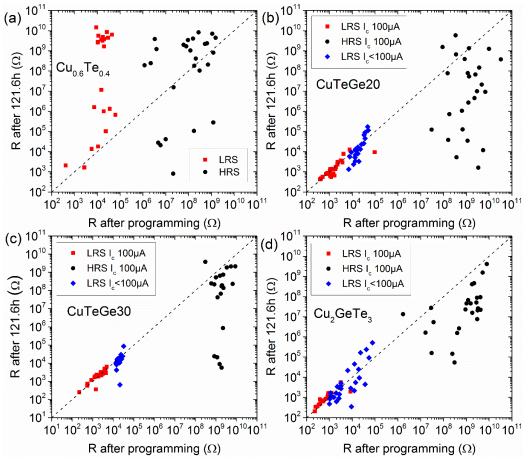

Figure S2. *Resistance after 121.6 hour baking at 85C as a function of the resistance after programming for memory cells with (a) $Cu_{0.6}Te_{0.4}$, (b) CuTeGe20, (c) CuTeGe30 and (d) Cu_2GeTe_3 as Cu supply layer.*

Paper V

Study of amorphous Cu-Te-Si thin films showing high thermal stability for application as a cation supply layer in Conductive Bridge Random Access Memory devices*

Abstract

In this work we demonstrate a thermally stable copper supply layer by Si alloying of $Cu_{0.6}Te_{0.4}$ for application in Conductive Bridge Random Access Memory (CBRAM) cells. A good thermal stability of the copper supply layer is necessary to allow its implementation in future memory devices. *In situ* X-ray diffraction is used to investigate the crystallization behaviour for $Cu_{0.6}Te_{0.4}$ layers with Si contents up to 20 at%. Low Si concentrations result in crystallization, phase separation and transformations at temperatures below $400°C$, whereas addition of 20 at% Si results in a layer that remains amorphous up to temperatures exceeding $500°C$, making it compatible with back end of line temperatures. Moreover, atomic force microscopy measurements show a very smooth surface morphology up to temperatures exceeding $400°C$. The absence of grain boundaries in the amorphous layer is expected to contribute to the uniformity of the supply layer, and hence it should be beneficial for integration in scaled devices. We attribute the good ability of Si to keep the material amorphous to the high coordination number of Si and the formation of strong bonds which are difficult to break, making rearrangement in a lattice more difficult to proceed. This is further evidenced by XPS measurements, which suggest the occurrence of both Si-Si and Si-Te bonds. CBRAM functionality of this composition is demonstrated by integrating the material in 580 µm diameter dot Pt/Cu-Te-Si/Al_2O_3/n^+ Si CBRAM cells.

*Manuscript in preparation

A. Introduction

New memory technologies are currently explored as an alternative for charge-based memories. Among the emerging technologies one finds the resistive types of Random Access Memory (RRAM)[1]. In these devices, the different memory states (i.e. logic 0 or 1) are stored as different resistive states of the cells. Conductive Bridge Random Access Memory (CBRAM) is a type of RRAM and relies on the formation and dissolution of conductive filaments through an insulating layer, allowing cycling between a high (HRS) and low resistive state (LRS)[2,3]. A typical CBRAM cell consists of a Cu (or Ag) containing layer, an insulating layer and an inert bottom electrode. A positive bias on the Cu supply layer results in oxidation of Cu and migration of these cations through the insulating layer. A filament is grown and the cell switches to the low resistive state when the filament bridges both electrodes. The cell can be switched back to the high resistive state by applying a negative bias on the cation supply layer, resulting in filament dissolution.

A multitude of materials are reported that can be used as cation supply layer and switching layer. Chalcogenide materials[4–6], polymers[7–9] and binary metal oxides[10,11] are commonly used as a switching layer. For the cation supply layer, next to pure Cu[10,12] or Ag[4,13] electrodes, also alloys containing Cu or Ag like Cu-Te[14–16] or Ag-Te[17] have been demonstrated. The reason to use Cu or Ag alloys is to improve the CBRAM switching performance/cycling behaviour[15,17,18] and retention properties[19,20] (i.e. how good a programmed memory state is maintained). The Cu_xTe_{1-x} alloy showed improved CBRAM performance over pure Cu in the composition range $0.5 < x < 0.7$ when implemented in macroscopic Pt/Cu_xTe_{1-x}/Al_2O_3/n^+ Si CBRAM dot cells[15]. However, care should be taken to ensure good thermal stability of the alloy to be compatible with the processing temperatures that are applied during integration of the material in a device. For back end of line (BEOL) compatibility, the material should be stable up to typically $400°C$. The copper-telluride system has a complex phase diagram[21], showing multiple intermetallic phases. If the composition is different from these, phase separation might occur which could result in fluctuation of device parameters when integrated in memory devices. Moreover, multiple high temperature phases occur which imply phase transformations of the material under annealing.

Silicon as an alloying element has been reported to be effective in increasing the crystallization temperature in materials for phase change memories[22]. In this work, we show that addition of Si to a $Cu_{0.6}Te_{0.4}$ layer is very effective to inhibit crystallization of Cu-Te phases, and addition of 20 at% keeps the material amorphous up to temperatures exceeding $500°C$, making this a very temperature stable material. The influence of Si and the bonds that it forms is further investigated by X-ray photoelectron spectroscopy. Furthermore, the Cu_2SiTe_3 compound[23] is also investigated and compared to Cu_2GeTe_3. The glass transition temperature,

which is a lower limit for the crystallization temperature, is calculated for both compounds using the model of Lankhorst[24], which further contributes to the understanding of the influence of Si.

As the $Cu_{0.6}Te_{0.4}$ alloyed with 20 at% Si shows very good thermal stability, its functionality as a cation supply layer in CBRAM is investigated. The material is integrated in 580 µm diameter dot Pt/CuTeSi20/Al_2O_3/n^+ Si memory cells, where the Al_2O_3 serves as a dedicated switching layer. The resistive switching behaviour and the retention of the memory states is then studied.

B. Experimental procedures

The Cu-Te-Si alloys were deposited by co-sputtering from pure Cu, Te and Si sputter targets. The compositions can easily be varied by adjusting the sputter power applied on the different targets, while the sputter time determines the total layer thickness. Layers which were 50 nm thin with a constant Cu/Te ratio of 1.5 and with 5, 10 and 20 at% Si were deposited to investigate the influence of the Si content. The thin films were deposited on silicon substrates that were covered with 20 nm Al_2O_3, where the alumina was deposited by a H_2O based atomic layer deposition (ALD) process. Also a film with the correct stoichiometry to obtain the single Cu_2SiTe_3 phase was deposited. The compositions were verified by means of Rutherford backscattering spectroscopy (RBS).

The thermal stability of the films in terms of crystallization and phase separation were investigated by means of *in situ* X-ray diffraction. A Bruker D8 Discover diffractometer equipped with a home-built annealing chamber allows to record the XRD pattern in a fixed 2θ range of 20° during anneal. In this work, the films were annealed at a heating rate of $0.5°C/\mathrm{s}$ in inert He atmosphere and an XRD pattern was collected every 4 s. In this way, phase transformations can be monitored, giving information on the thermal stability of the material. The morphology of the layers was inspected by means of atomic force microscopy (AFM). The measurements are performed on a a Bruker Dimension Edge AFM, operated in tapping mode.

X-ray photoelectron spectroscopy (XPS) was used to study the bond formation of Si. The measurements are conducted on a Theta Probe system of Thermo Scientific, operating at a base pressure of $\sim 10^{-10}$ mbar. The system has an Al X-ray excitation source and a channel plate detector. For all XPS measurements, a surface scan is collected and the surface carbon peak at 284.6 eV was used as a binding energy reference. Then spectra were acquired after removing the surface contamination by Ar sputtering using an EX05 Ar ion gun.

The functionality of the Cu-Te-Si alloy as a cation supply layer in CBRAM is investigated by integrating the material in 580 µm diameter dot CBRAM cells with a dedicated Al_2O_3 switching layer. To this end, a Pt/Cu-Te-Si stack (50/50 nm)

is deposited by magnetron sputter deposition through a shadow mask on a 3 nm Al_2O_3/n^+ Si substrate. A Keithley 2601A sourcemeter is used to cycle the cells. Linear DC voltage sweeps with a sweep rate of $0.5\,V/s$ are applied on the Pt top electrode with respect to the bottom electrode. In the set sweep, the current is limited to a compliance current (I_c) to avoid overgrown filaments. Retention of the programmed memory states is investigated at $85°C$. After cycling the cells two times, the cells are programmed to their high or low resistive state. The cells are then baked up to 121.6 h in He atmosphere while they are periodically taken out of the oven to measure their resistance.

C. Results and discussion

Thermal stability of the alloys

The compositions of the Si alloyed films that are further investigated in this work are determined by RBS, and are given in table 1. The films with a Cu/Te ratio of $\sim$1.5 and where 5, 10 and 20 at% Si is added are further denoted as CuTeSi5 up to CuTeSi20. The layers were investigated by means of *in situ* XRD to investigate the crystallization behavior and to identify the phases that occur. Figure 1 shows the result for the different samples, and a reference of $Cu_{0.6}Te_{0.4}$ is given in Figure 1a. If no Si is added, the hexagonal $Cu_{2-x}Te$[25] phase is formed already during deposition, and multiple transformations occur upon annealing, as was discussed already in previous work[26,27]. Addition of only $\sim$5 at% Si avoids the crystallization of $Cu_{2-x}Te$[25] up to $138°C$. The crystallization temperature (T_x) in this work is defined as the temperature where the maximum change in the diffraction peak intensity occurs. Addition of 10 at% Si further increases T_x towards $255°C$, although the (006) peak of $Cu_{2-x}Te$[25] becomes visible already at temperatures slightly below $200°C$. Also the formation of the high temperature $Cu_{2-x}Te$[28] phase occurs at higher temperatures (i.e. slightly below $500°C$) compared to the samples with less Si. Addition of 20 at% Si results in a large temperature window where the material stays amorphous. Clear diffraction peaks associated to the high temperature $Cu_{2-x}Te$[28] phase start to appear only at $537°C$. Hence an amorphous window up to at least $500°C$ is obtained for this material. It can be observed that from $350°C$ on, some broad features appear near 24-27°, which is typical for an amorphous or nano-crystalline material, where no sharp diffraction peaks appear. Figure 2 shows the XRD patterns of the different Si containing layers after quenching at $350°C$, showing for the layer with 20 at% Si a signature of an amorphous halo at diffraction angles typical for hexagonal $Cu_{2-x}Te$[25].

The surface morphology of the CuTeSi20 layer was investigated by AFM and compared to $Cu_{0.6}Te_{0.4}$. Figure 3 shows the AFM images for the as-deposited layers and after anneal to $400°C$. While the as-deposited $Cu_{0.6}Te_{0.4}$ layer is rel-

Table 1. *Composition of the deposited Cu-Te-Si alloys as determined by RBS.*

Deposition	Cu (at%)	Te (at%)	Si (at%)	Cu/Te
CuTeSi5	59	37.1	3.9	1.59
CuTeSi10	56.3	35.7	8	1.58
CuTeSi20	50.7	31.8	17.5	1.59
Cu_2SiTe_3	34.8	49.7	15.5	0.70

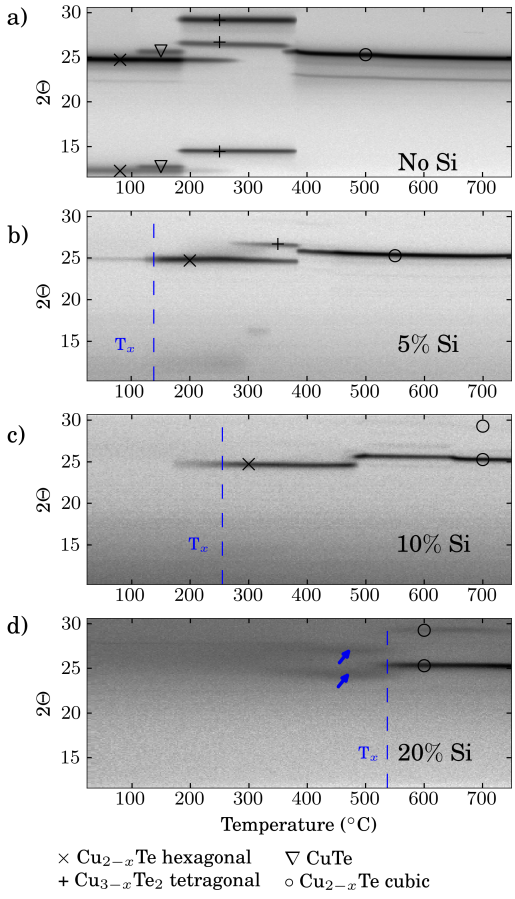

Figure 1. *In situ XRD patterns during anneal at 0.5°C/s of a 50 nm $Cu_{0.6}Te_{0.4}$ thin film and when 5 (b), 10 (c) and 20 at% Si (d) is added. The nanocrystalline traces are indicated with arrows in (d).*

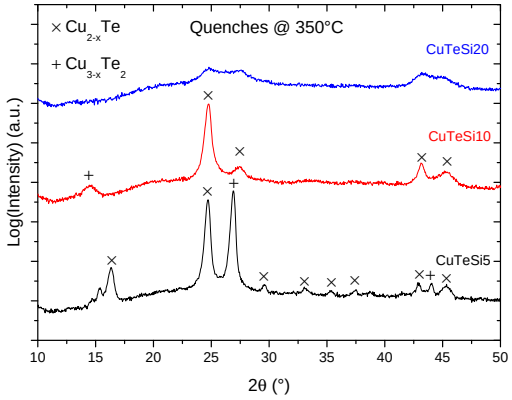

Figure 2. *XRD patterns of the 50 nm thin films of the different Cu-Te-Si alloys after quenching at 350°C.*

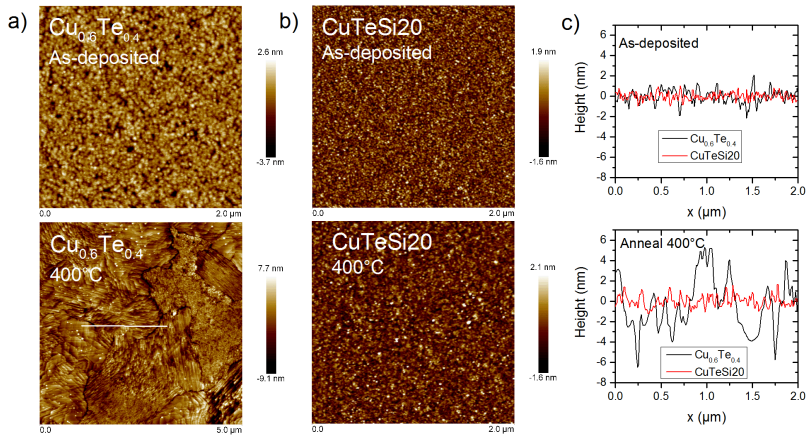

Figure 3. *AFM images of (a) a $Cu_{0.6}Te_{0.4}$ and (b) a CuTeSi20 layer, both as-deposited and after anneal to 400°C. (c) A horizontal cross section through the center of the images of the as-deposited samples (top) and after anneal (bottom). As the image for $Cu_{0.6}Te_{0.4}$ is on a larger scale, the shown cross section is indicated in the image.*

ative smooth with a root mean square roughness (rms) of 0.84 nm, the surface roughness drastically increases after anneal to 400°C (rms=2.19 nm). A polycrystalline rough layer is formed and cracks occur, preferentially at grain boundaries. The CuTeSi20 layer on the other hand remains very smooth, with rms of 0.49 and 0.52 nm before and after anneal respectively. The layer does not show any cracks after anneal to 400°C. To summarize this section, it is clear that the ther-

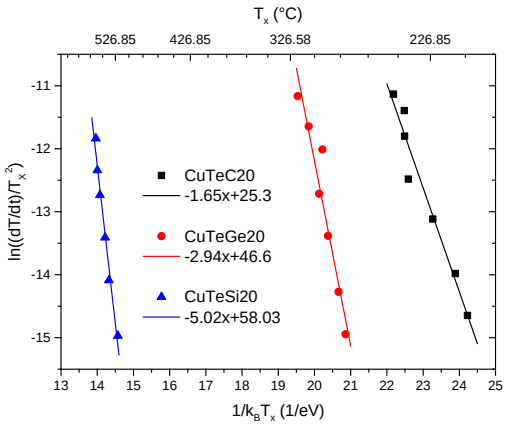

Figure 4. *Extraction of the activation energy for crystallization of 50 nm thin films of CuTeC20, CuTeGe20 and CuTeSi20.*

mal stability is significantly improved by Si alloying because of the absence of crystallization and phase separation, and the smooth surface morphology up to $400°C$.

Crystallization of the alloys

The question remains why Si is that efficient to avoid crystallization. In previous work we investigated the influence of carbon[27] and germanium[29] on the Cu-Te phase formation. For both materials, the as-deposited layers were amorphous and the crystallization temperature increased towards $200°C$ for a concentration of 20 at% of the alloying element[27,29]. For Si, the crystallization temperature is increased towards $500°C$. Hence Si turns out to be more effective to increase the crystallization temperature. This was also quantified by means of Kissinger analysis[30]. Additional samples of 50 nm $Cu_{0.6}Te_{0.4}$ alloyed with 20 at% C and Ge (further denoted as CuTeC20 and CuTeGe20 respectively) were prepared to perform Kissinger analysis and to compare with CuTeSi20. More information on this analysis is given in the Supporting Information. The samples are annealed at different heating rates ranging from 0.1 to $5°C/$s, and the crystallization temperature was extracted (see Figure S1 in the Supporting Information). By plotting $\ln((\mathrm{d}T/\mathrm{d}t)/T_x^2)$ as a function of $1/k_BT_x$, the activation energy (E_a) is extracted from a linear fit, as illustrated in Figure 4. For the CuTeSi20 layer, E_a is 5.02 eV and significantly higher than for CuTeGe20 and CuTeC20, which have E_a of 2.94 and 1.65 eV respectively.

The high E_a for crystallization and the high T_x for the Si alloyed sample can be explained by the high bond strength of Si with Cu and Te, and the strong Si-Si

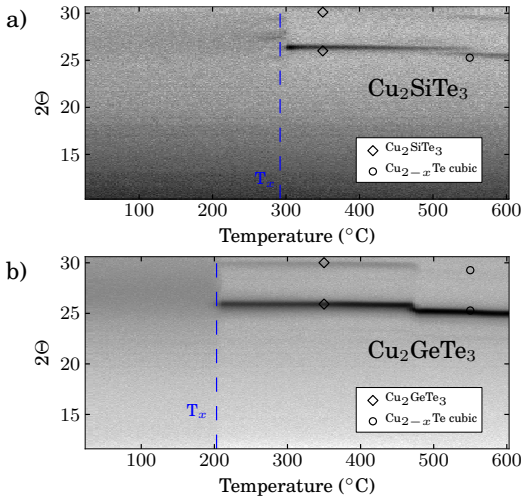

Figure 5. *In situ XRD pattern of a 50 nm thin film of (a) Cu_2SiTe_3 and (b) Cu_2GeTe_3, collected at a heating rate of 0.5°C/s in He atmosphere.*

bonds that are formed. These bonds need to be broken to allow reorganization of the atoms in a lattice, explaining the increased T_x [22,31,32]. Lankhorst [24] proposed a model to calculate the glass transition temperature (T_g), which is a lower limit for T_x. It has been successfully applied to calculate T_g and T_x for phase change materials [22,33,34]. The model takes both the number of bonds and their strength into account. It assumes that the bonding between the elements is mainly covalent, meaning that maximum four bonds with neighbouring atoms can be formed. Unfortunately, the model cannot be applied to CuTeSi20 because there is not enough Te to account for a mean coordination number of 4 or less. However, the model can be applied to the compounds Cu_2SiTe_3 and Cu_2GeTe_3. These can be compared to investigate the influence of the alloying element. The crystallization temperature is determined from *in situ* XRD, and is depicted in Figure 5 for both a Cu_2SiTe_3 and Cu_2GeTe_3 layer (more details on Cu_2GeTe_3 can be found in previous work [29]). It is clear that also here the compound with Si has the highest crystallization temperature. The glass forming temperature for these compounds is calculated using the model of Lankhorst [24]. An empirical relation between the glass forming temperature and the mean bond enthalpy H_a exists [24]:

$$T_g(K) = 3.44H_a - 480. \tag{1}$$

The mean bond enthalpy of the alloy can be calculated from the weighted sum of the heteronuclear bond enthalpies between the elements. The heteronuclear bond enthalpy H_{AB} between elements A and B can be extracted from the homonuclear

Table 2. *Homonuclear bond entalpies (H_{AA}), electronegativity (S) and the number of valence electrons (N_A) of Ge, Si, Te and Cu[24]. The heteronuclear bond enthalpies (H_{AB}) are calculated from Pauling's equation.*

Element	N_A	S_A	Bond	H_{AA} (kJ/mol)	H_{AB} (kJ/mol)
Ge	4	2.01	Ge-Ge	186	
Si	4	1.9	Si-Si	225	
Te	6	2.1	Te-Te	197	
Cu	1	1.9	Cu-Cu	19	
			Ge-Te		192.3
			Si-Te		214.85
			Cu-Si		122
			Cu-Ge		103.66
			Cu-Te		111.8

bond enthalpies (H_{AA} and H_{BB}) using Pauling's equation[24]

$$H_{AB} = \frac{H_{AA} + H_{BB}}{2} + 96.14 * (S_A - S_B)^2, \tag{2}$$

where S_A is the electronegativity of element A. These are given in table 2 for the elements relevant to this work. The total bonding enthalpy can then be found as[24]

$$H_a = \sum n_{AB} H_{AB}, \tag{3}$$

where n_{AB} is the number of A-B bonds. Hence the stronger the bonds, the higher T_g and the higher T_x. Note that from table 2 it is clear that bonds of Si with Te and Cu are all stronger compared to Ge, which suggests already a higher T_x for the Si compound. To calculate T_g, n_{AB} needs to be calculated and a few assumptions are made here. First every element in the covalent structure has a preferred coordination number (or number of bonds) which satisfies the 8-N rule, with N the number of s and p valence electrons. As the bonding between the elements is covalent, maximum four bonds with neighbouring atoms can be formed. The mean coordination number Z hence cannot be larger than four for the model to be applicable. As Cu has only one valence electron, this would lead to more than four bonds. To solve this, a formal transfer of electrons from the chalcogenide atoms to the Cu atoms is introduced, and in this way the coordination number of the chalcogen atom is increased and that of the Cu atom reduced to four. It is clear that this is only possible for compositions where enough Te is present. The model can be applied to Cu_2(Si,Ge)Te_3 as the mean coordination number is 4. The total number of bonds is then equal to the mean coordination number divided by 2 to

Table 3. *Calculation of the glass transition temperatures of Cu_2SiTe_3 and Cu_2GeTe_3, and the measured crystallization temperature.*

Material	Z	A-B bond	H_{AB} (kJ/mol)	n_{AB}	H_a (kJ/mol)	T_g ($^\circ C$)	T_x ($^\circ C$)
Cu_2SiTe_3	4				292.31	252.4	292
		Si-Te^{IV}	214.85	0.6668			
		Cu^{IV}-Te^{IV}	111.8	1.3332			
Cu_2GeTe_3	4				277.3	200.68	203
		Ge-Te^{IV}	192.3	0.6668			
		Cu^{IV}-Te^{IV}	111.8	1.3332			

avoid double counting of bonds. The other assumptions that are made are that heteronuclear bonds are preferred over homonuclear bonds and that bonds are formed in the sequence of decreasing bond enthalpy. The glass transition temperatures of Cu_2SiTe_3 and Cu_2GeTe_3 were calculated in this way and this is given in table 3. Both Si and Ge have 4 valence electrons, whereas Cu has only one. Two Te atoms will give each 2 electrons to a Cu atom, and the Te atom that is left will give one electron to each Cu atom. In this way, all elements have 4 valence electrons and the mean coordination number Z is 4. The number of bonds is Z/2 and equal to 2. The formal valence of 4 for Cu and Te is denoted as a roman number in superscript to emphasize the formal electron transfer. For Cu_2SiTe_3, the Si-Te bond has the highest bond enthalpy and is formed first. There is a fraction of 0.1667 Si atoms wich will form 4 bonds with Te. Hence 0.1667 Te atoms are consumed and 0.6668 Si-Te bonds are formed (n_{Si-Te}). There are 0.333 Te atoms left that will form 4 bonds with the remaining 0.333 Cu atoms, forming a total number of 1.3332 Cu-Te bonds (n_{Cu-Te}). The same reasoning applies to Cu_2GeTe_3.

The calculated T_g is indeed lower than T_x (see table 3), and T_g of Cu_2SiTe_3 is higher than for Cu_2GeTe_3. From this model, the higher crystallization temperature is due to the stronger Si-Te bond compared to Ge-Te. Accordingly, this can also explain the higher crystallization temperature for the Si alloyed $Cu_{0.6}Te_{0.4}$. Saito et al.[22] applied the model of Lankhorst to Si alloyed GeTe thin films and found for higher Si contents a higher crystallization temperatures than expected from calculations[33]. They attributed this to the strong homonuclear Si-Si bond (table 2 shows a homonuclear bond enthalpy for Si that is larger than all other homo- or heteronuclear bonds) and the formation of strong Si-Si bonds next to heteronuclear bonds. Hence the formation of Si-Si chains might also occur and contribute to the inhibited crystallization of Cu-Te phases, resulting in the high crystallization temperature of CuTeSi20.

To further investigate the role of Si, XPS measurements were performed on the

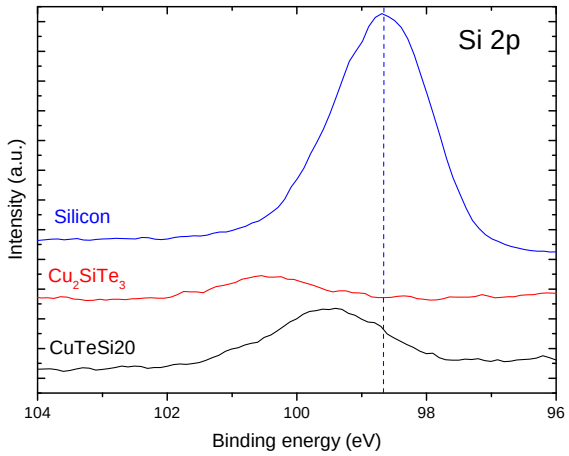

Figure 6. *XPS spectra of the Si 2p peaks of a pure sputtered Si layer, a Cu_2SiTe_3 and a CuTeSi20 film.*

CuTeSi20 and Cu_2SiTe_3 sample. Figure 6 shows the Si 2p peaks for both samples together with a reference of a pure sputtered Si film. It is clear that the peak is shifted towards higher binding energies for the alloys compared to the pure sputtered Si film. This can be related to the formation of Si-Te bonds, where Te will get reduced and Si will get oxidized due to the higher electronegativity of Te. It is interesting to note that the Si peak for CuTeSi20 is in between pure Si and the peak of Cu_2SiTe_3. This suggests the occurrence of more Si-Si bonds in the CuTeSi20 layer compared to Cu_2SiTe_3. This is in agreement with literature[22], and was also ascribed already to the high Si-Si bond enthalpy. Hence the XPS results are in agreement with the high T_x of CuTeSi20 that was measured, where it was suggested that strong Si-Si chains might be formed, hampering crystallization. Note that it is also reasonable that more Si-Si bonds are formed in CuTeSi20 compared to Cu_2SiTe_3 due to the lower fraction of Te for the former, whereas much more Te is present in the latter, making Si-Te interaction more likely there.

CBRAM functionality

In the previous section we showed that a $Cu_{0.6}Te_{0.4}$ layer with 20 at% Si showed the most promising thermal stability of the investigated Cu-Te-Si compositions. This material is now integrated as a cation supply layer in Pt/CuTeSi20/Al_2O_3/n^+ Si CBRAM cells and the as-deposited cells are characterized. A typical current-voltage sweep is depicted in Figure 7a. The LRS and HRS for 45 devices $\times$ 10 cycles (I_c=100 µA) is given in a boxplot in Figure 7b, showing a median resistive window of more than 4 orders of magnitude. Functional CBRAM cells are

obtained, that can be reset very efficiently. This is evidenced from the low leakage current and hence high HRS resistance before the cell switches to LRS in cycle 10, which is similar to the pristine resistance. This is very similar as for pure $Cu_{0.6}Te_{0.4}$ [26] and was attributed to the preferred formation of Cu-Te bonds, which is an additional driving force for Cu from the filament to go back to the supply layer, enhancing the reset [15,26,29]. The efficient reset that is also observed for CuTeSi20 based cells results in promising endurance properties of the memory cells. Figure 7c shows the LRS and HRS for 1000 subsequent cycles of a memory cell, where a median resistive window of more than 4 orders of magnitude is maintained.

Retention of the programmed memory states was investigated by programming the cells to a high or low resistive state, after initially cycling the cells two times. A current compliance (I_c) of 100 µA was used but the LRS usually ends up in very low resistances (<10 kΩ). To obtain more cells in a LRS with higher resistance, a lower I_c of 50 µA was also used, as a lower compliance generally leads to higher LRS resistance [35]. Figure 8a shows the resistance of every memory cell as function of the baking time and Figure 8b shows the corresponding cumulative distribution of the resistances after programming and after 121.6 h baking at $85°C$. From the plots it is clear that the LRS states with resistance below 10 kΩ stay in a low resistive state during the whole test. For the LRS states between 10 and 100 kΩ, about 50 % tend to go to a HRS (i.e. R>1 MΩ) after 5 days baking. This can be understood because the states with higher resistances generally have smaller filaments, which are more easily dissolved, resulting in a less stable LRS [36]. If we compare those results with previous work on pure $Cu_{0.6}Te_{0.4}$ and when Ge is used as alloying element [29], we see that the LRS retention is better than the unalloyed supply layer, where more than 50 % of the cells in LRS return to HRS. However, LRS is less stable compared to a Ge alloyed $Cu_{0.6}Te_{0.4}$ layer, where all cells maintain their LRS. In the case of Ge alloying, we related the improved LRS retention to the preferred formation of Ge-Te bonds [29]. This lowers the influence of Te on Cu to form Cu-Te and lowers the driving force for Cu from the filament to go back to the supply layer, resulting in a more stable Cu filament. Note that this is also in agreement with the heteronuclear bond enthalpies in table 2, showing a higher bond enthalpy for the Ge-Te bond compared to Cu-Te. However, the Si-Te bond is even stronger according to table 2. The reason why the retention is not as good as with Ge can then be explained in two ways. First the XPS measurements suggest that next to Si-Te also Si-Si bonds can be formed because of the high homonuclear bond enthalpy of Si. Hence the influence or passivating effect of Si on Te might be smaller compared to Ge. Secondly it can be noted that the bond enthalpy of Cu-Si is also high (it is calculated to be even higher than Cu-Te), which can also be responsible for Cu consumption from the filament, resulting in LRS degradation. However, in our opinion this is less likely because in that case LRS

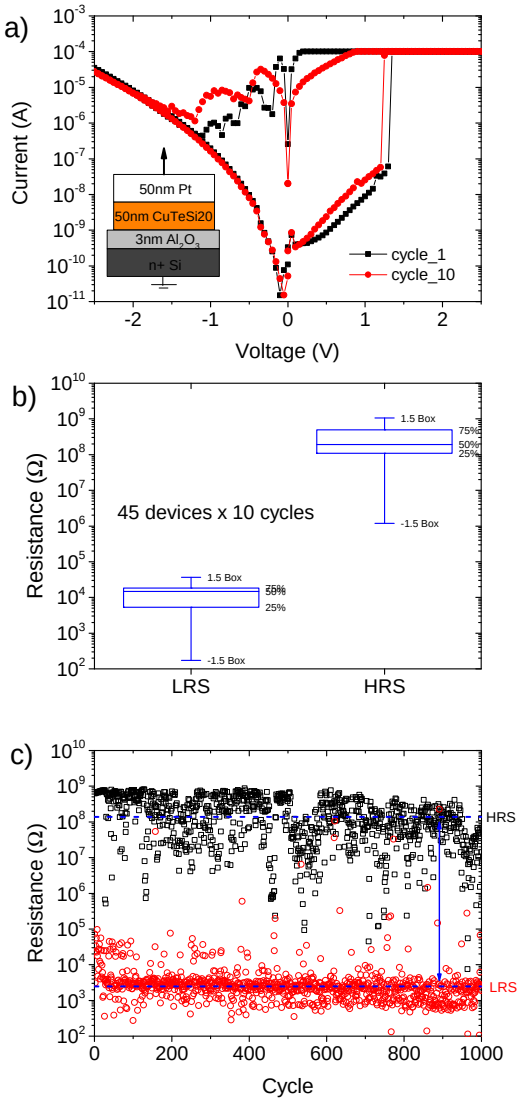

Figure 7. *(a) Current-voltage sweeps of a Pt/CuTeSi20/Al_2O_3/n^+ Si memory cell. (b) Boxplot showing LRS and HRS for 45 devices cycled 10 times with I_c of 100 µA. (c) Endurance test showing the LRS and HRS resistance of 1000 subsequent set-reset operations by applying a 100 mV read pulse after every set or reset sweep. The median LRS and HRS is indicated by a dashed line.*

retention is expected to be even worse compared to $Cu_{0.6}Te_{0.4}$ because the bond enthalpy of Cu-Si is even slightly higher than Cu-Te. So we mainly attribute the

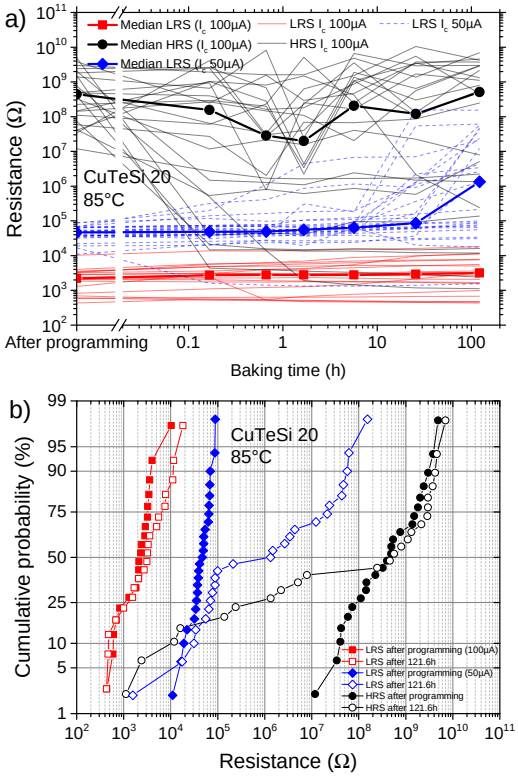

Figure 8. *Retention test of Pt/CuTeSi20/Al_2O_3/n^+ Si cells at 85°C. (a) The resistance of every memory cell is plotted as a function of the baking time. Cells with LRS<10 kΩ and cells with 10 kΩ<LRS<100 kΩ (programmed with I_c=50 µA) are plotted separately. The median resistance values are given by the thick line. (b) The corresponding cumulative distributions of the resistances after programming and after 121.6 h baking at 85°C.*

difference to a lower fraction of Si-Te bonds compared to Ge-Te due to more Si-Si bonds, resulting in a larger influence of Te on Cu-filament stability.

The median HRS stays above 10 MΩ during the whole test, and hence a median resistive window of two orders of magnitude is still present after 5 days baking at 85°C. However, there is a tail in the HRS distribution toward lower resistances. About 25 % of the cells in HRS go to a resistance below 1 MΩ. Note that this is a similar fraction as with Ge alloyed $Cu_{0.6}Te_{0.4}$ [29]. We mainly relate this to the low resistances that are reached during the first cycles, which induce a large filament template path in the Al_2O_3 layer, that acts as a defect for Cu migration and filament reconstruction. Moreover, when low resistances are reached, more Cu might be left in the switching layer after reset that can cause filament reconstruction and

HRS loss. The influence of LRS resistance on HRS retention was reported before, indicating worse HRS retention for cells that reached low LRS resistances[37]. A better current control by a select transistor might improve this[38].

D. Conclusion

We investigated the influence of Si as an alloying element on the thermal stability of a $Cu_{0.6}Te_{0.4}$ layer. The crystallization temperature increased with increasing Si content and when 20 at% Si is added, the crystallization is increased up to temperature above $500°C$. AFM measurements show a very smooth surface morphology up to $400°C$ while the $Cu_{0.6}Te_{0.4}$ reference layer is polycrystalline and very rough after anneal at these temperatures. The absence of grain boundaries further contributes to the uniformity of the layer, which should be beneficial for integration in nano-scaled devices. Its high thermal stability makes this material compatible with the temperatures applied during device processing and hence it is a viable candidate for integration in future memory devices. The high crystallization temperature can be explained by the strong Si-Te and Si-Si bonds, which hamper reorganization of the atoms in a crystal. The occurrence of these bonds was confirmed by XPS measurements. This was also illustrated by the model of Lankhorst which allows the calculation of the glass forming temperature for the Cu_2SiTe_3 and Cu_2GeTe_3 compounds, where a higher crystallization temperature was predicted and measured for the Si containing compound. Due to its good thermal stability, the $Cu_{0.6}Te_{0.4}$ layer with 20 at% Si was selected to implement in 580 µm diameter dot Pt/CuTeSi20/Al_2O_3/n^+ Si CBRAM cells. Functional CBRAM cells are obtained which can efficiently be set/reset for up to 1000 DC cycles. Furthermore the retention of the memory states was investigated and the cells with LRS resistance below 10 kΩ did not degrade for baking times of more than 5 days at $85°C$. The cells programmed to a LRS with resistances between 10 and 100 kΩ showed a 50 % chance to return to a high resistive state, which is explained by smaller filaments that are more easily dissolved.

Acknowledgments

This research was supported by a PhD grant of the *Agency for Innovation by Science and Technology (IWT)* and by the UGent-BOF GOA 01G01513. CD furthermore acknowledges the Hercules Foundation for funding SPINAL (AUGE/09/014).

References

[1] Pan, F., Gao, S., Chen, C., Song, C., and Zeng, F. *Mater. Sci. Eng., R* **83**, 1 – 59 (2014).

[2] Waser, R., Dittmann, R., Staikov, G., and Szot, K. *Adv. Mater.* **21**(25-26), 2632–2663 (2009).

[3] Valov, I. and Kozicki, M. N. *J. Phys. D: Appl. Phys.* **46**(7), 074005 (2013).

[4] Kozicki, M., Park, M., and Mitkova, M. *IEEE Trans. Nanotechnol.* **4**(3), 331–338 (2005).

[5] Vianello, E., Molas, G., Longnos, F., Blaise, P., Souchier, E., Cagli, C., Palma, G., Guy, J., Bernard, M., Reyboz, M., Rodriguez, G., Roule, A., Carabasse, C., Delaye, V., Jousseaume, V., Maitrejean, S., Reimbold, G., De Salvo, B., Dahmani, F., Verrier, P., Bretegnier, D., and Liebault, J. In *2012 IEEE Int. Electron Devices Meet. (IEDM)*, 31.5.1–31.5.4. IEEE, IEEE, (2012).

[6] Nam, K.-H., Kim, J.-H., Cho, W.-J., and Chung, H.-B. *Appl. Phys. Lett.* **102**(19), 192106 (2013).

[7] Wu, S., Tsuruoka, T., Terabe, K., Hasegawa, T., Hill, J. P., Ariga, K., and Aono, M. *Adv. Funct. Mater.* **21**(1), 93–99 (2011).

[8] Gao, S., Song, C., Chen, C., Zeng, F., and Pan, F. *J. Phys. Chem. C* **116**(33), 17955–17959 (2012).

[9] Gao, S., Song, C., Chen, C., Zeng, F., and Pan, F. *Appl. Phys. Lett.* **102**(14), 141606 (2013).

[10] Belmonte, A., Kim, W., Chan, B. T., Heylen, N., Fantini, A., Houssa, M., Jurczak, M., and Goux, L. *IEEE Trans. Electron Devices* **60**(11), 3690–3695 (2013).

[11] Gao, S., Chen, C., Zhai, Z., Liu, H. Y., Lin, Y. S., Li, S. Z., Lu, S. H., Wang, G. Y., Song, C., Zeng, F., and Pan, F. *Appl. Phys. Lett.* **105**(6), 063504 (2014).

[12] Bernard, Y., Renard, V. T., Gonon, P., and Jousseaume, V. *Microelectron. Eng.* **88**(5), 814–816 (2011).

[13] Seung, H.-M., Song, M.-J., Park, J.-G., and Kwon, K.-C. *J. Korean Phys. Soc.* **64**(7), 949–953 (2014).

[14] Aratani, K., Ohba, K., Mizuguchi, T., Yasuda, S., Shiimoto, T., Tsushima, T., Sone, T., Endo, K., Kouchiyama, A., Sasaki, S., Maesaka, A., Yamada, N., and Narisawa, H. *Int. Electron Devices Meet.* , 783 –786 (2007).

[15] Goux, L., Opsomer, K., Degraeve, R., Muller, R., Detavernier, C., Wouters, D. J., Jurczak, M., Altimime, L., and Kittl, J. A. *Appl. Phys. Lett.* **99**(5), 053502 (2011).

[16] Goux, L., Sankaran, K., Kar, G., Jossart, N., Opsomer, K., Degraeve, R., Pourtois, G., Rignanese, G. M., Detavernier, C., Clima, S., Chen, Y. Y., Fantini, A., Govoreanu, B., Wouters, D., Jurczak, M., Altimime, L., and Kittl,

J. A. *IEEE Symp. VLSI Technol.* , 69–70 (2012).

[17] Devulder, W., Opsomer, K., Meersschaut, J., Deduytsche, D., Jurczak, M., Goux, L., and Detavernier, C. *ACS Comb. Sci.* **17**(5), 334–340 (2015).

[18] Radhakrishnan, H. In *15th IEEE Mediterranean Electrotechnical Conference*, 515–520, (2010).

[19] Tada, M., Sakamoto, T., Banno, N., Okamoto, K., Iguchi, N., Hada, H., and Miyamura, M. *IEEE Trans. Electron Devices* **60**(10), 3534–3540 (2013).

[20] Jameson, J., Blanchard, P., Cheng, C., Dinh, J., Gallo, A., Gopalakrishnan, V., Gopalan, C., Guichet, B., Hsu, S., Kamalanathan, D., Kim, D., Koushan, F., Kwan, M., Law, K., Lewis, D., Ma, Y., McCaffrey, V., Park, S., Puthenthermadam, S., Runnion, E., Sanchez, J., Shields, J., Tsai, K., Tysdal, A., Wang, D., Williams, R., Kozicki, M., Wang, J., Gopinath, V., Hollmer, S., and Van Buskirk, M. In *2013 IEEE Int. Electron Devices Meet. (IEDM)*, 30.1.1–30.1.4, (2013).

[21] Pashinkin, A. and Fedorov, V. *Inorg. Mater.* **39**(6), 539–554 (2003).

[22] Saito, Y., Sutou, Y., and Koike, J. *J. Phys. D: Appl. Phys.* **45**(40), 405302 (2012).

[23] International Centre for Diffraction Data, Newtown Square, PA. *JCPDS Data Card no. 03-065-5591*, (2004).

[24] Lankhorst, M. *J. Non-Cryst. Solids* **297**(2-3), 210 – 219 (2002).

[25] International Centre for Diffraction Data, Newtown Square, PA. *JCPDS Data Card no. 00-049-1411*, (2004).

[26] Devulder, W., Opsomer, K., Seidel, F., Belmonte, A., Muller, R., De Schutter, B., Bender, H., Vandervorst, W., Van Elshocht, S., Jurczak, M., Goux, L., and Detavernier, C. *ACS Appl. Mater. Interfaces* **5**(15), 6984–6989 (2013).

[27] Devulder, W., Opsomer, K., Franquet, A., Meersschaut, J., Belmonte, A., Muller, R., De Schutter, B., Van Elshocht, S., Jurczak, M., Goux, L., and Detavernier, C. *J. Appl. Phys.* **115**(5), 054501 (2014).

[28] International Centre for Diffraction Data, Newtown Square, PA. *JCPDS Data Card no. 00-045-1288*, (2004).

[29] Devulder, W., Opsomer, K., Rampelberg, G., De Schutter, B., Devloo-Casier, K., Jurczak, M., Goux, L., and Detavernier, C. *J. Mater. Chem. C* **3**, 12469–12476 (2015).

[30] Mastai, Y., editor. *Advances in Crystallization Processes*. Intech, (2012).

[31] Yu, J., Liu, B., Zhang, T., Song, Z., Feng, S., and Chen, B. *Appl. Surf. Sci.* **253**(14), 6125 – 6129 (2007).

[32] Lu, Y., Song, S., Song, Z., Rao, F., Wu, L., Zhu, M., Liu, B., and Yao, D. *Appl. Phys. Lett.* **100**(19), 193114 (2012).

[33] Raoux, S., Salinga, M., Jordan-Sweet, J. L., and Kellock, A. *J. Appl. Phys.* **101**(4), 044909 (2007).

[34] Sutou, Y., Kamada, T., Sumiya, M., Saito, Y., and Koike, J. *Acta Mater.*

60(3), 872 – 880 (2012).

[35] Russo, U., Kamalanathan, D., Ielmini, D., Lacaita, A., and Kozicki, M. *IEEE Trans. Electron Devices* **56**(5), 1040–1047 (2009).

[36] Guy, J., Molas, G., Vianello, E., Longnos, F., Blanc, S., Carabasse, C., Bernard, M., Nodin, J., Toffoli, A., Cluzel, J., Blaise, P., Dorion, P., Cueto, O., Grampeix, H., Souchier, E., Cabout, T., Brianceau, P., Balan, V., Roule, A., Maitrejean, S., Perniola, L., and De Salvo, B. In *2013 IEEE Int. Electron Devices Meet. (IEDM)*, 30.2.1–30.2.4, (2013).

[37] Xu, X., Lv, H., Liu, H., Luo, Q., Gong, T., Wang, M., Wang, G., Zhang, M., Li, Y., Liu, Q., Long, S., and Liu, M. *Nanoscale Res. Lett.* **10**(1), 61 (2015).

[38] Kinoshita, K., Tsunoda, K., Sato, Y., Noshiro, H., Yagaki, S., Aoki, M., and Sugiyama, Y. *Appl. Phys. Lett.* **93**(3), 033506 (2008).

Supporting Information

The activation energy for crystallization of a CuTeC20, CuTeGe20 and CuTeSi20 layer is determined by the Kissinger method [30]. The 50 nm CuTeC20 layer and CuTeGe20 layer were deposited by means of magnetron sputter deposition on 20 nm Al_2O_3/Si substrates, as described elsewhere [26, 29]. The composition of the CuTeC20 layer was verified by means of EDX (as described in [26]) and the compositions of the CuTeGe20 layer by XRF (as described in [29]). The compositions are summarized in Table S1. The samples were then annealed at different heating rates ranging from $0.1°C/\mathrm{s}$ to $5°C/\mathrm{s}$ in He atmosphere and the XRD spectrum was recorded. The crystallization temperature T_x is then defined as the temperature in the temperature interval [T_{min}, T_{max}] where the maximum intensity change occurs in the selected 2θ range [θ_{min},θ_{max}], as is illustrated in Figure S1. This 2θ range is selected based on the diffraction peaks of the phase that first crystallizes. This is illustrated in Figure S1 for the three different materials, annealed at a heating rate of $0.5°C/\mathrm{s}$. Using the relation [30]

$$\ln\left[\left(\frac{\mathrm{d}T}{\mathrm{d}t}\right)\frac{1}{T_x^2}\right] = -\frac{E_A}{k_B T_x} + C, \tag{4}$$

the activation energy E_A can be extracted. In this equation (dT/dt) is the heating rate, T_x the crystallization temperature, k_B the Boltzmann constant and C is a constant. By plotting $\ln((\mathrm{d}T/\mathrm{d}t)/T_x^2)$ as a function of $1/k_B T_x$, E_A is extracted from a linear fit, as illustrated in Figure 4 in the manuscript.

Table S1. *Compositions of the layers used for Kissinger analysis.*

Sample	Cu (at%)	Te (at%)	Alloying element (at%)
CuTeSi20	50.7	31.8	17.5 (Si)
CuTeC20	49.4	32.8	17.8 (C)
CuTeGe20	48	30.5	21.5 (Ge)

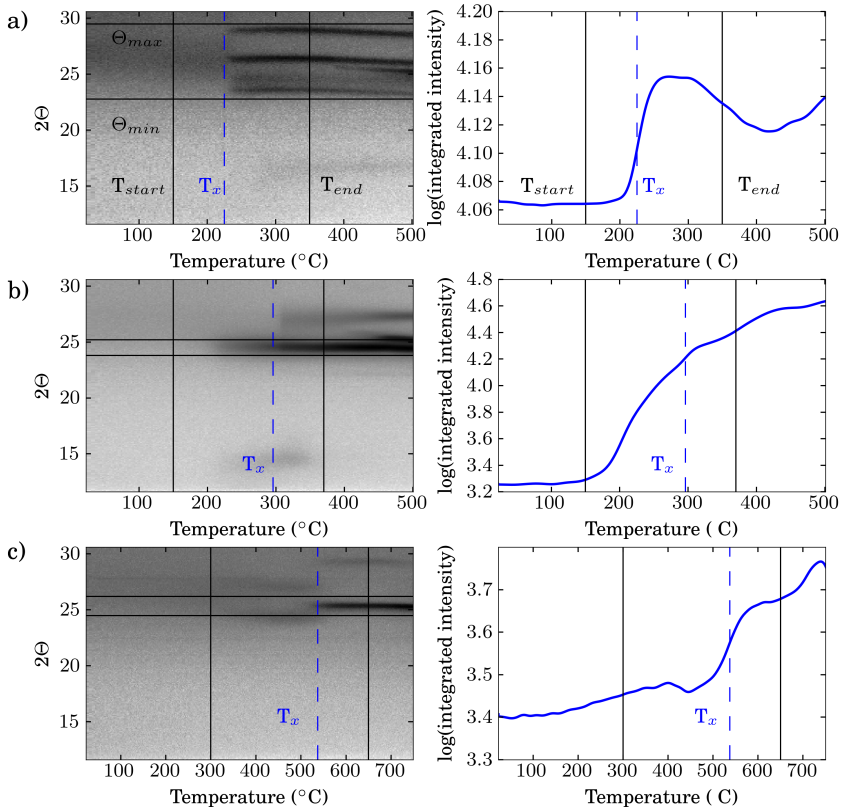

Figure S1. *In situ XRD patterns of a (a) CuTeC20, (b) CuTeGe20 and (c) CuTeSi20 layer, collected at a heating rate of 0.5°C/s in He. The graphs at the right show the integrated intensity in the [θ_{min},θ_{max}] region as a function of the temperature. The crystallization temperature T_x is determined as the temperature where the maximum increase in integrated intensity occurs in the temperature range [T_{start}, T_{end}].*

6 Ternary chalcogenides

In chapter 4, binary tellurides based on Cu-Te and Ag-Te were investigated as a cation supply layer. In chapter 5, $Cu_{0.6}Te_{0.4}$ was alloyed to improve the thermal stability and the CBRAM properties. It was shown that in order to avoid phase separation of the alloys under thermal budget, the materials should stay amorphous, or they should crystallize in a single phase. Silicon turns out to be able to avoid crystallization up to $500°C$, while for the germanium alloyed samples, the crystallization temperature is below $400°C$ and hence the single phase composition Cu_2GeTe_3 was preferred there. In this chapter, the ternary compounds $CuInTe_2$ and $CuAlTe_2$ are investigated. They have a high melting temperature, and while Cu_2GeTe_3 is a line phase, these compounds have a freedom in composition for a few atomic percent, which makes composition requirements less stringent. The thermal stability of these materials and their functionality as a cation supply layer in CBRAM devices are investigated.

6.1 $CuInTe_2$

6.1.1 Literature

The pseudo-binary Cu_2Te-In_2Te_3 phase diagram is shown in Figure 6.1. The diagram shows that a variation in Cu composition is allowed, which should also make deposition easier because the composition control during deposition is less critical. Note also that the temperature where it transforms is above the required $400°C$ for BEOL compatibility. $CuInTe_2$ belongs to the group of $M^{I}M^{III}E_2$ (M^{I}= Cu, Ag;

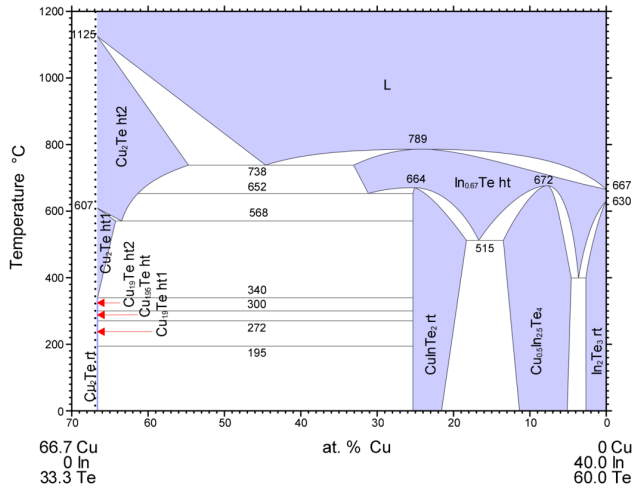

Figure 6.1. *Pseudo-binary phase diagram of the Cu_2Te-In_2Te_3 system [1].*

M^{III}= Al, Ga, In; E=S, Se, Te) chalcopyrite semiconductors [2] and has a reported band-gap of about 1.02 eV [3]. These chalcopyrite compounds are reported to exhibit next to electronic, also ionic conductivity [4]. As was mentioned already in chapter 4, this might be beneficial to evacuate Cu species from the Al_2O_3 switching layer and hence improve the reset behaviour. Hence a similar behaviour can be expected for $CuInTe_2$ [5].

6.1.2 Thermal stability

A 50 nm layer of the $CuInTe_2$ alloy was deposited by co-sputtering from a $Te_{0.9}Cu_{0.1}$, a pure Cu and a pure In sputter target. The Cu/In and Cu/Te ratios were determined by XRF after calibrating the XRF system with a Cu-Te and a Cu-In sample that were both characterized by RBS. Note that RBS is not able to discriminate between In and Te in a mixed Cu-In-Te sample, which explains the need for two calibrations. The composition was determined as 25.6 at% Cu, 24.6 at% In and 49.8 at% Te.

The *in situ* XRD pattern is given in Figure 6.2a, together with a full XRD scan of the as-deposited layer and after quenching at 300 and 400°C. The as-deposited layer is amorphous and crystallizes at 103°C. The $CuInTe_2$ phase [6] exists up to 660°C, where the (112) peak of the chalcopyrite structure disappears. One expects a phase transformation to an In-Te phase for bulk material, but no diffraction peaks are observed. However, it is clear that the material is stable up to temperatures far above 400°C.

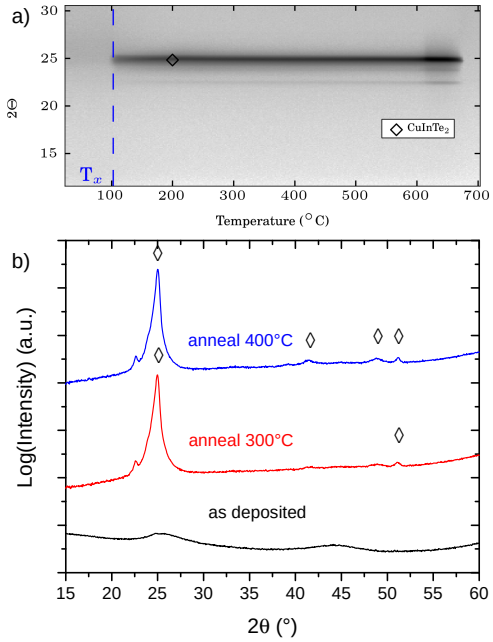

Figure 6.2. *(a) In situ XRD pattern of a $CuInTe_2$ layer at a constant heating rate of $0.5°C/s$ in He atmosphere. The material crystallizes in the chalcopyrite structure at $103°C$ and exists up to $660°C$. (b) XRD patterns of the as-deposited layer and after anneal to 300 and $400°C$.*

Note that for this alloy, the model of Lankhorst can also be applied to calculate the glass transition temperature T_g [7]. The calculation is given in table 6.1, where a temperature of $90°C$ is found for T_g. This temperature is an under limit for T_x and is in agreement with the crystallization temperature of $103°C$ found in this work.

6.1.3 CBRAM functionality

The functionality of the $CuInTe_2$ alloy as a cation supply layer was investigated in a similar way as in previous chapters. The material is deposited in $Pt/CuInTe_2/Al_2O_3/n^+$ Si cells and the as-deposited cells are characterized. A typical DC set-reset sweep is given in Figure 6.3a, showing functional CBRAM. Again it is observed that a deep (i.e. to high HRS resistances) reset is possible. This is also clear from Figure 6.3c, where HRS resistances are measured that are very similar to the pristine resistance. This figure shows also that the LRS resistances extracted from the set and reset sweeps are very similar, which suggests already a better LRS resistance compared to pure $Cu_{0.6}Te_{0.4}$. The reset currents

Table 6.1. *Calculation of the glass transition temperature of $CuInTe_2$. Z is the mean coordination number, H_{AB} the heteronuclear bond enthalpy, n_{AB} the number of A-B bonds, H_a the bond enthalpy of the alloy, T_g the glass transition temperature and T_x the crystallization temperature.*

Material	Z	A-B bond	H_{AB} (kJ/mol)	n_{AB}	H_a (kJ/mol)	T_g ($^\circ C$)	T_x ($^\circ C$)
$CuInTe_2$	4				245.14	90.15	103
		In^{IV}-Te^{IV}	133.35	1			
		Cu^{IV}-Te^{IV}	111.8	1			

for LRS$>$1 kΩ are slightly higher than for $Cu_{0.6}Te_{0.4}$, which suggests a larger thermal contribution to the reset. This might be necessary to reset the cell when the drift contribution is smaller (e.g. when the affinity from Cu from the filament towards the supply layer is lower), and hence suggests a filament that is more stable against dissolution. A similar analysis was performed for the cells after anneal to crystallize the layer (see Figure 6.4), showing similar results and demonstrating that also the crystalline material is functional as cation supply layer.

The retention results of the as-deposited cells are shown in Figure 6.5a and 6.5b. Next to a programming current of 100 µA, a lower I_c was used to obtain more cells in a LRS with higher resistance. However, only a small fraction of the cells ended up in the desired resistance range. Hence in this plot, a few cells programmed using 100 µA with LRS$>$5 kΩ were grouped together with the LRS programmed using a lower I_c, explaining why I_c is not included in the legend of Figure 6.5. The retention test shows that the LRS states with R$<$5 kΩ do not get lost after more than 5 days baking at 85$^\circ C$. The cells with LRS in the range 5 to 100 kΩ do show a degradation and about 25 % go back to the high resistive state[1]. Hence the retention turns out to be slightly better than for $Cu_{0.6}Te_{0.4}$, where about 75 % drifted towards a higher resistance and 50 % went to a HRS. In Chapter 5, the improved retention for $Cu_{0.6}Te_{0.4}$ that was alloyed with Ge was explained by the preferred formation of Ge-Te bonds over Cu-Te, due to the higher bond enthalpy. In this way, the influence of Te to form tellurides with Cu and hence the driving force for Cu from the filament toward the supply layer would be lower. One could apply the same reasoning for $CuInTe_2$, however much more Te (i.e. 50 at%) is present in this compound, which makes Cu-Te interaction more likely which might explain the slightly lower LRS retention. Note that for Cu_2GeTe_3, there is also a high Te content, while good LRS retention was measured. However, according to the calculated bond enthalpies (see tables 2.2 and 6.1), the In-Te bond enthalpy is lower compared to Ge-Te, suggesting a higher tendency for Ge-Te bonds compared

[1] HRS is defined as R$>$1 MΩ.

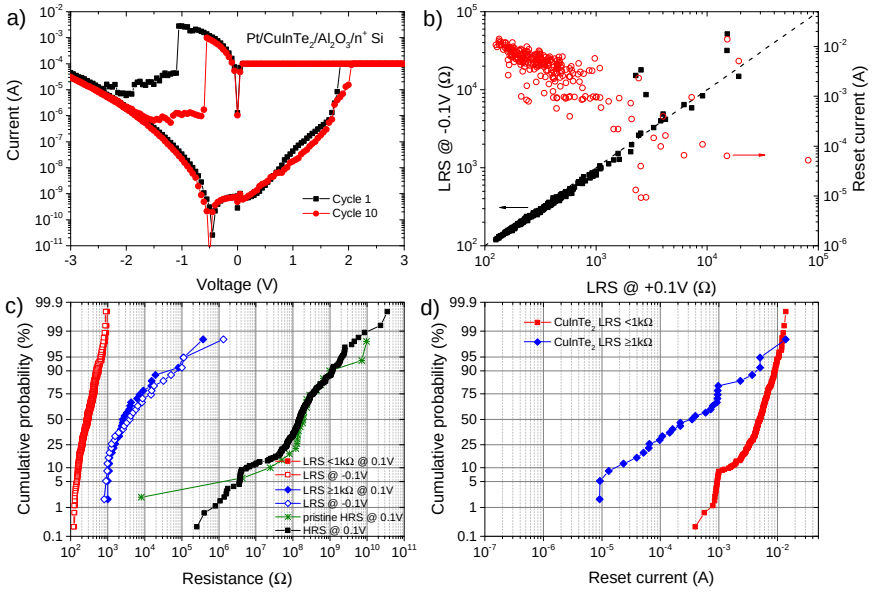

Figure 6.3. *(a) Typical IV-sweep of a Pt/CuInTe$_2$/Al$_2$O$_3$/n$^+$ Si cell (sweep rate 0.5 V/s). (b) Resistance extracted from the reset sweep (at -0.1 V) as a function of the resistance extracted from the set sweep (at +0.1 V) and the reset current as a function of the LRS resistance before the reset. (c) The corresponding cumulative probability of these resistances and of the HRS and pristine cell resistances. (d) Cumulative probability of the reset currents. Note that a distinction was made in (c) and (d) between LRS larger and smaller than 1 kΩ. (Data from 25 devices × 10 cycles.)*

to In-Te. This is in agreement with the lower LRS stability for $CuInTe_2$.

6.2 $CuAlTe_2$

6.2.1 Literature

Instead of indium, aluminum was used to form $CuAlTe_2$ which also belongs to the group $M^IM^{III}E_2$ (M^I= Cu, Ag; M^{III}= Al, Ga, In; E=S, Se, Te). The motivation to use Al instead of In is because of its ease of deposition (In is much softer and more difficult to work with). It is reported as a semiconductor with a band gap of 1.65 eV at 293 K [8]. The pseudo-binary Cu_2Te-Al_2Te_3 phase diagram is shown in Figure 6.6. Also for this material, a certain freedom in composition is allowed. Moreover, the phase diagram shows no transformations up to temperatures above $900°C$.

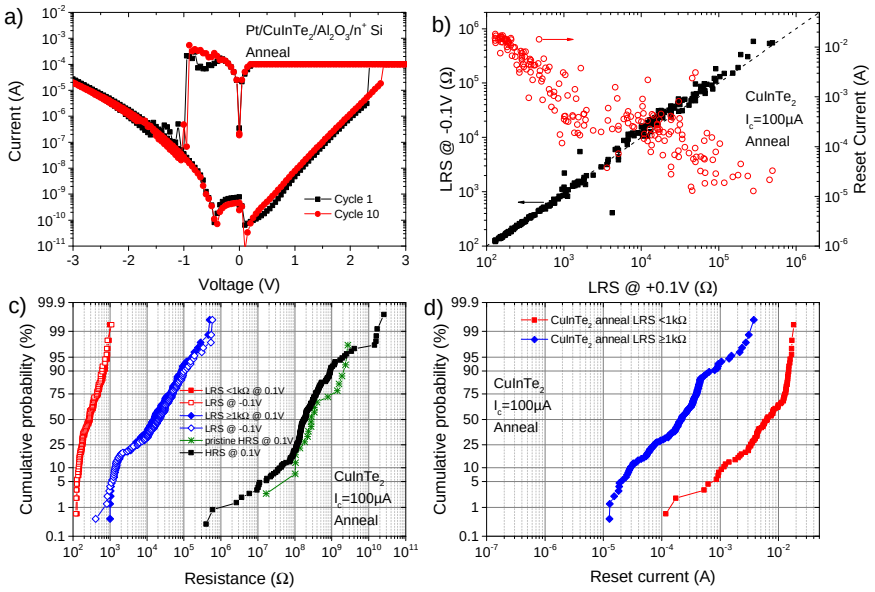

Figure 6.4. *Switching analysis of $CuInTe_2$ based cells after anneal to crystallize the layer. (a) Typical IV-sweep of a Pt/$CuInTe_2$/Al_2O_3/n^+ Si cell (sweep rate 0.5 V/s). (b) Resistance extracted from the reset sweep (at -0.1 V) as a function of the resistance extracted from the set sweep (at +0.1 V) and the reset current as a function of the LRS resistance before the reset. (c) The corresponding cumulative probability of these resistances and of the HRS and pristine cell resistances. (d) Cumulative probability of the reset currents. Note that a distinction was made in (c) and (d) between LRS larger and smaller than 1 kΩ. (Data from 25 devices × 10 cycles.)*

6.2.2 Thermal stability

A 50 nm layer of $CuAlTe_2$ was deposited by co-sputtering from a $Te_{0.9}Cu_{0.1}$, a pure Cu and a pure Al sputter target. The composition was determined by RBS, and EDX could be used for other samples after calibration of the system with the reference sample. The composition was determined by EDX as 25 at% Cu, 26 at% Al and 49 at% Te. The crystallization and phase stability are investigated by *in situ* XRD. Figure 6.7 shows the result for two 2θ windows, centred around 21 and 40° respectively. Note that a 50 nm TiN layer was added to avoid oxidation of the layer, because the Al turned out to be very prone to oxidation. The full XRD patterns of the as-deposited layer and after quenching at 300 and 450°C are given in Figure 6.8. The as-deposited layer is amorphous, and crystallizes at 223°C. From 400°C on, the diffraction peak at 26° becomes less intense, and the diffraction peaks near 43 and 51° become more intense. Hence as was expected, also this material turns out to be stable up to temperatures exceeding the required 400°C. The glass

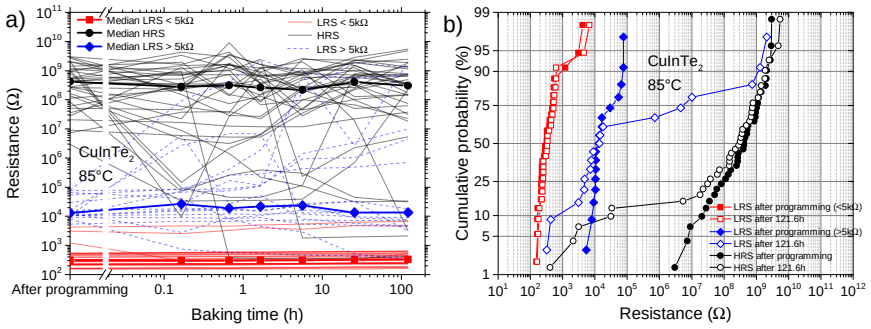

Figure 6.5. *(a) LRS (red and blue) and HRS (black) resistance of $Pt/CuInTe_2/Al_2O_3/n^+$ Si cells. The resistance of every cell as a function of the baking time is shown, even as the median at every time step (thick line). (b) Cumulative probability of the LRS and HRS resistances after programming and after 121.6 h baking at 85°C.*

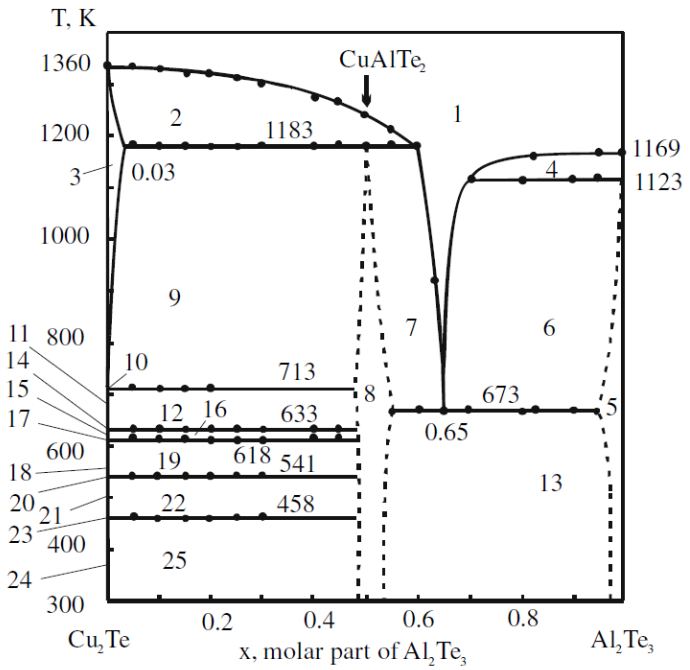

Figure 6.6. *Pseudo-binary phase diagram of the Cu_2Te-Al_2Te_3 system. Region 8 is the $CuAlTe_2$ phase. [9]*

transition temperature was calculated according to the model of Lankhorst [7], and is given in table 6.2. It is observed that the calculated T_g is 232°C and is slightly

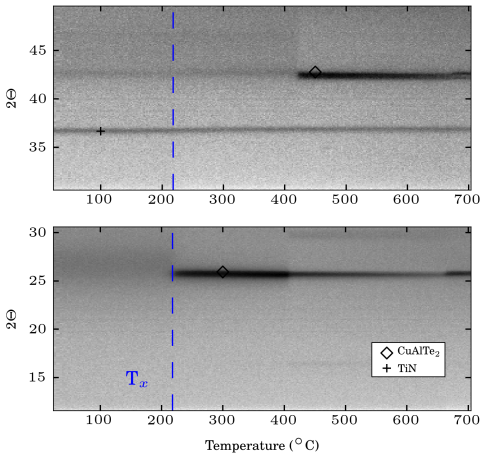

Figure 6.7. *In situ XRD pattern of a TiN/CuAlTe$_2$ layer (50/50 nm), measured at a constant heating rate of 0.5°C/s in He. Two 2θ windows are shown.*

Table 6.2. *Calculation of the glass transition temperature of CuAlTe$_2$.*

Material	Z	A-B bond	H_{AB} (kJ/mol)	n_{AB}	H_a (kJ/mol)	T_g (°C)	T_x (°C)
CuAlTe$_2$	4				286.4	232	223
		Al^{IV}-Te^{IV}	174.6	1			
		Cu^{IV}-Te^{IV}	111.8	1			

higher than T$_x$ (223°C), while the glass transition temperature should be a lower limit for crystallization. Note that this is most likely due to the large uncertainty for Cu-Cu bond enthalpy. Indeed, in the paper of Lankhorst, this was mentioned to range from -67 kJ/mol to +19 kJ/mol. In previous calculations, the maximum value was used, in accordance to other work [10]. Hence this suggests that a slightly lower value should be used. Note that Raoux. et al [11] used a value of -24 kJ/mol in the work where they validated the Lankhorst model. However, in this work, when using always the same value, the calculated glass transition temperature serves as a good reference to compare the theoretical crystallization behaviour of the different materials. Indeed, the calculated T$_g$ for CuAlTe$_2$ is higher compared to CuInTe$_2$ in agreement with the measured higher crystallization temperature.

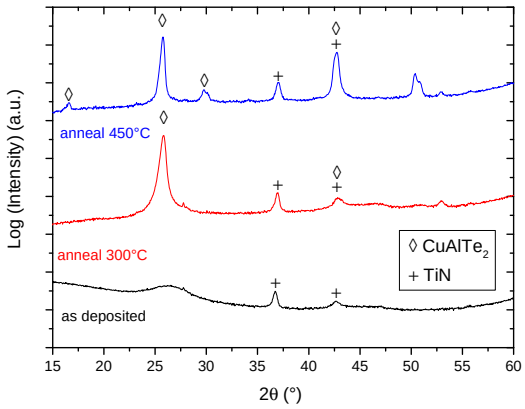

Figure 6.8. *XRD patterns of the as-deposited layer and after anneal to 300 and 450°C.*

6.2.3 CBRAM functionality

Figure 6.9 summarizes the CBRAM functionality of memory cells with $CuAlTe_2$ as cation supply layer. Very similar results as $CuInTe_2$ are observed. The retention results are shown in Figures 6.10a and 6.10b. The cells were cycled and programmed using a current compliance of 100 µA. In order to get more cells in LRS with a resistance in the range 5 to 100 kΩ, a programming current of 50 µA was used. Also here, the LRS states with R$>$ 5 kΩ tend to increase in resistance and turns out to be very similar to $CuInTe_2$, and the same reasoning can be applied. Note that a larger fraction of the cells in HRS lose their memory state compared to $CuInTe_2$.

6.3 Conclusion

The ternary chalcogenides $CuInTe_2$ and $CuAlTe_2$ were characterized and tested on their functionality as a cation supply layer in CBRAM. The *in situ* XRD patterns for both materials show that they crystallize in the chalcopyrite phase upon crystallizaton, without transformations or phase separation up to temperatures exceeding 400°C. Hence these materials show a good thermal stability. Both materials show functional CBRAM when implemented in Pt/Cu(In,Al)Te_2/Al_2O_3/n^+ Si memory cells. Retention was tested at 85°C, showing good LRS stability for resistances below 5 kΩ. On the other hand, about 25 % of the cells programmed to LRS states between 5 and 100 kΩ degrade to a HRS after 5 days baking. However, this is still better compared to $Cu_{0.6}Te_{0.4}$.

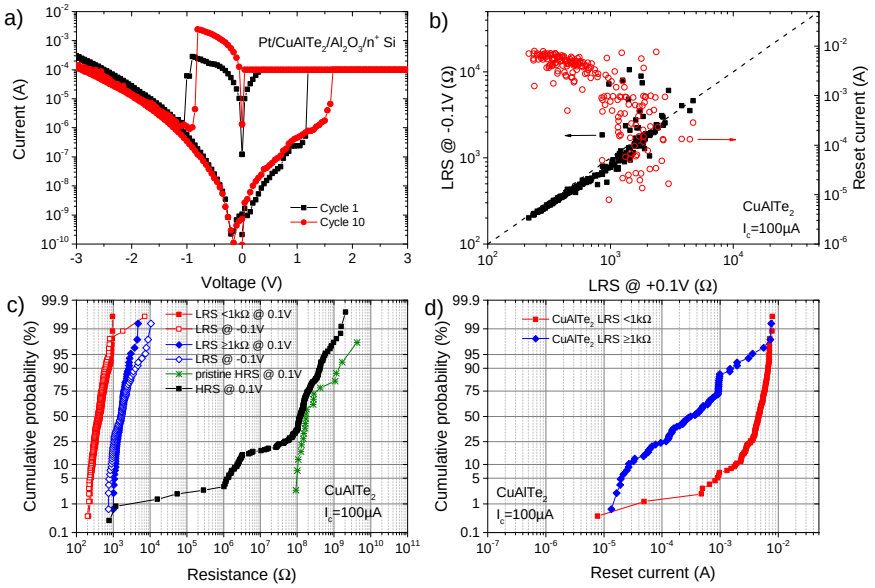

Figure 6.9. *(a) Typical IV-sweep of a Pt/CuAlTe$_2$/Al$_2$O$_3$/n$^+$ Si cell (sweep rate 0.5 V/s). (b) Resistance extracted from the reset sweep (at -0.1 V) as a function of the resistance extracted from the set sweep (at +0.1 V) and the reset current as a function of the LRS resistance before the reset. (c) The corresponding cumulative probability of these resistances and of the HRS and pristine cell resistances. (d) Cumulative probability of the reset currents. Note that a distinction was made in (c) and (d) between LRS larger and smaller than 1 kΩ. (Data from 20 devices × 10 cycles.)*

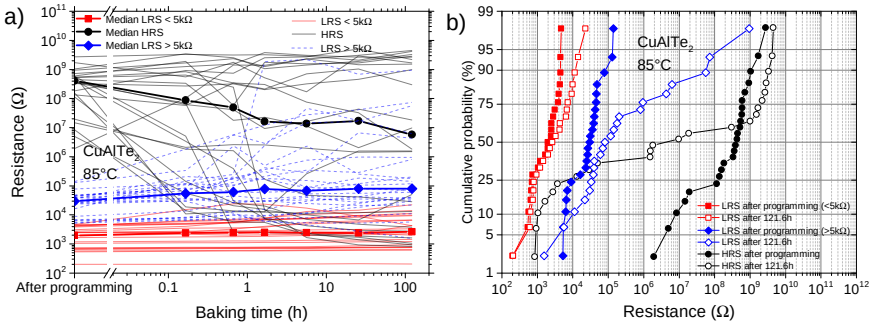

Figure 6.10. *(a) LRS (red and blue) and HRS (black) resistance of Pt/CuAlTe$_2$/Al$_2$O$_3$/n$^+$ Si cells. The resistance of every cell as a function of the baking time is shown, even as the median at every time step (thick line). (b) Cumulative probability of the LRS and HRS resistances after programming and after 121.6 h baking at 85°C.*

References

[1] Springer & Material Phases Data System (MPDS), Switzerland & National Institute for Materials Science (NIMS), Japan, 2014, http://materials.springer.com/isp/phase-diagram/docs/c_0926619, *LINUS PAULING FILE Multinaires Edition - 2012 Dataset ID c_0926619*.

[2] C. C. Landry, J. Lockwood, and A. R. Barron, *Chem. Mater.* **7**(4), 699–706 (1995).

[3] R. Liu, L. Xi, H. Liu, X. Shi, W. Zhang, and L. Chen, *Chem. Commun.* **48**, 3818–3820 (2012).

[4] D. Soltz, G. Dagan, and D. Cahen, *Solid State Ionics* **28**, 1105 – 1110 (1988).

[5] T. Ahmad, Master's thesis, Universiteit Gent, (2015).

[6] International Centre for Diffraction Data, Newtown Square, PA, *JCPDS Data Card no. 01-081-1937*, (2004).

[7] M. Lankhorst, *J. Non-Cryst. Solids* **297**(2-3), 210 – 219 (2002).

[8] B. V. Korzun, A. A. Fadzeyeva, A. V. Mudryi, and S. Schorr, *Phys. Status Solidi C* **3**(8), 2626–2629 (2006).

[9] B. Korzun, A. Fadzeyeva, K. Bente, and T. Doering, *J. Mater. Sci.: Mater. Electron.* **19**(3), 255–260 (2008).

[10] Y. Sutou, T. Kamada, M. Sumiya, Y. Saito, and J. Koike, *Acta Mater.* **60**(3), 872 – 880 (2012).

[11] S. Raoux, M. Salinga, J. L. Jordan-Sweet, and A. Kellock, *J. Appl. Phys.* **101**(4), 044909 (2007).

7

Conclusions and suggestions for future work

7.1 Summary and conclusions

In this thesis work, binary and ternary chalcogenides were investigated for application as a cation supply layer in Conductive Bridge Random Access Memory devices. The *functionality* of these materials in memory devices, and their *thermal stability* are studied. The ITRS lists reliability (including endurance and retention) of the memory cells, and the integration of new materials and their compatibility with the thermal budget during processing as issues for CBRAM that need to be overcome. Both issues are dealt with for the different materials that were studied in this thesis.

Copper-tellurium was investigated and $Cu_{0.6}Te_{0.4}$ showed good CBRAM functionality when implemented in 580 µm diameter Pt/$Cu_{0.6}Te_{0.4}$/Al_2O_3/n^+ Si memory cells. The cells show a more efficient reset compared to pure Cu, which is attributed to the preferred formation of copper-tellurides. Hence there is an additional driving force for the Cu to go back to the copper supply layer. In analogy, silver-tellurium was investigated, showing also this improved reset behaviour. However, Ag-Te based CBRAM showed a lower filament stability, resulting in more volatile switches. Hence Cu_xTe_{1-x} with $x \sim 0.6$ was further used in this thesis. The thermal stability of Cu-Te (and $Cu_{0.6}Te_{0.4}$ more specifically) is rather limited, but is a very important parameter to allow integration in future memory devices and hence the thermal stability was improved by alloying. The CBRAM

functionality of the new alloys was also investigated.

7.1.1 Thermal stability

The thermal stability was improved by alloying the $Cu_{0.6}Te_{0.4}$ layer. If a material crystallizes and has a composition different from an intermetallic compound, phase separation occurs, leading to uncontrolled lateral inhomogeneity at the interface between the supply layer and switching layer. This might lead to fluctuations in device characteristics from device to device. Therefore, the supply layer should stay amorphous or crystallize into a single homogeneous phase (i.e. that is uniform in composition throughout the supply layer). This was investigated for the Cu-Te-C, -Ge and -Si alloys by means of *in situ* XRD, which allows detection of crystallization and phase transformations during annealing.

Amorphous materials $Cu_{0.6}Te_{0.4}$ was alloyed with C, Ge and Si and addition of these elements proved to be effective to increase the crystallization temperature. Si is the most efficient in keeping the material amorphous up to temperatures above $400°C$, making it compatible with the temperatures applied in BEOL processes. This is ascribed to the strong bonds that are formed between Si and Cu and Te, but also due to strong Si-Si bonds forming chains that hamper the reorganization of the elements in a lattice. For Ge, the bonds are weaker and a lower crystallization temperature is measured. Carbon on the other hand does not bind to Cu and Te, but most likely carbon chains are formed due to the strong C-C bonds, which also hamper crystallization. This was also investigated by means of XPS, and it was theoretically justified by applying the model of Lankhorst.

Single phase material If crystallization cannot be avoided, a composition of an intermetallic phase is preferred because this phase will then crystallize. This was done for Cu_2GeTe_3, $CuInTe_2$ and $CuAlTe_2$. These materials show a single phase upon crystallization and have a melting temperature exceeding $400°C$, which makes them suitable for integration in memory devices. $CuInTe_2$ and $CuAlTe_2$ moreover allow some freedom in composition, which makes composition control during deposition less critical.

We can conclude the following:

- Two strategies to improve the thermal stability were proposed. Alloying elements can be added to avoid crystallization, or a composition that crystallizes into a single phase can be used.

- In this way, thermally stable materials were obtained: amorphous CuTeSi20, Cu_2GeTe_3, $CuInTe_2$ and $CuAlTe_2$.

- Hence solutions have been proposed for the first *issue* of the ITRS roadmap (see section 1.3) that was dealt with in this work, that is thermal stability of new materials.

7.1.2 CBRAM functionality

The investigated alloys were investigated on their functionality as a cation supply layer in CBRAM cells with a dedicated Al_2O_3 switching layer. To this end, the materials were implemented in 580 µm diameter Pt/Cu-alloy/Al_2O_3/n^+ cells. Functional CBRAM was demonstrated for the investigated alloys, showing a more efficient reset compared to pure Cu, as was observed for $Cu_{0.6}Te_{0.4}$. The retention of the memory states for the different alloys was investigated and compared to $Cu_{0.6}Te_{0.4}$. The following conclusions can be made:

- Improved LRS retention was observed compared to $Cu_{0.6}Te_{0.4}$, especially for the Ge alloyed cells. This is explained by the preferred formation of bonds of the alloying element to Te, lowering the driving force for Cu to form tellurides. Hence there is a lower driving force for the Cu from the filament to go back to the supply layer, improving filament stability.

- For all materials, some degradation of the HRS was observed, which is attributed to the low LRS resistances that are reached during cycling, which most likely forms a large template path for filament reconstruction and HRS degradation. Moreover, some Cu might be left in the switching layer, which can also contribute to filament reconstruction.

- HRS degradation was the worst for the carbon alloyed cells, which is ascribed to the absence of bonds of C with Cu, resulting in a low tendency for carbon to keep Cu in the supply layer. As a result, Cu is expected to be released more easily and diffuse in the filament template path.

- The Cu_2GeTe_3 compound showed a combination of good thermal stability with good retention properties, making it the best compound from this study to implement in future memory devices. Hence an improvement in the retention of the memory, one of the *reliability issues* that was put forward by the ITRS (see section 1.3), has been realized.

7.2 Suggestions for further work

Scaling to nano-sized devices The electrical measurements in this thesis have been performed on large devices (580 µm diameter dots). In a next step, the functionality on nano-scaled devices has to be tested. CBRAM has been demonstrated to be highly scalable ($\sim$10 nm), and hence it should be investigated if the alloys

show good uniformity and if uniform switching characteristics are observed in all the memory cells over a full wafer. Integration in small devices, with an appropriate current limiter (e.g. a transistor) is also necessary to avoid parasitic effects as much as possible (see section 3.5.3) and to carefully investigate the *endurance* properties of the devices.

The large capacitance of the cells will mainly lead to a large discharge current through the cell upon switching to LRS. This mainly limits the possibility to investigate the *low current* operation of the devices. For that reason, no attempt was done to operate the cells under low currents (rather high currents were used, i.e. $\geq$10 µA and usually 100 µA). In nano-scaled devices (preferably with a transistor as current limiter) low current operation ($<$1 µA) is possible and should be investigated. Moreover, better current control could avoid that the cells reach very low LRS resistances during the set operation, allowing also a better investigation of HRS retention. Under high currents on the other hand, a similar behaviour as for the large dot cells is expected.

New materials The investigated material systems in this work resulted in a selection of compositions that show the best trade off between thermal stability and CBRAM functionality. The role of Te on the switching, and the influence of alloying elements on CBRAM functionality and thermal stability was presented. Both Cu and Ag tellurides and different alloying elements were investigated. The only element that has not been varied is the chalcogen element. Hence as a suggestion for future work, Se or S may be used instead of Te. One can expect an increase of T_x, because Se-Se bonds (and hence also Se-X bonds) are stronger compared to Te, leading to a higher glass transition temperature and T_x (which can be deduced from the model of Lankhorst). The bonds with Cu or Ag will also have a higher ionic degree (based on difference in electronegativity).

Influence of the switching layer The research in this thesis was on materials for the cation supply layer. To carefully investigate this, the switching layer was always the same, i.e. a 3 nm Al_2O_3 layer. However, this layer plays an important role. Indeed, it was demonstrated in section 2.3.2.1 to determine the nucleation sites during filament growth and hence it influences the filament morphology. As a result, it can be expected that the device characteristics might be further tuned and improved by optimizing the switching layer.

Influence of moisture The influence of moisture on the switching behaviour of CBRAM was reported in a few papers, as discussed in section 2.3.2.2. Hence in the cells that were fabricated in this thesis work, this might also play a role. This can be further investigated by performing electrical measurements in vacuum. Integration of the materials in test structures under a controlled atmosphere and

with passivation of the cells afterwards also allows a tighter control of the influence of moisture.

MIEC materials Most of the materials studied in this work are reported as *mixed ionic electronic conductors*, showing both ionic and electronic conductivity. It was argued that this effect could also contribute to the observed efficient reset, because it allows an efficient evacuation of the switching layer from Cu ions, as they can move into the cation supply layer during reset. These materials are also reported to be applicable in *selector* devices. This type of device should avoid *sneak path currents* when the memory devices are integrated in passive cross bar arrays. This can also further be investigated, and could lead to a material that can be used both as a cation supply layer in CBRAM as well as the active layer in a selector device.

A

Cu-Te-Ge phase diagrams

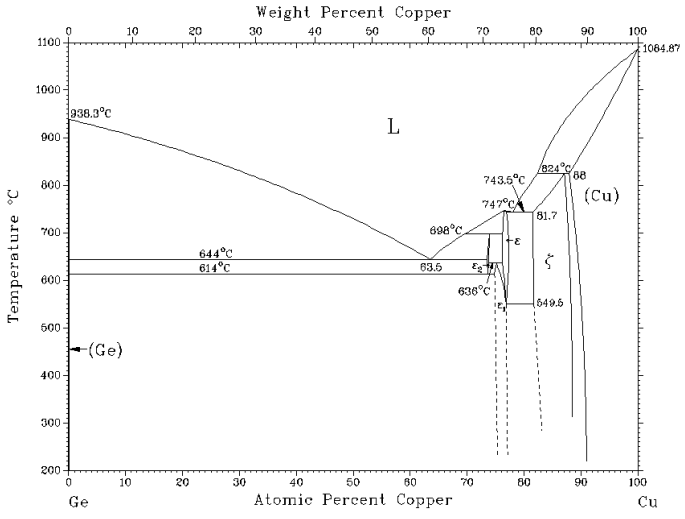

Figure A.1. *Binary Cu-Ge phase diagram. [1]*

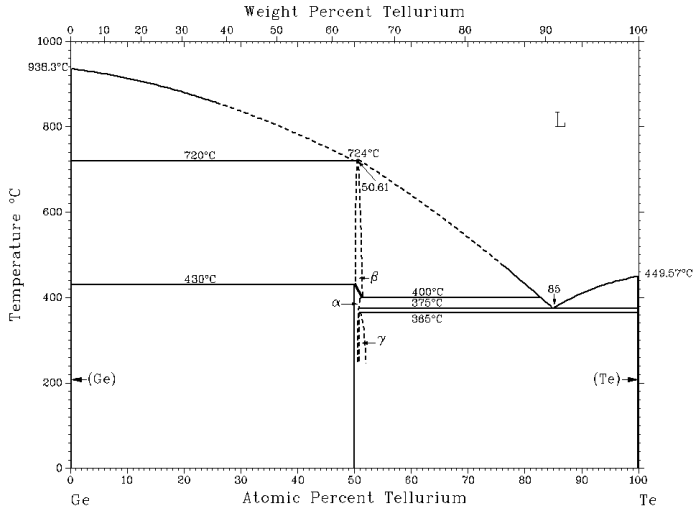

Figure A.2. *Binary Ge-Te phase diagram. [1]*

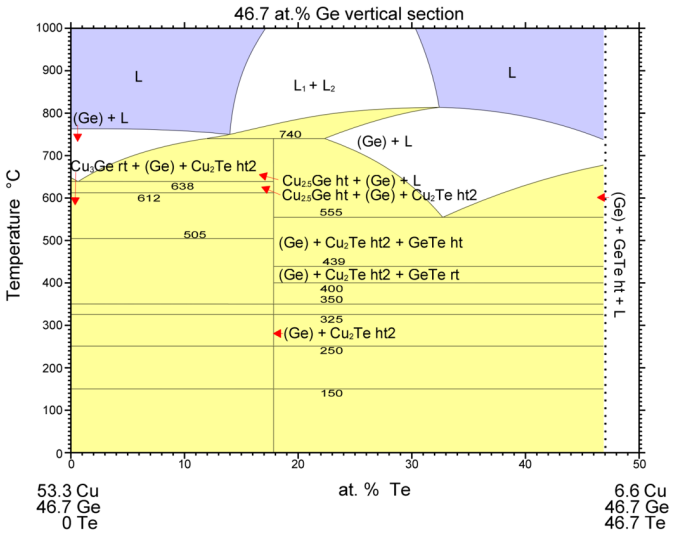

Figure A.3. *Cross section of the Cu-Te-Ge phase diagram from 53.3 at% Cu and 46.7 at% Ge to 6.6 at% Cu, 46.7 at% Ge and 46.7 at% Te as a function of the Te content (diagram c_0926575). [2]*

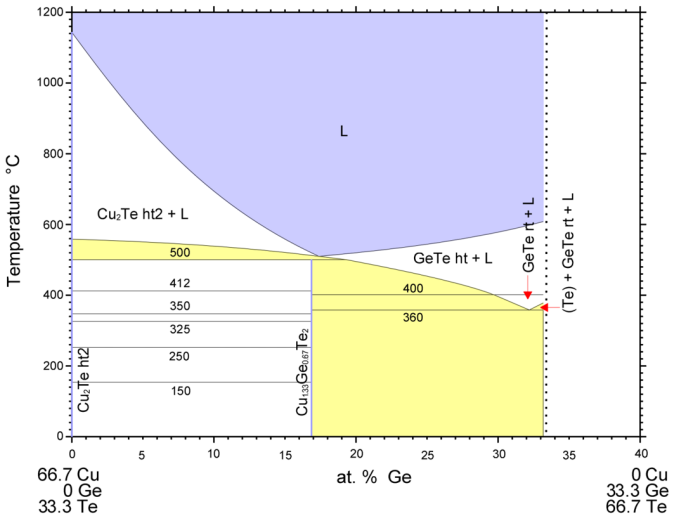

Figure A.4. *Cross section of the Cu-Te-Ge phase diagram from 66.7 at% Cu and 33.3 at% Te to 66.7 at% Te and 33.3 at% Ge as a function of the Ge content (diagram c_0926573). [3]*

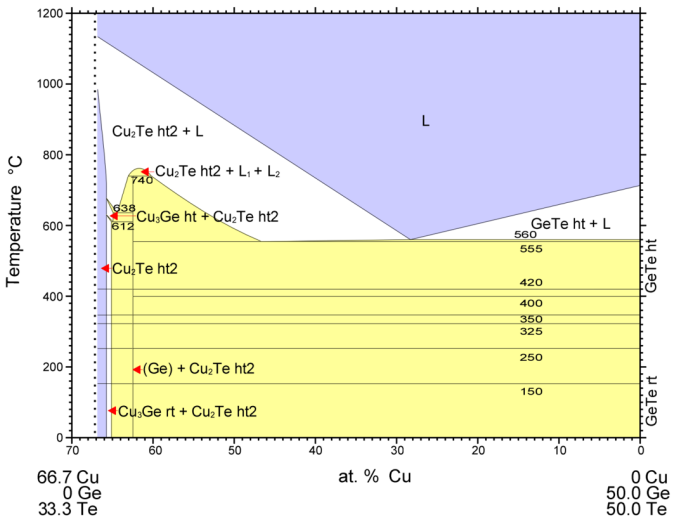

Figure A.5. *Cross section of the Cu-Te-Ge phase diagram from 66.7 at% Cu and 33.3 at% Te to 50 at% Te and 50 at% Ge as a function of the Cu content (diagram c_0926570). [4]*

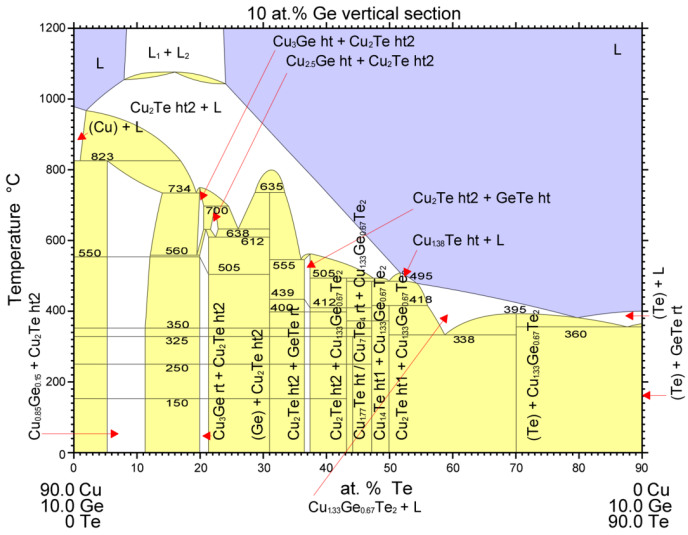

Figure A.6. *Cross section of the Cu-Te-Ge phase diagram from 90 at% Cu and 10 at% Ge to 90 at% Te and 10 at% Ge as a function of the Te content (diagram c_0926574). [5]*

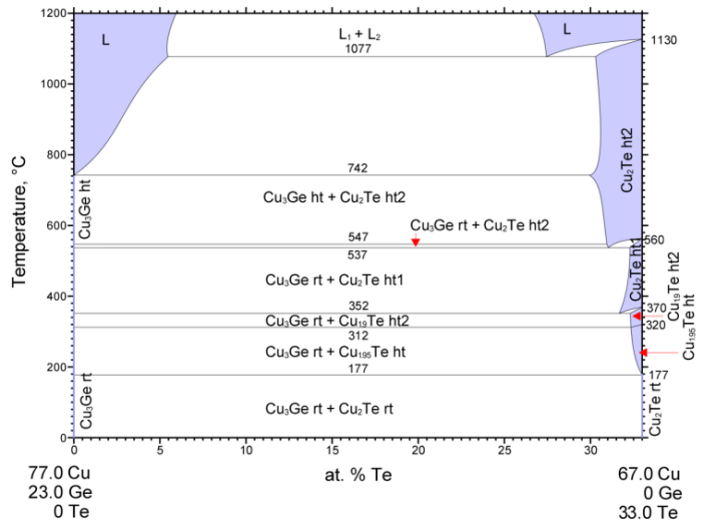

Figure A.7. *Cross section of the Cu-Te-Ge phase diagram from 77 at% Cu and 23 at% Ge to 67 at% Cu and 33 at% Te as a function of the Te content (diagram c_1500208). [6]*

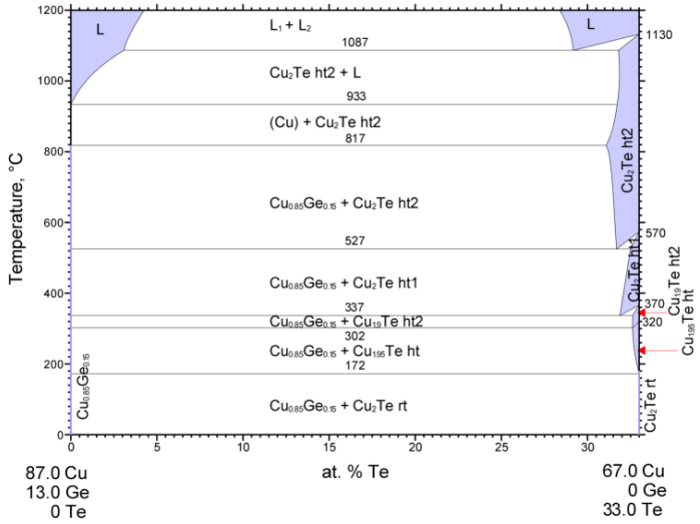

Figure A.8. *Cross section of the Cu-Te-Ge phase diagram from 87 at% Cu and 13 at% Ge to 67 at% Cu and 33 at% Te as a function of the Te content (diagram c_1500209). [7]*

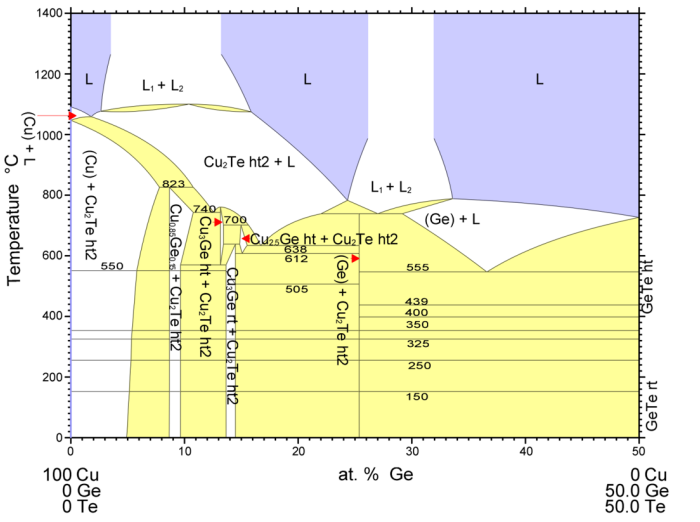

Figure A.9. *Cross section of the Cu-Te-Ge phase diagram from 100 at% Cu to 50 at% Te and 50 at% Ge as a function of the Ge content (diagram c_0926568). [8]*

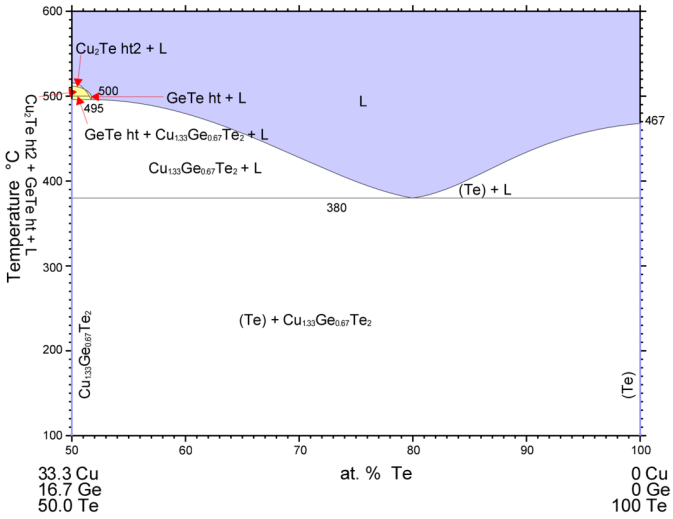

Figure A.10. *Cross section of the Cu-Te-Ge phase diagram from 33 at% Cu, 50 at% Te, 16.7 at% Ge to 100 at% Te as a function of the Te content (diagram c_0926569). [9]*

References

[1] ASM International, The Materials Information Society. *Binary Alloy Phase Diagrams (Second Edition Plus Updates)*, (1990).

[2] Springer & Material Phases Data System (MPDS), Switzerland & National Institute for Materials Science (NIMS), Japan, 2014, http://materials.springer.com/isp/phase-diagram/docs/c_0926575. *LINUS PAULING FILE Multinaires Edition - 2012 Dataset ID c_0926575.*

[3] Springer & Material Phases Data System (MPDS), Switzerland & National Institute for Materials Science (NIMS), Japan, 2014, http://materials.springer.com/isp/phase-diagram/docs/c_0926573. *LINUS PAULING FILE Multinaires Edition - 2012 Dataset ID c_0926573.*

[4] Springer & Material Phases Data System (MPDS), Switzerland & National Institute for Materials Science (NIMS), Japan, 2014, http://materials.springer.com/isp/phase-diagram/docs/c_0926570. *LINUS PAULING FILE Multinaires Edition - 2012 Dataset ID c_0926570.*

[5] Springer & Material Phases Data System (MPDS), Switzerland & National Institute for Materials Science (NIMS), Japan, 2014, http://materials.springer.com/isp/phase-diagram/docs/c_0926574. *LINUS PAULING FILE Multinaires Edition - 2012 Dataset ID c_0926574.*

[6] Springer & Material Phases Data System (MPDS), Switzerland & National Institute for Materials Science (NIMS), Japan, 2014, http://materials.springer.com/isp/phase-diagram/docs/c_1500208. *LINUS PAULING FILE Multinaires Edition - 2012 Dataset ID c_1500208.*

[7] Springer & Material Phases Data System (MPDS), Switzerland & National Institute for Materials Science (NIMS), Japan, 2014, http://materials.springer.com/isp/phase-diagram/docs/c_1500209. *LINUS PAULING FILE Multinaires Edition - 2012 Dataset ID c_1500209.*

[8] Springer & Material Phases Data System (MPDS), Switzerland & National Institute for Materials Science (NIMS), Japan, 2014, http://materials.springer.com/isp/phase-diagram/docs/c_0926568. *LINUS PAULING FILE Multinaires Edition - 2012 Dataset ID c_0926568.*

[9] Springer & Material Phases Data System (MPDS), Switzerland & National Institute for Materials Science (NIMS), Japan, 2014, http://materials.springer.com/isp/phase-diagram/docs/c_0926569. *LINUS PAULING FILE Multinaires Edition - 2012 Dataset ID c_0926569.*

B

Cu-Te-Si phase diagrams

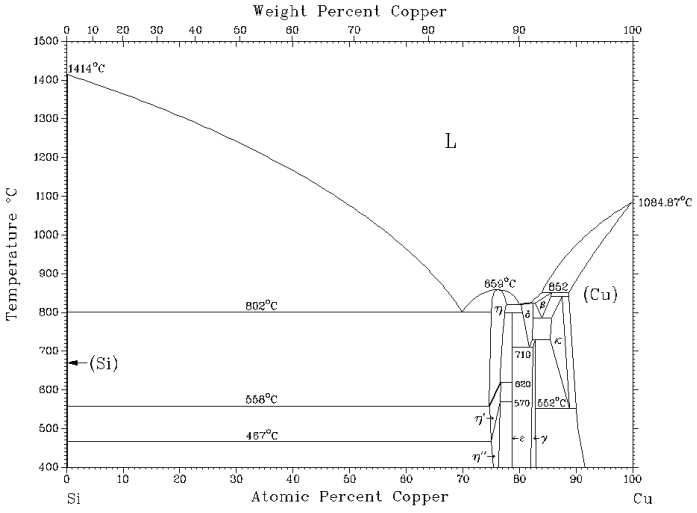

Figure B.1. *Binary Cu-Si phase diagram. [1]*

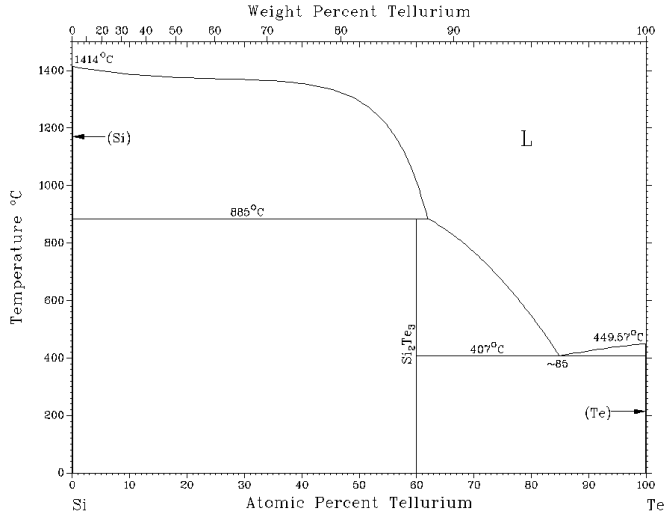

Figure B.2. *Binary Si-Te phase diagram. [1]*

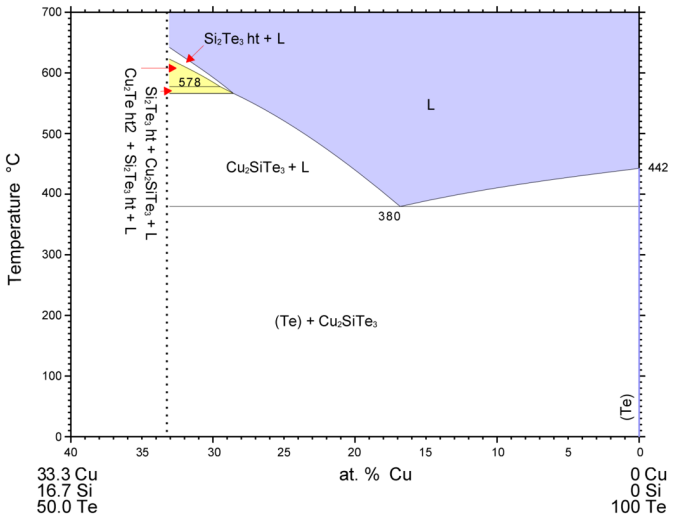

Figure B.3. *Cross section of the Cu-Te-Si phase diagram from 33.3 at% Cu, 50 at% Te and 16.7 at% Si to pure Te as a function of the Cu content (diagram c_0927203). [2]*

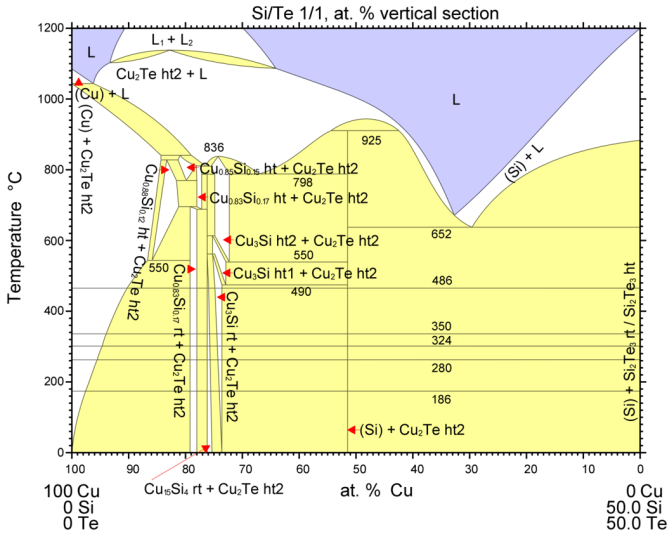

Figure B.4. *Cross section of the Cu-Te-Si phase diagram from pure Cu to 50 at% Te and 50 at% Si as a function of the Cu content (diagram c_0927206). [3]*

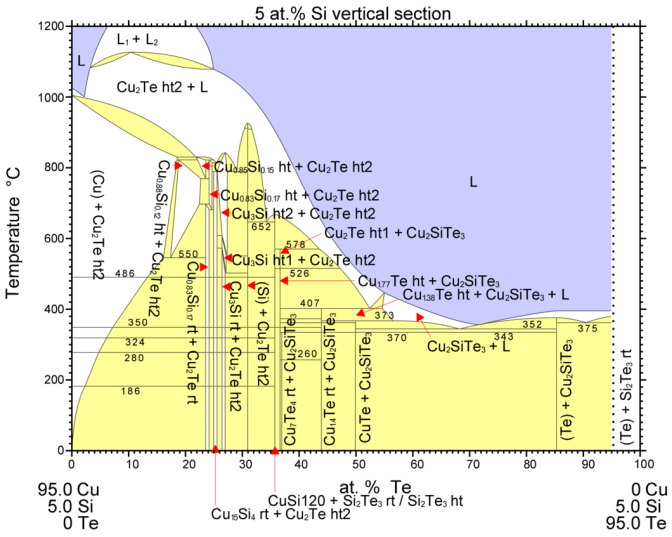

Figure B.5. *Cross section of the Cu-Te-Si phase diagram from 95 at% Cu, and 5 at% Si to 95 at% Te and 5 at% Si as a function of the Te content (diagram c_0927207). [4]*

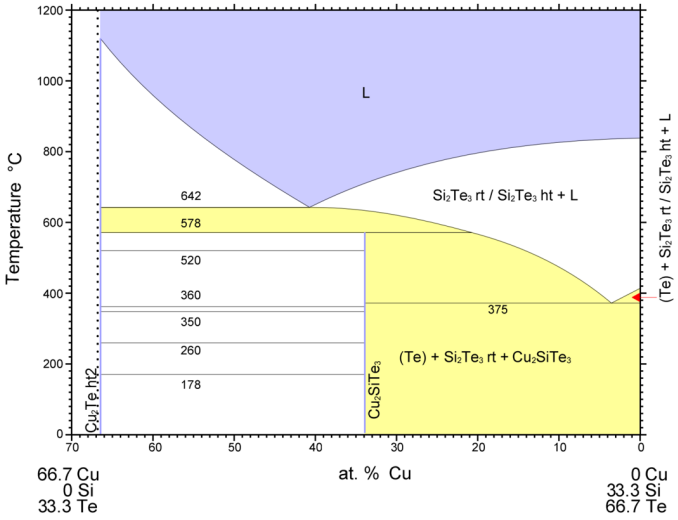

Figure B.6. *Cross section of the Cu-Te-Si phase diagram from 66.7 at% Cu and 33.3 at% Te to 66.7 at% Te and 33.3 at% Si as a function of the Cu content (diagram c_0927204). [5]*

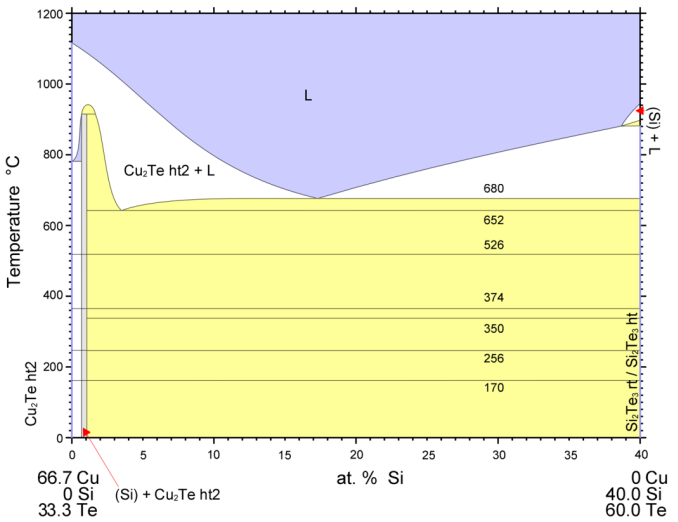

Figure B.7. *Cross section of the Cu-Te-Si phase diagram from 66.7 at% Cu and 33.3 at% Te to 60 at% Te and 40 at% Si as a function of the Si content (diagram c_0927205). [6]*

References

[1] ASM International, The Materials Information Society. *Binary Alloy Phase Diagrams (Second Edition Plus Updates)*, (1990).

[2] Springer & Material Phases Data System (MPDS), Switzerland & National Institute for Materials Science (NIMS), Japan, 2014, http://materials.springer.com/isp/phase-diagram/docs/c_0927203. *LINUS PAULING FILE Multinaires Edition - 2012 Dataset ID c_0927203*.

[3] Springer & Material Phases Data System (MPDS), Switzerland & National Institute for Materials Science (NIMS), Japan, 2014, http://materials.springer.com/isp/phase-diagram/docs/c_0927206. *LINUS PAULING FILE Multinaires Edition - 2012 Dataset ID c_0927206*.

[4] Springer & Material Phases Data System (MPDS), Switzerland & National Institute for Materials Science (NIMS), Japan, 2014, http://materials.springer.com/isp/phase-diagram/docs/c_0927207. *LINUS PAULING FILE Multinaires Edition - 2012 Dataset ID c_0927207*.

[5] Springer & Material Phases Data System (MPDS), Switzerland & National Institute for Materials Science (NIMS), Japan, 2014, http://materials.springer.com/isp/phase-diagram/docs/c_0927204. *LINUS PAULING FILE Multinaires Edition - 2012 Dataset ID c_0927204*.

[6] Springer & Material Phases Data System (MPDS), Switzerland & National Institute for Materials Science (NIMS), Japan, 2014, http://materials.springer.com/isp/phase-diagram/docs/c_0927205. *LINUS PAULING FILE Multinaires Edition - 2012 Dataset ID c_0927205*.

List of Figures

List of Tables

List of Publications

- **Study of amorphous Cu-Te-Si thin films showing high thermal stability for application as a cation supply layer in Conductive Bridge Random Access Memory devices**
  W. Devulder, K. Opsomer, M.M. Minjauw, J. Meersschaut, M. Jurczak, L. Goux and C. Detavernier
  RSC Adv. 6, 32106-32114 (2016).

- **Improved thermal stability and retention properties of Cu-Te based CBRAM by Ge alloying**
  W. Devulder, K. Opsomer, G. Rampelberg, B. De Schutter, K. Devloo-Casier, M. Jurczak, L. Goux, and C. Detavernier
  J. Mat. Chem. C. 3(48), 12469-12476 (2015).
  (This article is part of themed collection: *2015 Journal of Materials Chemistry C Hot Papers*)

- ***In situ* X-ray diffraction study of the controlled oxidation and reduction in the VO system for the synthesis of VO_2 and V_2O_3 thin films**
  G. Rampelberg, B. De Schutter, W. Devulder, K. Martens, I. Radu and C. Detavernier
  J. Mat. Chem. C. 3, 11357-11365 (2015).

- **Combinatorial Study of Ag-Te Thin Films and Their Application as Cation Supply Layer in CBRAM Cells**
  W. Devulder, K. Opsomer, J. Meersschaut, D. Deduytsche, M. Jurczak, L. Goux, and C. Detavernier
  ACS Comb. Sci. 17(5), 334-340 (2015).

- **Electronic defect study on low temperature processed Cu(In,Ga)Se_2 thin-film solar cells and the influence of an Sb layer**
  L. Van Puyvelde, J. Lauwaert, A. Tempez, W. Devulder, S. Nishiwaki, F.

Pianezzi, C. Detavernier, AN Tiwari and H. Vrielinck
J. Phys. D: Appl. Phys. 48(17), 175104 (2015).

- **Phase formation in intermixed Ni-Ge thin films: influence of Ge content and low-temperature nucleation of hexagonal nickel germanides**
B. De Schutter, W. Devulder, A. Schrauwen, K. Van Stiphout, T. Perkisas, S. Bals, A. Vantomme and C. Detavernier
Microelectron. Eng. 120, 168-173 (2014).

- **Controllable nitrogen doping in as deposited TiO_2 film and its effect on post deposition annealing**
S. Deng, S. W. Verbruggen, S. Lenaerts, J. A. Martens, S. Van den Berghe, K. Devloo-Casier, W. Devulder, J. Dendooven, D. Deduytsche and C. Detavernier
J. Vac. Sci. Technol., A 32(1), 01A123 (2014).

- **Influence of carbon content on the copper-telluride phase formation and on the resistive switching behavior of carbon alloyed Cu-Te conductive bridge random access memory cells**
W. Devulder, K. Opsomer, A. Franquet, J. Meersschaut, A. Belmonte, R. Muller, B. De Schutter, S. Van Elshocht, M. Jurczak, L. Goux, and C. Detavernier
J. Appl. Phys. 115(5), 054501 (2014).

- **Optimization of $W\backslash Al_2O_3\backslash Cu$(-Te) material stack for high-performance conductive-bridging memory cells**
L. Goux, W. Kim, K. Opsomer, A. Belmonte, G. Kar, F. De Stefano, V.V. Afanas'ev, U. Celano, M. Houssa, W. Devulder, C. Detavernier, R. Muller, W. Vandervorst and M. Jurczak
ECS Transactions 58(7), 4229250 (2013).

- **Influence of Carbon Alloying on the Thermal Stability and Resistive Switching Behavior of Copper-Telluride Based CBRAM Cells**
W. Devulder, K. Opsomer, F. Seidel, A. Belmonte, R. Muller, B. De Schutter, H. Bender, W. Vandervorst, S. Van Elshocht, M. Jurczak, L. Goux, and C. Detavernier
ACS Appl. Mater. Interfaces 5(15), 6984-6989 (2013).

- **Comparison of two single-image phase-retrieval algorithms for in-line x-ray phase-contrast imaging**
M. Boone, W. Devulder, M. Dierick, L. Brabant, E. Pauwels and L. Van Hoorebeke
J. Opt. Soc. Am. A 29(12), 2667-2672 (2012).

Acknowledgements

Na meer dan 4 jaar onderzoek ben ik aan het laatste deel van mijn doctoraat gekomen, het dankwoord. Het is bijna niet te beschrijven wat ik allemaal heb bijgeleerd gedurende dit doctoraatsonderzoek. Verschillende mensen hebben mij hierbij geholpen en ik zou die personen dan ook graag willen bedanken.

In de eerste plaats wil ik mijn promotor, Christophe, bedanken. Eerst en vooral om mij de kans te geven om in zijn onderzoeksgroep CoCooN aan een doctoraat te beginnen, en voor het vertrouwen dat hij in mij had om een IWT-voorstel in te dienen en te verdedigen. Daarnaast uiteraard ook voor de begeleiding gedurende dit onderzoek en de vrijheid die ik gekregen heb. Verder wil ik ook Karl, mijn half-imec en half-CoCooN collega, bedanken. Bij hem kon ik altijd terecht voor het bespreken van resultaten en suggesties voor nieuwe experimenten.

Een woord van dank gaat uiteraard naar al mijn collega's van CoCooN. Het was leuk om in een hechte groep te kunnen werken waarin iedereen van iedereen bijleert. Kilian, Matthias en Karl wil ik bedanken voor het eeuwige geduld met al mijn XPS samples en voor ze telkens opnieuw op te meten. Davy en Geert zou ik willen bedanken om altijd bereid te zijn te helpen bij allerlei problemen in het labo. Bob en Kevin, bedankt voor de hulp, uitleg en discussies over LabView. Ik heb hier enorm veel uit opgestoken om mijn LabView projecten naar een hoger niveau te tillen. Ook alle andere (gewezen) groepsleden, Filip, Ranjith, Boris, Jan, Véronique, Tareq, Jeroen, Michiel, Felix, Eduardo, Thomas, Shaoren, Delphine, Jolien, Liesje, Jakob en Celine, wil ik bedanken voor de leuke samenwerking. Reinert en Tareq, ik vond het heel plezant om jullie te mogen begeleiden bij jullie masterthesis rond CBRAM. Het is leuk als studenten interesse hebben in het onderwerp waar je rond werkt, en bovendien zijn jullie er in geslaagd een mooie thesis te maken, met resultaten die heel nuttig waren. Bedankt daarvoor!

Stefaan, Lode en Jo, bedankt voor alle hulp en oplossingen die jullie hadden voor de technische kant van mijn doctoraat, waarbij ik bepaalde opstellingen moest (om)bouwen om mijn onderzoek te kunnen uitvoeren. Verder wil ik Nico bedanken voor de introductie tot XPS en Olivier voor de hulp bij SEM en EDX metingen (en uiteraard ook voor de vele interessante discussies, gaande van weten-

schap tot de koers en het veldrijden!). Ook de mensen van het secretariaat, Kristof, Wouter en Elly wil ik bedanken voor de hulp bij allerlei administratieve zaken. Uiteraard wil ik ook alle andere S1-collega's bedanken voor de voorbije vier jaar.

Dit doctoraatsonderzoek is uitgevoerd in samenwerking met imec, en ook al de mensen die hierbij betrokken waren wil ik langs deze weg bedanken. I especially would like to thank Ludovic, for all the discussions on CBRAM, the suggestions and ideas for further work, and the help with the interpretation of the data. This was very important an helpful for me to finish this work. Also Robert, Attilio, Umberto, Felix and Francesca, for all the help and interesting discussions. Ook de mensen van de Materials and Components Analysis groep wil ik bedanken voor de karakterisering van verschillende samples. In het bijzonder Johan Meersschaut voor de vele RBS metingen.

Om te eindigen wil ik mijn familie en vrienden bedanken voor alle leuke momenten, en om zo even mijn gedachten te verzetten. In het bijzonder al mijn loopvrienden van AC Deinze, de trainingen in de Brielmeersen en de verschillende wedstrijden waren steeds een moment om naar uit te kijken. Last but not least wil ik mijn ouders bedanken, gewoon voor alles dat ze voor mij doen en gedaan hebben, en voor de steun tijdens mijn doctoraat.

Wouter
Gent, januari 2016